UNIVERSITY OF CALIFORNIA SAN DIEGO

Preparation of Hot and Cold Ions for Photoelectron-Photofragment Coincidence Spectroscopy

A dissertation submitted in partial satisfaction of the

requirements for the degree Doctor of Philosophy

in

Chemistry

by

Ben B. Shen

Committee in charge:

Professor Robert E. Continetti, Chair
Professor Andrew Kummel
Professor Tadeusz F. Molinski
Professor Kalyanasundaram Seshadri
Professor Amitabha Sinha

2018

The Dissertation of Ben B. Shen is approved and it is acceptable in quality and form for publication on microfilm and electronically:

_____

_____

_____

_____

_____

Chair

University of California, San Diego

2018

DEDICATION

To my family, Estela Shen, Gwo-Jenn Shen, Frances Shen,

And Yoshi Shen

TABLE OF CONTENTS

LIST OF FIGURES

LIST OF TABLES

ACKNOWLEDGEMENTS

This thesis would not be possible without the support of many people both directly and indirectly. My thanks first and foremost is to my wife, Estela and my family. Without their support, I would have been lost and unable to push through difficult times. I would also like to thank my advisor Bob Continetti for his unending optimism, unwavering support, and effort to guide me to develop not only as a scientist but as a person as well. The skills I am walking away with are not just skills for the lab, but for life in general.

I would also like to thank all members of the Continetti Lab, both past and present. When I first joined, Chris Johnson was the only graduate student in the lab and he was kind enough to give me some of his time to help me understand concepts I was struggling with on top of guiding me on all aspects of the lab. In deciding which lab to join I still recall sitting down with him and asking if he was willing to put up with a constant stream of questions from me since there was no one else besides Bob to ask. Many members have since joined the lab with Berwyck Poad being the first post-doc I worked with. He was kind enough to give me guidance and worth with me on the tert-butoxide project. Amelia Ray has been invaluable as a friend and lab mate to lend an ear for me to bounce ideas off of and for assisting me in running experiments. Her assistance in fixing any issues that arose with the machine has also been a great help. She is also the primary cause of my coffee addiction in graduate school, which is not necessarily a bad thing. While I have not directly worked on a project with Rico Otto, his past work has been the basis for COAT and he has always been willing to assist me with answers to my questions not only regarding that project but many others as well. His advice has been

extremely helpful in completing COAT. It has also been a pleasure and a joy working with Katharine Lunny and Yanice Benitez. They worked with me closely on getting COAT up and running as well as during the troubleshooting period for the EIBT. Their laughter is infectious and have kept me positive when troubleshooting sometimes just seemed unending. I hope the machine treats them better than it has treated me. I would also like to thank our staff scientist Joseph Taulane who has been invaluable for helping me manufacture parts needed and assisting in planning projects. I would also like to thank Clayton Anderson, who was an undergrad working in our lab. I had fun working with him figuring out how to make/design HV switches. I would also like to thank the visiting scientists who have contributed to the work in this thesis. In particular Rich Thomas for sitting with me on late nights as I look for optimized settings for COAT and his willingness to get his hands dirty optimizing the RF generator and adjusting COAT positioning.

Other members of the lab who I have worked less closely with include Joel Rivera and Jen Daluz. I wish both of you the best and hope you do well. While they are on different projects, I have enjoyed the company of Morgan Miller, Katherine Nadler, and Brian Adamson. Morgan has been a riot to talk to for our mutual interest in computers and games in addition to letting me pester him with a few questions about circuits. Katherine has been a pleasure talking to on a variety of topics as and is always quick to laugh. Brian has been a wonderful resource for circuit design tips and who I owe thanks for repairing an expensive circuit board of theirs that I broke. Jemma Gibbard has also been wonderful to talk to and I hope I left enough working parts on Machine A for her to complete her project.

Besides the members of the Continetti lab, there are many people on campus assisted me. Carmen Alfaro has been a great assistance for the administrative portions of being in graduate school. Everyone in the Chemistry office for guiding graduate students. A special thanks to the UCSD machine shop as well, in particular Don and Bob for their ingenuity in solving problems that we have brought to them ranging from machining components and lending tools to advising on the best way to accomplish mechanical tasks.

Chapter 3, in full, is a reprint of the material as it appeared in Shen, B.; Poad, B.; Continetti, R., Photoelectron-Photofragment Coincidence Studies of the tert-Butoxide Anion $(CH3)_3CO^-$, the Carbanion Isomer $(CH3)_2CH_2COH^-$, and Corresponding Radicals. *Journal of Physical Chemistry a* **2014,** *118* (44), 10223-10232. The dissertation author is the primary author and the disertation advisor is the corresponding author.

Chapter 4 is a manuscript in preparation with authors Shen, B.; Lunny, K.; Benitez, Y; Continetti, R with the working title Photoelectron-photofragment coincidence spectroscopy with ions prepared in a cryogenic octopole accumulation trap. The dissertation author is the primary author and the dissertation advisor is the corresponding author.

Chapter 5, in full, is a reprint of the material as it appeared in Shen, B.; Benitez, Y.; Lunny, K.; Continetti, R., Internal energy dependence of the photodissociation dynamics of $O3^-$ using cryogenic photoelectron-photofragment coincidence spectroscopy. *Journal of Chemical Physics* **2017,** *147* (9). The dissertation author is the primary author and the disertation advisor is the corresponding author.

VITA

2009	Bachelor of Science, California State University, San Marcos
2009-2016	Research Assistant, University of California San Diego
2011	Master of Science, University of California San Diego
2018	Doctor of Philosophy, University of California San Diego

PUBLICATIONS

Shen, B. B.; Lunny, K. G.; Benitez, Y.; Continetti, R. E.; "Photoelectron-photofragment coincidence spectroscopy with ions prepared in a cryogenic octopole accumulation trap", *In preparation.*

Shen, B. B.; Benitez, Y.; Lunny, K. G.; Continetti, R. E.; "Internal energy dependence of the photodissociation dynamics of O_3^- using cryogenic photoelectron-photofragment coincidence spectroscopy", *The Journal of Chemical Physics*, 2017, 147, 094307; doi: http://dx.doi.org/10.1063/1.4986500

Ray, A. W.; Agarwal, J.; Shen, B. B.; Schaefer, H. F.; Continetti, R. E. "Energetics and Transition-State Dynamics of the the F + $HOCH_3$ → HF + OCH_3 Reaction," *Physical Chemistry Chemical Physics*, in press (2016); doi: 10.1039/c6cp06409d.

Ray, A. W.; Shen, B. B.; Poad, B. L. J.; Continetti, R. E. "State-Resolved Predissociation Dynamics of the Formyloxyl Radical," *Chemical Physics Letters*, 2014, *592*, 30–35; doi:10.1016/j.cplett.2013.11.06

Shen, B. B.; Poad, B. L. J.; Continetti, R. E. "Photoelectron Photofragment Coincidence Studies of the tert-Butoxide Anion $(CH_3)_3CO^-$, the Carbanion Isomer $(CH_3)_2CH_2COH^-$ and Corresponding Radicals" *The Journal of Physical Chemistry A;*2014, 118(44), 10223-10232; doi: 10.1021/jp5090235

Johnson, C. J., Shen, B. B., Poad, B. L. J. and Continetti, R. E., "Photoelectron-photofragment coincidence spectroscopy in a cryogenically cooled electrostatic ion beam trap," The *Review of Scientific. Instruments.* 2011, **82**, 105105; doi: 10.1063/1.3641875

Johnson, C. J., Poad, B. L. J., Shen, B. B., and Continetti, R. E., "Communication: New Insight into the barrier governing CO_2 formation from OH + CO," *Journal of Chemical Physics.* 2011, **134**, 171106; doi: http://dx.doi.org/10.1063/1.3589860

ABSTRACT OF THE DISSERTATION

Preparation of Hot and Cold Ions for Photoelectron-Photofragment Coincidence Spectroscopy

by

Ben B. Shen

Doctor of Philosophy in Chemistry

University of California San Diego, 2018

Professor Robert E. Continetti, Chair

Transient species play a central role in governing the chemical dynamics of reactions, but are difficult to study due to their short lifetime and high reactivity. By using kinematically complete techniques such as photoelectron-photofragment coincidence (PPC) spectroscopy, characteristics such as energetics and dissociative pathways for transient species can be studied. One major limitation of such a technique is

limited knowledge of the internal energy of the precursor ion prior to photoexcitation. While for some species, this information is less critical and can be inferred from combining theoretical calculations with experimental observations, other species are much more ambiguous.

One example is the tert-butoxy radical $(CH_3)_3CO$ which is a reaction intermediate in the combustion of tert-butyl alcohol, a candidate for alternative fuels. Due to the lack of α hydrogens with respect to the radical center leading to a low reactivity with O_2 as well as a large barrier to isomerization, unimolecular decomposition as the primary gas phase reaction pathway for this radical. Due to the method of ion selection being by mass, isomers of the tert-butoxy radical were taken into consideration for determining the dissociation dynamics observed. *Ab initio* calculations found that the dissociation of highly vibrationally excited tert-butoxy to methyl radical + acetone products is energetically very similar to theoretical *ab initio* calculations for the dissociative dynamics of its carbanion isomer ($(CH_3)_2C(CH_2)OH^-$) to methyl radical + propen-2-ol. Utilizing Franck-Condon simulations the observed dissociation dynamics was assigned to the photoexcitation of highly vibrationally excited tert-butoxide anion precursor.

While efforts to generate cold precursor ions to photoelectron photofragment coincidence spectroscopy have been carried out through the installation of an electrostatic ion beam trap, studies on tert-butoxy radical have shown that high frequency vibrations are not sufficiently cooled through supersonic expansion alone. To address this issue, the source for the PPC spectrometer has been redesigned to include a Wiley McLaren style ion extraction coupled with a cryogenic octopole accumulation trap (COAT) to allow for the preparation of both hot and cold of ions for PPC spectroscopy. The demonstration of

the effectiveness of COAT is demonstrated through the measurement of the dissociation dynamics of ozonide (O_3^-). Photoexcitation of O_3^- at 3.20 eV results in a stable channel and two dissociative pathways, $O^- + O_2$ and $O + O_2^-$. The $O + O_2^-$ channel in particular is observed as an autodetachment channel where an electron in O_2^- autodetaches when $v > 3$. At $hv = 3.20$ eV, the product O_2 ($v > 3$) is only energetically accessible from vibrationally excited O_3^- making this channel particularly sensitive to vibrational excitation of the precursor ion, O_3^-. Utilizing different trapping times and temperatures for COAT, the intensity of the autodetachment channel demonstrates the ability to generate not only vibrationally cold ions, but hot ions as well. Additionally, it was found that the autodetached electrons from $O_2^-(v'' = 4)$ exhibits resolved features consistent with bend (ν_2), asymmetric stretch (ν_3) and a stretching combination band ($\nu_1 + \nu_3$) in the intermediate electronic state.

Chapter 1 : Introduction and Background

The understanding of chemical reactions has evolved over the centuries from early alchemy to modern chemical reaction dynamics, all with the goal of better understanding how atoms and molecules interact in the natural world. The pace of progress in understanding of chemical processes has increased exponentially in the last century with the advent of quantum mechanics and the development of tools to test these theories - such as lasers and computers. For physical chemistry, the development of these tools has led to the field of spectroscopy, the study of the interaction between matter and electromagnetic radiation. Spectroscopy has played a central role in providing insight into the structures of chemicals and the dynamics of reactions by allowing for probing of chemical properties at the molecular and atomic level. In particular, photoelectron spectroscopy has been used to probe the electronic and geometric structure of molecules.[1-6] Photofragment translational spectroscopy provides insight into dissociative electronic states and reaction mechanisms of photodissociation processes.[7-9] Combined,[10] these two techniques lay the ground work for a deeper understanding of chemical reactions, potentially facilitating discovery into new ways to take advantage of chemical reactions to achieve goals such as dealing with climate change, exploring alternative fuels, and discovering more efficient ways to convert energy.

While recent advances have been significant, novel techniques must continue to be developed in order to further our understanding of the chemical and physical processes that govern chemical reactions. As our understanding of chemical reaction advance, so

too does our understanding of the complexity of chemical reactions. For example, consider the unimolecular decomposition of a triatomic molecule:

$$ABC \rightarrow \begin{cases} A + BC \\ AB + C \\ A + B + C \end{cases} \quad (1.1)$$

In this example, ABC has three product channels each of which have unique properties such as dissociation energy, transition states, and product states. The challenge for studying such a reaction lies in either controlling the reaction in such a way as to look at each pathway individually, or to use an experimental method that allows for the disentanglement of competing pathway.

The focus of this thesis is on the controlled preparation of ions used for studies of the energetics and reaction dynamics of transient species relevant to atmospheric and combustion reactions. Experimental studies were carried out using photoelectron-photofragment coincidence spectroscopy. In particular, dissociation dynamics of systems where vibrational excitation of precursor anion allows energetic access to different reaction dynamics were studied. To control the initial vibrational temperature of the ions, a cryogenic octopole accumulation trap was designed and implemented. But first, this chapter will review photoelectron and photofragment spectroscopy and the benefits of combining them into a kinematically complete experiment.

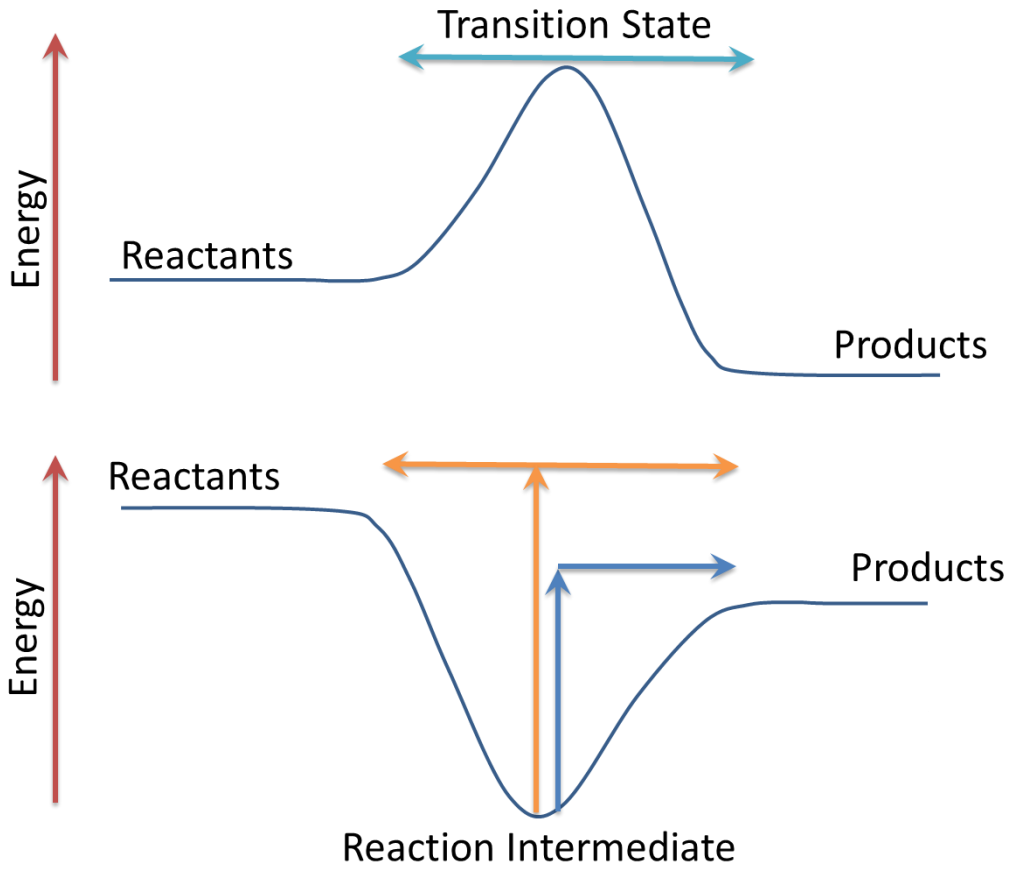

Figure 1.1. Reaction coordinate diagram for elementary reactions. Transition states (top) exist at potential energy maximum where energy is needed to proceed to products. Reaction intermediates (bottom) may proceed to products or be stabilized to a reaction intermediate.

1.1. Short-Lived Species: Reactive Free Radicals and Reaction Intermediates

Transient species can exist as elementary reactions proceed. As the evolution towards products can often be rapid, these transient species will be consumed and often exhibit very short lifetimes.[11] They may play a central role in governing the chemical dynamics of a reaction. These transient species can generally be classified into two main categories: transition states or reaction intermediates. To understand their role in a reaction, it is useful to consider the following generic chemical reaction:

$$AB + C \rightarrow [ABC] \rightarrow A + BC \qquad (1.2)$$

where A, B, and C are atoms or molecules and [ABC] is a transition state or reaction intermediate. As shown in Figure 1.1, the transition state lies at a potential energy maximum along the reaction coordinate and only exists for an instant as reactants are transformed into products by surmounting a barrier.[11] Reaction intermediates (bottom of Figure 1.1), on the other hand, exist for a period of time longer than a single molecular vibration and can be generated in a multi-step reaction mechanism in which they are later consumed. These reaction intermediates can be trapped prior to forming the products, if energy is removed, or if they are formed without enough energy to proceed to products. Free radicals, which are atoms or molecules with an unpaired electron, are one type of reaction intermediate. The unpaired electron makes free radicals highly chemically reactive, resulting in their comparatively short lifetime in bulk environments. Historically, the existence of reaction intermediates were inferred from chemical kinetic or thermodynamics experiments. Given their nature as short-lived, transient species are difficult to study as an experimentalist due to difficulty in generating and isolating them

on demand.[12] Conveniently, some reaction intermediates have a stable anion counterpart allowing for their manipulation through electrostatic interactions in the gas phase.

1.2. Experimental Techniques for Studying Reaction Intermediates

Due to their short lifetimes, transient reaction intermediates are difficult to isolate and study despite their importance in chemical reactions. Recent advances in experimental techniques have allowed for studying transient species in gas phase through methods including molecular beam scattering, state-resolved spectroscopy, and precursor-ion neutralization.[4, 10, 13] With the emergence of ultrafast lasers, transient species can be generated through photoexcitation or photodetachment, allowing for their selective formation on demand. This direct generation of the transient species allows transition states to be observed as "half-collisions," where the reaction dynamics post collision can be measured directly.[9] The focus of this thesis will be on the generation of transient neutral species of interest through photoexcitation or photodetachment of the corresponding closed-shell anion counterpart and studying the subsequent dissociation dynamics.

The generation and isolation of a reaction intermediate is a difficult and challenging task. Their short lifetimes make them difficult to isolate and study, while those intermediates which are stable are still difficult to generate in sufficient quantities. To circumvent this issue, stable precursor ions, with long lifetimes, followed by neutralization to generate the reaction intermediate are an attractive alternative. This can be done for cationic species, either through recombination with low-energy electrons or through charge exchange with an electron donor. Negative ions, as used in this thesis, can

be neutralized *via* photodetachment.[1, 4, 13] There are a number of methods employed as sources for negative ions, including thermal ion molecular reactor sources, electron transfer techniques and active electrical discharge.[14] The technique used in the current configuration of our instrument is an active electrical discharge which is known to generate ions with high vibrational excitation.[14, 15, 16] In addition, this type of source has been known to leave some ambiguity to the isomeric form of the ion generated.[14] These limitations can be tempered by utilizing a supersonic expansion of gas for the discharge to act on in order to reduce the vibrational excitation of ions generated. Supersonic expansions are generated by passing gas from high pressure to low pressure through a small orifice producing an adiabatic expansion of gas. Ideally, the carrier gas will cool the ions of interest during this process, leaving the center of the expansion vibrationally and rotationally cool. Supersonic expansions have been heavily utilized in gas-phase experiments for producing molecules with vibrational temperatures below 100 K and rotational temperatures below 20 K.[17] While this method has proven to be effective in cooling small ions,[18] larger ions have been found to still retain high vibrational temperatures as discussed in chapter 3.

Using ions to study transient species is convenient in that their manipulation can be achieved through well-established ion beam techniques. These ions can then be probed with a fixed wavelength laser to probe the potential energy surface, such as is done in photoelectron spectroscopy,[1, 4, 14] photofragment spectroscopy,[9] or photoexcitation.[19] Many variants on these techniques are used to elucidate molecular information, such as bond lengths, angles, and vibrational frequencies[3, 20] as well as energetic information

such as adiabatic electron affinity (AEA) and excited state information for transient species. These will be discussed in detail in sections 1.3.

1.3. Photoelectron Spectroscopy

Photoelectron spectroscopy has proven to be an invaluable technique to gain insight into the thermochemistry and electronic structure of molecules.[1, 4-6] It has also proven to be useful for studying transient species.[1, 4, 21] In anion photoelectron spectroscopy, negative ions are probed with a photon of fixed wavelength with energy greater than the AEA as follows:

$$ABC^- \xrightarrow{h\nu} ABC + e^- \quad (1.3)$$

The energy upon photoabsorption can be partitioned into either of the two products as kinetic energy for the electron or internal energy for the neutral. The internal energy for the neutral can be difficult to directly measure, but utilizing conservation of energy, the measured quantity, electron kinetic energy (eKE), can be defined by:

$$eKE = E_{hv} - AEA - E_{int} \quad (1.4)$$

where E_{int} is the internal energy of the resultant neutral. A typical direct photodetachment process is outlined in Figure 1.2 with E_{int} being partitioned to vibrational excitation of a stable neutral. Vibrational excitation in the anion (red lines) can lead to "hotbands" that show up with eKE higher than expected for a $0 \leftarrow 0$ transition. The amplitude for the hotbands is highly dependent on source conditions generating vibrationally excited precursor ions[18, 22, 23] but are usually small due to low population of ions in the

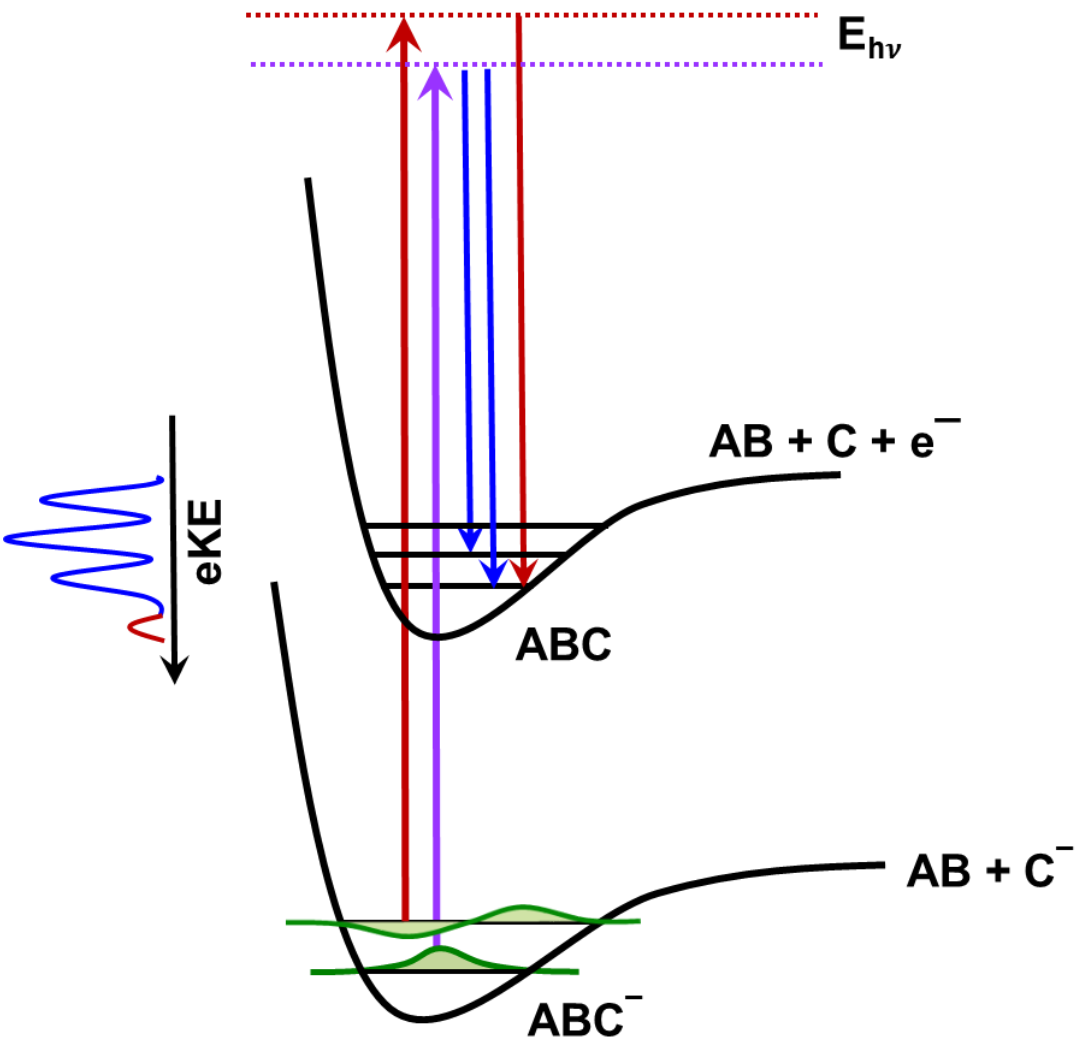

Figure 1.2. Schematic for anion photoelectron spectroscopy experiments. Absorption of a photon (purple) leaves the system in a neutral state with excess energy carried away by the outgoing electron (blue). Vibrationally excited anion can lead to higher eKE (red) than expected for a 0 ← 0 transition.

vibrationally excited states. The E_{int} energy of the products can be partitioned into electronic, vibrational, and/or rotational energy.

The observed energy partitioning in the products for E_{int} is dependent on the Franck-Condon principle. The Franck-Condon principle states that during an electronic transition, a change from one vibrational energy to another is more likely to happen if the two electronic wave functions overlap.[11] To understand when this occurs, it useful to work under the Born-Oppenheimer approximation,[24] the assumption is the nuclear motion in a molecule can be separated from the electron motion, ($\psi_{en} = \psi_e\psi_n$).[25] This assumption is reasonable due to electronic transitions occurring on a timescale that is "fast" relative nuclear motion so the atoms of a molecule can be considered "frozen" in space for the duration of an electronic transition.[9] Schematically, this is shown as a vertical arrow in Figure 1.2 with the anion geometry being projected onto the neutral potential energy surface. The intensity of an electronic transition can be described by:

$$I = \int \psi'^{*}_{el}\, \mu_{el} \psi_{el} d\tau_e \int S'^{*}_{vib} S_{vib}\, dR \qquad (1.5)$$

where $\psi'^{*}_{el}$and ψ_{el} are the anion and neutral electronic wavefuncions respectively. The first integral describes the electron-transition dipole moment and the second integral describes the vibrational overlap.[26] The square of the second integral is known as the Franck-Condon Factor (FCF) and can be considered a measure of the similarity in geometry between the initial and final states of an electronic transition.[11, 26, 27] A schematic demonstrating the Franck-Condon principle is shown in Figure 1.3. The wavefunctions for the ground, first excited, and second excited states are shown with the vertical arrow indicating the electronic transition. The overlap of the wavefunctions

contribute to the amplitude of the FCF as shown on the left side of Figure 1.3. Since the geometries of the anion and ground states are similar, and thus similar potential energy surfaces, the overlap of the 0 ← 0 vibrational transition is good giving a large amplitude to the FCF for that transition. The geometry difference between the anion and first excited state though are larger, and thus the 0 ← 0 vibrational transition is small. The 2 ← 0 vibrational transition has the largest FCF since it has the largest wavefunction overlap with the anion v = 0 state. The same principle holds for transitions from vibrationally excited states of the anion as seen in the red lines. The relative intensities in a photoelectron spectrum for vibrational transitions are given by:

$$I(v'', v') = \sigma_0 v_c FCF(v'', v'; K)\, e^{\left[-\frac{G_0''(v'')}{kT''}\right]} \quad (1.6)$$

where $\sigma_0$is a scaling factor, v_c is velocity for the corresponding electron kinetic energy, and the exponential factors in the relative population of the vibrational states at a temperature T''.[28] As stated previously, the amplitudes from vibrationally excited states of the anion are often experimentally observed as low due to the comparatively small populations for vibrationally excited ions.[27]

As seen from the stick structures on the left side of Figure 1.3, vibrational excitation causes significant spectral congestion due to sequence bands. This has been observed in experiments on O_3^- discussed in Chapters 4 and 5 as well as in the first photoelectron spectrum of O_3^- reported.[29]

While photoelectron experiments can provide a wealth of knowledge, one weakness is the lack of a direct measure of atomic or molecular products after photodetachment. Any dissociation dynamics of the resultant molecule are not directly

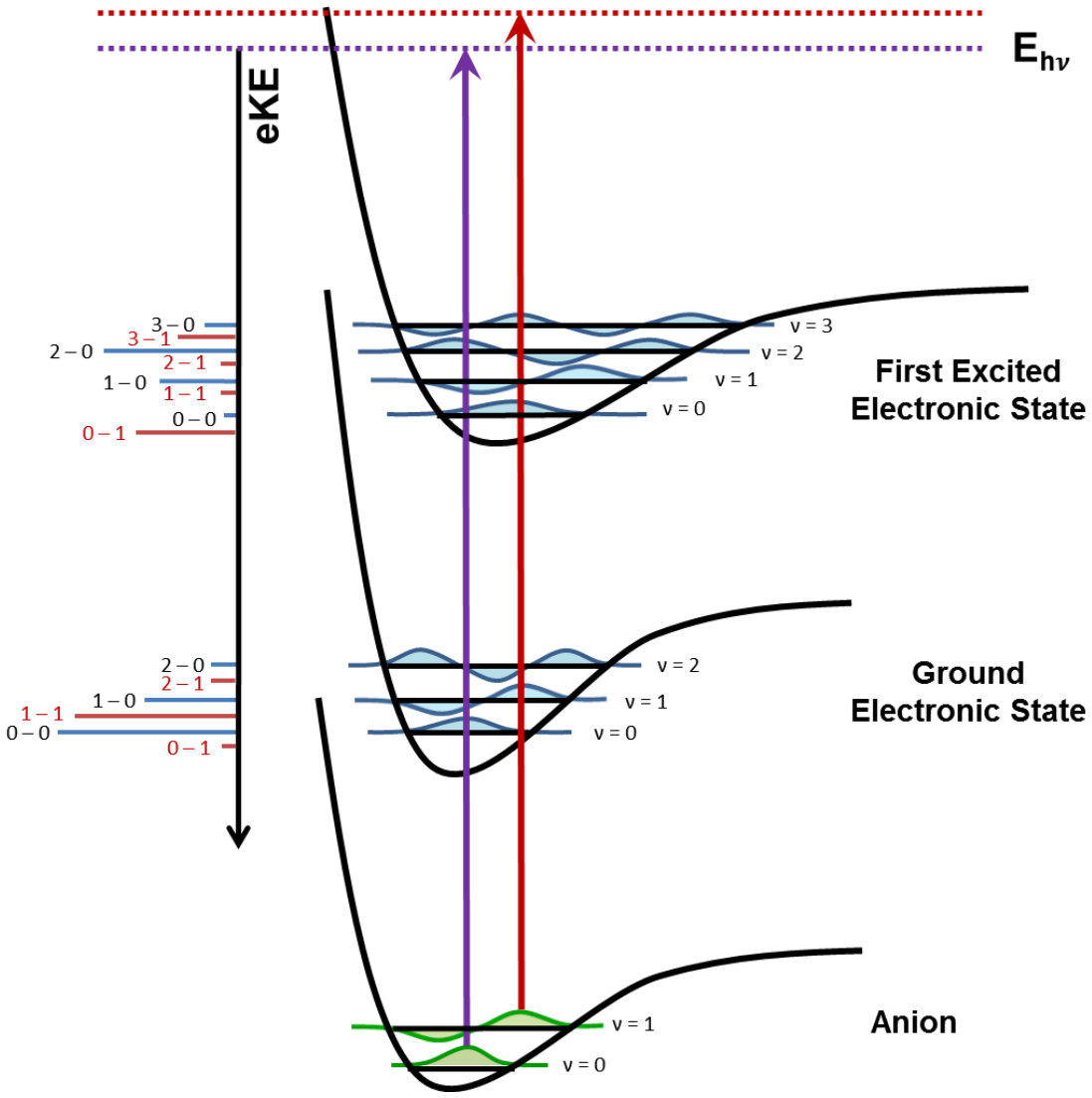

Figure 1.3. Schematic (not to scale) visualizing wave function overlap with the corresponding Franck-Condon Factors shown on the left side for ground state and with one quanta of vibrational excitation in the anion.

observed and are therefore "lost," but this does not preclude inferring dissociation dynamics from theoretical calculations in combination with features from photodetachment. This is the case for the first photoelectron studies on ozonide (O_3^-) where the low kinetic energy electrons detected, from autodetachment of O_2^- after photodestruction of O_3^-, was assumed to be a new electronic state of neutral ozone (O_3).[29] Later, it was correctly identified as autodetachment of O_2^- in a photodetachment study by Mann and coworkers.[30]

1.4. Photofragment Translational Spectroscopy

As photoelectron spectroscopy measures the amount of energy that is imparted onto the ejected electron upon a photodetachment event, photofragment translational spectroscopy measures the energy that is partitioned to kinetic energy for a dissociative event. This technique has been used for probing the dissociation dynamics of molecules and complexes determining photofragment product excited states and energetics.[7, 9, 19] The general schematic for photofragment translational spectroscopy is shown in Figure (1.4) where a molecule (ABC^-) is fragmented to AB^- + C. The energy partitioned to kinetic energy release (KER) can be determined through analysis of the momenta of each fragment. The KER is defined by:

$$KER = E_{h\upsilon} - \Delta D°(ABC^-) - E_{int} \quad (1.7)$$

Where $E_{h\upsilon}$ is the photon energy, $\Delta D°$ is the dissociation energy, and E_{int} is energy partitioned into internal degrees of freedom for both fragments. Since KER is measured,

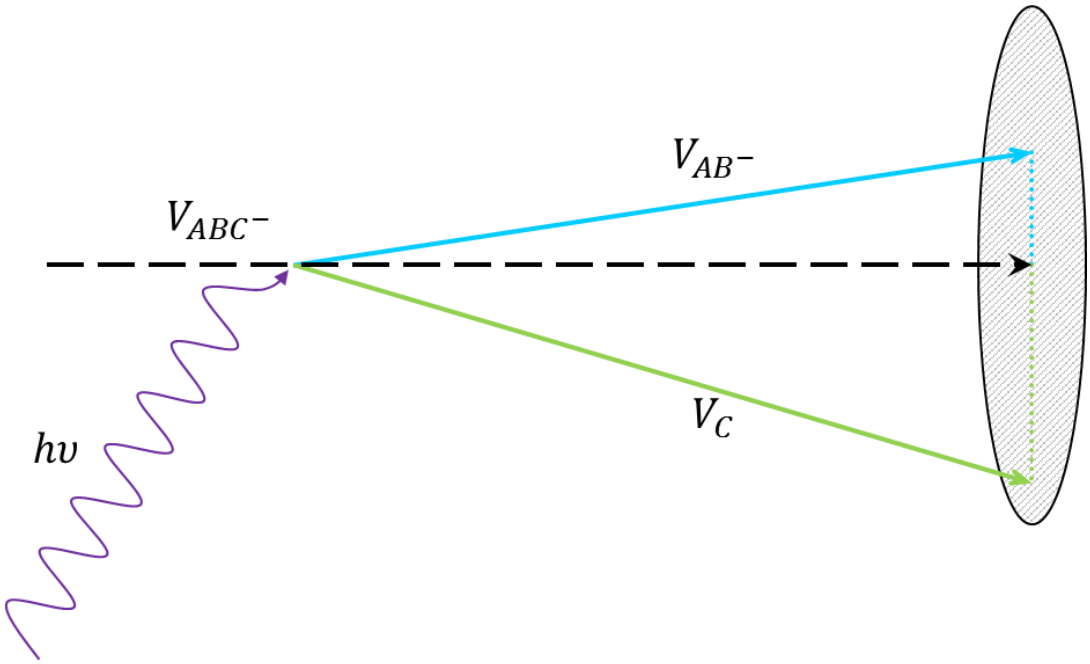

Figure 1.4. Experimental setup for photofragment translational spectroscopy. Kinetic energy release (KER) upon fragmentation is observed as the translational energy of the fragments relative to the center of mass velocity.

E_{int} can be determined through conservation of energy where any energy that is not attributed to the fragment or electron kinetic energies must be assigned to internal excitation. If multiple fragmentation pathways exist, they can be distinguished through calculating the product masses utilizing conservation of momentum. While the linear momentum of the two fragments are equal the differences in mass means a difference in velocity in turn affecting the location they impact the detector. The lighter fragment will impact the detector further away from the centerline of the ion beam than the heavier particle.

If photoexcitation results in a photodetachment event yielding a transient species in an unbound state, as shown in Figure (1.5), KER of the fragments can be defined as:

$$KER = \mathrm{E_{h\upsilon}} - eKE - \Delta D°(ABC^-) - AEA(C^-) - E_{int} \qquad (1.8)$$

Where eKE is the electron kinetic energy, and AEA is the adiabatic electron affinity. As shown in the schematic, the KER is determined by the vertical FCF overlap with the dissociative curve. This, of course, requires that eKE be measured in order to draw a complete picture of the reaction dynamics. This limitation is demonstrated in Figure 1.4 where the internal excitation of the products may yield similar KER with the difference in energy carried away by the electron. Photofragment translational spectroscopy alone would not allow for fully determining product internal excitation.

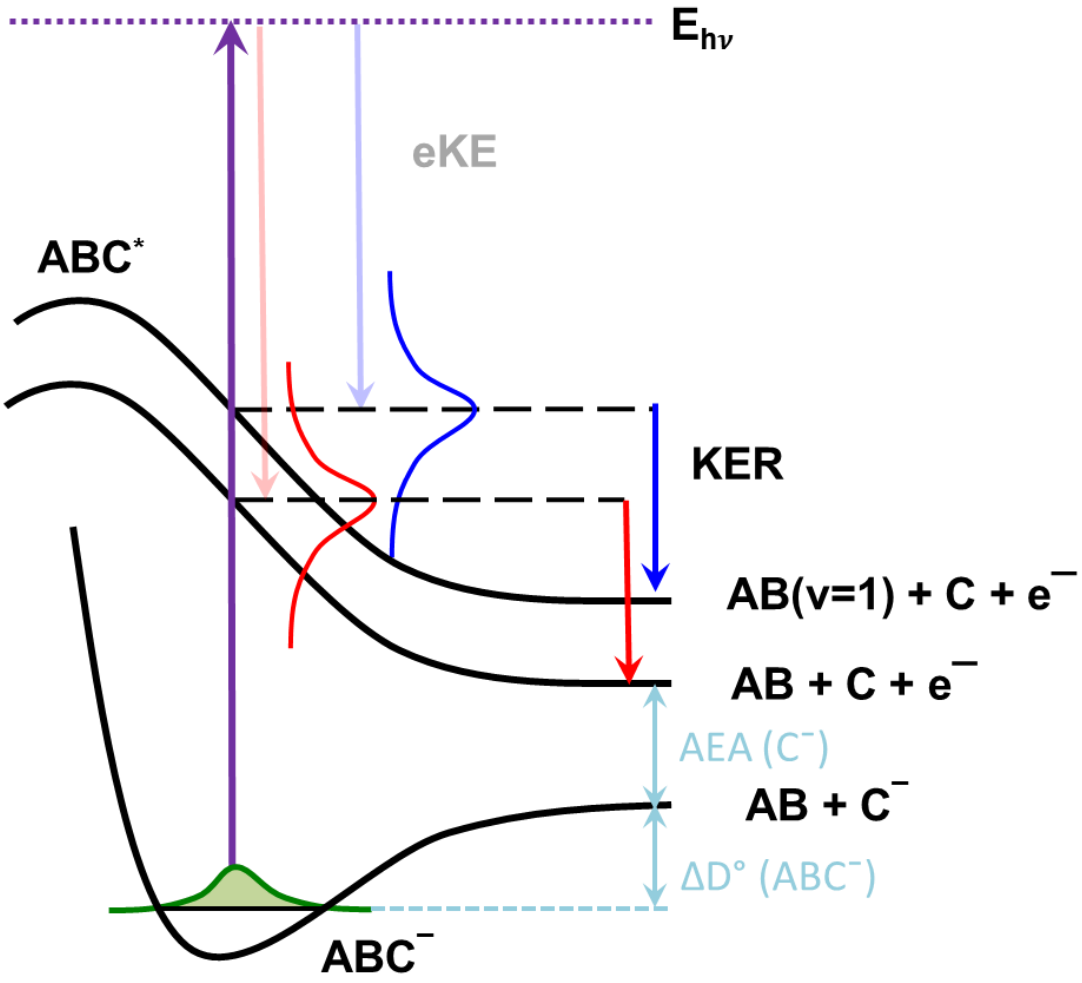

Figure 1.5. Reaction coordinate diagram showing energy partitioning for dissociative photodetachment translational spectroscopy. Absorption of a photon (purple) accesses dissociative curves releasing translational energy with excess energy carried away by the outgoing electron.

1.5. Photoelectron-Photofragment Coincidence Spectroscopy

To bridge this gap, photoelectron-photofragment coincidence spectroscopy (PPC) is an experimental technique that combines the strength of both photoelectron and photofragment spectroscopic techniques to characterize the dissociation dynamics of transient neutrals in a kinematically complete fashion.[10, 13, 31] This technique is utilized in this thesis to measure the photoelectron kinetic energy in coincidence with the kinetic energy release (also referred to as translational energy release (E_T)) to measure all energy partitioned to kinetic energy allowing for partitioning in the E_{int} to be deduced. PPC spectroscopy has also allowed for discerning different product electronic and vibrationally excited states[32] as well as studying transient species with tunneling lifetimes on the same order as the time of flight from the interaction region to the detector.[18, 33]

The kinetic energies for all particles can be plotted in a coincidence spectrum to reveal reaction dynamics such as energy partitioning. Two pathways are shown in Figure (1.6): direct and indirect dissociation. In both pathways, the maximum kinetic energy (KE_{max}) is determined by assuming all products and precursor anions are in their ground vibrational and rotational states (E_{int} = 0), treating all energy as being partitioned into translational energy:

$$KE_{MAX} = E_{h\upsilon} - AEA(C^-) - \Delta D°(ABC^-) \quad (1.9)$$

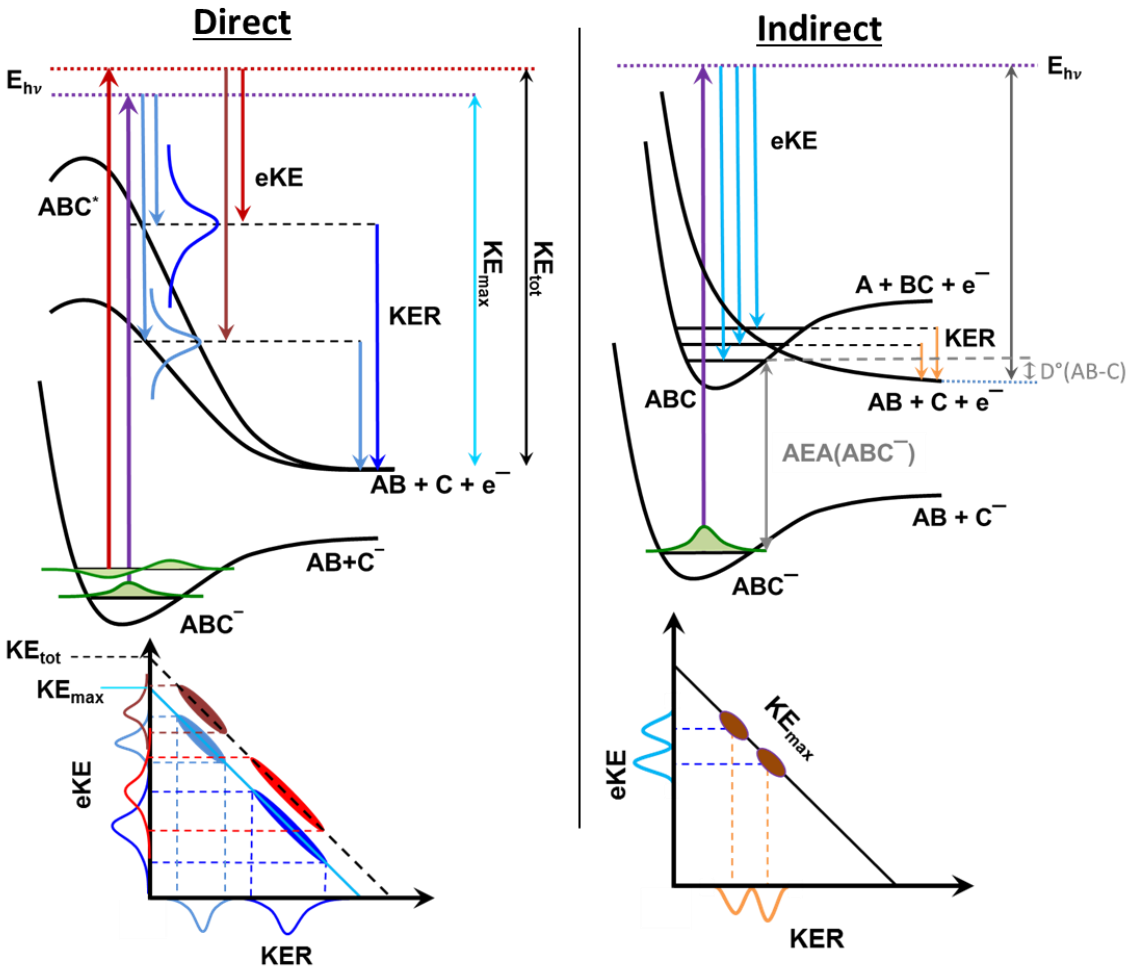

Figure 1.6. Schematic for direct (left) and indirect (right) dissociative photodetachment with corresponding PPC spectroscopy coincidence plots.

where $E_{h\upsilon}$ is photon energy, AEA is the adiabatic electron affinity of C^-, and $\Delta D°$ is the dissociation energy of (ABC^-). In some cases, the total translational energy (KE_{tot} = eKE + KER) is greater than the KE_{max} which is usually a result of either assuming the wrong dissociation dynamics or vibrationally excited precursor anions resulting in vibrational energy in addition to photon energy is available for reaction dynamics. Direct dissociative photodetachment results from accessing purely repulsive surfaces. In this example (Figure 1.6, left side) two curves are shown to demonstrate how the data would shift depending on the shape of the dissociative curve. Wavefunction overlap with a higher energy repulsive surface results in lower eKE and a higher KER, whereas a lower energy surface results in higher eKE and lower KER. On the other hand, indirect dissociative photodetachment (Figure 1.6, right side) occurs when a dissociative surface crosses a bound surface. For this dissociation pathway, photodetachment yields the neutral (ABC) in which only the vibrationally excited neutral with > 1 quanta of vibrational excitation have a probability of hopping onto the dissociative surface, assuming they have a lifetime of one vibration. This results in a series of peaks separated by the vibrational energy of the neutral along a KE_{tot}.[34]

In cases where dissociation along a reaction coordinate must cross a transition state barrier to reach final products, horizontal lines can also be drawn on the coincidence plot to indicate electron kinetic energy limits for the dissociative process. For a given dissociation, the maximum energy that can be carried away by the electron can be calculated by:

$$eKE_{MAX} = \mathrm{E_{h\upsilon}} - E(ABC)^{\ddagger} - AEA(ABC^-) \qquad (1.10)$$

where $E(ABC)^{\ddagger}$ is the difference in energy between the neutral (ABC) and the transition state. The amount of energy that is not carried away by the electron is the amount of energy left in E_{int}. If this quantity is less than the energy required to cross the transition state, then dissociation would be energetically forbidden.

Precursor ion temperatures pose problems with analyzing reaction dynamics due to the distribution of initial internal energy ($E_{int} > 0$) rather than the typically assumed $E_{int} = 0$. If the precursor anions are vibrationally excited, the total available energy increases, allowing an observed KE_{tot} that is greater than the expected KE_{max}. This can also be problematic when looking at eKE_{max}, due to internal excitation allowing for higher eKE as observed for the *tert*-butoxy radical discussed in Chapter 3.

While some features are observed as diagonal lines in the coincidence plot, additional complicated reaction mechanisms, such as tunneling to dissociation, metastable neutrals, autodetachment, and multiphoton processes, leave identifying signatures in the form of horizontal bands. In the case of tunneling, dissociation below the energetic limit in combination with a horizontal band were featured.[18, 35, 36] In the case of autodetachment (discussed in detail in Chapter 4), a series of horizontal bands at low eKE with the energetic spacing for O_2 confirmed the assignment. These mechanisms can be fully identified using PPC spectrometry due to the ability to completely account for the kinetic energies of all particles.

1.6. Ion Storage Techniques

The challenge of studying transient species lies heavily in the ability to generate them in large enough number densities and in a known initial state. To assist with this

goal, ion storage devices have been utilized to store charged particles, allowing for their manipulation and study. These devices generally fall into two categories: beam traps which confine the ions with a well-defined velocity along a trajectory like an electrostatic ion beam trap (EIBT)[22, 37] and radiofrequency (RF) traps which confine the ions within a volume with low kinetic energy such as a Paul[38] or Penning trap.[39]

Ion beam traps have been used in a variety of experimental setups such as electron collision studies,[40] to linear beam traps used as high resolution mass spectrometers.[41, 42] Currently, the PPC spectrometer utilizes an EIBT as a method for recycling ions - allowing repetitive probing of an ion packet over a period of time. The linear beam traps store an ion beam by oscillating the ions between two electrostatic mirrors. This is detailed further in Chapter 2. The primary goal for installation of the EIBT was to allow for the generation of precursor anions with less internal excitation, for which it was extremely successful,[18, 22] though it was found that some high frequency modes for ions were not efficiently cooled.[16] Unfortunately, since the ion storage must take place in ultra-low vacuum, collisional cooling is not possible. This leaves the primary method of cooling within the EIBT to be radiative, which is typically a very slow process.[43, 44]

RF traps such as the Paul trap are most well known for being utilized in mass spectrometers though their use includes trapping atoms for quantum computing,[45, 46] and cooling ions for experimentation.[47-49] These traps generally operate using time dependent RF fields to trap the ions within a volume. While the traditional Paul trap has worked very well for ion cooling, the storage volume for ions is small. One variant of the localizing traps is the linear ion trap which are often referred to by the number of RF rods

used to confine the ions within the space. These traps are elongated along one axis with multiple rods surrounding the trapping volume to increase the quantity of ions that can be stored as well as decreasing the influence of the RF on the ions.[50] The number of rods for these traps range from 4 to 22 with the benefit of the larger number of poles being a flatter potential minima in the center of the trap, allowing for minimal disturbance of the ions trapped within.[50-52]

These linear traps have been utilized to cool ions down to temperatures as low as 10 K via buffer gas cooling. [53, 54] Buffer gas cooling operates through collision of ions with gases such as He and H_2 at cryogenic temperatures allowing the ions to thermalize with the inert gases. Operating temperatures, however, are not limited to cryogenic temperatures. Thermalization of ions with buffer gas also works over a large range of temperatures providing a method for controlling ion temperatures.[55] Ultimately these properties led to the addition of a cryogenic octopole accumulation trap (COAT) to the PPC spectrometer discussed in detail in Chapters 2 and 3.

1.7. Thesis Outline

This introduction provides the necessary theory and background to understand the data presented in the subsequent chapters of this thesis. The next chapter details the experimental apparatus and data analysis including the installation of a cryogenic octopole accumulation trap (a linear radiofrequency ion trap) as well as a modified electron detector. The experimental results start with the study of the tert-butoxide anion in chapter 3. The remaining chapters (4 and 5) focus on the implementation and

characterization of COAT, as well as the change in reaction dynamics in the photodissociation of ozonide upon heating and cooling ozonide.

1.8. References

1. Lineberger, W.; Johnson, M.; Martinez, T., Once upon Anion: A Tale of Photodetachment. *Annual Review of Physical Chemistry, Vol 64* **2013,** *64*, 21-36.

2. Ervin, K.; Anusiewicz, W.; Skurski, P.; Simons, J.; Lineberger, W., The only stable state of O-2(-) is the X (2)Pi(g) ground state and it (still!) has an adiabatic electron detachment energy of 0.45 eV. *Journal of Physical Chemistry a* **2003,** *107* (41), 8521-8529.

3. Arnold, D.; Xu, C.; Kim, E.; Neumark, D., Study Of Low-Lying Electronic States Of Ozone By Anion Photoelectron-Spectroscopy Of O-3(-). *Journal of Chemical Physics* **1994,** *101* (2), 912-922.

4. Neumark, D. M., Probing Chemical Dynamics With Negative Ions. *Journal of Chemical Physics* **2006,** *125* (13).

5. Mabbs, R.; Surber, E.; Sanov, A., Photoelectron Imaging of Negative Ions: Atomic Anions to Molecular Clusters. *Analyst* **2003,** *128* (6), 765-772.

6. Sanov, A.; Mabbs, R., Photoelectron Imaging of Negative Ions. *International Reviews in Physical Chemistry* **2008,** *27* (1), 53-85.

7. Oudejans, L.; Miller, R., Photofragment Translational Spectroscopy of Weakly Bound Complexes: Probing the Interfragment Correlated Final State Distributions. *Annual Review of Physical Chemistry* **2001,** *52*, 607-637.

8. Sherwood, C.; Hanold, K.; Garner, M.; Strong, K.; Continetti, R., Translational Spectroscopy Studies of the Photodissociation Dynamics of O-4(-). *Journal of Chemical Physics* **1996,** *105* (24), 10803-10811.

9. Ashfold, M.; Lambert, I.; Mordaunt, D.; Morley, G.; Western, C., Photofragment Translational Spectroscopy. *Journal of Physical Chemistry* **1992,** *96* (7), 2938-2949.

10. Continetti, R. E., Coincidence Spectroscopy. *Annual Review of Physical Chemistry* **2001,** *52* (1), 165-192.

11. McQuarrie, D. A.; Simon, J. D., *Physical Chemistry a Molecular Approach*. University Science Books: Sausalito, CA, 1997; p 1360.

12. Klippenstein, S.; Pande, V.; Truhlar, D., Chemical Kinetics and Mechanisms of Complex Systems: A Perspective on Recent Theoretical Advances. *Journal of the American Chemical Society* **2014,** *136* (2), 528-546.

13. Continetti, R. E., Photoelectron-Photofragment Coincidence Studies of Dissociation Dynamics. *International Reviews in Physical Chemistry* **1998,** *17* (2), 227-260.

14. Corderman, R.; LineBerger, W., Negative-Ion Spectroscopy. *Annual Review of Physical Chemistry* **1979,** *30*, 347-378.

15. Sanz, M.; McCarthy, M.; Thaddeus, P., Vibrational Excitation and Relaxation of Five Polyatomic Molecules in an Electrical Discharge. *Journal of Chemical Physics* **2005,** *122* (19).

16. Shen, B.; Poad, B.; Continetti, R., Photoelectron-Photofragment Coincidence Studies of the tert-Butoxide Anion $(CH_3)_3CO^-$, the Carbanion Isomer $(CH_3)_2CH_2COH^-$, and Corresponding Radicals. *Journal of Physical Chemistry a* **2014,** *118* (44), 10223-10232.

17. Smalley, R. E.; Wharton, L.; Levy, D. H., Molecular Optical Spectroscopy with Supersonic Beams and Jets. *Accounts of Chemical Research* **1977,** *10* (4), 139-145.

18. Johnson, C.; Otto, R.; Continetti, R., Spectroscopy and Dynamics of the HOCO Radical: Insights into the OH + CO -> H + CO2 Reaction. *Physical Chemistry Chemical Physics* **2014,** *16* (36), 19091-19105.

19. Ng, C.; Johnson, M.; Martinez, T., State-to-State Spectroscopy and Dynamics of Ions and Neutrals by Photoionization and Photoelectron Methods. *Annual Review of Physical Chemistry, Vol 65* **2014,** *65*, 197-224.

20. Johnson, C. J.; Harding, M. E.; Poad, B. L. J.; Stanton, J. F.; Continetti, R. E., Electron Affinities, Well Depths, and Vibrational Spectroscopy of cis- and trans-HOCO. *Journal of the American Chemical Society* **2011,** *133* (49), 19606-19609.

21. Neumark, D., Time-resolved Photoelectron Spectroscopy of Molecules and Clusters. *Annual Review of Physical Chemistry* **2001,** *52*, 255-277.

22. Johnson, C. J.; Shen, B. B.; Poad, B. L. J.; Continetti, R. E., Photoelectron-Photofragment Coincidence Spectroscopy in a Cryogenically Cooled Linear Electrostatic Ion Beam Trap. *Review of Scientific Instruments* **2011,** *82* (10), 105105.

23. Corderman, R.; Engelking, P.; Lineberger, W., Laser Photoelectron Spectrometry Measurement Of Characteristic Electronic And Vibrational Temperatures Of Sputtered Negative-Ions. *Applied Physics Letters* **1980,** *36* (7), 533-535.

24. Born, M.; Oppenheimer, R., Quantum Theory of Molecules. *Annalen Der Physik* **1927,** *84* (20), 0457-0484.

25. Tully, J., Perspective on "Zur Quantentheorie der Molekeln" - Born M, Oppenheimer R (1927) Ann Phys 84 : 457. *Theoretical Chemistry Accounts* **2000,** *103* (3-4), 173-176.

26. Bernath, P. F., *Spectra of Atoms and Molecules*. Second Edition ed.; Oxford University Press Oxford New York, 2005; p 439.

27. Ervin, K.; Ho, J.; Lineberger, W., Ultraviolet Photoelectron-Spectrum of NO2-. *Journal of Physical Chemistry* **1988,** *92* (19), 5405-5412.

28. Ervin, K. M.; Lineberger, W. C., *Photoelectron Spectroscopy of Molecular Anions*. JAI Press Inc.: 1992; Vol. 1.

29. Novick, S.; EngelKing, P.; Jones, P.; Futrell, J.; Lineberger, W., Laser Photoelectron, Photodetachment, And Photodestruction Spectra Of O-3-. *Journal of Chemical Physics* **1979,** *70* (6), 2652-2662.

30. Mann, J.; Troyer, M.; Jarrold, C., Photoelectron Imaging and Photodissociation of Ozonide in O-3(-)center dot(O-2)(n) (n=1-4) clusters. *Journal of Chemical Physics* **2015,** *142* (12).

31. Hanold, K. A.; Luong, A. K.; Clements, T. G.; Continetti, R. E., Photoelectron-Multiple-Photofragment Coincidence Spectrometer. *Review of Scientific Instruments* **1999,** *70* (5), 2268-2276.

32. Hanold, K. A.; Continetti, R. E., Photoelectron-photofragment Coincidence Studies of the Dissociative Photodetachment of O_4^-. *Chemical Physics* **1998,** *239* (1-3).

33. Johnson, C. J.; Continetti, R. E., Dissociative Photodetachment Studies of Cooled HOCO- Anions Revealing Dissociation Below the Barrier to H + CO2. *Journal of Physical Chemistry Letters* **2010,** *1* (12), 1895-1899.

34. Ray, A.; Shen, B.; Poad, B.; Continetti, R., State-resolved Predissociation Dynamics of the Formyloxyl Radical. *Chemical Physics Letters* **2014,** *592*, 30-35.

35. Johnson, C. J.; Poad, B. L. J.; Shen, B. B.; Continetti, R. E., Communication: New Insight into the Barrier Governing CO2 Formation From OH+CO. *Journal of Chemical Physics* **2011,** *134* (17), 4.

36. Johnson, C. J.; Continetti, R. E., Dissociative Photodetachment Studies of HOCO-: Insights into the OH Plus CO Entrance Channel for the Reaction OH Plus CO -> H + CO2. *Abstracts of Papers of the American Chemical Society* **2013,** *245*.

37. Zajfman, D.; Rudich, Y.; Sagi, I.; Strasser, D.; Savin, D.; Goldberg, S.; Rappaport, M.; Heber, O., High Resolution Mass Spectrometry Using a Linear Electrostatic Ion Beam Trap. *International Journal of Mass Spectrometry* **2003,** *229* (1-2), 55-60.

38. Paul, W., Electromagnetic Traps For Charged And Neutral Particles. *Reviews of Modern Physics* **1990,** *62* (3), 531-540.

39. Brown, L.; Gabrielse, G., Geonium Theory - Physics Of A Single Electron Or Ion In A Penning Trap. *Reviews of Modern Physics* **1986,** *58* (1), 233-311.

40. Heber, O.; Witte, P.; Diner, A.; Bhushan, K.; Strasser, D.; Toker, Y.; Rappaport, M.; Ben-Itzhak, I.; Altstein, N.; Schwalm, D.; Wolf, A.; Zajfman, D., Electrostatic Ion Beam Trap for Electron Collision Studies. *Review of Scientific Instruments* **2005,** *76* (1).

41. Greenwood, J.; Kelly, O.; Calvert, C.; Duffy, M.; King, R.; Belshaw, L.; Graham, L.; Alexander, J.; Williams, I.; Bryan, W.; Turcu, I.; Cacho, C.; Springate, E., A Comb-Sampling Method for Enhanced Mass Analysis in Linear Electrostatic Ion Traps. *Review of Scientific Instruments* **2011,** *82* (4).

42. Bhushan, K.; Gadkari, S.; Yakhmi, J.; Sahni, V., Electrostatic Ion Trap and Fourier Transform Measurements for High-Resolution Mass Spectrometry. *Review of Scientific Instruments* **2007,** *78* (8).

43. Dunbar, R.; Chen, J.; So, H.; Asamoto, B., Infrared Fluorescence Relaxation of Photoexcited Gas-Phase Ions By Chopped-Laser 2-Photon Dissociation. *Journal of Chemical Physics* **1987,** *86* (4), 2081-2086.

44. Dunbar, R., Infrared Radiative Cooling Of Isolated Polyatomic-Molecules. *Journal of Chemical Physics* **1989,** *90* (12), 7369-7375.

45. Seidelin, S.; Chiaverini, J.; Reichle, R.; Bollinger, J.; Leibfried, D.; Britton, J.; Wesenberg, J.; Blakestad, R.; Epstein, R.; Hume, D.; Itano, W.; Jost, J.; Langer, C.; Ozeri, R.; Shiga, N.; Wineland, D., Microfabricated Surface-Electrode Ion Trap for Scalable Quantum Information Processing. *Physical Review Letters* **2006,** *96* (25).

46. Leibfried, D.; Wineland, D.; Blakestad, R.; Bollinger, J.; Britton, J.; Chiaverini, J.; Epstein, R.; Itano, W.; Jost, J.; Knill, E.; Langer, C.; Ozeri, R.; Reichle, R.; Seidelin, S.; Shiga, N.; Wesenberg, J., Towards Scaling Up Trapped Ion Quantum Information Processing. *Hyperfine Interactions* **2007,** *174* (1-3), 1-7.

47. Leuthner, H.; Werth, G., Buffer-Gas-Cooled Ion Clouds in a Classical Paul Trap: Superimposed Stability Diagrams and Trapping Capacity Investigations. *Applied Physics B-Lasers and Optics* **2014,** *114* (1-2), 89-98.

48. Kamrath, M.; Garand, E.; Jordan, P.; Leavitt, C.; Wolk, A.; Van Stipdonk, M.; Miller, S.; Johnson, M., Vibrational Characterization of Simple Peptides Using Cryogenic Infrared Photodissociation of H-2-Tagged, Mass-Selected Ions. *Journal of the American Chemical Society* **2011,** *133* (16), 6440-6448.

49. Wang, X.; Wang, L., Development of a Low-Temperature Photoelectron Spectroscopy Instrument Using an Electrospray Ion Source and a Cryogenically Controlled Ion Trap. *Review of Scientific Instruments* **2008,** *79* (7).

50. Gerlich, D., Inhomogeneous RF-Fields - A Versatile Tool For The Study Of Processes With Slow Ions. *Advances in Chemical Physics* **1992,** *82*, 1-176.

51. Gerlich, D., Ion-Neutral Collisions In A 22-Pole Trap At Very-Low Energies. *Physica Scripta* **1995,** *T59*, 256-263.

52. Asvany, O.; Schlemmer, S., Numerical Simulations of Kinetic Ion Temperature in a Cryogenic Linear Multipole Trap. *International Journal of Mass Spectrometry* **2009,** *279* (2-3), 147-155.

53. Hock, C.; Kim, J.; Weichman, M.; Yacovitch, T.; Neumark, D., Slow Photoelectron Velocity-Map Imaging Spectroscopy of Cold Negative Ions. *Journal of Chemical Physics* **2012,** *137* (24).

54. Boyarkin, O.; Kopysov, V., Cryogenically Cooled Octupole Ion Trap for Spectroscopy of Biomolecular Ions. *Review of Scientific Instruments* **2014,** *85* (3).

55. Wester, R., Radiofrequency Multipole Traps: Tools for Spectroscopy and Dynamics of Cold Molecular Ions. *Journal of Physics B-Atomic Molecular and Optical Physics* **2009,** *42* (15).

Chapter 2 : Experimental Methods and Data Analysis

The challenges in studying transient species include stabilizing and generating them in large enough quantities for study with a controlled method. These challenges are addressed by utilizing a photoelectron-photofragment coincidence (PPC) spectrometer to carry out the experiments discussed in this thesis,[1] shown in Figure 2.1. The PPC spectrometer consists of an ion source, accelerator and ion optics, a laser interaction region, and microchannel-plate based electron and multi-particle neutral detectors. The inclusion of both detectors enables determination of energy partitioning for a photoinduced event by detection of photodetached electrons in coincidence with neutrals. This is achieved by utilizing fast (keV) ion beam techniques to control precursor anions, including the ability to separate out masses by time of flight, having a well-defined ion beam for center-of-mass (CM) calculations, and allowing for detection of neutral particles that would normally be undetectable with MCPs at low kinetic energies. The strength of the PPC spectrometer lies in its ability to determine the momenta of all products - allowing for the calculation of product mass ratios, scattering angles, and CM kinetic energy release for dissociation events as discussed in Sections 2.3.2 and 2.4.3. By limiting the experimental rate to one event per laser shot, products corresponding to events from the interaction between the laser shot and a single molecule can be correlated.

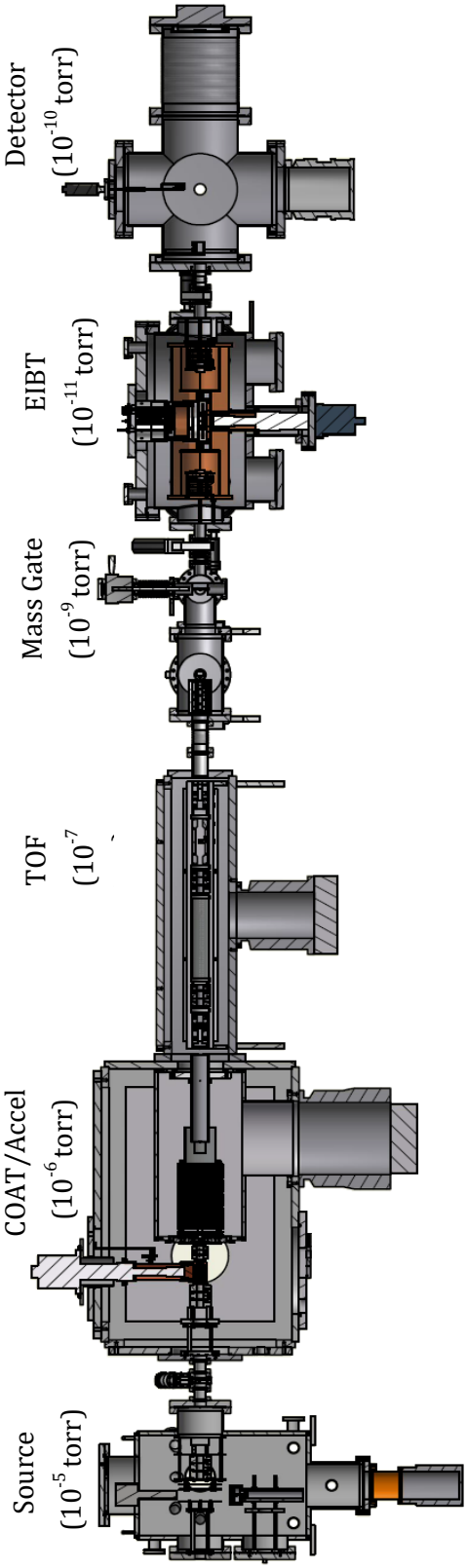

Figure 2.1. Cross-section of the PPC spectrometer including operational pressures.

2.1 Photoelectron-Photofragment Coincidence Spectrometer

The experiments in this thesis consist of using the PPC spectrometer in two configurations, prior to the installation and use of a cryogenic octopole accumulation trap (COAT). The previous configuration has been described in detail in the theses of Christopher Johnson[1] and Amelia Ray,[2] so only a brief overview will be included here and the focus of this section will be on the configuration after the installation of COAT. While the installation of a RF trap had been considered previously,[3] the experimental requirement of having a high duty cycle led to the decision to install an electrostatic ion beam trap (EIBT) instead. With the installation of an EIBT, the ability to recycle ions allowed for the decoupling of the source duty cycle from the experiment duty cycle, which did result in some cooling of precursor ions.[3, 4] This decoupling of duty cycles also opened up the option to install COAT, in an effort to more thoroughly control ion production, without any detriment to experiment duty cycle. This chapter will provide an overview of the major components in the PPC spectrometer including a detailed discussion of modifications to the ion source, installation of COAT, as well as some modifications to the electron detector.

2.1.1 Ion Source

The generation of ions of interest in a controlled way is of upmost importance, since without them, there is no reason for carrying out any experiment on the PPC spectrometer. The only requirement for the ion source is to generate ions of interest in large enough quantities to allow for the experiment to be performed. A number of approaches have been utilized by others to meet this requirement including electrospray

ionization, sputter-ion sources, and laser vaporization sources.[5-8] The source used for the PPC spectrometer consists of ionization in a pulsed supersonic expansion. A supersonic expansion is generated when gas is passed through an orifice from a high-pressure (3-5 atm) volume to a low-pressure (<1 mtorr) volume. During this expansion, the molecules that makeup the gas undergo many collisions, which transfers their internal energy in the form of vibrational and rotational energy to kinetic energy, significantly cooling the ions at the center of the expansion. Though supersonic expansions have been found to generate ions with vibrational temperatures < 100 K and rotational temperatures <20 K,[9] the cooling is generally system specific and non-thermal.[10, 11] Experiments on OH^- after the installation of the EBIT on the PPC spectrometer, for example, have measured a rotational temperature of 64 ±5 K.[4]

Ionization is achieved using an electrical discharge, stabilized by a 1 keV electron beam, acting upon the supersonic expansion. Ions generated by this method are typically hot with vibrational energy up to roughly 1000 K.[5, 10] The chemistry behind ion generation using an electrical discharge generally fall into two mechanisms: (1) direct ionization of molecules with subsequent collisions forming clusters and other ions via charge transfer or (2) attachment of free low-energy electrons to form anions. To minimize the vibrational energy for the ions upon their creation, the electrical discharge is located early in the expansion to maximize the cooling effects by maximizing the number of collisons.[12, 13]

With the installation of COAT, a new chamber has been added to the previously described instrument,[3] to house the redesigned source as shown in Figure 2.2.The new

source, much like the old source, uses a supersonic expansion generated from a piezoelectric pulsed valve[14] (PPV) actuated by a fast piezoelectric disc. Upon actuation, gas is passed through a cylindrical orifice that is 250 μm diameter from a high-pressure (4-5 atm) chamber within the PPV. A coaxial pulsed electrical discharge (typically 500-700 V) is mounted immediately outside the orifice and is activated to fragment and ionize the gas molecules. However, the electron beam now counter-propagates down the expansion to seed the discharge as well as to generate high-energy electron-molecule collisions and low-energy secondary electrons in a low-pressure plasma. The ion cloud expands to fill the volume between two plates configured in a Wiley-McLaren style mass spectrometer[15] for perpendicular extraction of the ions onto the ion beam axis of the PPC spectrometer. It should be noted that ions in the old source were produced along the beam axis and therefore did not require orthogonal extraction.

One requirement for the new source design was the ability to adjust the distance between the PPV and the Wiley-McLaren plates, which affects the degree of cooling and the ions extracted from the supersonic expansion, without having to vent the source. To meet this requirement, a gear system was designed and implemented to allow for a rotary feedthrough to be used to raise and lower the PPV. The new chamber also features a window to create a visible pathway down to the time-of-flight region of the spectrometer for improved ease of alignment for the IR excitation laser described in the thesis of Amelia Ray.[2]

2.1.2 COAT

Ions extracted by the Wiley-McLaren mass spectrometer are focused and injected into COAT where they can be trapped and stored for a set period of time. COAT is a

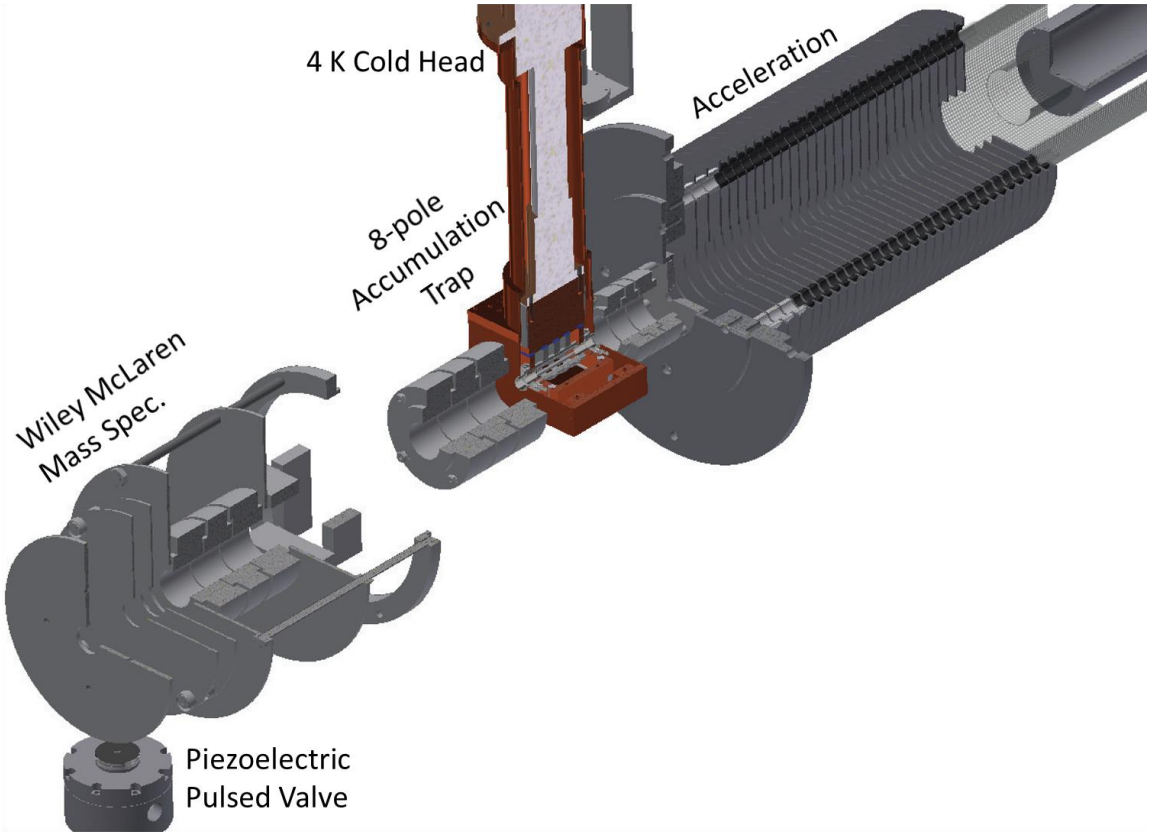

Figure 2.2. Overview of the source for the instrument.

linear multipole trap, as shown in Figure 2.3, based on a similar design used by Wester and coworkers.[16] Its capabilities are discussed in detail in Chapter 4 of this thesis. The design consists of RF rods arranged in a circle to form an inner diameter of 7.5 mm. Each rod has a RF voltage applied that is 180 degrees out of phase with each adjacent rod generating an octopole field trapping potential. The RF field is generated using a home-built RF generator based on designs by Anderson and coworkers. [17, 18] Ions are trapped longitudinally by two endcaps with the ability to switch to let ions enter and exit. Upon entering the trap, the ions collide with the buffer gas, removing translational kinetic energy allowing them to be trapped. While trapped within COAT, the ions continue to collide with buffer gas to thermalize to the temperature of the trap. The timing for the coordination of elements within the trap are discussed later. COAT is mounted on the 2nd stage of a Sumitomo RDK-205D 4K Cryocooler cold head, allowing for trapping temperatures to cool down to < 10 K. The trap is surrounded by radiative shielding to limit the effects of black body radiation. The ions within the trap are pushed to be stored near the exit side of the trap with shaping electrodes to create potential ramp.

The primary function for COAT is to trap and thermalize ions to low temperatures through buffer gas cooling, optimally with a He/H2 80:20 mix.[6, 19, 20] To introduce the buffer gas into the trap, a pulsed valve similar to one designed by Gerlich and coworkers[21] is used to pulse gas into COAT through a copper tube raising the pressure within to ~10^{-2} mbar. The copper tube is in good thermal contact with the 1st stage of the Cryocooler allowing for precooling of the buffer gas before it is introduced to the COAT environment. Within COAT, collisions with surfaces inside cool the gas further.

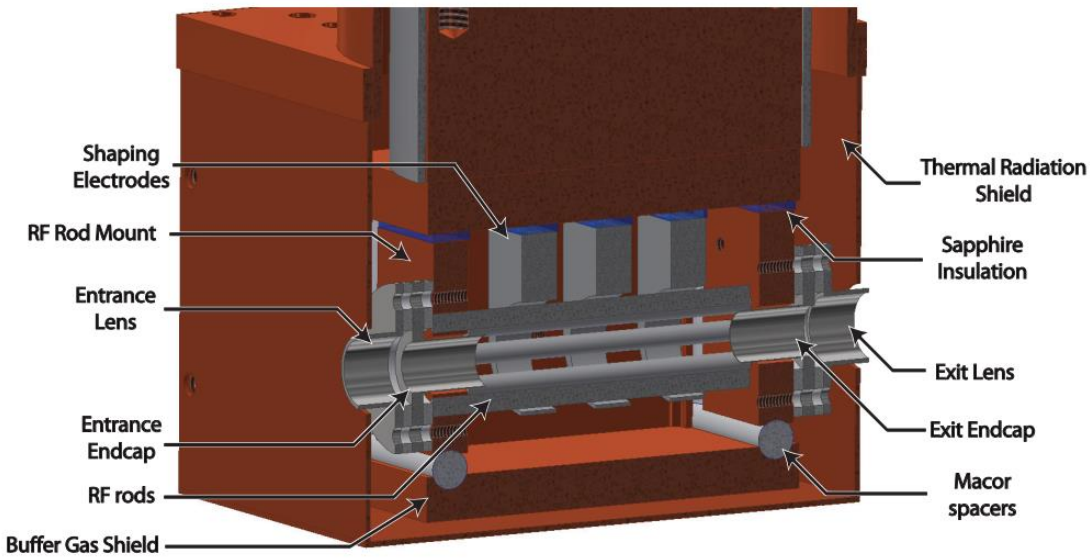

Figure 2.3. Cross-section of COAT and its components.

A sample voltage map from the Wiley-McLaren to COAT is shown in Figure 2.4 showing the voltages during the loading, trapping, and ejecting phases. The COAT potentials are floated to slow the ions down as they enter into COAT with ion optics to help focus the ions to minimize losses from bad trajectories. During the loading phase, the entrance endcap to the trap is held open allowing the ions to enter while the exit endcap is held near the maximum potential of the first plate of the Wiley-McLaren extraction plates. Collisions with the background gas will reduce the anions' translational kinetic energy allowing them to be trapped. During the trapping period, the entrance endcap is raised to trapping potential preventing ions from exiting through the entrance endcap. Once the trapping period is over, the exit endcap is switched to an attractive potential to pull the anions out of the trap.

COAT can generally operate in four modes: pass-through, heating, cooling, and accumulation. The pass-through mode can be configured in two ways. One configuration is to simply leave all the trapping electrodes within COAT (endcaps, RF, shaping electrodes) at ground and let the ions pass through. A timing diagram for the source/COAT elements is shown in Figure 2.5. The entrance and exit lens of COAT can be used to focus the ions to ensure a larger quantity successfully passes through the trap. The second pass-through configuration consists of simply lifting COAT out of the ion beam path vertically through a custom designed flange used to attach the cold head to the top of the COAT chamber. This mode is generally used when initially looking for ions as it reduces the number of variables during the search for optimal settings for generating specific ions. COAT can also be used to heat ions by optimizing settings to increase the

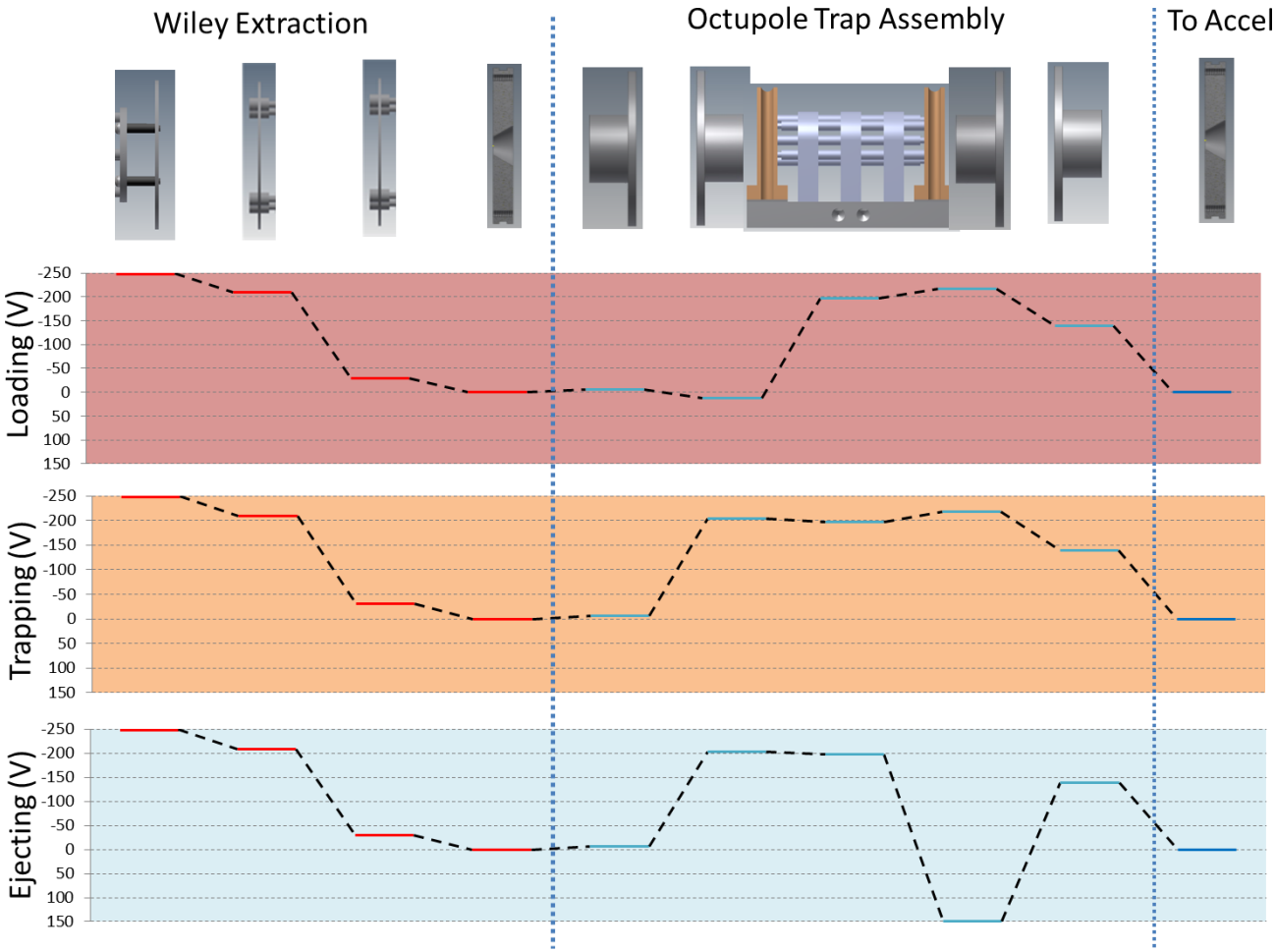

Figure 2.4. Potential map for the source of the instrument

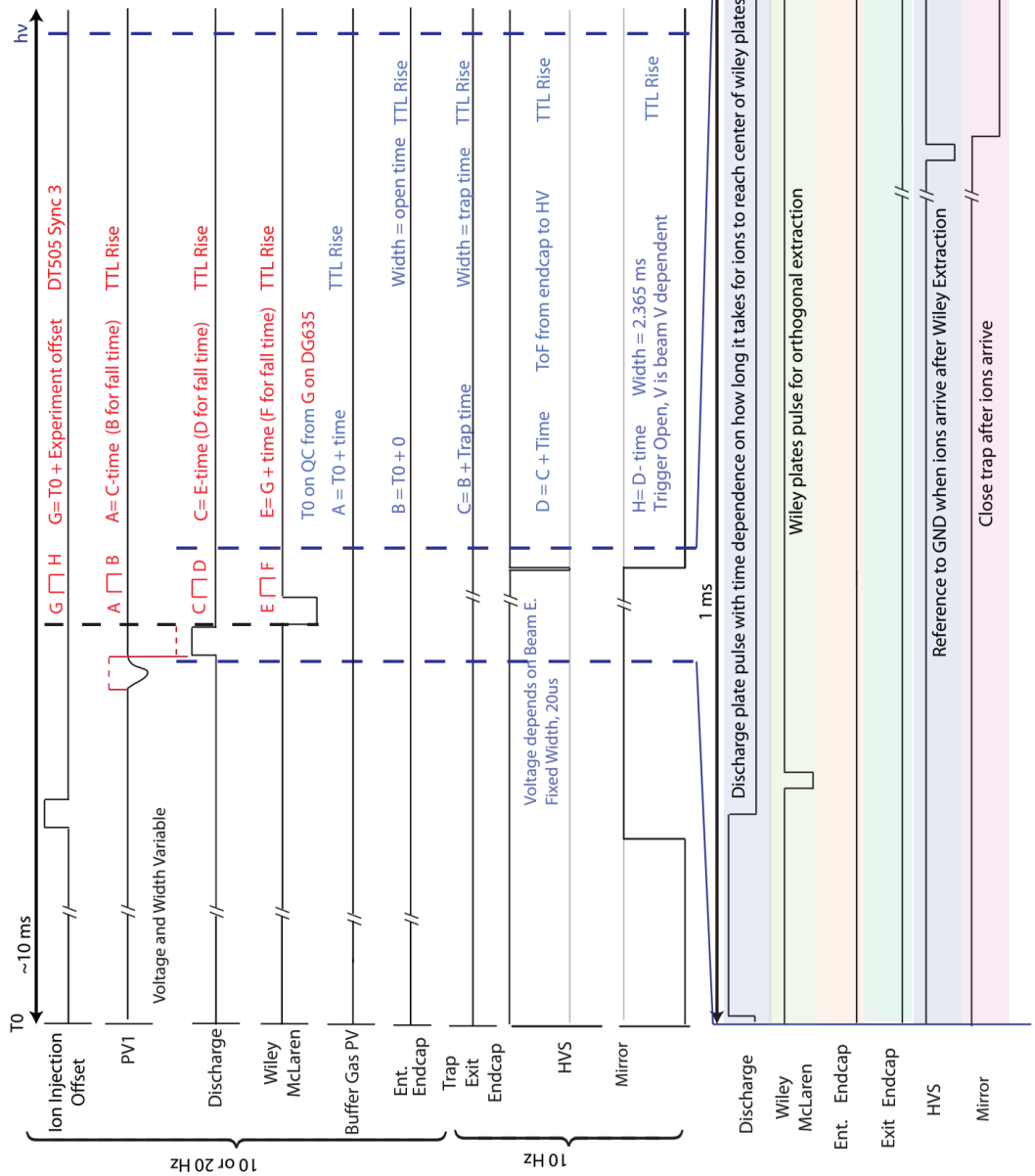

Figure 2.5. Timing diagram for COAT under pass through mode.

translational energy of the ions upon their entry into COAT. The collision of the precursor ions with the buffer gas converts translational energy into internal energy of the ions. To maximize this, the floating potential on COAT electrodes are adjusted to allow the ions to approach COAT at higher translational energies. Additionally, the entrance focusing lens plays a key role in accelerating the ions as they enter the relatively high-pressure region in COAT, which increases the collision energy with the buffer gas. The primary factor for ion temperature is the duration of trapping of COAT. The timing diagram under heating mode is shown in Figure 2.6. Trapping the ions for a brief period of time (500 μs) limits the number of collisions the ions can have with the buffer gas allowing them to retain their internal excitation. Since the primary method of heating is the initial collision of the ions with the buffer gas, the temperature of COAT has only a minor effect on the temperature of the precursor ions.

For cooling mode, the trapping time is extended to allow for the ions to thermalize with the buffer gas. The timing diagram for COAT under cold conditions is shown in Figure 2.7. The trapping duration for COAT is normally 80 ms which allows enough time for the ions to thermalize with the surrounding buffer gas. While similar traps have been shown to cool ions within 30 ms,[6] it is still ideal to minimize the ion temperature from initial collisions with buffer gas. This includes limiting the float voltage for COAT to reduce the ion velocity on its approach into COAT and minimizing the entrance lens voltage while still maintaining a good quantity of ions. This mode will thermalize the ions to the temperature of COAT, so it can also “cool” the ions to room temperature.

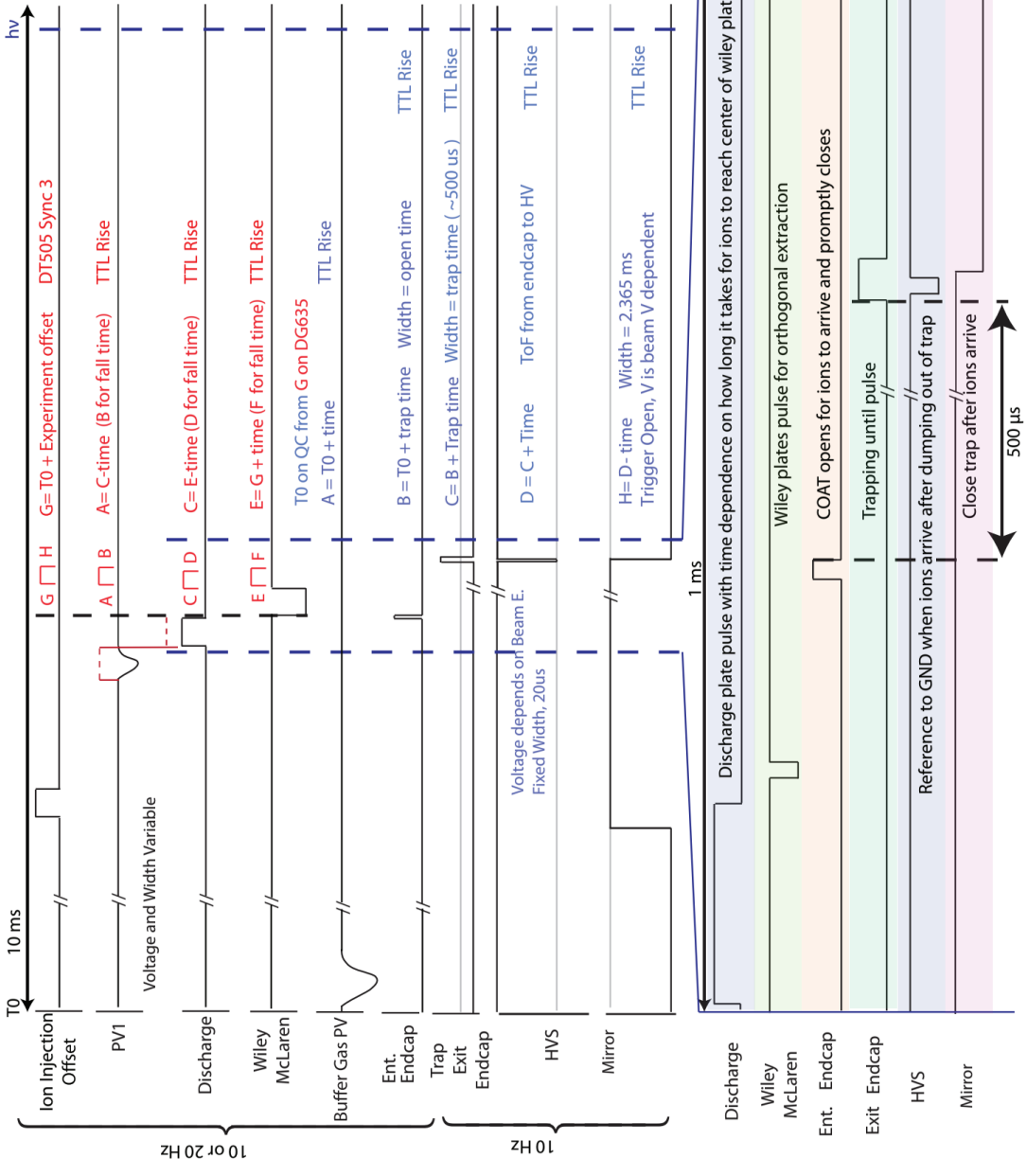

Figure 2.6. Timing diagram for instrument source under heating mode.

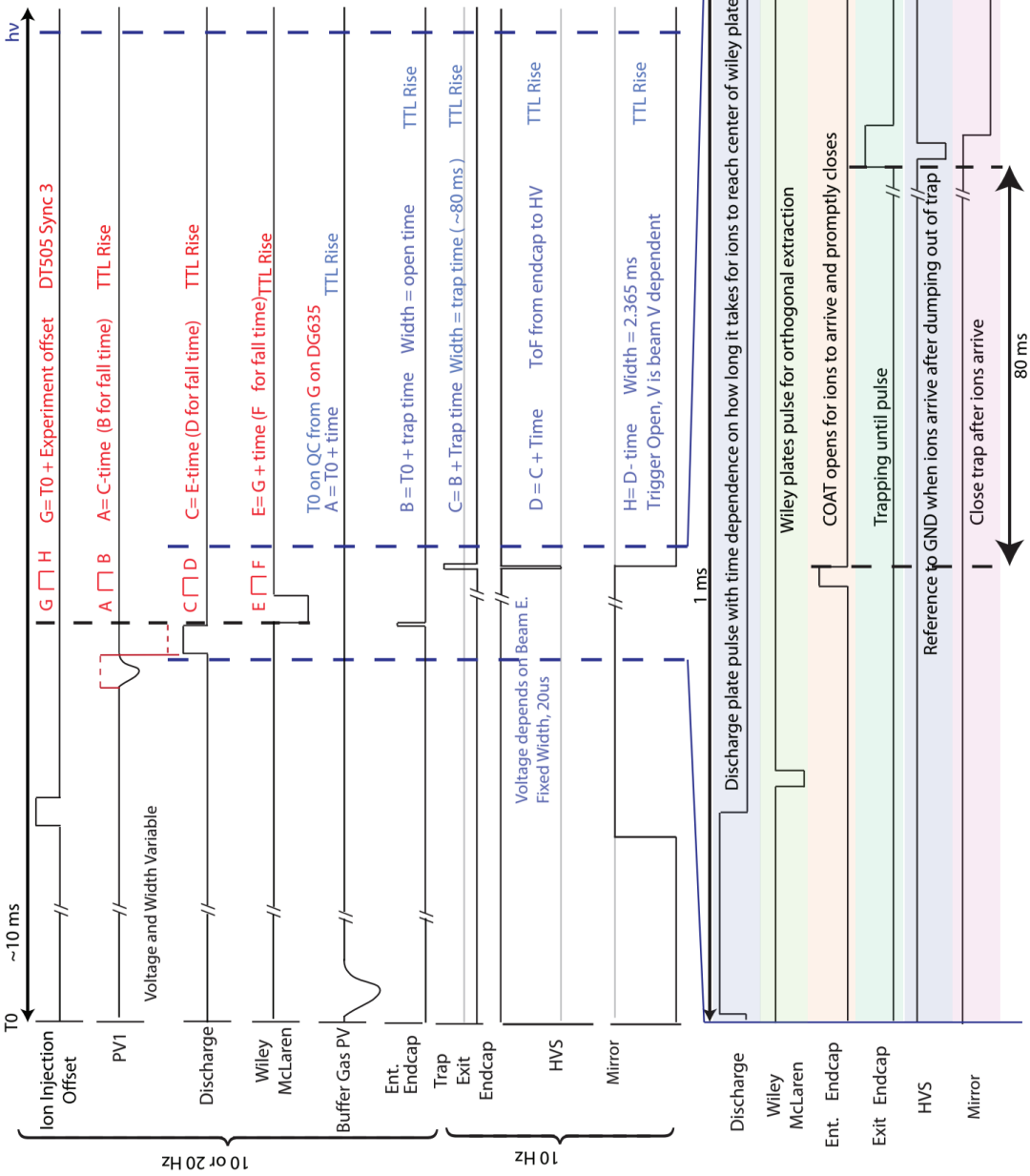

Figure 2.7. Timing diagram for instrument source under cooling mode.

Accumulation mode is useful when either the EIBT trapping time is extended or if the source pulse repetition rate is increased while maintaining a 10 Hz cycle for the EIBT. The timing diagram for accumulation mode is shown in (Figure 2.8) where the main difference between this mode and others is the entrance endcap remains at trapping potential and is not switched. This allows for ions from multiple supersonic expansions to be accumulated within COAT. One limitation for this method, however, is that not all the ions will undergo the full 80 ms of cooling since ions will be continually added to the trap.

2.1.3 Acceleration

Ions ejected from COAT are accelerated by a stack of plates with progressively increasing voltage applied by a resistor-chain voltage divider. Plates near the center of the accelerator stack are wired to be independently controlled to allow for them to be used in an einzel lens configuration for focusing the ion beam as it is accelerated. After passing through the acceleration region, the ions enter a 30 cm long metal tube (HV switch) with an entrance aperture of 3mm and exit aperture of 5mm that is floated at the final acceleration voltage. While inside the tube, the potential is rapidly switched to ground using a fast high-voltage switch (Behlke HTS 101-01) re-referencing the ions to ground to alleviate the need for the rest of the machine to be floated at the acceleration potential.[22] The ions exiting the acceleration region are collimated with minimal energy spread.

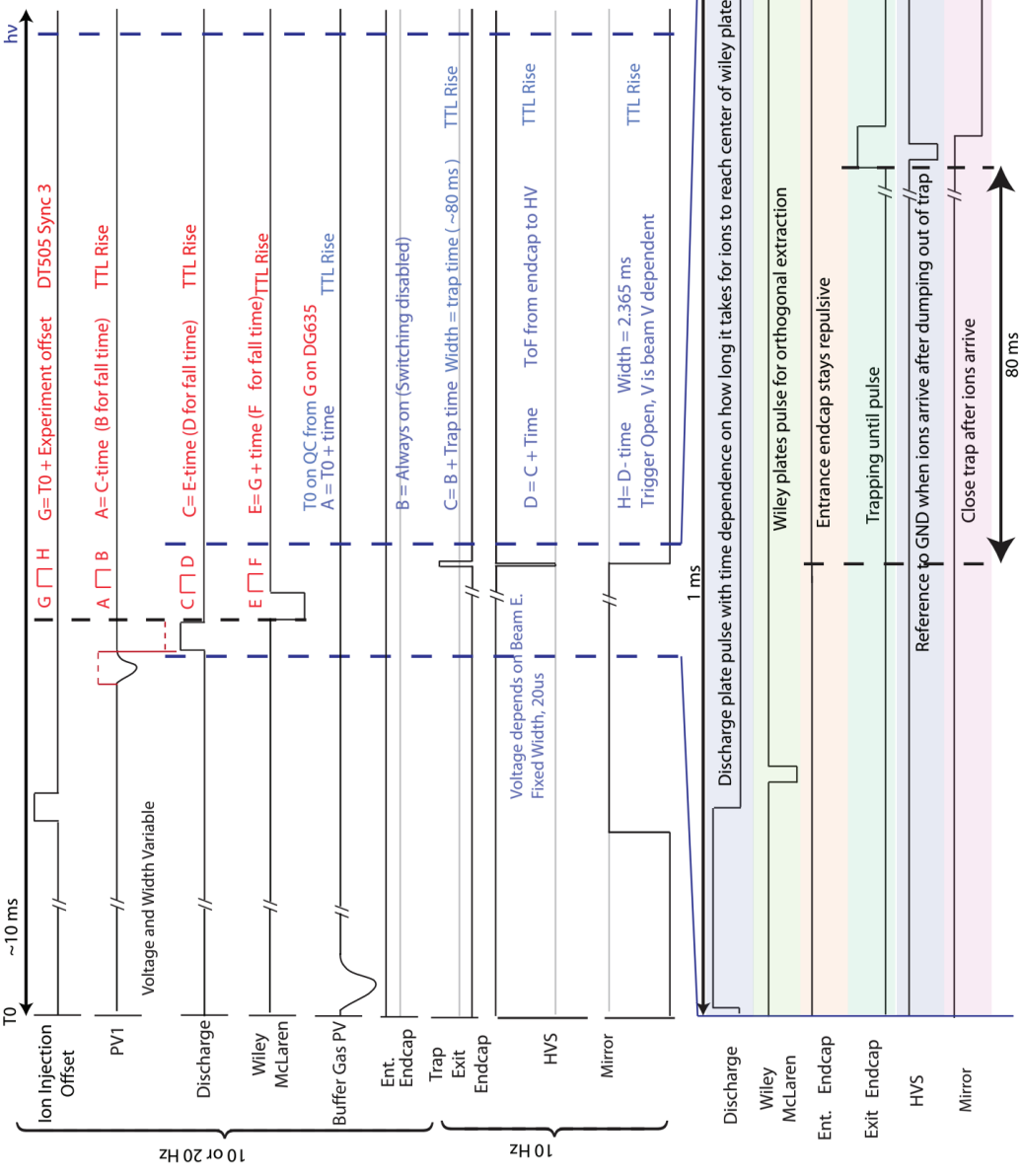

Figure 2.8. Timing diagram for instrument source under accumulation mode.

2.1.4 Time-of-Flight and Mass gate

The ion beam is a mixture of a number of different species with differing mass/charge (m/Q) ratios. Since the ions all have the same kinetic energy, they have differing lab frame velocities allowing ions of differing masses to separate out as they travel over a long distance. Right after acceleration, however, the spatial and temporal length of the ion packet is largely governed by the length of the HV switch. This decreases the resolution of the TOF mass spectrometer, sometimes making it difficult to identify single mass unit differences in the ion packets. To alleviate this issue, a "Bakker-style" chopper[23] can be used to increase the resolving power of the TOF mass spectrometer. The chopper consists of two parallel plates where one is rapidly switched from a selected potential (V) to ground while the other is held at V/2 while the ion packet is passing through. As the voltage is switched, only ions midway between the two plates have no net change in trajectory, allowing for a narrow cross section of the ion packet to proceed through the time-of-flight, yielding narrower and better resolved ion packets. This chopper is generally only used to observe what ions are being created in the source and is typically off during data collection as it significantly decreases ion transmission.

To guide the ions over the length of the time-of-flight region, two sets of einzel lenses and two sets of vertical and horizontal deflectors are used to collimate and guide the ions. The einzel lenses consist of three cylindrical electrodes where the two outer electrodes are held at ground while the center electrode can be varied in potential. The deflectors consist of two sets of metal plates mounted horizontally and vertically with the ion packet traveling between the plates. The plates can be variably biased to deflect the ion beam both horizontally or vertically. Additionally, a neutral beam block (NBB) is

used to remove any neutrals from the ion beam axis. The NBB consists of deflectors that repel the ion beam upwards vertically over a metal block, followed by repelling the ions back downwards to return the ions to their original trajectory. Recently, the NBB has been modified to include a mirror, to counter propagate a laser through the ion packet towards the source for IR excitation experiments. Details about its installation and use can be found in the thesis of Amelia Ray.[2]

While the EIBT can trap ions of multiple masses, additional masses can add unnecessary complications to the spectra. To select a mass of interest from the ion packet, an electrostatic chopper (mass gate), is used to truncate the ion packet. The mass gate consists of two parallel plates at equal and opposite potentials which deflect all ions until the selected time window, corresponding to the time-of-flight for the mass of interest. At that point, both plates are switched to ground. allowing the ions of interest to pass, before returning to potential and deflecting all subsequent ions.

2.1.5 Electrostatic Ion Beam Trap

The EIBT is used to trap ions over a variable period of time, allowing for the ion packet to be repeatedly probed with a laser. The EIBT consists of two focusing electrostatic mirrors between which stored ions oscillate as shown in Figure 2.9. When ions initially enter, the entrance mirror and lens are held at ground and quickly brought up to trapping potential before the ions can return after bouncing off the exit side mirror. The ions can remain trapped for greater than 5 seconds,[3] where the primary mechanism for ion loss is collisions with background gas. To prevent ion heating from black body radiation and to encourage radiative cooling, the entire trapping region is cooled to ~20K.

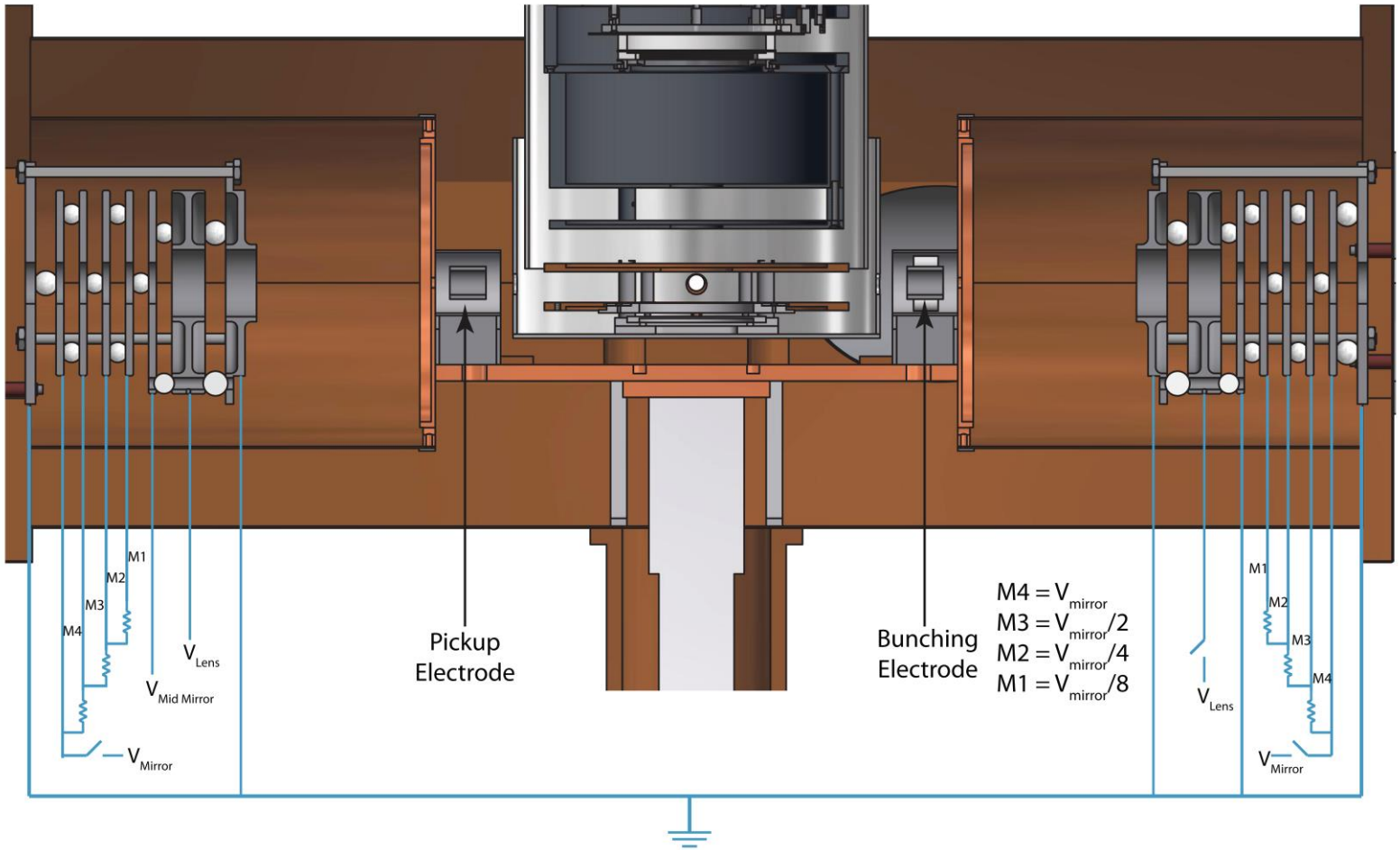

Figure 2.9. Cross section schematic for the EIBT

The detailed implementation of the EIBT can be found in the thesis of Christopher Johnson.[24]

At the center of the EIBT lies the ion-laser interaction region with the electron detector that is discussed later in sections 2.3.1. The ions are probed at this area at a rate of 1 kHz over the duration of the trapping period. The resulting photoelectrons are extracted and mapped onto the electron detector, while photodetached neutrals recoil out of the trap and are detected by the neutral particle detector 1.29 m downstream, discussed in section 2.3.2.

Over time, ions within the trap will spread out in distance due to kinetic energy differences and Coulomb interactions resulting in decreased density of the ion packet at the interaction region during a laser shot. To maintain the shape of the ion packet, a cylindrical RF-bunching electrode is located near the entrance side of the EIBT between the mirror and the electron detector. This may be done by application of a low-amplitude RF with the frequency close to the natural oscillation frequency of ions at the m/Q of interest. By phase locking this signal to the mode-locked pulse train of the Ti:Sapphire laser, the ion packet density and time-structure can be maintained. This is referred to as "bunching" the packet and allows the ion packet oscillation to be synchronized with the laser such that the ion packet overlap with the laser always occurs while the ion packet is traveling towards the neutral detector. This results in a significantly higher rate of data collection, as no laser shots are "wasted" on ions traveling towards the source where neutrals cannot be detected.

2.1.6 Detector Chamber

The detector chamber contains two detectors, a neutral particle detector and an ion timing detector. The neutral particle detector, described in detail in section 2.3.2, is positioned along the ion beam axis of the PPC spectrometer and is mounted on a vertically translatable mount. The ability to translate the detector vertically allows for fine tuning the center of the neutral particle distribution on the detector. The ion timing detector serves as the method for measuring ion time-of-flight during beam optimization. It is located above the ion beam far enough to not inhibit any neutral particles from hitting the neutral detector. To direct ions up to the ion detector, two parallel plates are located at the entrance to the chamber to deflect the ion beam up to the ion detector. The detector consists of a stack of two 1" diameter microchannel plates whose amplified electron cloud is collected by a stainless-steel anode and amplified by a high-speed preamplifier (Ortec VT-120).

2.1.7 Vacuum System

Given that the desired systems of study are highly reactive gas phase intermediates, the success of generating and maintaining large quantities of ions is highly dependent on a robust, high performance vacuum system. The primary reason to maintain low pressures for an ion beam apparatus is to minimize the number of collisions between ions and background gas, which can cause loss or heating of ions. The number of collisions is a function of the number density of the background gas, as well as the distance the ions are traveling. While collisions of the ions with background gases are typically minimized by maintaining high vacuum in most of the instrument, two regions in the PPC spectrometer require comparatively high pressures: 1) the supersonic expansion, where the collisions help cool the ions, and 2) under well controlled conditions in COAT, where the collisions functionally thermalize or heat the ions in

region where they are constrained both radially and longitudinally to minimize ion loss. Although the PPC spectrometer is not small, the bulk of the anion path length occurs within the EIBT, where ions travel back and forth approximately one meter at frequencies ranging from 100 to 260 kHz depending on the species. .[3] As a result, mean free paths greater than 10^6 m are required several seconds of EIBT storage time. To meet these demanding requirements, the vacuum system was carefully designed and is outlined briefly below.

The vacuum systems can be divided into three subsystems, two for the high vacuum system with pressures of ~10^{-7}, and the third system for ultrahigh vacuum with pressures of ~10^{-8} or lower. These three systems can be operated independently from one another, through the use of an interlock, to allow for each system to be individually shut down for maintenance through a series of pneumatic valves as well as manual valves as shown in figure 2.10. The details for the interlock system are shown in Appendix A. This is particularly important since the source region requires frequent maintenance and the ultrahigh vacuum region requires more time to reach operating pressures after venting.

A new source chamber was added with the installation of COAT and is evacuated by a turbomolecular pump (TMP) with a pumping speed of 240 L/s (Edwards nEXT 240) which is backed by an Edwards XDS 35i scroll pump (35 m^3/h). As the source for the ions, this chamber is vented most frequently due to required maintenance on the electron gun and discharge plates. For this reason, the source chamber is separated from the COAT chamber by a beamline gate valve allowing for it to be independently vented. The COAT, acceleration, and time-of-flight chambers are each enclosed in separate differentially pumped chambers with small orifices limiting gas flow while still allowing

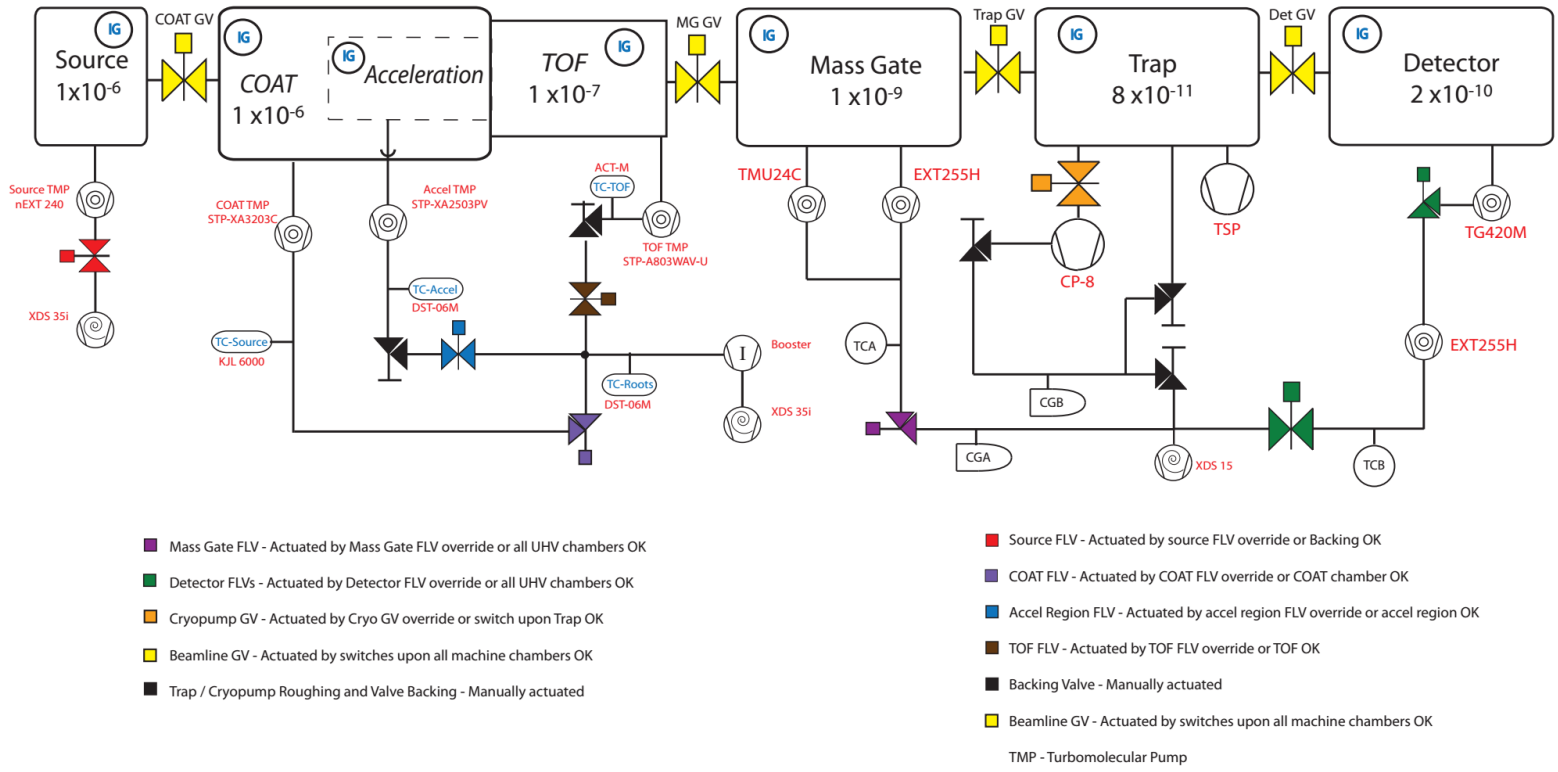

Figure 2.10. Vacuum diagram for the instrument

ions to pass through each section. This is particularly important since buffer gas is being introduced through COAT. Each of these sections is evacuated by magnetically-levitated TMPs with pumping speeds of 3200 L/s (Edwards STP XA3203C), 2200 L/s (Edwards STP-A2503PV), and 800 L/s (Edwards STP-A803WAV-U) on the COAT, acceleration and time-of-flight chamber respectively. All three TMPs are backed by another Edwards XDS 35i (35 m^3/h) scroll pump.

Every subsequent chamber in the PPC spectrometer is designed with the ability to be isolated via a combination of manual and pneumatic valves. This is required due to the different cleanliness requirements for ultrahigh vacuum and the time requirements to go from vent to fully operational. The mass gate chamber is pumped by two TMPs each with ~250 L/s pumping speed to reduce the gas load from the source as much as possible before the EIBT trap chamber. The trap chamber is pumped by a 2500 L/s cryopump (Oxford Instruments, Cryo-Plex 8) and a home-built 3000 L/s titanium sublimation pump (TSP). The detector chamber is pumped by a magnetically levitated 400 L/s TMP which is backed by another 250 L/s TMP to ensure hydrogen and helium are adequately pumped. The mass gate TMPs and the detector chamber TMPs are both backed by an Edwards nXDS 10i (12.7 m^3/h) scroll pump. As shown in Figure 2.10, a complex roughing manifold is connected to the nXDS 10i to allow for roughing out the trap chamber as well as for evacuating the cyropump during maintenance.

2.2 Laser System

PPC spectroscopy requires a high duty cycle due to low-signal rates as well as high temporal resolution. Both requirements can be met by using a short-pulse

picosecond laser with a high repetition rate. For all the experiments described in this thesis, a cavity-dumped, mode locked Titanium:Sapphire-based laser is used.

The laser system used is a Clark MXR CPA-2000 Ti:Sapphire regenerative amplifier system with a fundamental output of 775.5 nm light with a 1.1 ps pulse width, 400 μJ/pulse, and a repetition rate of 1037 Hz. Lasers with such short pulse widths generally have a very high peak power that can damage optical components in the laser cavity. To avoid damaging optics, a chirped pulse amplification (CPA) scheme is used. The CPA scheme lengthens the pulse width temporally with dispersive elements to tens of picoseconds. The elongated pulses have a lower peak power allowing for safe amplification within the laser cavity. After amplification, the pulse can be recompressed using a similar dispersive system to generate a high powered short pulse.

The regenerative amplifier in the CPA-2000 is composed of a series of lasers and optical systems. A diode pumped fiber laser at 43.58 MHz provides picosecond seed pulses. The seed pulses are elongated then injected at 1037 Hz into the Ti:Sapphire amplifier cavity, which is pumped by a high-power Q-switched Nd:YAG laser. The elongated seed pulse makes several passes through the Ti:Sapphire crystal until it reaches its maximum energy. Once the maximum energy is reached, the pulse is ejected using a Pockels cell (fast-polarization rotator) and recompressed to give the final output pulse.

The output pulse can be further manipulated using nonlinear optics to generate a range of photon energies used in the experiments. The 775.5 nm (1.60 eV) laser pulse can be doubled (387.8 nm, 3.20 eV) using a beta-Barium-Borate (BBO) crystal which can then be used to pump a traveling-wave parametric amplifier for superflourescence (TOPAS) system. The TOPAS system can be used to produce radiation over a range from

460 to 720 nm and 830 nm to 2 μm at the cost of significantly lower pulse energies. The TOPAS system generates a superflourescent beam in BBO from which the desired wavelength can be selected and amplified using a multi-stage optical parametric amplifier. The output of the TOPAS can also be manipulated using nonlinear optics to further extend the wavelength range.

Once the desired wavelength has been generated, the beam is directed towards the instrument and passed through a series of irises for alignment through the PPC spectrometer. The laser beam can be focused using a 500 mm focal length lens to produce a spot size of < 1 mm in the interaction region in the EIBT, or it can be collimated. The collimated configuration offers two benefits, one is a smaller flux of photons through the interaction region limiting 2-photon events. The second benefit is when the 775.5 nm output is tripled to 258.5 nm, which has enough energy to overcome the work function of surfaces within the EIBT, stray electrons ejected are detected by the electron detector. Collimating the laser in combination with installing baffles on the vacuum side of the entrance and exit laser ports greatly reduces the number of irrelevant detected electron events.

2.3 Detectors

For a kinematically complete experiment, each detector needs to be able to map the particle [v_x, v_y, v_z], in order to calculate the momentum and therefore the kinetic energy of each particle. To accomplish this, the PPC spectrometer is equipped with time and position sensitive detectors for the electrons and neutral particle detector. Both detectors function in a similar manner in that the particle (electron or neutral

atom/molecules) collides with a microchannel plate (MPCs) starting a cascade of electrons resulting in electron clouds of ~10^7 electrons which then impinge onto an anode to record the position. Though the electron amplification methods are similar, the position detection methods are very different. The electron detector uses velocity-map-imaging (VMI) in combination with a wedge-and-strip anode to map the electron into energy dependent concentric circles with higher kinetic energies resulting in a larger radius from the center. The neutral particle detector uses a four-quadrant crossed delay-line anode for position detection. The time and position for the neutrals and electrons are recorded on an event-by-event basis to allow for energetically reconstructing dissociative events.

2.3.1 Time and Position-Sensitive Electron Detector

Photoelectrons are extracted perpendicular to the ion beam axis and the laser axis in the interaction region by the VMI electrodes. The VMI electrode configuration used for experiments conducted in Chapter 3, has been described previously.[3, 25] For the experiments in Chapter 4 and 5, the VMI has been modified as described below.

The new schematic is shown in Figure 2.11 consisting of a repeller plate (negative potential), corrector plate (positive potential), extraction lens (ground), focusing lens (positive potential) and a field-free region which ends with a stack of MCPs arranged in a Z configuration known as a Z stack. The VMI setup has been modified to add an additional focusing lens as well as widening the extraction lens. Additionally, the field free region was completely enclosed within a copper cylinder to eliminate any field distortions from the previous field free region.

The repeller is required to accelerate the photodetached electron toward the electron detector but unfortunately this also distorts the trajectory of the ions trapped

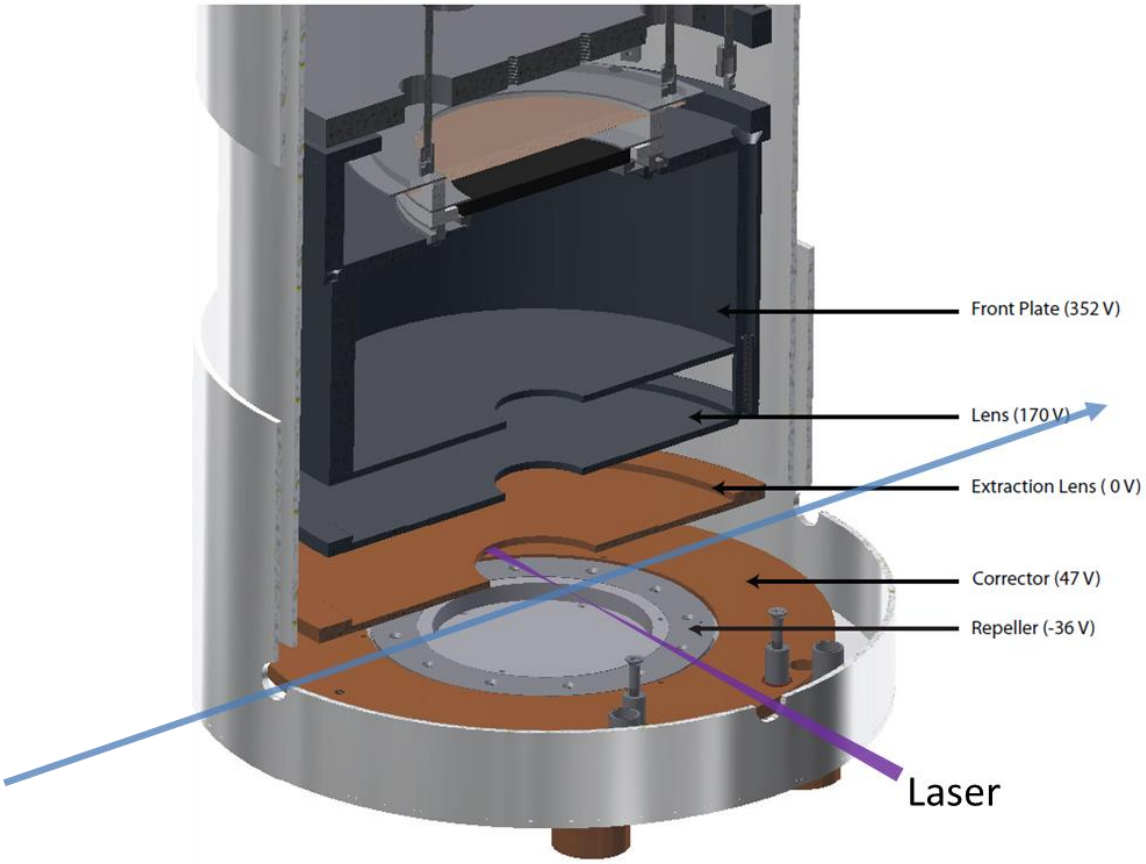

Figure 2.11. Cross section of the electron detector VMI extraction optics

within the EIBT. To counteract the distortion, the corrector plate counteracts the effects of the repeller in order to keep the ions on a trapping trajectory. Because the repeller, extractor, and focusing lens of the VMI are enclosed within the EIBT, they are kept at 20K while the detector body is held at room temperature.

The electron detector uses a wedge-strip anode shown in Figure 2.12 which uses charge division over three electrodes to determine position information.[26, 27] The three electrodes are the wedge, which consists of a comb of tapered fingers, the strip, another comb of fingers that increase in thickness in the direction perpendicular to the direction of the tapered wedge fingers, and the zig-zag, which fills in space between the wedge and strip. The detection of position on the electron detector requires the electron cloud to be large enough to cover portions of all three electrodes. The x and y position are determined by the equations:

$$x \propto \frac{Q_w}{Q_W+Q_s+Q_z} \tag{2.1}$$

$$y \propto \frac{Q_s}{Q_W+Q_s+Q_z} \tag{2.2}$$

where the charge on the wedge, strip, and zig-zag is Q_w, Q_s, and Q_z respectively. The ratio of Q_w locates the x coordinate of the electron position due to the taper on the fingers of the wedge, with a smaller charge fraction of the charge indicating an x coordinate towards the left of the anode and a larger fraction indicating an electron position closer to the right side of the anode. Similarly, the fraction of the total charge on the strip electrode locates the y coordinate with the smaller fraction indicating an electron position closer to the bottom of the anode and a larger fraction indicating a position closer to the top of the

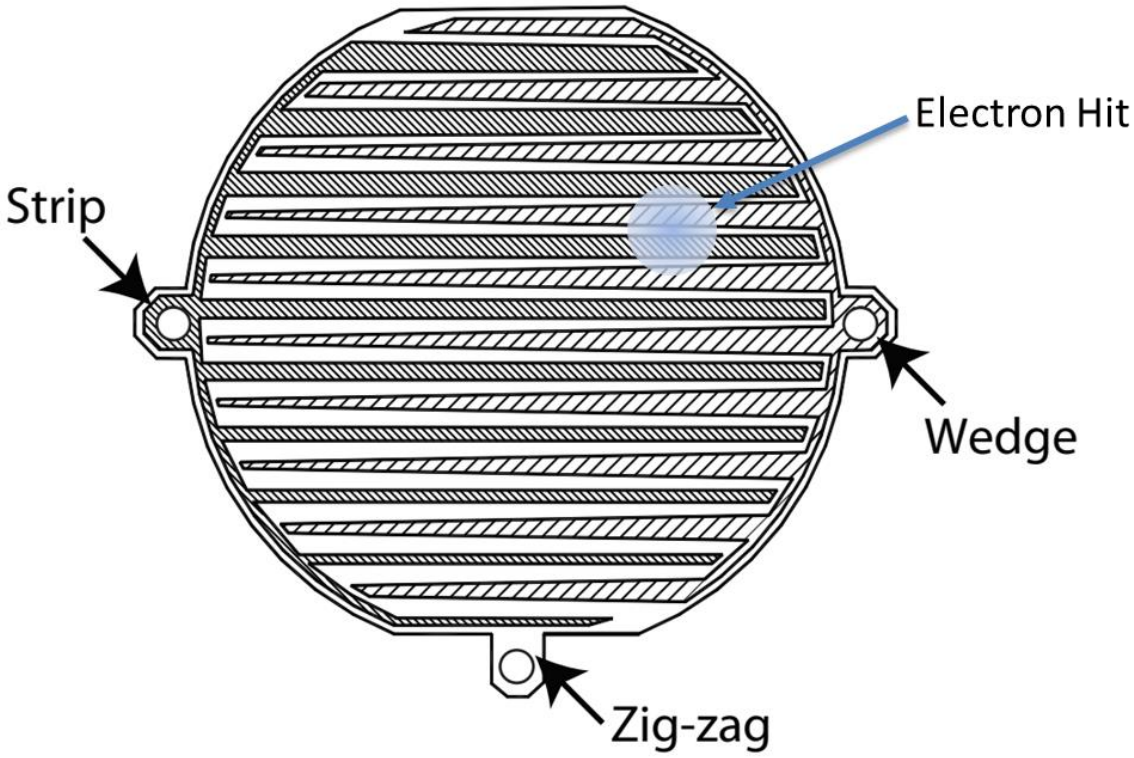

Figure 2.12. Schematic of the wedge-strip anode in the electron detector. The strip provides position information on the y-axis while the wedge provides information on the x-axis.

anode. The zig-zag captures electrons that do not hit either the wedge or strip to allow for charge normalization.

The signals from each electrode are amplified by charge-sensitive preamplifiers in combination with a shaping amplifier (Siegmund Scientific) which is then digitized using three channels on a 13-bit Ortec AD413 peak-sensing analog-to-digital converter (ADC). The time of arrival for the electron is detected from the wedge electrode with a capacitively coupled high-speed preamplifier (Ortec VT120). The output of the preamplifier is passed through a constant-fraction discriminator (CFD Ortec 935) which triggers at 20% of the peak height. The output from a photodiode placed near the output of the Ti:Sapphire laser is also passed through the CFD to mark the start of the electron time-of-flight. The difference between the laser pulse time, measured at the output of the Ti:Sapphire laser by a photodiode, and the detected arrival of the electron provides the electron time-of-flight. The time is recorded by a time-to-amplitude converter (TAC, Ortec 566) with 50 ns full scale. The output of the TAC is then digitized by another channel of the Ortec AD413. The ADCs and TACs interface with the data acquisition computer through a Computer-Automated Measurement and Control (CAMAC) crate and is processed using a custom LabVIEW acquisition software to record events.

2.3.2 Multiparticle Time and Position-Sensitive Neutral Detector

The unique capability of the PPC spectrometer is the ability to detect the neutrals of a dissociative event in coincidence with the ejected electron. The requirement for detecting even one more particle on the detector complicates the detection due to

requiring not only the position of each particle, but also the time of arrival for each which is beyond the capabilities of the wedge-strip anode used for the electron detector. Due to the method of detection, the wedge-strip anode is inherently limited in the detection of multiple particles due to having a deadtime of several microseconds per particle. While this can be worked around by splitting the anode into two detectors such that upon fragmentation, each particle hits on different halves of the detector, this still limits the neutral detector to only two fragments at a time.[27] To meet these requirements, a crossed delay line (XDL) anode is used to locate the x and y position of each particle.[28] The XDL is composed of electrodes running along the x and y coordinate forming a grid as shown in Figure 2.13. The grid for each direction is made from one long electrode running in a serpentine pattern electrically isolated from one another.

When the electron cloud from the MCP arrives at the XDL, it covers both of the delay line electrodes. The charge imparted onto each electrode travels in both directions along the delay line where the difference in time it takes to reach the end of each direction is directly proportional to the location along the delay line in which the charge originated. By measuring the difference in time for both the x and y delay lines (Equation 2.3), the location of the particle impact on the detector can be determined. This is demonstrated in the equation 2.4 showing the calculation for the x coordinate:

$$\Delta t_x = t_{x1} - t_{x2} = \left[\left(\frac{\frac{1}{2}l+x_1}{v_{charge}}\right) - \left(\frac{\frac{1}{2}l+x_2}{v_{charge}}\right)\right] \tag{2.3}$$

$$x = \left(\frac{v_{charge}\cdot\Delta t_x}{2}\right) \tag{2.4}$$

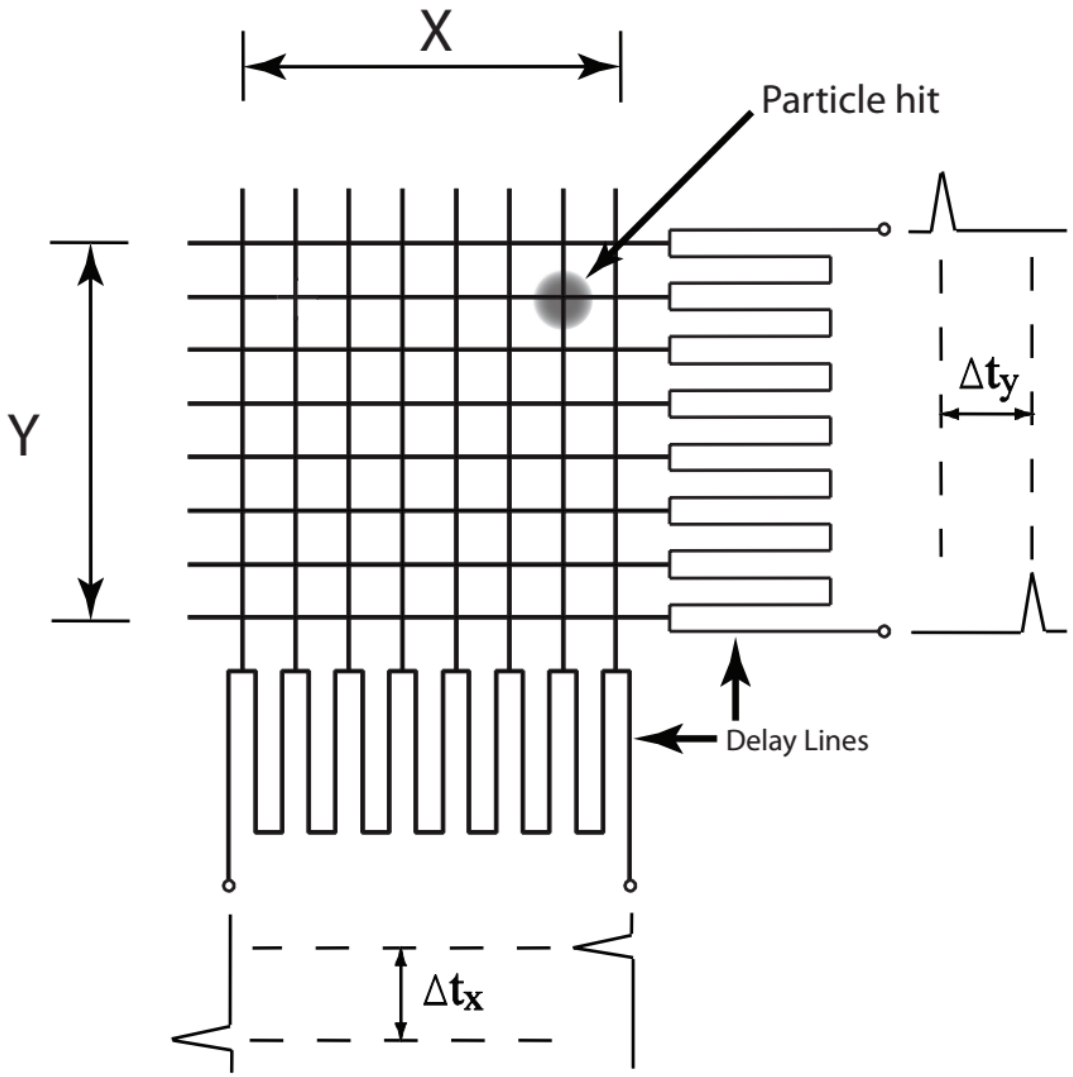

Figure 2.13. Diagram of the delay line anode in the neutral particle detector. The signal charge is sampled on both delay lines leading to the charge being detected on both ends of each line. The particle position can then be determined by the difference in time which the charge arrives on each end.

Where t_{x1} and t_{x2} are the time of arrival for the signal to reach the end of the electrode, l is the length of the delay line, and x is the position. The y coordinate is measured in the same manner. Since the delay lines have a fixed length, two particles impacting the same set of delay lines can be differentiated allowing for up to two particles to be detected for a single set of delay lines.

To further increase the number of particles that can be detected for a given photoinduced event, the neutral detector is split into four quadrants and is thus named the quad crossed-delay-line (QXDL) detector as shown in Figure 2.14. Each quadrant contains its own set of delay lines allowing up to 8 particles to be detected in coincidence. Each set of delay lines are identically setup with the signals from each delay line being amplified through a fast preamp and passed onto custom designed two-hit TACs (Siegmund Scientific). The TACs have a start and stop time which is fed into two cascading sets of CFDs. The first start and stop CFD outputs are routed to the particle one TAC while the second start and stop output is routed to particle two TAC. The output from the TACs are digitized using two 8-channel 12-bit peak-sensing ADCs (LeCroy Model 3351). The time of arrival for the neutral particles are is determined by a TDC (LeCroy 3371) in whose start time is determined by a pulse with a set time delay after the laser shot and a stop time is triggered by the first and second start CFDs of the y-coordinate TACs. The charge for each quadrant as well as the total charge from the MCPs is also amplified and digitized in another ADC. All ADCs and CFDs for the QXDL are house within the CAMAC crate that interfaces with the data acquisition PC via USB. These timing details are shown in Figure 2.15.

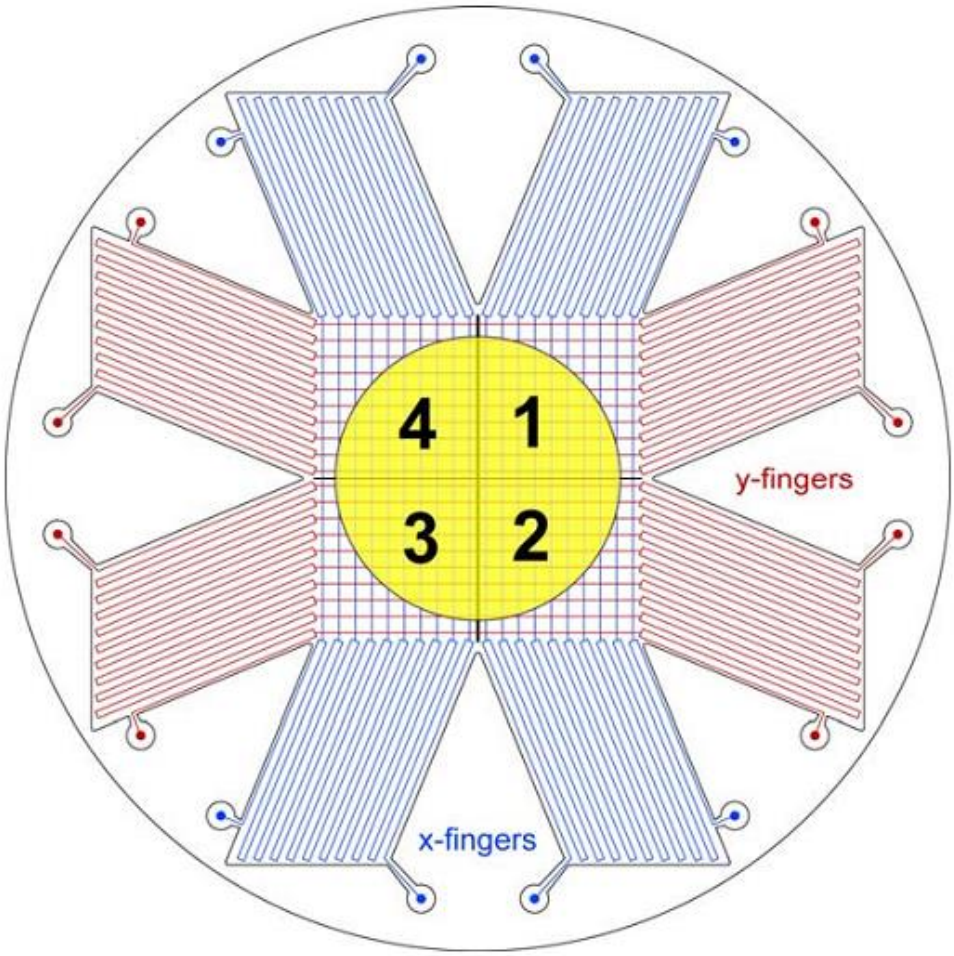

Figure 2.14. A schematic of the QXDL anode showing four quadrants with delay lines.

2.4 Data Analysis and Calibration

The signals from the CAMAC crate are sent to the data acquisition PC where they are sorted, processed, and collected. These signals must be discriminated to determine event multiplicity and then converted to positions and times to calculate velocity vectors. Once these values are calculated, a wealth of information is contained within each data set which can be plotted out in histograms to extract information.

2.4.1 Data Discrimination and Sorting

Once the data is passed to the data acquisition computer, each event is first discriminated by checking for valid coordinate and time information for each particle detected. For a detected electron, this means the charge detected on the wedge, strip, and zig-zag must not be zero or oversaturate the amplifiers and must have detected a valid time as well. For the QXDL, both x and y coordinates and time must be valid. Once the valid events are determined, the data is sorted by particle multiplicity. For example, if for one event, an electron and a neutral are detected, then it would be sorted as an electron in coincidence with a neutral (e^- + 1TAC). If an electron and two neutrals are detected as would be expected in a dissociative event, it would be sorted as an electron in coincidence with two neutrals (e^- + 2TAC).

The sorted data can then be loaded into a purpose-written Interactive Data Language (IDL) data analysis code, PATTI, where the data must pass through another set of discriminators that removes data that is known to be bad. Examples of these are multi-electron events, neutrals from masses other than the mass of interest, and other known mechanisms.

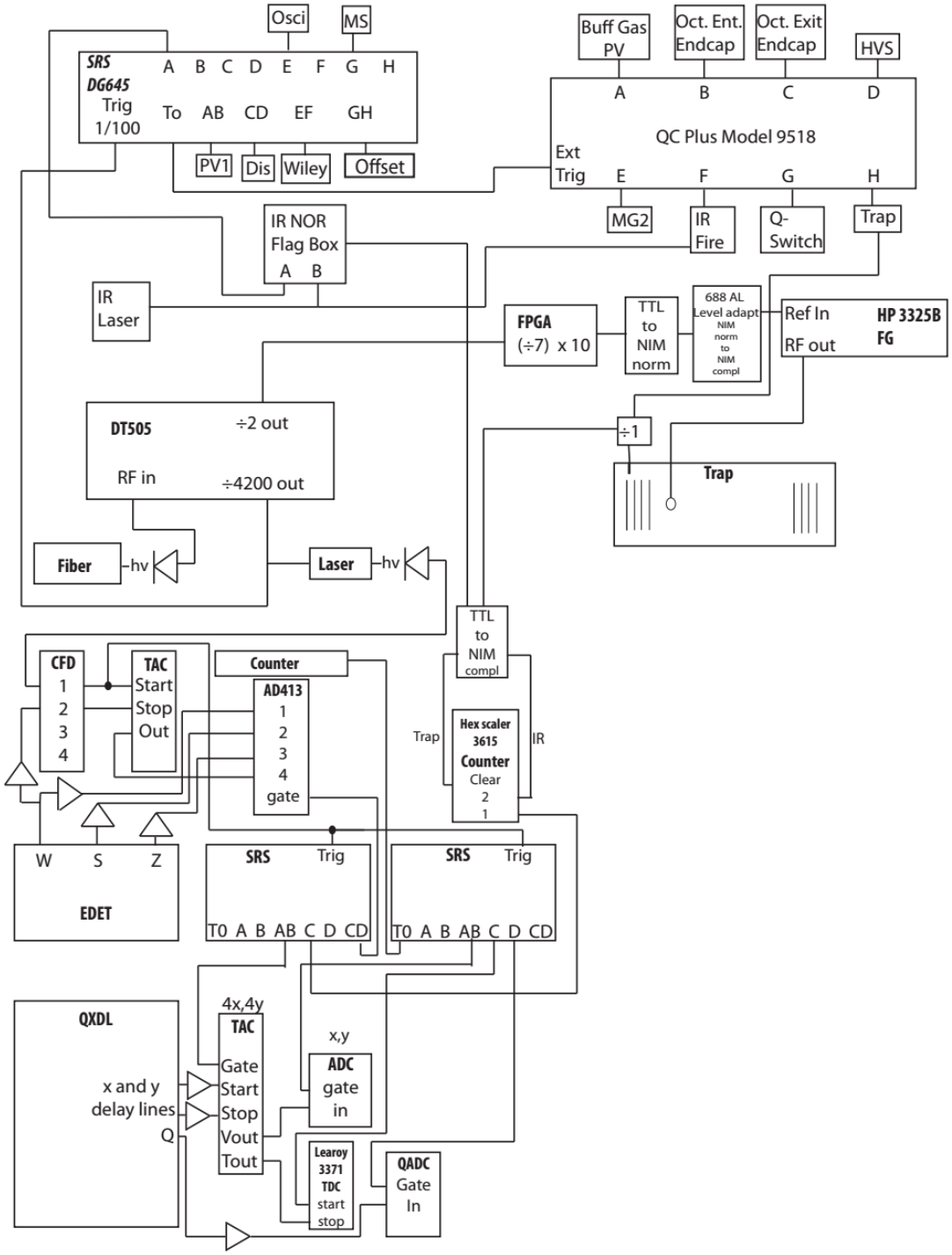

Figure 2.15. A timing signal map for the PPC spectrometer

2.4.2 Photoelectron Kinetics

The discriminated and sorted data must next be calibrated and converted to position and time information. As described earlier in section 2.3.1, the position of the electron impact on the detector is determined by calculating the charge division of the wedge, strip, and zig-zag anode from the electron cascade from the MCPs. In practice, capacitive coupling between the wedge, strip, and zigzag complicates the calculation. These factors are accounted for by the introduction of "cross-talk factors" into the calculation of the position of the electron impact:

$$X = \frac{\left(\frac{Q_W}{Q_W+Q_S+Q_Z} - C_{ZW}\right)p_{x1} - \left(\frac{Q_S}{Q_W+Q_S+Q_Z} - C_{SZ}\right)p_{x2}}{P_{x3}} \tag{2.5}$$

$$Y = \frac{\left(\frac{Q_S}{Q_W+Q_S+Q_Z} - C_{SZ}\right)p_{y1} - \left(\frac{Q_W}{Q_W+Q_S+Q_Z} - C_{ZW}\right)p_{y2}}{P_{y3}} \tag{2.6}$$

where Q is the charge of the wedge (w), strip (s) and zig-zag (z) and

$$p_{x1} = 1 - 2C_{SZ} - C_{WS} \tag{2.7}$$

$$p_{x2} = C_{WS} - C_{ZW} \tag{2.8}$$

$$p_{x2} = 1 - 2(C_{WS} + C_{SZ} + C_{ZW}) + 3(C_{WS}C_{ZW} + C_{SZ}C_{ZW} + C_{WS}C_{SZ}) \tag{2.9}$$

and the p_y can be calculated by swapping the C_{SZ} and C_{ZW}. These equations only establish the electron impact location. To determine the full 3-D position, the time of flight for the electron must also be determined. While the time of flight for the electron is recorded, to calculate the velocity of the electron, the focusing effects of the VMI setup must be taken into consideration:

$$TOF = DMC_t * N + DAC_t \quad (2.10)$$

where DMC_t is the multiplicative constant and the DAC_t is the additive constant. These constants are carefully determined using species with well-known electron affinities and electronic states, such as O^-, O_2^-, and I^-. The velocity for the electron in the x, y, and z directions are given by:

$$v_x = \frac{x}{TOF - t_{cal}} \quad (2.11)$$

$$v_y = \frac{y}{TOF - t_{cal}} \quad (2.12)$$

$$v_z = \frac{\Delta v_z}{\Delta(TOF - t_{cal})}(TOF - t_{cal} - TOF_0) \quad (2.13)$$

where TOF_0 is the effective TOF for an electron with zero energy in the z direction. From the velocity, the electron kinetic energy, eKE, can be calculated:

$$eKE = \frac{1}{2}m_e\left(v_x^2 + v_y^2 + v_z^2\right) \quad (2.14)$$

2.4.3 Neutral Fragment Kinetics

Once the calculation for the position of the particles are determined as described in section 2.3.2, the velocity vector for the neutrals must then be calculated. While the QXDL is capable of detecting up to eight particles in coincidence, only two-body neutral dissociations are discussed in this thesis. Details for three and four-body dissociation can be found in the theses of John Savee[29] and Todd Clements[30], respectively. Since the neutrals are not influenced by any electric fields and the position determination is not dependent on accurate charge measurement across the anodes, the velocity vectors are

straightforward to calculate. The positions are converted to velocities using the equations:

$$v_x = \frac{x}{TOF_{CM}} \tag{2.15}$$

$$v_y = \frac{y}{TOF_{CM}} \tag{2.16}$$

$$v_z = v_{beam} * (TOF - TOF_{CM}) \tag{2.17}$$

Where TOF_{CM} is the time of flight for the center of mass. One complication is that these equations do not take into consideration particles dissociating with kinetic energy released towards the detector arrive faster than the TOF_{CM}. This results in an underestimation of the particle-velocity vector. Similarly, particles dissociating with kinetic energy released away from the detector arrive slower than the CM resulting in underestimation of the particle-velocity vector. The effect is small for translational energies of interest in this thesis (< 1 eV), but the geometric corrections are implemented nonetheless with the algorithm detailed in the thesis of John Savee.[29]

The laboratory frame velocity vectors inherently contain an error in the CM causing a number of events to have a distribution of CM instead of a single point CM. This increases uncertainty in the momentum and energy calculations. To correct for this, the "true" CM can be calculated by assuming the masses of the fragments and calculating their CM through conservation of momentum for each event. Once these CM are determined and used to calculate the velocity vectors, the kinetic energy released can be determined using

$$KER = \frac{1}{2}\sum m_i * v_i^2 \quad (2.18)$$

where m_i is the mass for *i* fragments and *v* is their respective velocity vector.

For channels in which the dissociation channels are unclear or in question, the masses can be determined by calculating the masses of the fragments from the recoil radius at the detector and the parent mass.

$$m_{calc,i} = M_{parent} * \frac{d_1}{d_1+d_2} \quad (2.19)$$

$$d_i = \sqrt{x_{cm}^2 + y_{cm}^2 + z_{cm}^2} \quad (2.20)$$

In this case, the CM is assumed by setting the center of the neutral particle as the CM and d_1 and d_2 are the recoil distance from the CM. Plotting the calculated mass yields a histogram as shown in Figure 2.16 where the fragments in the top panel are calculated to be masses 18 and 64 while the bottom panel are 15 and 58. The imperfect nature of this measurement is shown in the error in the peak of the mass distributions. In this case, the top panel is for data taken using deuterated tert-butoxide while the bottom panel shows data taken using non-deuterated tert-butoxide.

2.4.4 Gating

Gating serves the purpose of improving the resolution of the experiment, reducing the contribution of bad data, and restricting the dataset to specific conditions such as trapping time or specific dissociative channels. When applied appropriately, gating can help isolate relevant data by removing data that is not consistent with the conditions that are of interest.

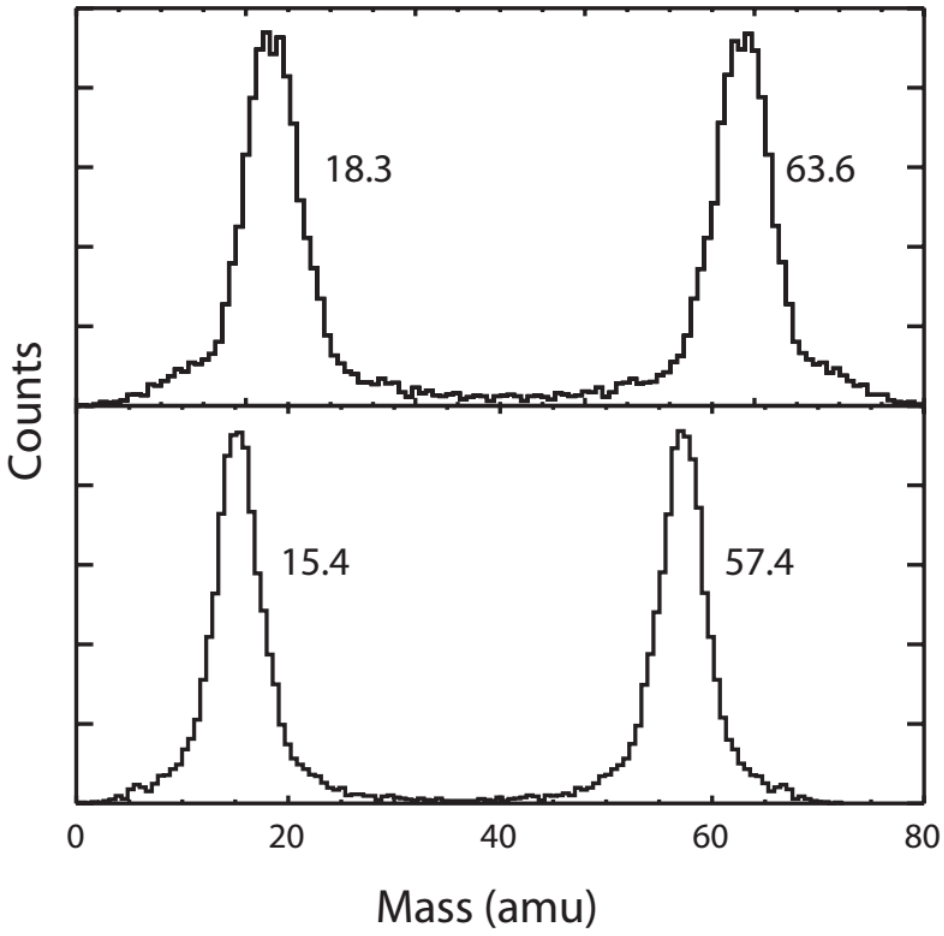

Figure 2.16. A sample mass histogram showing the calculated mass from an assumed center of mass.

For coincidence experiments, bad data can occur in a number of ways due to the detection efficiency of each detector being ~50%. For example, dissociation events where only one neutral particle is detected in coincidence with an electron is sorted as a stable photodissociation event. Alternatively, two photons interacting with two different anions resulting in two photodetachment events may result in the detection of two neutrals with one electron in coincidence sorted as a 2-TAC + 1 e event even though the neutrals are not a result of the same photodetachment event. A number of different combinations of bad data can occur which are all referred to as false coincidences. Centroid gating can help minimize the contribution of these events to the processed data. Centroids are calculated using conservation of momentum between particles defined by:

$$centroid_x = \sum m_i * v_{x,i} \tag{2.21}$$

Where m_i is the assumed mass and $v_{x,i}$ is the CM velocity in the x direction. The centroids for the y and z are calculated in the same way. Under ideal conditions, the centroids will have no distribution, but factors such as the interaction region being a volume of space and the finite velocity distribution results in centroids being a distribution. By decreasing the allowed range for centroid deviation, non-dissociative events can be better isolated by removing all events with neutral particle hits that deviate too far from the center of the centroid distribution. This would eliminate many dissociative events that are detected as stable. Limiting the centroids to a smaller range for dissociative events is also useful to removing false coincidence events that result from neutrals detected in coincidence from multiple dissociation events for a given laser shot. When running in multi-mass mode, the raw data is a distribution of events from multiple

parent masses. Gating on the neutral (time of arrival) can be used to narrow down the window in the time of arrival for the neutral particles for the parent mass of interest filtering out the data from all other masses.

When multiple dissociation channels are observed, centroid gating will not allow for the isolation of each channel due to all channels having the same parent mass and therefore same CM. The mass gate is a way to target data that is associated with particular dissociation channels. This gating method must be carefully used due to the masses being input by the user. Incorrect masses can lead to "bad" events being treated as good.

Since ions can be trapped within the EIBT for lengthy periods of time,[3] trap-time gating allows for the analysis of the time dependence of the internal energy of ions while trapped within a cryogenic environment. This allows for the observation of any radiative cooling that may occur as well as effects of intramolecular vibrational relaxation.

One of the most important gates for eKE resolution is the slicing along the z dimension. The uncertainty in the timing for the electron is significantly larger than the uncertainty in the position. This is due to the limitations of the timing measurement as well as some nonlinearities in the time to v_z conversion. Slicing the electron distribution to select only for those electrons with a v_z near 0 yields the highest resolution. This selection, however, induces a detector acceptance function (DAF) that emphasizes low eKE electrons and underrepresents the intensity of electrons with higher eKE. The DAF can be corrected by the following:

$$DAF = \begin{cases} \frac{|v|sin\,\theta}{v_z^{slice}}, & |v| > v_z^{slice}, \theta(|v|) > \theta^{slice}(|v|) \\ 1, & |v| \leq v_z^{slice} \\ 1, & \theta(|v|) \leq \theta^{slice}(|v|) \end{cases} \quad (2.22)$$

The effects of slicing and the DAF correction are shown in Figure 2.17 for the spectrum of O_2^- at 775 nm. The unsliced data is shown in the top panel while the sliced photoelectron spectra is shown in the middle panel demonstrating the significant gain in resolution. On the bottom panel, DAF correction has been applied where the lower eKE electrons are noticeably suppressed.

2.4.5 Coincidence Calculations

With both the electron and fragment kinetic energies calculated, the total kinetic energy can now be calculated:

$$E_{TOT} = eKE + KER \quad (2.23)$$

from which by conservation of energy, the internal energy of the fragments can be determined from:

$$E_{int} = KE_{MAX} - E_{TOT} \quad (2.24)$$

where KE_{MAX} is determined by the equation 1.8 as discussed in chapter 1.

A more convenient method to visualize the data is with a coincidence plot where the eKE is plotted on the y axis and the KER is plotted on the x axis to generate a two-dimensional histogram of the data. The benefit of viewing the data in this format is the ability to identify dissociative mechanisms which would be more ambiguous in a one-dimension experiment. Examples of this include identifying autodetachment channels after ionic photodissociation as discussed in Chapters 4 and 5. False coincidence can also

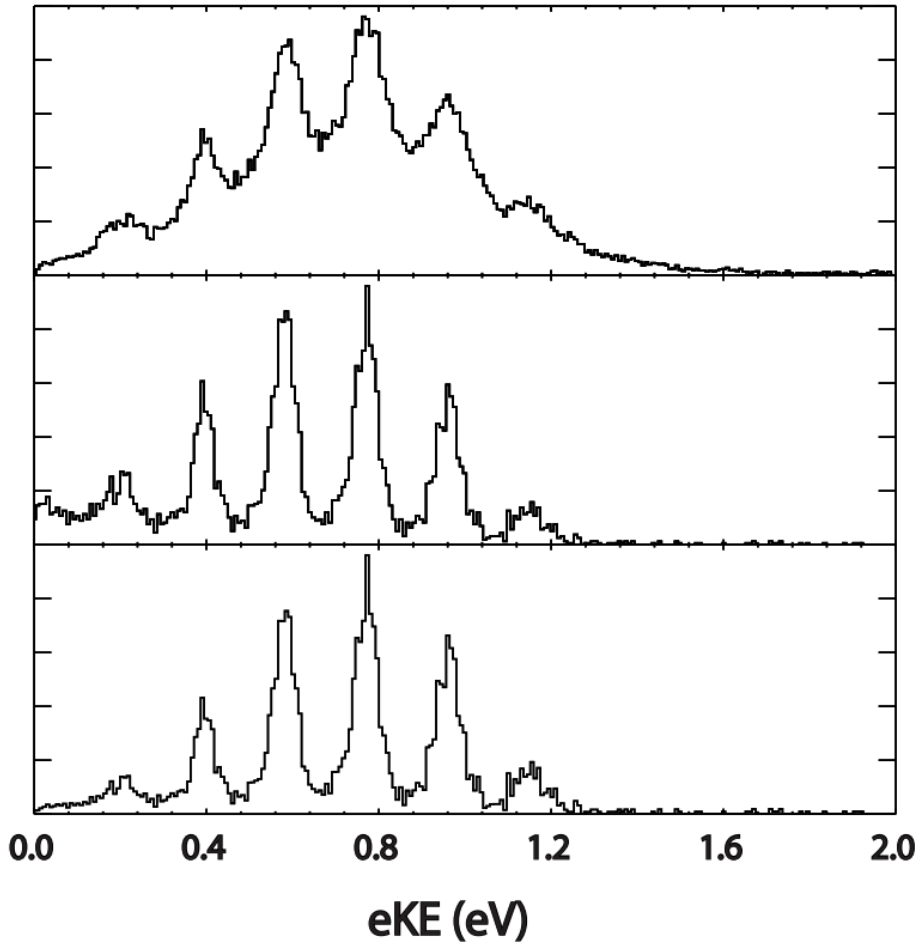

Figure 2.17. Photoelectron spectra showing the effects of slicing. The top image is the spectrum with no slicing. The middle panel shows the effects of slicing. The bottom panel shows the effects after DAF corrections.

be more readily identified in the coincidence plot due to features which have no physical explanation and behave oddly with gating.

1.1. References

1. Johnson, C. J. Investigation of the Reaction of OH and CO to Form H and CO 2 by Photoelectron Photofragment Coincidence Spectroscopy in a Cryogenic Ion Beam Trap University of California San Diego, 2011.

2. Ray, A. W. Dissociation Dynamics of Transient Molecules Studied by Photoelectron-Photofragment Coincidence Spectroscopy. University of California, San Diego, 2016.

3. Johnson, C. J.; Shen, B. B.; Poad, B. L. J.; Continetti, R. E., Photoelectron-Photofragment Coincidence Spectroscopy in a Cryogenically Cooled Linear Electrostatic Ion Beam Trap. *Review of Scientific Instruments* **2011,** *82* (10), 105105.

4. Johnson, C.; Otto, R.; Continetti, R., Spectroscopy and Dynamics of the HOCO Radical: Insights into the OH + CO -> H + CO_2 Reaction. *Physical Chemistry Chemical Physics* **2014,** *16* (36), 19091-19105.

5. Corderman, R.; LineBerger, W., Negative-Ion Spectroscopy. *Annual Review of Physical Chemistry* **1979,** *30*, 347-378.

6. Hock, C.; Kim, J.; Weichman, M.; Yacovitch, T.; Neumark, D., Slow Photoelectron Velocity-Map Imaging Spectroscopy of Cold Negative Ions. *Journal of Chemical Physics* **2012,** *137* (24).

7. Wang, L.; Ding, C.; Wang, X.; Barlow, S., Photodetachment Photoelectron Spectroscopy of Multiply Charged Anions Using Electrospray Ionization. *Review of Scientific Instruments* **1999,** *70* (4), 1957-1966.

8. Wang, X.; Wang, L., Photoelectron Spectroscopy of Multiply Charged Anions. *Annual Review of Physical Chemistry* **2009,** *60*, 105-126.

9. Smalley, R.; Wharton, L.; Levy, D., Molecular Optical Spectroscopy With Supersonic Beams and Jets. *Accounts of Chemical Research* **1977,** *10* (4), 139-145.

10. Sanz, M.; McCarthy, M.; Thaddeus, P., Vibrational Excitation and Relaxation of Five Polyatomic Molecules in an Electrical Discharge. *Journal of Chemical Physics* **2005,** *122* (19).

11. Shen, B.; Poad, B.; Continetti, R., Photoelectron-Photofragment Coincidence Studies of the tert-Butoxide Anion $(CH_3)_3CO^-$, the Carbanion Isomer $(CH_3)_2\ CH_2COH^-$, and Corresponding Radicals. *Journal of Physical Chemistry a* **2014,** *118* (44), 10223-10232.

12. Lu, Z.; Continetti, R., Dynamics of the Acetyloxyl Radical Studied by Dissociative Photodetachment of the Acetate Anion. *Journal of Physical Chemistry a* **2004,** *108* (45), 9962-9969.

13. Lu, Z.; Hu, Q. C.; Oakman, J. E.; Continetti, R. E., Dynamics on the HOCO Potential Energy Surface Studied by Dissociative Photodetachment of HOCO- and DOCO-. *Journal of Chemical Physics* **2007,** *126* (19), 194305.

14. Proch, D.; Trickl, T., A High-Intensity Multi-Purpose Piezoelectric Pulsed Molecular-Beam Source. *Review of Scientific Instruments* **1989,** *60* (4), 713-716.

15. Wiley, W.; McLaren, I., Time-of-Flight Mass Spectrometer With Improved Resolution. *Review of Scientific Instruments* **1955,** *26* (12), 1150-1157.

16. Otto, R.; Xie, J.; Brox, J.; Trippel, S.; Stei, M.; Best, T.; Siebert, M.; Hase, W.; Wester, R., Reaction Dynamics of Temperature-Variable Anion Water Clusters Studied With Crossed Beams and by Direct Dynamics. *Faraday Discussions* **2012,** *157*, 41-57.

17. Jones, R.; Gerlich, D.; Anderson, S., Simple Radio-Frequency Power Source for Ion Guides and Ion Traps. *Review of Scientific Instruments* **1997,** *68* (9), 3357-3362.

18. Jones, R.; Anderson, S., Simplified Radio-Frequency Generator for Driving Ion Guides, Traps, and Other Capacitive Loads. *Review of Scientific Instruments* **2000,** *71* (11), 4335-4337.

19. Wang, X.; Wang, L., Development of a Low-Temperature Photoelectron Spectroscopy Instrument Using an Electrospray Ion Source and a Cryogenically Controlled Ion Trap. *Review of Scientific Instruments* **2008,** *79* (7).

20. Kamrath, M.; Garand, E.; Jordan, P.; Leavitt, C.; Wolk, A.; Van Stipdonk, M.; Miller, S.; Johnson, M., Vibrational Characterization of Simple Peptides Using Cryogenic Infrared Photodissociation of H-2-Tagged, Mass-Selected Ions. *Journal of the American Chemical Society* **2011,** *133* (16), 6440-6448.

21. D. Gerlich, G. J., U. Mueck and U. Person Schnelles Ventil zur Erzeugung Sehr Kurzer Gasimpulse. http://www.tu-chemnitz.de/physik/ION/Technology.

22. Continetti, R.; Cyr, D.; Neumark, D., Fast 8-KV Metal-Oxide Semiconductor Field-Effect Transistor Switch. *Review of Scientific Instruments* **1992,** *63* (2), 1840-1841.

23. Bakker, J., Beam-Modulated Time-of-Flight Mass-Spectrometer 2. Experimental Work. *Journal of Physics E-Scientific Instruments* **1974,** *7* (5), 364-368.

24. Johnson, C. J. Investigation of the Reaction of OH and CO to Form H and CO 2 by Photoelectron Photofragment Coincidence Spectroscopy in a Cryogenic Ion Beam Trap University of California San Diego, 2011.

25. Eppink, A.; Parker, D., Velocity Map Imaging of Ions and Electrons Using Electrostatic Lenses: Application in Photoelectron and Photofragment Ion Imaging of Molecular Oxygen. *Review of Scientific Instruments* **1997,** *68* (9), 3477-3484.

26. Martin, C.; Jelinsky, P.; Lampton, M.; Malina, R.; Anger, H., Wedge-and-Strip Anodes For Centroid-Finding Position-Sensitive Photon And Particle Detectors. *Review of Scientific Instruments* **1981,** *52* (7), 1067-1074.

27. Continetti, R.; Cyr, D.; Osborn, D.; Leahy, D.; Neumark, D., Photodissociation Dynamics Of The N3 Radical. *Journal of Chemical Physics* **1993,** *99* (4), 2616-2631.

28. Hanold, K. A.; Luong, A. K.; Clements, T. G.; Continetti, R. E., Photoelectron-Multiple-Photofragment Coincidence Spectrometer. *Review of Scientific Instruments* **1999,** *70* (5), 2268-2276.

29. Savee, J. D. An Experimental Probe of Electronic Interactions in Excited Molecules Produced By Charge Exchange. University of California, San Diego, 2009.

30. Clements, T. G. Multi-Body Dissociative Photodetachment Dynamics of Small Molecular and Cluster Anions. University of California, San Diego, 2002.

Chapter 3: Photoelectron Photofragment Coincidence Studies of the tert-Butoxide Anion $(CH_3)_3CO^-$, the Carbanion Isomer $(CH_3)_2CH_2COH^-$ and Corresponding Radicals

3.1 Introduction

Oxygenated radicals play an important role as reaction intermediates in combustion processes as well as interstellar and atmospheric chemistry,[1-6] and are the subject of increased interest due to the expanding use of oxygenated biofuels. Alkoxy radicals have been observed as products and intermediates in atmospheric and combustion reactions principally formed *via* hydrogen abstraction from the OH moiety of alcohols, or through photodecomposition of alkyl nitrites.[7, 8] Alkylhydroxy radicals can be formed through reactions of alkanes and alkenes with OH radicals, and have recently been a focus of attention following the detection of enolic decomposition products in flames using photoionization mass spectrometry.[1, 9] Enols have now been observed in the combustion of a range of fuels.[1, 10-12] An understanding of the energetics and mechanism for the formation and decomposition of these important intermediates are key to accurate modeling of combustion processes.

The atmospheric and combustion chemistry of alkoxy radicals is typically dominated by three competing types of reactions: unimolecular decomposition, isomerization, and reaction with O_2.[4, 13] The *tert*-butoxy radical $(CH_3)_3CO$ presents an interesting case, owing to the lack of α hydrogens with respect to the radical center leading to a low reactivity with O_2 as well as a large barrier to isomerization.[6] This leaves unimolecular decomposition as the primary gas phase reaction pathway for this radical.[14,

[15] Unimolecular decomposition of the *tert*-butoxy radical occurs through ß-carbon-carbon bond cleavage, resulting in formation of acetone and methyl radical fragments with an activation energy of 0.65 eV.[6, 16-21] Previous experimental studies of the *tert*-butoxy radical include photofragment translational spectroscopy measurements of *tert*-butyl nitrite and *tert*-butyl hypochlorite (in which decomposition of *tert*-butoxy radical was observed as a secondary dissociation), laser-induced fluorescence and photoelectron spectroscopy of the *tert*-butoxide anion.[18, 19, 22-24] Quantum chemistry studies have been carried out to examine the energetics and reaction pathways involved in the unimolecular decomposition of the *tert*-butoxy radical.[6, 16, 25, 26 27, 28]

The $(CH_3)_2C(CH_2)OH$ α-alkylhydroxy radical isomer of the *tert*-butoxy radical, however, has received less attention. Studies of the combustion of *tert*-butanol have revealed formation of this radical through H atom abstraction from *tert*-butanol.[10] A flux analysis estimating the concentrations of species generated by combustion of *tert*-butanol in a flow reactor, using a kinetic model suggested by Grana *et al.*, indicates that the primary route for the decomposition is *via* hydrogen abstraction generating $(CH_3)_2C(CH_2)OH$ at moderate temperatures and relatively high pressures (775 K, 12.5 atm).[3, 11] The unimolecular decomposition of $(CH_3)_2C(CH_2)OH$ yielding propen-2-ol, a tautomer of acetone, and methyl radical is noted as one of the primary decomposition reactions in *tert*-butanol. [3, 11, 12, 29] The kinetic model suggested by Grana *et al.*, however, does not address the intermediate step in the dissociation of the $(CH_3)_2C(CH_2)OH$ radical and assumes isomerization of propen-2-ol to acetone, a process with a calculated barrier of 2.3 eV in the most recent CCSD(T) calculations.[3, 30,31] Kinetic modeling performed by Sarathy *et al*. accounts for enols, however the model overestimates the formation of

propen-2-ol.[12] The chemical dynamics and mechanisms formation of these transient species from alkylhydroxy radicals have been difficult to experimentally characterize.

Photoelectron-photofragment coincidence (PPC) spectroscopy allows the measurement of anion photoelectron spectra in coincidence with stable radicals and the identification of dissociation pathways through measurement of the energy partitioning in dissociative photodetachment (DPD) processes.[32, 33] In this study we extend our earlier studies of cyclic alkoxy radicals[34, 35] and the ethoxy radical[36] using this technique to the largest system to date, the isomeric $C_4H_9O^-$ anions (*m/z* = 73). Proton abstraction from *tert*-butanol in a pulsed electric discharge is expected to produce *tert*-butoxide along with a possibility of trace amounts of the less-stable α-hydroxy carbanion isomer, with subsequent photodetachment and DPD processes produced by simple bond fission outlined in Figure 1. Other possible isomeric forms, the *n*-butoxide and *sec*-butoxide isomers, are outlined in Figure 2. Studies of both $C_4H_9O^-$ and $C_4D_9O^-$ were carried out at 387, 537 and 600 nm. Photodetachment to produce stable radicals was found to be the dominant pathway, along with a minor DPD channel at all three wavelengths. The results and theoretical calculations used to interpret them will be discussed in detail following a review of the experimental method. The data shows that *tert*-butoxide thermalized to ~ 550 K yields stable radical products along with a dissociation channel arising from an unrelaxed non-Boltzmann distribution of highly excited *tert*-butoxide anions that undergo DPD to methyl radical (CH_3) + acetone ($(CH_3)_2CO$) products. In addition, evidence for a trace amount of the higher energy α-hydroxy carbanion $(CH_3)_2C(CH_2)OH^-$ is observed.

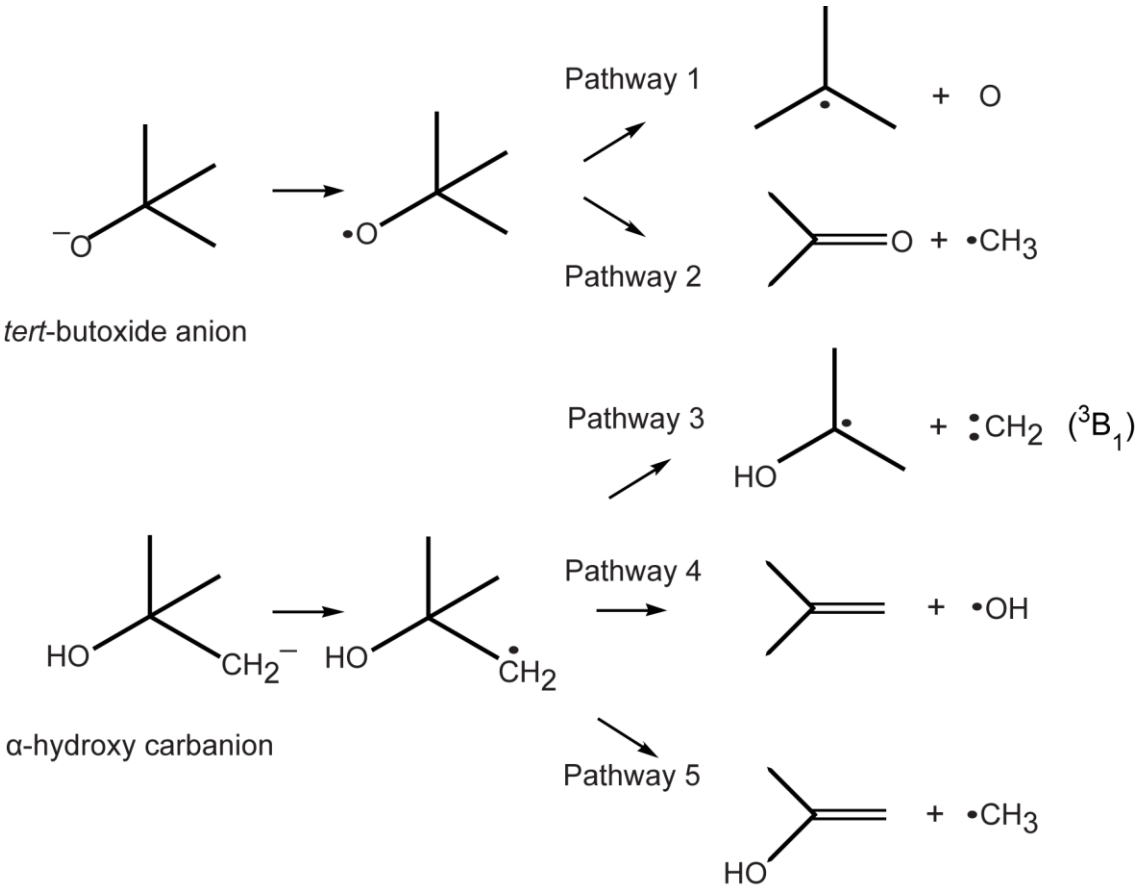

Figure 3.1. Schematic of possible dissociative pathways for *tert*-butoxide, $(CH_3)_3CO^-$, and the α-hydroxy carbanion, $(CH_3)_2C(CH_2)OH^-$ upon photodetachment.

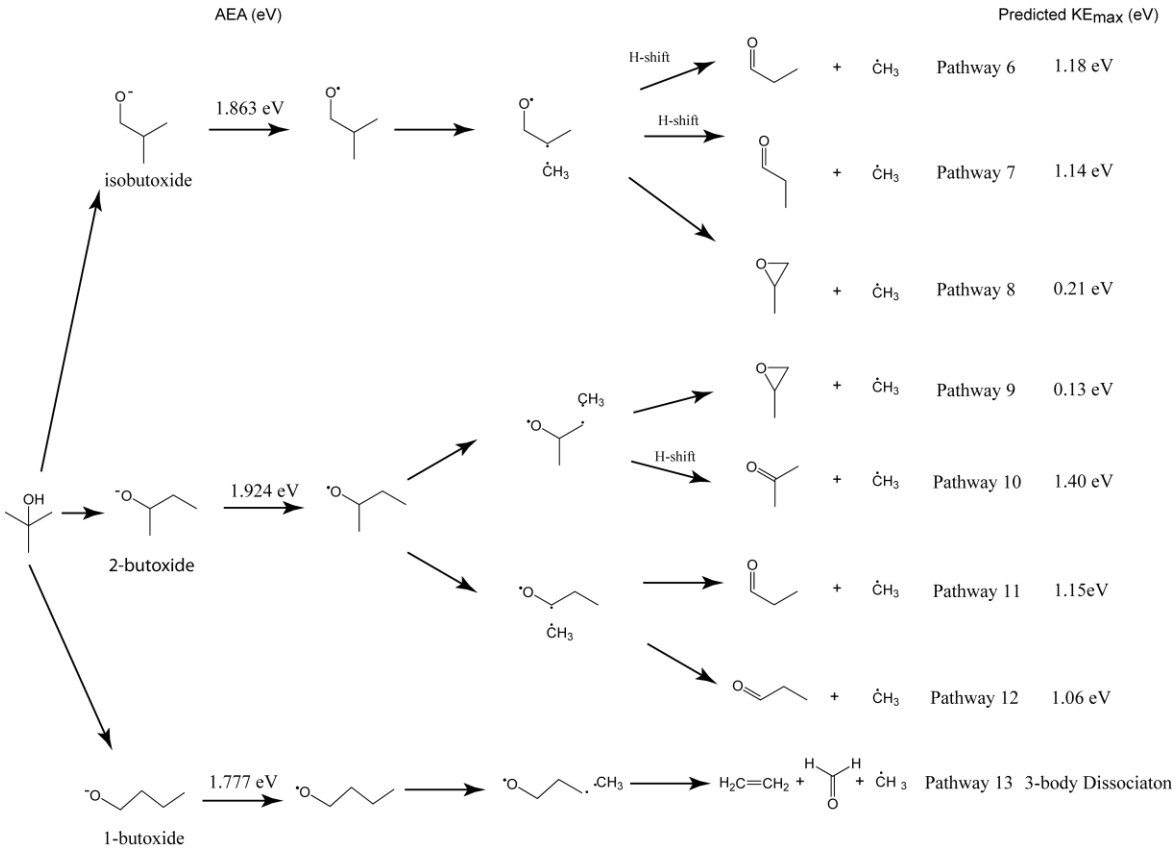

Figure 3.2. Calculated pathways, at the CBS-QB3 level of theory, consistent with the observed product mass distribution for mass 73 isomers assuming rearrangement of the carbon framework of *tert*-butoxide are shown. The adiabatic electron affinity (AEA) is indicated on the left while KE_{max} based on $E_{h\nu}$ = 3.20 eV is shown on the right. The largest KE_{max} of the rearrangement precursors is Pathway 10 but is a poor match with the PPC spectra, as this is smaller than the experimental KE_{max} by 0.4 eV.

3.2 Experimental

Photoelectron-photofragment coincidence experiments were conducted on a fast ion beam apparatus using an electrostatic ion beam trap (EIBT) as described in detail elsewhere, and only briefly reviewed here.[37] Isomeric precursor anions were synthesized in a pulsed ion source consisting of a coaxial discharge (400-500 V) acting upon a supersonic expansion of a 10:1 Ar/N_2O gas mixture at a pressure of 60 psig bubbled through room temperature *tert*-butanol (Fisher Scientific) and then intersected by a 1 keV electron beam. Deuterated *tert*-butanol (99% d-10, Cambridge Isotope Laboratories) was used to synthesize the deuterated isomers. The putative mechanism for ion formation is dissociative electron attachment to N_2O producing O^- that abstracts protons from *tert*-butanol, yielding *m/z* 73 anions for *tert*-butanol and *m/z* 82 for *tert*-butanol-d10. The anions were accelerated to 7 keV, re-referenced to ground, mass selected by time of flight, and trapped in a cryogenically cooled EIBT for a period ranging from 100 ms to 5 seconds. The effective parent-ion mass resolution for neutrals ejected from the trap is $m/\Delta m \sim 5000$ at *m/z* 73. While trapped, the ions were bunched and phase locked using an RF oscillator synchronized with a field-programmable gate array to the output from a Ti:Sapphire regenerative amplifier (Clark MXR CPA-2000; λ=774.4 nm, 1037 Hz repetition rate, 1.8 ps pulse width). The output was frequency doubled to 387.2 nm ($E_{h\nu}$ = 3.20 eV) and intersected with the ion packet at the center of the trap to induce photodetachment. Wavelengths of 537 nm ($E_{h\nu}$ = 2.31 eV) and 600 nm ($E_{h\nu}$ = 2.07 eV)

were generated by directing the 387 nm radiation into an optical parametric amplifier (Light Conversion TOPAS 4-400).

Photodetached electrons were extracted orthogonal to the plane of the laser and ion beams using a velocity map imaging electrode configuration coupled with a time- and position-sensitive electron detector. With this information, the center-of-mass electron kinetic energy (eKE) and recoil direction for single electrons were recorded on an event-by-event basis yielding photoelectron spectra. The electron time-of-flight measurement (the z-velocity component, where the x-y plane is parallel to the detector face) has the largest uncertainty, so higher resolution spectra were obtained by selecting only electrons with minimal z velocity components as an equatorial slice. In this case the fraction of detected electrons decreases as electron velocity increases, biasing the intensity distribution of sliced photoelectron spectra in favor of low kinetic energy electrons. This detector-acceptance function (DAF) was corrected for to generate the P(eKE) spectra presented here.[38] Photoelectron energies were calibrated using O_2^- photodetachment with a resolution $\Delta P(eKE)/P(eKE)$ ~3% at eKE = 1.1 eV using $E_{h\nu}$ = 2.31 eV, and O^- photodetachment at photon energies of 3.20 eV and 2.07 eV with a resolution of ~4% at eKE = 1.7 eV and 0.6 eV, respectively.

The corresponding neutral products or stable radicals then flew out of the trap and were detected by a time- and position-sensitive multi-particle neutral detector at a distance of 1.31 m from the interaction region.[39] Stable radicals are observed as a single particle arriving at the centroid (time and position) of the parent anion beam. Dissociation events were selected from the data by enforcing coincidence between the detection of one electron and two momentum-matched neutral fragments. The dissociative fraction was

found to be 3-5% of the total number of events, varying with ion source conditions. Neutral particle masses were calculated by momentum conservation using the three-dimensional (v_x,v_y,v_z) velocity information for each particle determined from the measured position and time-of-arrival (x,y,t) at the multiparticle detector, allowing calculation of the translational energy release (E_T) for that event. The product mass distributions have a resolution limited by the distribution of centroids, dictated by the angular divergence and energy spread of the ions in the laser-ion beam interaction volume in the EIBT, resulting in a Gaussian full-width at half-maximum (FWHM) of 2.5 amu. Given the kinematics of dissociative events observed in this experiment, the effect of the heavy particle DAF on collection efficiencies is not significant,[40] so the product translational energy distributions are reported as the measured $N(E_T)$ distributions. The resolution of the E_T measurement was determined using O_4^- dissociative photodetachment to be $\Delta E_T/E_T \approx 10\%$ at $E_T = 0.8$ eV.[41]

3.3 *Ab initio* Calculations and Franck-Condon Simulations

To aid interpretation of the experimental results, *ab initio* calculations of the structures, energetics and isomerization barriers for anionic and neutral forms of the C_4H_9O isomers were carried out. The relevant simple-bond-fission dissociation pathways shown in Figure 1 and Figure 2 were performed at the MP2/6-311++G(d,p) level as well as the Complete Basis Set CBS-QB3 composite method implemented in the Gaussian03 program suite.[42-44] The CBS-QB3 method uses B3LYP optimized geometries and frequencies followed by MP2 energy calculations with complete basis set (CBS) extrapolation in addition to MP4 and coupled-cluster CCSD(T) energy corrections allowing for low computational cost while still performing well on the G2 test set.[42]

Adiabatic electron affinities (AEA) are reported as the energy difference between the optimized geometries of the anion and neutral radical while vertical detachment energies (VDE) were calculated as the energy difference between the anion and neutral radical fixed in the same geometry as the anion. Transition states with first-order saddle points were initially identified with the synchronous transit-guided quasi-Newton (QST3) algorithm at the MP2/6-311++G(d,p) level using the optimized reactant and product structures along with a guess for the transition state. The resulting transition state geometries were optimized using the CBS-QB3 method for consistency in level of theory, and confirmed using the intrinsic reaction coordinate routine (IRC) at the B3LYP/6-311++G(d,p) level of theory.[45, 46] All energy values are zero-point corrected at 0 K and are listed in Table 1. Spin contamination for all open-shell calculations was found to be low, with $<S^2>$ found to differ from the ideal value of 0.75 by less than 10%.[47]

Using the structures and Cartesian force constants at the MP2 level of theory, Franck-Condon (FC) simulations were carried out for both *tert*-butoxide and the carbanion. The FC factors were calculated assuming independent harmonic oscillators taking into account Duschinsky rotation effects between the geometries of the anion and the neutral, implementing the Sharp-Rosenstock-Chen method using the PESCAL program.[48] Carrying out these calculations on a system with 36 modes, a finite temperature and no symmetry (the carbanion) is computationally challenging and will be further discussed below.

Table 3.1. Zero-point corrected energies for species relevant to pathways indicated in Figure 1 and Figure 2.

Species	Method	
	MP2/6-311++G(d,p) (Hartrees)	CBS-QB3 (Hartrees)
$(CH_3)_3COH$	-232.913409	-233.235589
$(CH_3)_3CO^-$	-232.316808	-232.639927
$(CH_3)_3CO$	-232.245902	-232.567541
$(CH_3)_2CO$	-192.571331	-192.819657
$(CH_3)_2C(CH_2)OH^-$	-232.278856	-232.598410
$(CH_3)_2C(CH_2)OH$	-232.258859	-232.574298
$(CH_3)_2COH$	-192.533929	-193.354654
$(CH_3)C(CH_2)OH$	-192.549973	-192.800431
$(CH_3)_2CCH_2$	-156.639600	-156.770858
$OCH_2CH(CH_3)_2^-$	----------	-232.627517
$OCH_2CH(CH_3)_2$	----------	-232.559047
$OCH_2CH_2CH_2CH_3^-$	----------	-232.620984
$OCH_2CH_2CH_2CH_3$	----------	-232.555686
$OCH(CH_3)CH_2CH_3^-$	----------	-232.630437
$OCH(CH_3)CH_2CH_3$	----------	-232.559734
$OCHCH_2CH_3$	----------	-192.806828
Propylene Oxide	----------	-192.772899
CH_3	-39.678492	-39.744795
CH_2	-38.989604	-39.069832
OH	-75.571161	-75.649716
O	-74.921781	-74.987629

3.4 Results

In the following sections, the experimental results for photodetachment of *m/z* 73 and *m/z* 82 at $E_{h\nu}$ = 3.20, 2.31 and 2.07 eV are presented, with an initial focus on the 3.20 eV data where the branching between stable photodetachment and DPD was observed along with evidence for the α-hydroxy carbanion. This will be followed by the vibrationally resolved spectra at $E_{h\nu}$ = 2.31 and 2.07 eV as well as a discussion of the Franck-Condon simulations.

3.4.1 Photodetachment at $E_{h\nu}$ = 3.20 eV

Photoelectron spectra acquired at $E_{h\nu}$ = 3.20 eV are shown in Figure 3. Figure 3(a) shows the P(eKE) spectrum for stable radicals (one electron + one stable radical; black histogram), with the minor dissociative channel (one electron + two momentum-matched photofragments; red histogram) shown to scale. The spectrum for the stable channel peaks at 1.2 eV, and the spectrum is qualitatively consistent with an assignment to *tert*-butoxide, given the previous measurements of the AEA = 1.91 eV for this system denoted by the blue line at eKE = 1.29 eV.[24, 49] The high energy tail is consistent with the carbanion at a theoretical AEA of 0.66 eV (denoted by the green line at 2.54 eV). Figure 3(b) shows the dissociative photoelectron spectrum rescaled, and it can be seen that it is shifted to lower energy by ~0.2 eV, peaking near 1.0 eV.

PPC spectroscopy enables deeper analysis of the dissociative pathway, in particular the product masses and the correlation of the photofragment and photoelectron kinetic energies. Figure 4 shows the product mass distributions observed in the DPD of *m/z* 73 ($C_4H_9O^-$) and *m/z* 82 ($C_4D_9O^-$) anions in the $E_{h\nu}$ = 3.20 eV experiment. Signals

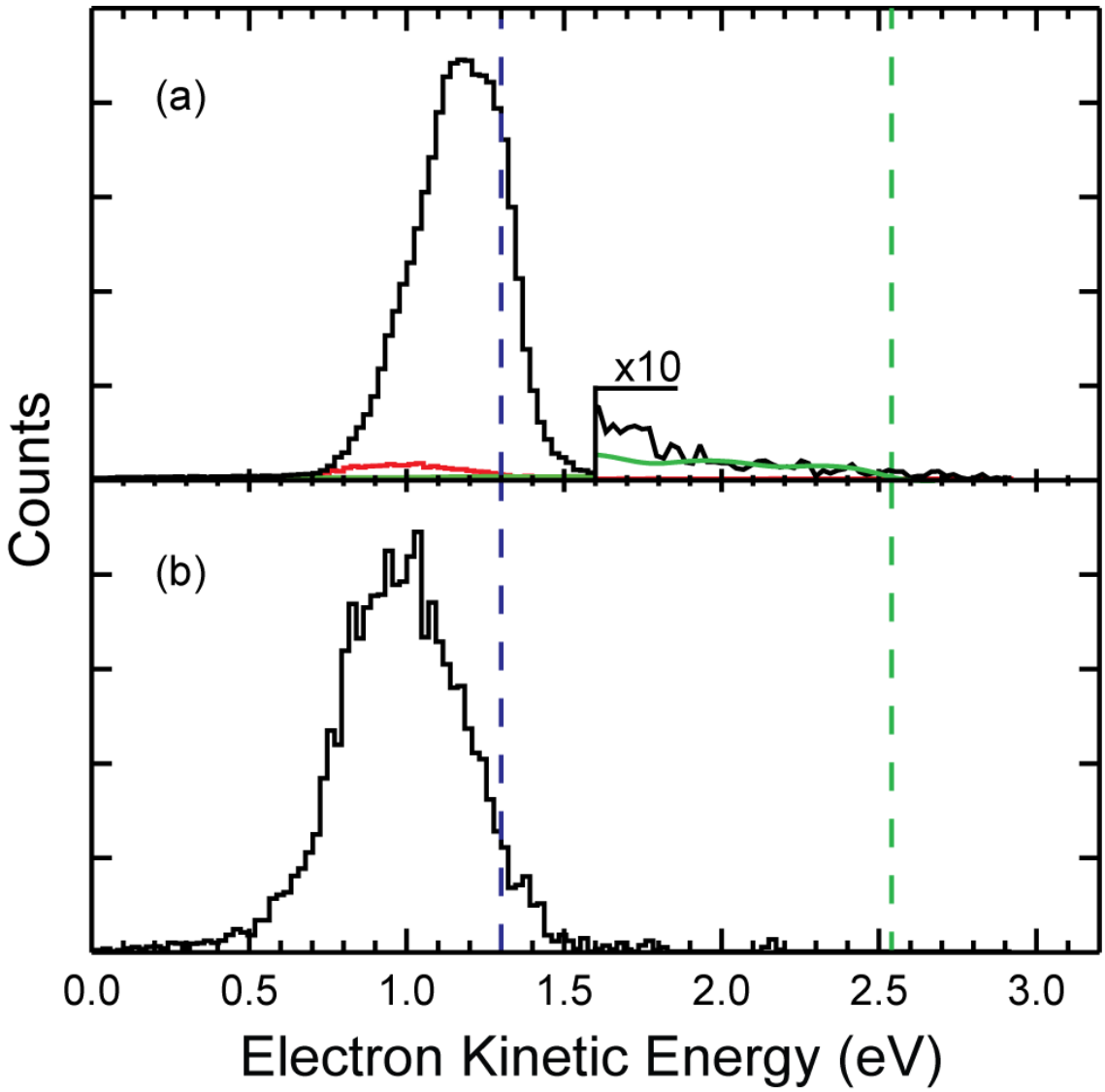

Figure 3.3. Photoelectron spectra for the stable and dissociative channels measured at $E_{h\nu}$ = 3.20 eV. Vertical lines are placed at the experimental AEA for the *tert*-butoxy radical (blue) and theoretical AEA for the alkyhydroxy radical (green). The top spectrum (a) shows the stable (black) and dissociative (red) P(eKE) plotted on the same y axis scale with the minor contribution from the carbanion (green). The bottom spectrum (b) shows the dissociative P(eKE) spectrum scaled to the peak intensity.

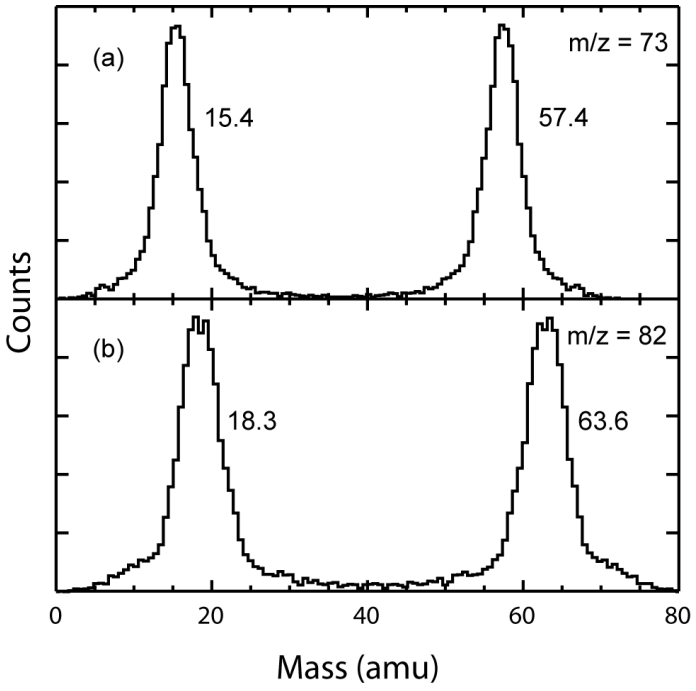

Figure 3.4. Product mass distribution for the (a) non-deuterated and (b) deuterated species. Gaussian fits to the lighter mass fragments give peaks of 15.4 and 18.3 amu as shown.

for the light fragments peak at 15.4 and 18.3 amu for the non-deuterated and deuterated isotopologs, respectively, consistent with loss of a CH_3 (CD_3) methyl radical, however the limited product mass resolution does not rule out the possibility of minor dissociative pathways within ±2 amu. The PPC spectra, shown in Figure 5 for both $C_4H_9O^-$ and $C_4D_9O^-$ at $E_{h\nu}$ = 3.20 eV, directly show the translational energy partitioning between the photoelectron and the photofragments. The corresponding one-dimensional P(eKE) and $N(E_T)$ spectra are shown as the projections along the y and x axes, respectively, and are found by integrating over the complementary kinetic energy. For both isotopologs, significant repulsion between the neutral photofragments is observed as evidenced by E_T peaking away from 0 eV. The $C_4H_9O^-$ $N(E_T)$ spectrum peaks at E_T ~ 0.45 eV, while the $C_4D_9O^-$ spectrum peaks at E_T ~ 0.40 eV. In addition, a peak is seen in both spectra near E_T = 0 eV owing to false coincidences with the dominant stable radical channel.

To help determine the origin of the dissociation process it is useful to consider the energetics of the parent anions, corresponding neutral radicals and dissociation products as determined by quantum chemical calculations. The two isomeric anions that can be produced by proton abstraction from *tert*-butanol are *tert*-butoxide and the α-hydroxy carbanion. The α-hydroxy carbanion is less stable than *tert*-butoxide by 1.13 eV, as shown in the energy diagram in Figure 6 and the *ab initio* energies in Table 1. Preferential formation of *tert*-butoxide is expected since *ab initio* calculations indicate that proton abstraction from the alcohol group is exoergic by 0.43 eV while proton abstraction from a methyl substituent is endoergic by 0.70 eV. Given the high energy environment during anion generation in a discharge ion source, endothermic chemical

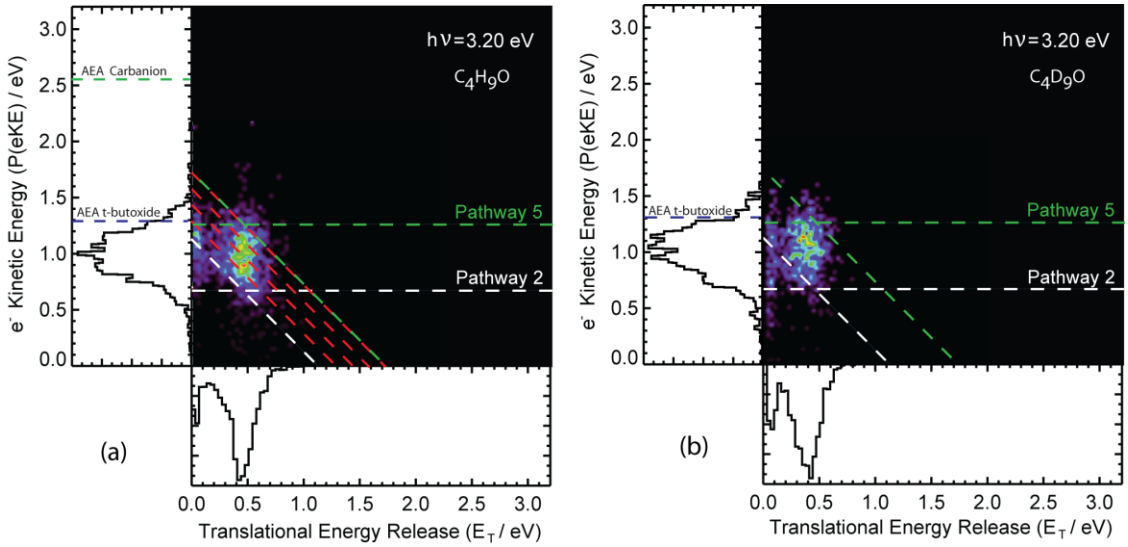

Figure 3.5. Photoelectron photofragment coincidence spectra for (a) $C_4H_9O^-$ and (b) $C_4D_9O^-$ at $E_{h\nu}$ = 3.20 eV. The horizontal dashed lines represent eKE_{MAX} (Table 7) indicating the calculated barriers for dissociation while the diagonal dashed lines indicate the KE_{MAX} (Table 6) for Pathways 2 and 5 in white and green respectively. The progression of red diagonal dashed lines shown in (a) represents the shift in the KE_{MAX} with each quanta of excitation in the ν_{16} vibrational mode of the anion.

processes may occur and the ion formation mechanism may be far more complicated than proton abstraction by O^-.[50, 51] While the *tert*-butoxide anion is more stable relative to the $(CH_3)_2C(CH_2)OH^-$, the supersonic expansion following the electrical discharge in the ion source can allow for the cooling and stabilization of $(CH_3)_2C(CH_2)OH^-$ in the parent ion beam, an approach that has been exploited previously to preferentially synthesize $HOCO^-$ over the isomeric and energetically more stable HCO_2^- anion.[33, 37, 52]

In consideration of these two isomers, *ab initio* optimized geometries for both *tert*-butoxide and the carbanion along with their respective neutrals are summarized in Tables 2 and 3 at both the MP2 and CBS-QB3 level of theory. The *tert*-butoxide anion optimizes to a C_{3V} geometry, ignoring Jahn-Teller distortions, at both levels of theory with the corresponding degenerate vibrational modes (Table 4) while the neutral optimizes to a C_s geometry with a $^2A'$ ground state, consistent with an expected Jahn-Teller distortion of the C-O bond away from the threefold symmetry axis in this open shell system.[24, 53, 54] Relatively small changes in geometry are predicted upon photodetachment, with 0.04 Å the largest calculated C-C bond length change. The optimized geometry for the carbanion and alkylhydroxy radical, on the other hand, indicate large geometry changes with the C-O bond length shortening by 0.11 Å as a result of a change in the HOMO from anti-bonding in character to bonding and large shifts in the HOCC and HCCO dihedral angles. The largest C-C bond length change is relatively small, with a difference of 0.03 Å, and virtually no changes in C-H bond lengths with the exception of the CH_2 substituent. The VDE and AEA for the *tert*-butoxide anion were calculated to be 2.12 and 1.97 eV, respectively; significantly higher than the corresponding values for the carbanion (0.87 and 0.66 eV, respectively).

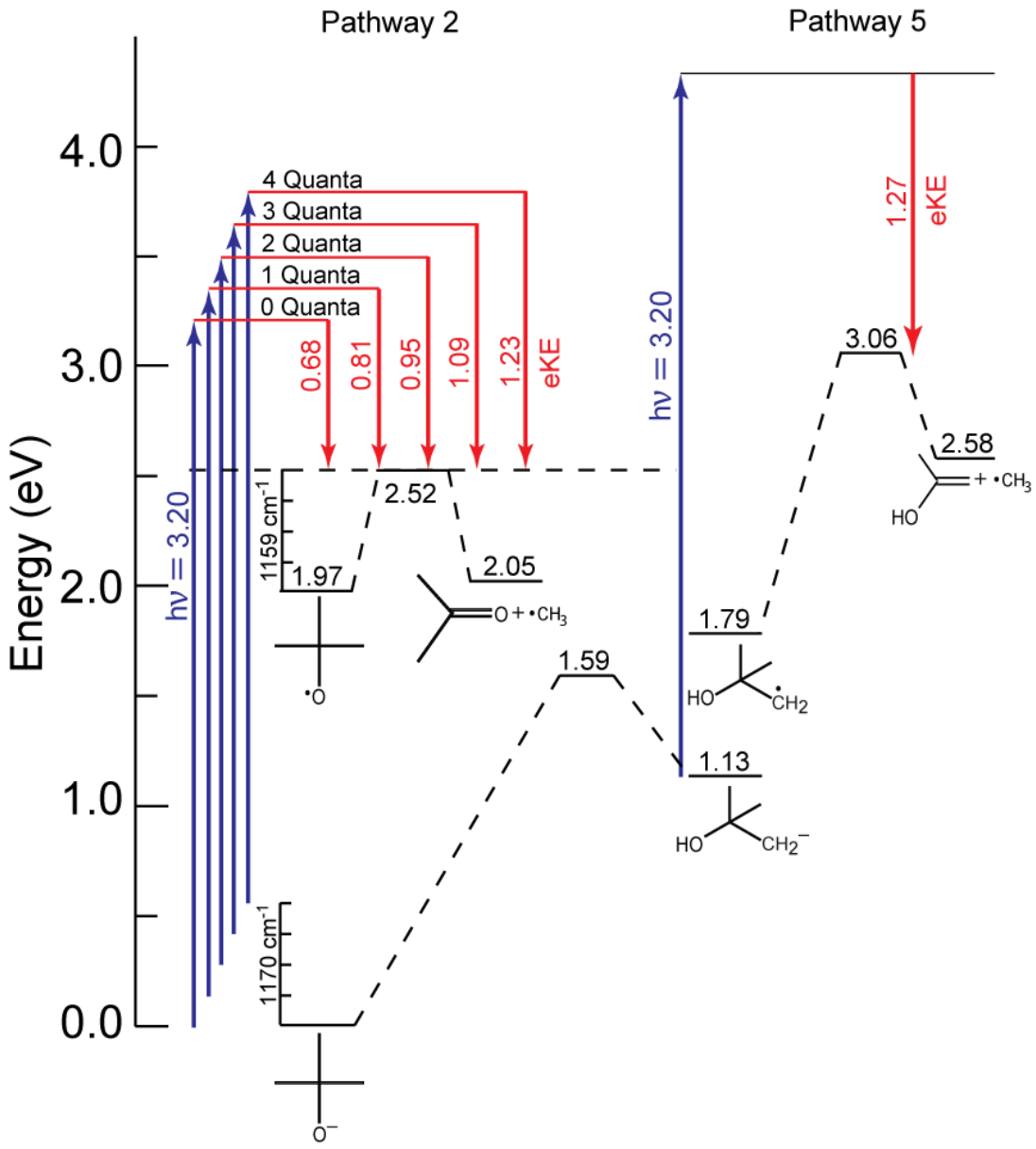

Figure 3.6. CBS-QB3 energetics for Pathway 2 and Pathway 5 referenced to the *tert*-butoxide anion. Vibrational transitions from ν_{16} = 0 – 4 in *tert*-butoxide to ν_{16} =4 in the *tert*-butoxy radical are shown along with the corresponding eKE for these transitions.

Table 3.2. Geometries optimized *tert*-butoxide anion, radical and dissociative transition state with bond lengths in Å and angles in degrees.

Anion

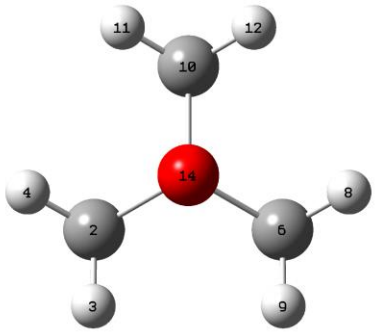

Radical

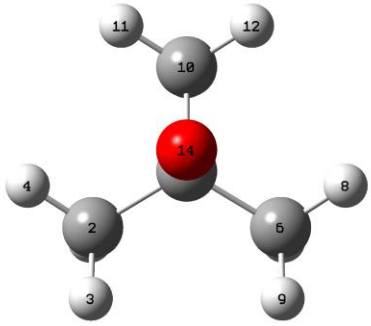

		MP2/6-311++G(d,p)			CBS-QB3				
		Anion	Δ	Radical	Anion	Δ	Radical	Δ	Dissociative TS
Bond Length	C(1)-C(2)	1.56	-0.03	1.53	1.58	-0.04	1.54	-0.01	1.53
	C(1)-C(6)	1.56	-0.03	1.53	1.58	-0.04	1.54	0.58	2.12
	C(1)-C(10)	1.56	-0.02	1.54	1.58	-0.02	1.56	-0.03	1.53
	C(1)-O(14)	1.35	0.06	1.39	1.32	0.06	1.38	-0.13	1.25
	C(2)-H(3)	1.09	0.00	1.09	1.09	0.00	1.09	0.00	1.09
	C(2)-H(4)	1.09	0.00	1.09	1.09	0.00	1.09	0.00	1.09
	C(2)-H(5)	1.10	-0.01	1.09	1.10	-0.01	1.09	0.00	1.09
	C(6)-H(7)	1.10	-0.01	1.09	1.10	-0.01	1.09	-0.01	1.08
	C(6)-H(8)	1.09	0.00	1.09	1.09	0.00	1.09	-0.01	1.08
	C(6)-H(9)	1.09	0.00	1.09	1.09	0.00	1.09	-0.01	1.08
	C(10)-H(11)	1.09	0.00	1.09	1.10	-0.01	1.09	0.01	1.10
	C(10)-H(12)	1.09	0.00	1.09	1.10	-0.01	1.09	0.00	1.09
	C(10)-H(13)	1.10	-0.01	1.09	1.10	-0.01	1.09	0.00	1.09
Angle	C(10)-C(1)-C(6)	107.1	3.4	110.5	106.8	3.1	110.0	-10.9	99.1
	C(6)-C(1)-C(2)	107.1	4.6	111.7	106.8	5.2	112.0	-12.9	99.1
	C(2)-C(1)-O(14)	111.8	-1.6	110.2	112.0	-1.2	110.8	8.4	119.2
	C(10)-C(1)-O(14)	111.8	-8.4	103.4	112.0	-9.1	102.9	16.3	119.2
Dihedral	H(4)C(2)C(1)(O14)	58.5	-1.3	57.2	57.9	-2.4	55.5	26.3	81.8
	H(11)C(10)C(1)O(14)	-58.5	-2.0	-60.5	-57.9	-2.5	-60.4	-21.4	-81.8
	H(8)C(6)C(1)O(14)	-58.5	1.3	-57.2	-57.9	2.4	-55.5	-4.1	-59.6

Table 3.3. Geometries of the optimized anion, radical, and dissociative transition state of $(CH_3)_2C(CH_2)OH$ with bond lengths in in Å and angles in degrees.

Anion Radical

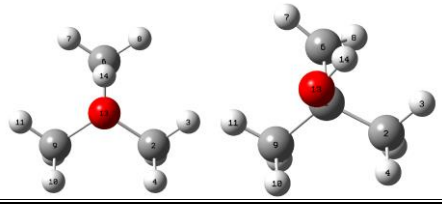

		MP2/6-311++G(d,p)			CBS-QB3				
		Anion	Δ	Radical	Anion	Δ	Radical	Δ	Dissociative TS
Bond Length	C(1)-C(2)	1.53	0.00	1.53	1.54	0.00	1.54	0.70	2.24
	C(1)-C(6)	1.47	0.03	1.50	1.47	0.03	1.50	-0.12	1.38
	C(1)-C(9)	1.53	0.00	1.53	1.54	0.00	1.54	-0.03	1.51
	C(1)-O(13)	1.54	-0.10	1.44	1.56	-0.11	1.45	-0.07	1.38
	C(2)H(3)	1.10	0.00	1.10	1.09	0.00	1.09		
	C(2)H(4)	1.10	-0.01	1.09	1.10	-0.01	1.09		
	C(2)H(5)	1.09	0.00	1.09	1.09	0.00	1.09		
	C(6)H(7)	1.10	-0.01	1.08	1.10	-0.02	1.08		
	C(6)H(8)	1.10	-0.01	1.08	1.10	-0.02	1.08		
	C(9)H(10)	1.10	0.00	1.09	1.10	0.00	1.10		
	C(9)H(11)	1.10	0.00	1.09	1.10	0.00	1.10		
	C(9)H(12)	1.09	0.00	1.09	1.09	0.00	1.09		
	O(13)H(14)	0.96	0.00	0.96	0.96	0.00	0.96		
Angle	C(9)-C(1)-C(6)	112.7	-1.8	110.9	112.5	-1.3	111.2	11.1	122.3
	C(6)-C(1)-C(2)	112.7	-1.7	111.0	112.5	-1.0	111.5	-12.6	98.9
	C(2)-C(1)-O(13)	103.2	6.7	109.9	102.6	7.0	109.6	11.1	98.5
	C(9)-C(1)-O(13)	103.2	1.3	104.5	102.6	1.6	104.2	-6.0	110.2
Dihedral	H(14)O(13)C(1)C(2)	122.7	-55.5	67.3	122.8	-54.7	68.1		
	H(10)C(9)C(1)O(13)	-47.3	-11.5	-58.8	-47.9	-10.2	-58.1		
	H(7)C(6)C(1)O(13)	-69.3	26.0	-43.3	-62.7	14.9	-47.8		
	H(4)C(2)C(1)O(13)	47.3	9.6	56.9	47.9	8.4	56.3		

Table 3.4. List of calculated frequencies sorted by wavenumber for *tert*-butoxide anion (C_{3v}) and the tert-butoxy radical (C_s) with irreducible representations for each vibrational mode.

Mode	$(CH_3)_3CO^-$			$(CH_3)_3CO$			
	MP2/6-311++G(d,p)	CBS-QB3	C_{3V} Symmetry	MP2/6-311++G(d,p)	C_s Symmetry	CBS-QB3	C_s Symmetry
1	203.7	188.1	A2	178.5	A"	177.1	A"
2	286.1	246.4	E	251.1	A"	236.2	A"
3	286.1	246.4	E	266.3	A'	242.7	A'
4	336.6	321.7	E	334.1	A'	323.7	A'
5	336.6	321.7	E	334.2	A"	327.7	A"
6	409.9	388.3	A1	410.2	A"	405.3	A'
7	480.2	469.5	E	410.7	A'	413.1	A"
8	480.2	469.5	E	434.1	A'	430.0	A'
9	723.2	662.3	A1	767.4	A'	729.5	A'
10	837.4	756.7	E	913.2	A"	870.2	A'
11	837.4	756.7	E	915.3	A'	894.8	A"
12	919.5	890.7	A2	945.9	A'	922.5	A'
13	1020.3	991.2	A1	971.6	A"	957.2	A"
14	1023.2	991.2	E	1026.4	A"	995.5	A"
15	1023.2	1015.7	E	1037.7	A'	1009.7	A'
16	1210.1	1169.5	E	1221.5	A'	1159.2	A'
17	1210.1	1169.5	E	1242.9	A"	1174.8	A"
18	1241.3	1271.4	A1	1283.2	A'	1244.8	A'
19	1336.8	1316.1	E	1395.3	A'	1373.3	A'
20	1336.8	1316.1	E	1400.3	A"	1380.5	A"
21	1365.5	1345.2	A1	1429.7	A'	1413.3	A'
22	1466.7	1445.9	A2	1484.7	A"	1462.9	A"
23	1476.8	1461.8	E	1494.1	A"	1478.9	A"
24	1476.8	1461.8	E	1499.7	A'	1487.8	A'
25	1490.4	1472.5	E	1511.9	A"	1489.8	A"
26	1490.4	1472.5	E	1512.1	A'	1493.2	A'
27	1505.9	1493.4	A1	1533.7	A'	1517.4	A'
28	2993.5	2920.3	E	3067.9	A"	3027.1	A"
29	2993.5	2920.3	E	3071.9	A'	3032.7	A'
30	3008.1	2945.2	A1	3077.6	A'	3039.5	A'
31	3094.3	3019.7	E	3159.4	A"	3095.4	A"
32	3094.3	3019.7	E	3164.8	A'	3101.8	A'
33	3105.6	3034.1	A1	3171.7	A"	3109.6	A"
34	3127.0	3045.8	A2	3172.9	A'	3111.0	A'
35	3134.2	3056.1	E	3177.4	A'	3118.0	A'
36	3134.2	3056.1	E	3182.8	A"	3129.9	A"

Assuming *tert*-butoxide and the carbanion are the initial species, the simple bond fission dissociation reactions shown in Figure 1 with energetics listed in Tables 1 and 2 can be considered. These are all possible given the relatively low mass resolution in the experiment for the neutral photofragments, however, only two channels producing CH_3 radicals, Pathway 2 for *tert*-butoxy radical ($(CH_3)_3CO \rightarrow CH_3 + (CH_3)_2CO$) and Pathway 5 for the carbanion radical ($(CH_3)_2C(CH_2)OH \rightarrow CH_3 + CH_3C(CH_2)OH$), are consistent with the change in the photofragment mass distribution observed upon deuteration. Table 6 outlines the DPD energetics (KE_{max}) for the reaction channels and barrier heights for dissociation of the neutral radicals (eKE_{max}) expected at $E_{h\nu} = 3.20$ eV. An energy level diagram at the CBS-QB3 level of theory for Pathways 2 and 5, including calculated barriers, is shown in Figure 6 with the energies reported relative to the *tert*-butoxide anion.

Using the results of the *ab initio* calculations, the coincidence spectra can be annotated with maximum kinetic energy (KE_{MAX}) diagonal lines, defined as the maximum available kinetic energy for DPD events of internally cold precursor anions producing ground rovibronic state neutral products plus a free electron. The energetic limits marked on Figure 5 correspond to DPD of *tert*-butoxide: $(CH_3)_3CO^- + h\nu \rightarrow CH_3 + (CH_3)_2CO + e^-$ for Pathway 2 and $(CH_3)_2C(CH_2)OH^- + h\nu \rightarrow CH_3 + CH_3C(CH_2)OH + e^-$ for Pathway 5, as well as the perdeuterated isomers. Data points with a lower total kinetic energy (E_{TOT}), defined by $E_{TOT} = eKE + E_T$ for a given event, lie within the triangle formed between KE_{MAX} and the axes. The horizontal lines indicate maximum eKE (eKE_{MAX}) values that allow a nascent radical to have sufficient internal energy to surmount the barrier to dissociation.

Table 3.5. Calculated Energetics of Open Dissociation Pathways with CBS-QB3 Theory

Reaction	Endoergicity of Reaction (eV)
$(CH_3)_3CO \rightarrow (CH_3)_3C + O$	4.00
$(CH_3)_3CO \rightarrow (CH_3)_2CO + CH_3$	0.08
$(CH_3)_2C(CH_2)OH \rightarrow (CH_3)_2COH + CH_2$	4.08
$(CH_3)_2C(CH_2)OH \rightarrow (CH_3)_2CCH_2 + OH$	1.27
$(CH_3)_2C(CH_2)OH \rightarrow CH_3C(CH_2)OH + CH_3$	0.79

Table 3.6. *Ab Initio* DPD Energetics Calculated at 3.20 eV Photon Energy

Path	Reaction	AEA	VDE	KE_{MAX} (eV)	eKE_{MAX} (eV)
		CBS-QB3	MP2 6-311++G(d,p)	CBS-QB3	CBS-QB3
2	$(CH_3)_3CO^- \rightarrow (CH_3)_2O + CH_3 + e^-$	1.97	2.20	1.15	0.68
	$(CD_3)_3CO^- \rightarrow (CD_3)_2O + CD_3 + e^-$	1.95		1.11	0.69
5	$(CH_3)_2C(CH_2)OH^- \rightarrow CH_3C(CH_2)OH + CH_3 + e^-$	0.66	0.87	1.75	1.27
	$(CD_3)_2C(CD_2)OD^- \rightarrow CD_3C(CD_2)OD + CD_3 + e^-$	0.65		1.73	1.27

Assuming the parent anions are vibrationally cold, the limits show that from the perspective of overall energy conservation (KE_{MAX}) and available energy above the calculated barrier (eKE_{MAX}) the dissociative signal is consistent only with Pathway 5 for the carbanion. Pathway 2, for *tert*-butoxide, can only result from significant levels of vibrational excitation in the nascent *tert*-butoxy radicals, which is unexpected given the use of the cryogenic EIBT for this study. This apparatus has been shown to resolve significant issues with anion vibrational excitation in studies of $HOCO^-$.[33] In the current study, however, the parent anion is significantly larger, which may hamper cooling by the supersonic expansion.[55] These questions motivated further measurements at lower photon energies to aid in confirming the parent anion identity and DPD mechanism.

3.4.2 Photodetachment at $E_{h\nu}$ = 2.31 and 2.07 eV

Reduction of the photon energy permits higher-resolution measurements of the P(eKE) spectra, as shown in the spectra for $C_4H_9O^-$ at $E_{h\nu}$ = 2.07 eV and 2.31 eV in Figure 7. These spectra show resolved vibrational structure that is lost for the higher eKE electrons produced by photodetachment at $E_{h\nu}$ = 3.20 eV. Peak positions are given in Table 7, with peak **a** representing the 0_0^0 transition consistent with spectra assigned by Ramond *et al*. to $(CH_3)_3CO^-$ with an AEA for the *tert*-butoxy radical of 1.91±0.02 eV.[24] The corresponding vibrationally resolved spectrum for $(CD_3)_3CO^-$ at $E_{h\nu}$ = 2.31 eV is shown in Figure 8. These $(CH_3)_3CO^-$ spectra also include finite temperature Franck-Condon simulations with a vibrational temperature of 550 K in the four most FC active vibrational modes (the ν_4, ν_6, ν_7, and ν_{18} modes in the anion) as well as the three most FC-active modes involving C-C bond stretches relevant to dissociation (the ν_9, ν_{16}, and ν_{19} modes), leaving the balance of the modes unexcited. The mode-matching between anion

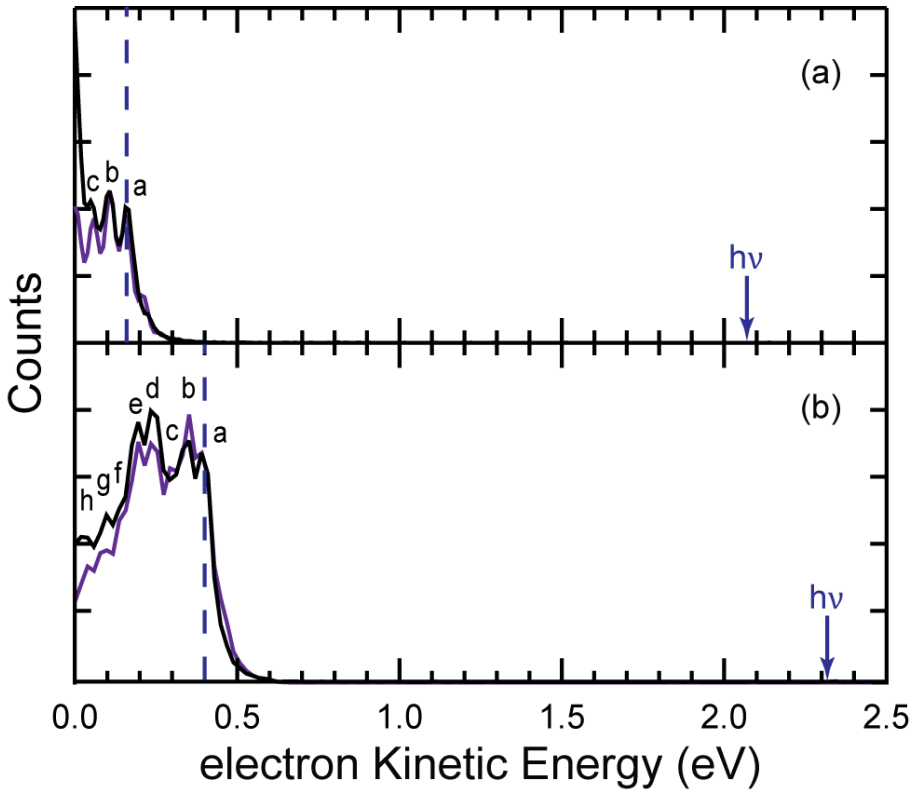

Figure 3.7 Photoelectron spectra at $E_{h\nu}$ = 2.07 eV and 2.31 eV for $(CH_3)_3CO^-$, in frames (a) and (b) respectively, leading to stable radicals with 550 K FC simulations shown in purple. Peak assignments at $E_{h\nu}$ = 2.31 are indicated in Table 5.

Table 3.7. Peak positions (electron kinetic energy (eKE), eV, ±0.02 eV) for photodetachment of $(CH_3)_3CO^-$ at $E_{h\nu}$ = 2.31 eV compared to the results of Ramond *et al.*[24] Assignments are based on FC simulations and CBS-QB3 vibrational frequencies are listed in the Table 2.

Peak	eKE (eV)	Known *tert*-butoxide eKE[24]	Assignment
A	0.402	0.401	0_0^0
B	0.352	0.347	6_0^1
C	0.302	0.295	$6_0^1\ 8_0^1$
D	0.252	0.252	18_0^1
E	0.201	0.200	$6_0^1 18_0^1$
F	0.134	0.143	$6_0^1 8_0^1 18_0^1$
G	0.102	0.102	$6_0^2 18_0^1$
H	0.019	-----	$18_0^2 2_0^1$

Table 3.8. Sample Boltzmann Factors for internal excitation at 1400 K in the ν_{16} mode of the anion for transitions leaving enough energy in the ν_{16} mode of the neutral for dissociation.

Anion Quanta in ν_{16}	Boltzmann Factor (1400 K)	Neutral Quanta in ν_{16}	Franck-Condon Factor	Intensity
1	2.88E-01	4	5.39E-03	1.55E-03
2	8.31E-02	4	4.78E-02	3.97E-03
3	2.40E-02	4	2.40E-02	3.73E-03
4	6.91E-03	4	1.56E-01	1.08E-03

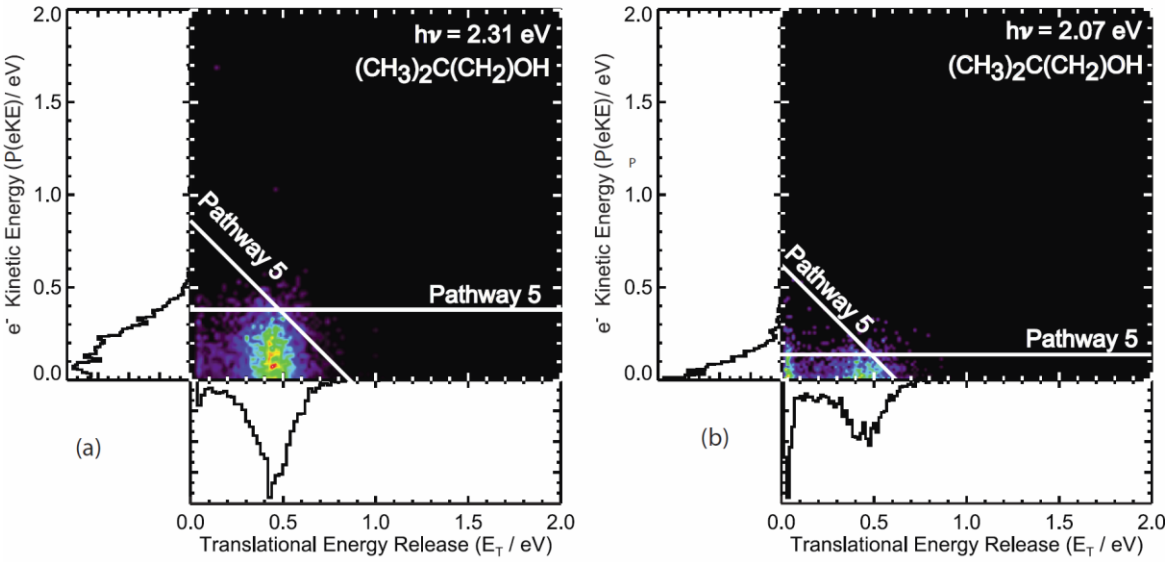

Figure 3.8. Photoelectron photofragment coincidence plots for non-deuterated species are shown at the photon energies indicated. The horizontal lines represent eKE_{MAX} expected for dissociation over the barriers for Pathway 5 [(a) 0.38 eV (b) 0.14 eV] while the diagonal lines indicate the calculated conservation of energy KE_{MAX} for Pathway 5 [(a) 0.86 eV (b) 0.62 eV].

and radical modes are shown in Table 8. The high energy tails on the spectra above the AEA are well-matched by the 550 K simulations. Trapping times of up to 5 seconds indicated no significant signs of radiative vibrational relaxation, suggesting excitation of vibrational modes with long radiative lifetimes. In addition to these stable photoelectron spectra, dissociative photoelectron spectra and PPC spectra were also observed. The dissociative channels at all photon energies are shown on a magnified scale in Figure 9 and the measured PPC spectra at the two lower photon energies are shown in Figure 10.

3.4.3 Evidence for the Low Electron Affinity Carbanion

The data shows that *tert*-butoxide is the dominant anion leading to stable radicals, but the origin of the dissociative channel remains to be determined. This will be examined in the Discussion section, but given the low calculated AEA = 0.66 eV for the carbanion, photoelectrons up to eKE = 2.54 eV would be observed at $E_{h\nu}$ = 3.20 eV. In the bottom frame of Figure 3(a) at $E_{h\nu}$ = 3.20 eV, a high energy photoelectron channel is observed, consistent with the calculated energetics for the carbanion. This signal was found to be source-condition dependent, and under the source conditions yielding vibrationally resolved data at the lower photon energies was not observed. However, as the $E_{h\nu}$ = 3.20 eV spectrum shows, evidence for photodetachment of the carbanion producing stable radicals is observed and will be considered further.

3.5 Discussion

The PPC experiment on mass-selected anions formed by proton abstraction from *tert*-butanol indicates the presence of both stable and dissociative photodetachment pathways. These experimental observations and the supporting quantum chemistry

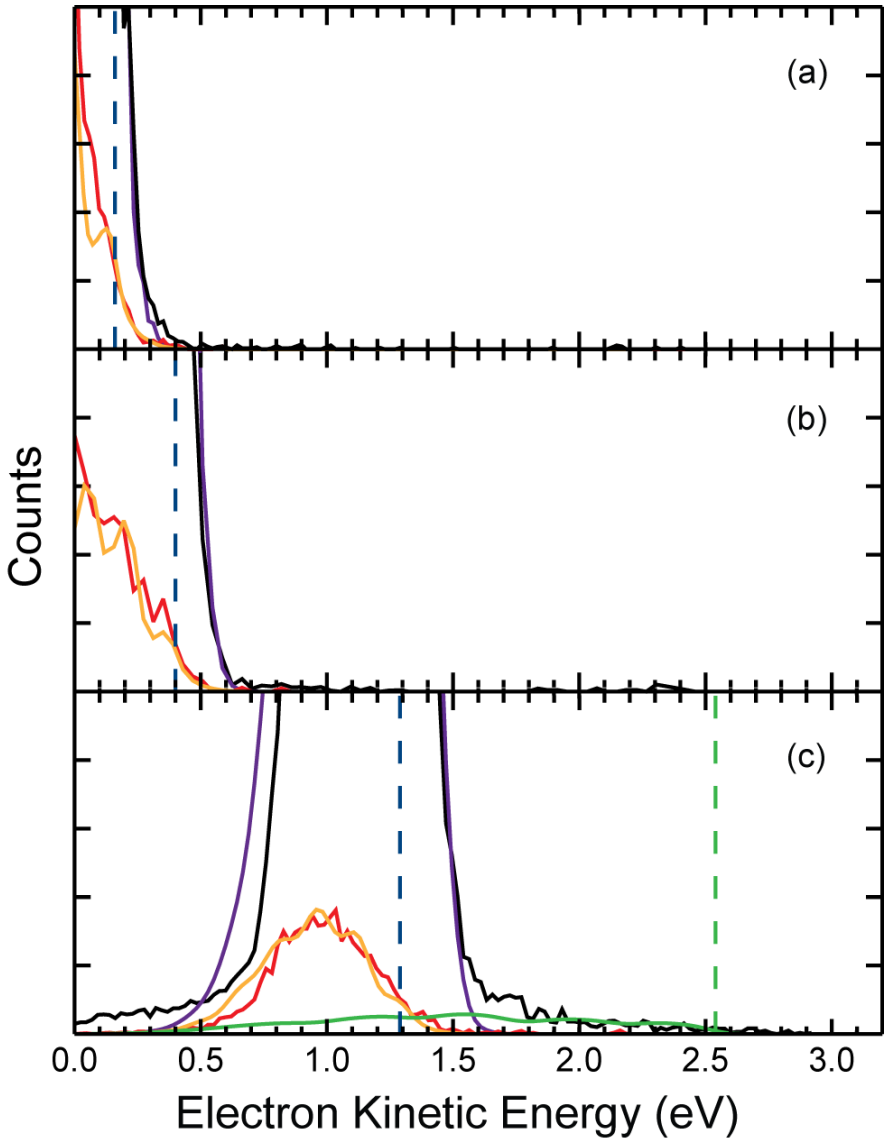

Figure 3.9. Photoelectron spectra (P(eKE)) at (a) $E_{h\nu}$ =2.07, (b) 2.31 and (c) 3.20 eV magnified by a factor of 10 showing the stable (black) and dissociative (red) distribution with the 550 K FC envelope (purple) for photodetachment of $(CH_3)_3CO^-$ producing stable radicals. The 1400 K FC envelope for transitions leading to ≥ 4 quanta in ν_{16} in the radical is shown in orange. The FC simulation for $(CH_3)_2C(CH_2)OH^-$ is shown in green in (c). Dashed lines indicate the predicted AEA for $(CH_3)_3CO^-$ and $(CH_3)_2C(CH_2)OH^-$ anions in blue and green respectively.

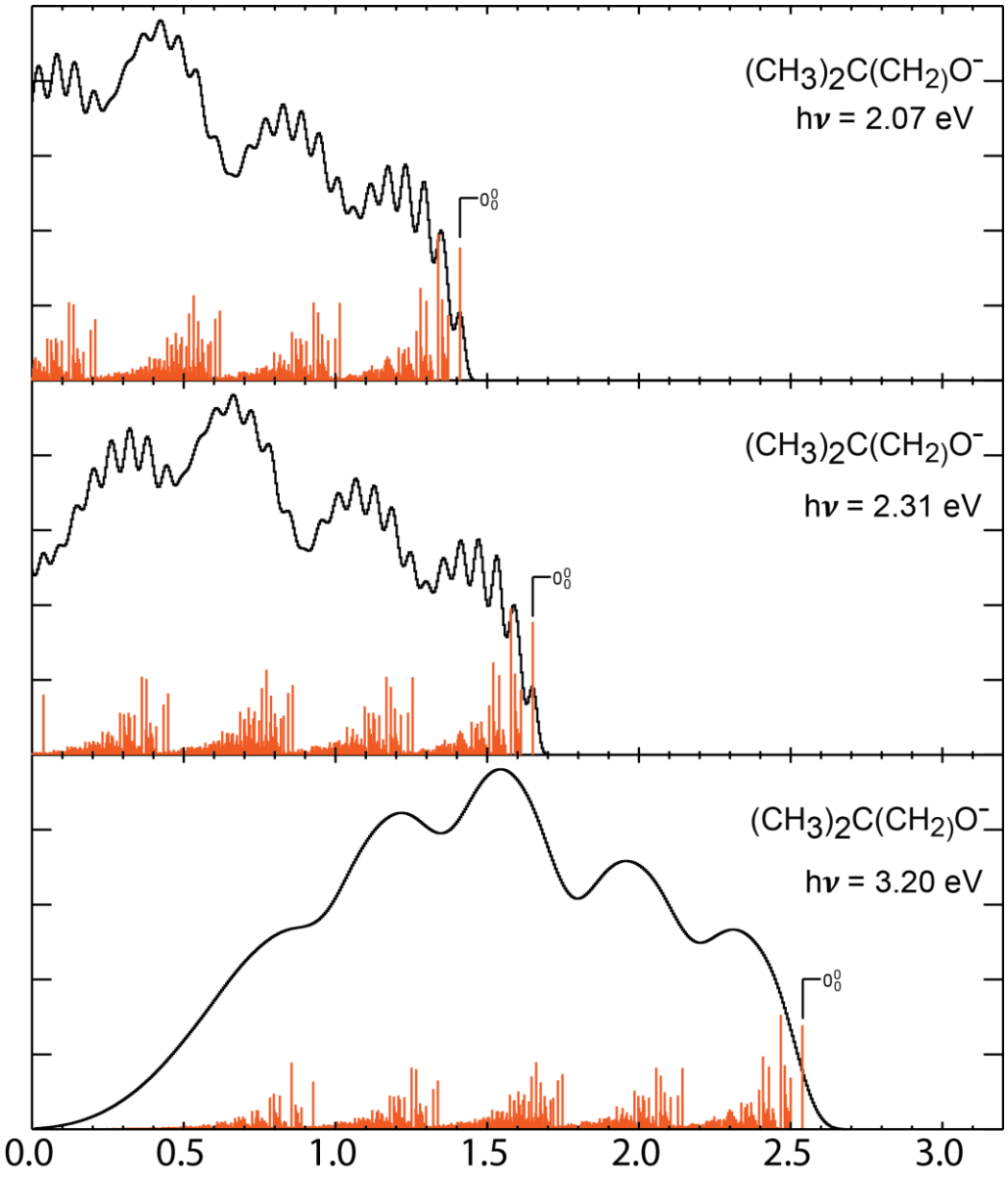

Figure 3.10. Simulated spectrum of the carbanion with stick spectrum of the FC envelope at the noted photon energies assuming an initial temperature of 0 K.

calculations are consistent with the formation of two isomeric precursor anions; the *tert*-butoxide anion $(CH_3)_3CO^-$ that undergoes photodetachment to the stable *tert*-butoxy radical and a minor channel, the higher-energy α-hydroxy carbanion $(CH_3)_2C(CH_2)OH^-$ that undergoes photodetachment to stable $(CH_3)_2C(CH_2)OH$ radicals. The primary subject of this discussion will be the identification of the source for the observed DPD channel. As the isotopic substitution effects on the photofragment mass distribution and the measured partitioning of kinetic energy in the PPC spectra show, either *tert*-butoxide or the α-hydroxy carbanion could explain DPD to CH_3 + acetone or CH_3 + propen-2-ol, respectively. For the carbanion, the fact that dissociation is detected even when photodetachment from the carbanion is not observed indicates that this isomer is not the source of the dissociative signal. The discussion will therefore focus on examining how *tert*-butoxide or other isomers could give rise to the observed dissociative signal.

3.5.1 Dissociative Photodetachment of Hot *tert*-Butoxide

The PPC method allows for the separation of precursor isomers in a mixed ion beam via coincidence detection of both the photodetached electron and either stable products or momentum-matched fragments arising from dissociation. For dissociative species, the partitioning of kinetic energy between the photoelectron and the photofragments further defines the energetics of the parent anions. The two most likely precursor anions, *tert*-butoxide $(CH_3)_3CO^-$ and the α-hydroxy carbanion $(CH_3)_2C(CH_2)OH^-$ have the five plausible dissociation pathways shown in Figure 1. Additional isomeric alkoxide isomers involving rearrangement of the carbon framework were considered as candidate anions but found to be unlikely pathways, given the

calculated reaction energetics in Figures S1 and S2 and the assignment of the vibrationally resolved spectra to *tert*-butoxide photodetachment.

The *tert*-butoxide anion has two DPD pathways (1 and 2) that could be consistent with the product mass distribution in the top frame of Figure 4. However, as shown in Table 5, Pathway 1 is endoergic by 4.0 eV and the change in product mass distribution upon deuteration is also not consistent with C-O bond fission. Pathway 2 is a known reaction pathway for the combustion of *tert*-butanol initiated by a β-C-C bond scission, similar to the pathway observed in the DPD of the ethoxide anion, resulting in acetone and a methyl radical.[6, 36, 56] The *ab initio* energetics for Pathway 2, displayed on the left side of Figure 6, show that this pathway is energetically accessible from ground state anions at these photon energies, with a transition state 0.55 eV above the *tert*-butoxy radical and a reaction endoergicity of 0.08 eV. The transition state barrier calculated using the CBS-QB3 method is in the lower range of previous calculated and experimental barriers ranging from 0.5 eV to 0.8 eV.[6, 16, 17, 20, 21, 25, 57-59] The CBS-QB3 method has been shown in a number of cases to underestimate barrier heights,[60] so this barrier can be taken as a theoretical upper limit for the eKE_{MAX} of Pathway 2, as shown by the horizontal lines marked Pathway 2 in the coincidence spectra in Figure 5. However, nearly all of the data is at $eKE > eKE_{MAX}$ for Pathway 2, indicating that dissociation does not occur from cold *tert*-butoxide anions. This is corroborated by the FC simulation for cold *tert*-butoxide anions indicating poor overlap with highly excited C-C stretch modes in the neutral radical, resulting from the small change in C-C bond length upon photodetachment. The theoretical KE_{MAX} of 1.15 eV for Pathway 2, representing the conservation of energy, also lies below essentially all of the experimental data.

Excluding C-C bond fission tunneling, the only other explanation for dissociation beyond the KE_{MAX} and eKE_{MAX} limits is vibrationally excited anions. Extending the FC calculations to include vibrational excitation in the C-C stretch modes of the *tert*-butoxide anion presents a way to examine the FC overlap with high vibrational levels in the neutral. As the PPC spectra in Figure 5 and the energetics diagram in Figure 6 show, transitions in the 0.70 to 1.4 eV eKE range at $E_{h\nu}$ = 3.20 eV would have sufficient energy to overcome the barrier for $(CH_3)_3CO \rightarrow CH_3 + (CH_3)_2CO$. Focusing on the ν_{16} vibrational mode as an example (CCO umbrella mode) FC simulations were performed assuming that transitions to 4 or more quanta in the neutral dissociate, and compared to the spectra at all three photon energies in Figure 9. The fits are reasonable, assuming an initial temperature of 1400 K in that mode. The largest contribution comes from the ν_{16} = 4←2 and ν_{16}=4←3 transitions, as shown in Table 9. This is well above the 550 K temperature found to match the vibrationally resolved stable radical spectra at the lower photon energies, but cooling during a supersonic expansion is often mode specific and can lead to non-Boltzmann final vibrational distributions, especially for larger molecules.[55] This is an approximate treatment as we have assumed a high-temperature thermal distribution and treated the vibrations as harmonic, but it provides a plausible explanation for formation of an unrelaxed high-energy tail of the hot anions initially produced in the source that can account for the observed DPD channel arising from hot *tert*-butoxide.

3.5.2 Photoelectron Spectra of $(CH_3)_2C(CH_2)OH^-$ and Dissociation of $(CH_3)_2C(CH_2)OH$

Table 3.9. List of mode matches ordered by anion frequency and K displacement vectors for and $(CH_3)_3CO$ and $(CH_3)_2C(CH_2)OH$.

Anion Vibrational mode	$(CH_3)_3CO$			$(CH_3)_2C(CH_2)OH$		
	anion	neutral	K displacement vector	anion	neutral	K displacement vector
1	203.73	178.48	1.72E-04	233.99	232.14	3.58E-01
2	286.13	266.28	-5.80E-02	268.83	349.45	8.24E-01
3	286.13	251.11	-9.91E-03	285.34	285.97	-2.47E-01
4	336.64	334.24	-1.09E-01	331.18	450.12	8.99E-02
5	336.64	334.09	-3.20E-02	391.16	314.51	6.68E-01
6	409.85	410.67	-2.74E-01	403.90	410.45	-2.62E-01
7	480.16	434.14	-2.27E-01	444.24	472.35	1.79E-01
8	480.16	410.17	5.75E-02	449.09	324.12	1.05E-01
9	723.23	767.38	-8.22E-02	491.87	163.25	-3.69E-01
10	837.42	945.88	2.37E-02	509.37	576.81	-3.79E-01
11	837.42	913.22	8.32E-03	627.06	1246.93	-2.69E-01
12	919.54	971.56	1.89E-06	821.24	780.00	7.25E-02
13	1020.31	915.28	-9.02E-02	932.86	957.54	4.18E-02
14	1023.15	1037.65	-5.80E-02	973.98	926.33	1.54E-01
15	1023.15	1026.39	-1.43E-02	1018.21	1013.90	5.34E-02
16	1210.12	1221.51	-6.34E-02	1040.43	1031.57	1.19E-02
17	1210.12	1242.86	1.49E-02	1120.91	1291.39	7.71E-02
18	1241.33	1283.20	1.92E-01	1144.10	1353.49	1.19E-01
19	1336.76	1395.33	1.02E-02	1274.19	1149.17	-5.44E-02
20	1336.76	1400.32	-1.03E-02	1346.23	950.80	1.82E-01
21	1365.49	1429.68	1.92E-03	1377.97	1405.15	7.64E-03
22	1466.74	1484.68	-6.93E-06	1393.36	1421.65	-5.86E-02
23	1476.82	1499.67	-5.97E-03	1450.07	1477.03	-1.43E-01
24	1476.82	1494.05	1.77E-05	1483.26	1491.74	-6.08E-03
25	1490.36	1512.07	2.78E-03	1488.57	1499.62	-1.08E-02
26	1490.36	1511.88	7.11E-04	1500.14	1514.04	3.45E-02
27	1505.88	1533.73	2.02E-02	1506.00	1523.44	8.81E-03
28	2993.48	3071.90	-2.22E-03	3035.54	3064.39	-2.61E-03
29	2993.48	3067.87	-2.75E-04	3039.07	3072.51	4.58E-02
30	3008.06	3077.64	-1.80E-02	3074.16	3189.87	-5.02E-01
31	3094.31	3177.44	9.11E-04	3119.72	3172.38	1.54E-02
32	3094.31	3159.37	1.26E-03	3123.84	3166.15	1.27E-02
33	3105.56	3172.86	7.61E-03	3142.28	3153.10	7.56E-02
34	3126.98	3171.72	9.53E-07	3145.57	3177.55	1.38E-02
35	3134.17	3164.80	1.89E-04	3159.29	3311.15	-3.85E-01
36	3134.17	3182.83	-5.05E-05	3828.19	3854.44	-3.47E-01

While these data show that the carbanion is not produced in great quantity in these experiments, it is worthwhile to consider the observed photoelectron spectra and the possible dissociation pathways of the carbanion radical. The photoelectrons recorded far above the AEA of *tert*-butoxide in the $E_{h\nu}$ = 3.20 eV spectrum shown in Figure 3(a) are energetically consistent with photodetachment from $(CH_3)_2C(CH_2)OH^-$ given the predicted AEA of 0.66 eV. The observed spectrum is very broad, so FC simulations were performed to aid in the assignment. FC simulations using Cartesian coordinate normal mode analysis are problematic because the molecule has C_1 symmetry and large changes in dihedral angles upon photodetachment, leading to anomalously large Cartesian displacements calculated for modes involving C-H motion.[61] To limit this effect, all high energy C-H stretches from methyl substituents were omitted since the optimized geometries for the carbanion and alkylhydroxy radical indicate virtually no change in C-H bond length for the methyl substituents. The C-H bond lengths in the CH_2 substituent, however, have larger bond-length changes upon photodetachment (0.02 Å as shown in Table 4) and are therefore likely to exhibit some FC activity. To account for the limitations of the Cartesian coordinate normal mode analysis, ν_{34} and ν_{35} C-H stretches were limited to transitions with up to two quanta. The three lowest frequency modes, ν_1, ν_2, ν_3 were also omitted to lower computational cost, and are expected to only contribute amplitude to the overall envelope. The resulting stick FC spectrum (Figure 11) indicates the most intense transition is at eKE = 2.45 eV, nearly as predicted by the theoretical VDE of 0.87 eV. Convolution of the stick spectrum with a Gaussian to account for the experimental resolution shifts the peak intensity of the overall envelope down to 1.5 eV eKE due to the increasing density of states at lower eKE. Thus, as shown in Figure 9(c),

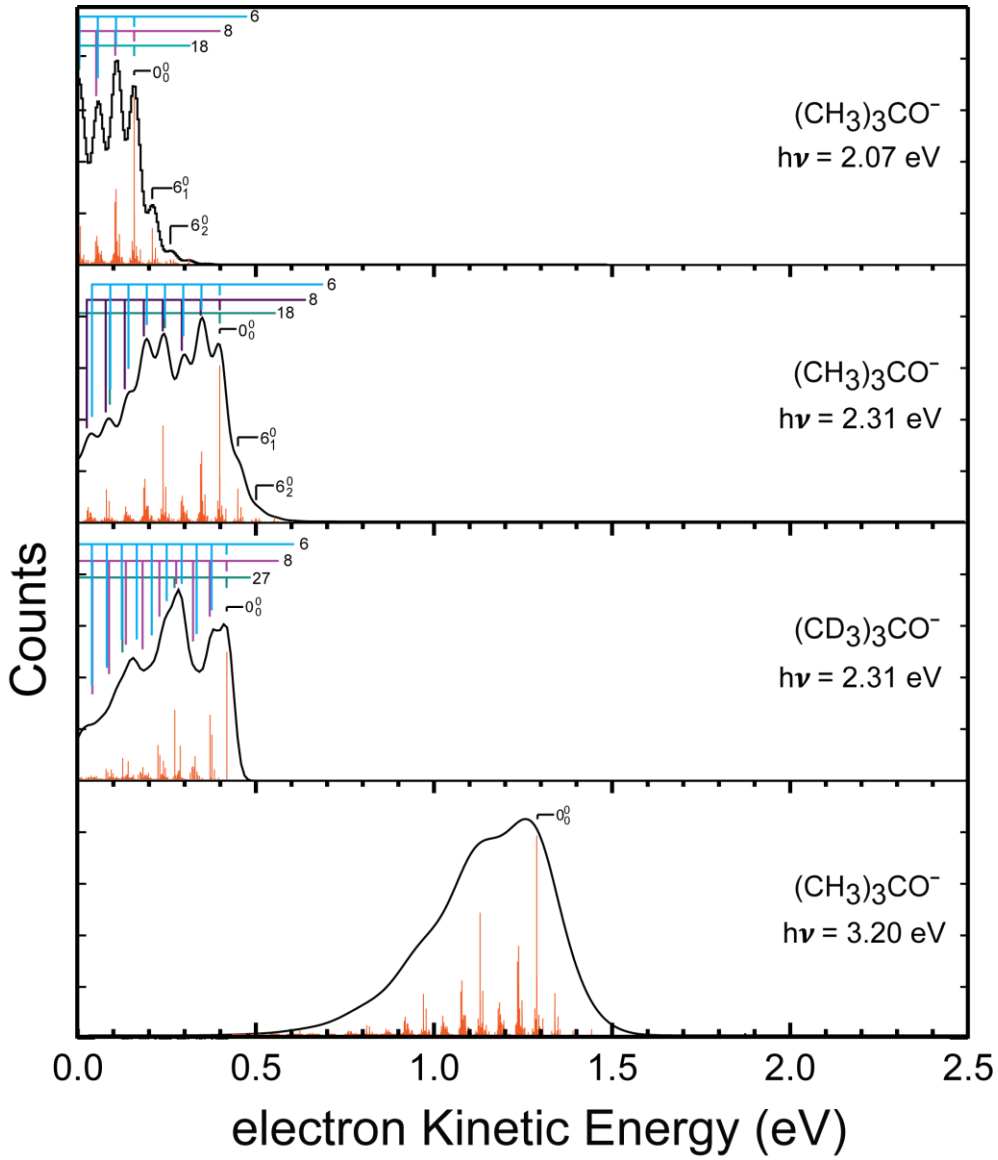

Figure 3.11. Simulated spectrum of the *tert*-butoxide with the stick spectrum of the FC envelope at the noted photon energies assuming an initial temperature of 550 K.

the simulated spectrum for the carbanion matches the high eKE features in the stable $E_{h\nu}$ = 3.2 eV spectrum. A more accurate method for generating FC factors for the carbanion would use a curvilinear internal coordinate system for describing the normal modes of vibration, however this is beyond the scope of the present work.[61]

Three possible dissociative pathways for the carbanion radical (Pathways 3, 4, and 5 in Figure 1) were examined. Pathway 3 involves breaking a C-C bond to form methylene (CH_2) and an alkylhydroxy radical, calculated to have a reaction endoergicity of 4.08 eV and therefore energetically inaccessible. Pathway 4 proceeds by C-O bond cleavage from the nascent radical to yield isobutene and OH. Isobutene is a known product in the combustion of *tert*-butanol, and the calculated reaction endoergicity for this reaction is 1.27 eV.[11] Pathway 5, already discussed, assumes beta cleavage of a C-C bond following formation of the nascent radical, yielding propen-2-ol + CH_3. The energetics of β-C-C bond scission for the $(CH_3)_2C(CH_2)OH$ radical is similar to the β-C-C bond scission observed in experiments on *tert*-butoxy radical, *tert*-butanol, as well as other alkoxy radicals and is the most plausible pathway for the formation of propen-2-ol observed in the combustion of *tert*-butanol.[6, 11, 36, 56, 62, 63] The calculated energetics for Pathway 5, shown on the right side of Figure 6, indicate a reaction endoergicity of 0.79 eV and a transition state that is 1.93 eV above the precursor anion. As discussed in the results section, this energetically matches the observed PPC spectra, but was ruled out by further measurements.

3.5.3 Dissociative Photodetachment Dynamics

Repulsive interactions during the DPD process cause a peak in the $N(E_T)$ spectrum between 0.4 and 0.5 eV that is related to the dissociation barrier height relative

to the asympototic products in the exit channel. This is in reasonable agreement with the product translational energy distribution observed for the secondary decomposition of the *tert*-butoxy radical following photodissociation of *tert*-butyl hypochlorite.[18] The computed barrier height for dissociation of the *tert*-butoxy radical by Pathway 2 at the CBS-QB3 level is 0.55 eV, a number that is consistent with the 1400 K FC fit in ν_{16} for hot *tert*-butoxide. The calculated barrier height relative to the CH_3 + $(CH_3)_2CO$ products was found to be 0.47 eV, essentially reproduced by the PPC data, assuming that vibrational energy along the reaction coordinate couples into product translational energy with little impulsive excitation of the polyatomic dissociation fragments. The transition state structure calculated for dissociation of *tert*-butoxy radical indicates a lengthening of the dissociative C-C bond and shortening of all other C-C and C-O bonds consistent with previous calculations.[59] The large geometry change for the transition state implies considerable internal excitation in the products, consistent with the broad eKE range. However, despite the wide range of eKE, the E_T distribution is narrow indicating that internal excitation in the photodetached radical orthogonal to the reaction coordinate does not couple effectively with product translation. Finally, it must be noted that the A′ and A″ electronic states defined by the orientation of the singly occupied molecular orbital on the O atom with respect to the plane of symmetry may play different roles in promoting the dissociation process. The *ab initio* calculations reported here indicate that the A′ state is the ground state, but we have not determined the splitting between the A′ and A″ states. Both states are expected to be produced by photodetachment of the closed shell anion, and the splitting is expected to be small.[24]

3.6 Conclusion

PPC spectra of *tert*-butoxide anion and the $(CH_3)_2C(CH_2)OH^-$ carbanion isomer were measured at $E_{h\nu}$ = 2.07 eV, 2.31 eV and 3.20 eV. Calculations were performed using the CBS-QB3 composite method to evaluate the reaction coordinate for the photodetachment and dissociation of *tert*-butoxy radical as well as the alkylhydroxy radical isomer. The stable channel is energetically consistent with the photodetachment of the *tert*-butoxide anion with a trace of the carbanion while the dissociative channel is energetically consistent with DPD from unrelaxed highly vibrationally excited *tert*-butoxide anions proceeding by C-C bond ß-scission resulting in methyl loss from the nascent radical yielding acetone + CH_3. Decomposition of the *tert*-butoxy radical is consistent with a 0.55 eV barrier for dissociation with the product E_T peaked between 0.4 and 0.5 eV, in agreement with the *ab initio* prediction for the barrier height relative to the $(CH_3)_2O + CH_3$ products in the exit channel (Pathway 2). Unfortunately, DPD of hot *tert*-butoxide obscures any trace of dissociation from the $(CH_3)_2C(CH_2)OH$ radical produced. This work shows that as PPC spectroscopy is extended to increasingly large polyatomic molecules, problems with hot anion precursors become more challenging, highlighting the need for cooling of the target anions prior to photodetachment.[64, 65] With cooled ions, PPC spectroscopy could provide a viable method for differentiating between isomers to probe the energetics and dynamics of larger oxygenated radicals.

Acknowledgments

This material is based upon work was supported by the U.S. Department of Energy, Office of Science, Office of Basic Energy Sciences under award number DE-FG03-98ER14879. BLJP acknowledges additional financial support from the Australian Research Council (Grant DE120100467).

Chapter 3, in full, is a reprint of the material as it appeared in Shen, B.; Poad, B.; Continetti, R., Photoelectron-Photofragment Coincidence Studies of the tert-Butoxide Anion (CH3)(3)CO-, the Carbanion Isomer (CH3)(2)CH2COH-, and Corresponding Radicals. *Journal of Physical Chemistry a* **2014,** *118* (44), 10223-10232. The dissertation author is the primary author and the disertation advisor is the corresponding author.

Supporting Information Available

Additional isomeric alkoxy radical pathways considered are listed along with the *ab initio* calculated zero point corrected energies for all related species utilizing Gaussian03.[44] The calculated vibrational frequencies of *tert*-butoxide, the $(CH_3)_2C(CH_2)OH$ alkylhydroxy carbanion and the corresponding radicals along with optimized geometries for anion, radical, and the dissociative transition states for $(CH_3)_3CO$ and $(CH_3)_2C(CH_2)OH$ are shown. Additional supporting data include a photoelectron spectrum of $(CD_3)_3CO$ with peak assignments, two coincidence spectra for dissociative photodetachment of $C_4H_9O^-$ isomers at $E_{h\nu}$ = 2.31 eV and 2.07 eV, and simulated photoelectron stick spectra with Gaussian convolutions for both the carbanion and *tert*-butoxide. The mode matching used for FC simulations is included along with sample Boltzmann factors for transitions resulting in dissociation. This information is available free of charge via the Internet at http://pubs.acs.org

3.7 References

1. Taatjes, C. A.; Hansen, N.; McIlroy, A.; Miller, J. A.; Senosiain, J. P.; Klippenstein, S. J.; Qi, F.; Sheng, L. S.; Zhang, Y. W.; Cool, T. A.; Wang, J.;

Westmoreland, P. R.; Law, M. E.; Kasper, T.; Kohse-Hoinghaus, K., Enols are Common Intermediates in Hydrocarbon Oxidation. *Science* **2005,** *308*, 1887-1889.

2. Sadezky, A.; Chaimbault, P.; Mellouki, A.; Rompp, A.; Winterhalter, R.; Le Bras, G.; Moortgat, G., Formation of Secondary Organic Aerosol and Oligomers From the Ozonolysis of Enol Ethers. *Atmos. Chem. Phys.* **2006,** *6*, 5009-5024.

3. Grana, R.; Frassoldati, A.; Faravelli, T.; Niemann, U.; Ranzi, E.; Seiser, R.; Cattolica, R.; Seshadri, K., An Experimental and Kinetic Modeling Study of Combustion of Isomers of Butanol. *Comb. Flame* **2010,** *157* (11), 2137-2154.

4. Atkinson, R., Atmospheric Reactions of Alkoxy and Beta-Hydroxyalkoxy Radicals. *Int. J. Chem. Kin.* **1997,** *29* (2), 99-111.

5. Wang, J.; Li, Y.; Zhang, T.; Tian, Z.; Yang, B.; Zhang, K.; Qi, F.; Zhu, A.; Cui, Z.; Ng, C., Interstellar Enols are Formed in Plasma Discharges of Alcohols. *Astrophys. J.* **2008,** *676* (1), 416-419.

6. Fittschen, C.; Hippler, H.; Viskolcz, B., The Beta C-C Bond Scission in Alkoxy Radicals: Thermal Unimolecular Decomposition of t-Butoxy Radicals. *Phys. Chem. Chem. Phys.* **2000,** *2* (8), 1677-1683.

7. Orlando, J. J.; Tyndall, G. S.; Wallington, T. J., The Atmospheric Chemistry of Alkoxy Radicals. *Chem. Rev.* **2003,** *103* (12), 4657-4690.

8. Peeters, J.; Fantechi, G.; Vereecken, L., A Generalized Structure-Activity Relationship for the Decomposition of (Substituted) Alkoxy Radicals. *J. Atmos. Chem.* **2004,** *48* (1), 59-80.

9. Cool, T. A.; Nakajima, K.; Mostefaoui, T. A.; Qi, F.; McIlroy, A.; Westmoreland, P. R.; Law, M. E.; Poisson, L.; Peterka, D. S.; Ahmed, M., Selective Detection of Isomers With Photoionization Mass Spectrometry for Studies of Hydrocarbon Flame Chemistry. *J. Chem. Phys.* **2003,** *119* (16), 8356-8365.

10. Osswald, P.; Guldenberg, H.; Kohse-Hoinghaus, K.; Yang, B.; Yuan, T.; Qi, F., Combustion of Butanol Isomers - A Detailed Molecular Beam Mass Spectrometry Investigation of Their Flame Chemistry. *Comb. Flame* **2011,** *158* (1), 2-15.

11. Lefkowitz, J. K.; Heyne, J. S.; Won, S. H.; Dooley, S.; Kim, H. H.; Haas, F. M.; Jahangirian, S.; Dryer, F. L.; Ju, Y., A Chemical Kinetic Study of Tertiary-Butanol in a Flow Reactor and a Counterflow Diffusion Flame. *Comb. Flame* **2012,** *159* (3), 968-978.

12. Sarathy, S. M.; Vranckx, S.; Yasunaga, K.; Mehl, M.; Osswald, P.; Metcalfe, W. K.; Westbrook, C. K.; Pitz, W. J.; Kohse-Hoinghaus, K.; Fernandes, R. X.; Curran, H. J., A Comprehensive Chemical Kinetic Combustion Model for the Four Butanol Isomers. *Comb. Flame* **2012,** *159*, 2028-2055.

13. Calvert, J. G.; Derwent, R. G.; Orlando, J. J.; Tyndall, G. S.; Wallington, T. J., *Mechanisms of Atmospheric Oxidation of the Alkanes*. Oxford University Press: New York, 2008.

14. Batt, L., Gas-Phase Decomposition of Alkoxy Radicals. *Int. J. Chem. Kin.* **1979,** *11* (9), 977-993.

15. Calvert, J. G.; Mellouki, A.; Orlando, J. J., *The Mechanisms of Atmospheric Oxidation of the Oxygenates*. Oxford University Press: New York, 2011.

16. Rauk, A.; Boyd, R. J.; Boyd, S. L.; Henry, D. J.; Radom, L., Alkoxy Radicals in the Gaseous Phase: Beta-Scission Reactions and Formation by Radical Addition to Carbonyl Compounds. *Can. J. Chem.* **2003,** *81* (6), 431-442.

17. Mereau, R.; Rayez, M. T.; Caralp, F.; Rayez, J. C., Theoretical Study of Alkoxyl Radical Decomposition Reactions: Structure-Activity Relationships. *Phys. Chem. Chem. Phys.* **2000,** *2* (17), 3765-3772.

18. Thelen, M. A.; Felder, P.; Frey, J. G.; Huber, J. R., Photodissociation of tert-Butyl Hypochlorite and Decomposition of the tert-Butoxy Radical Fragment. *J. Phys. Chem.* **1993,** *97* (23), 6220-6225.

19. Effenhauser, C. S.; Felder, P.; Huber, J. R., Photodissociation of Alkyl Nitrites in a Molecular Beam. Primary and Secondary Reactions. *J. Phys. Chem.* **1990,** *94* (1), 296-302.

20. Blitz, M.; Pilling, M. J.; Robertson, S. H.; Seakins, P. W., Direct Studies on the Decomposition of the tert-Butoxy Radical and its Reaction With NO. *Phys. Chem. Chem. Phys.* **1999,** *1* (1), 73-80.

21. Batt, L.; Hisham, M. W. M.; Mackay, M., Decomposition of the t-Butoxy Radical: II. Studies Over the Temperature Range 303-393 K. *Int. J. Chem. Kin.* **1989,** *21* (7), 535-546.

22. Wang, C. J.; Shemesh, L. G.; Deng, W.; Lilien, M. D.; Dibble, T. S., Laser-Induced Fluorescence Excitation Spectra of tert-Butoxy and 2-Butoxy Radicals. *J. Phys. Chem. A* **1999,** *103* (41), 8207-8212.

23. Carter, C. C.; Atwell, J. R.; Gopalakrishnan, S.; Miller, T. A., Jet-cooled Laser-Induced Fluorescence Spectroscopy of Some Alkoxy Radicals. *J. Phys. Chem. A* **2000,** *105*, 9165-9170.

24. Ramond, T. M.; Davico, G. E.; Schwartz, R. L.; Lineberger, W. C., Vibronic Structure of Alkoxy Radicals Via Photoelectron Spectroscopy. *J. Chem. Phys.* **2000,** *112* (3), 1158-1169.

25. Zhao, H. M.; Liu, K.; Ma, S. Y.; Li, Z. H., Theoretical Study of Stabling Function of the NO to the $(CH_3)_3CO$ Radical. *Int. J. Q. Chem.* **2005,** *101* (1), 113-117.

26. Chiu, S. W.; Lau, J. K. C.; Li, W. K., A Gaussian-2 and Gaussian-3 Study of Alkoxide Anion Decompositions. 1. H-2 and CH_4 Eliminations of the Methoxide, Ethoxide, Isopropoxide, and tert-Butoxide Anions. *J. Phys. Chem. A* **2001,** *105* (2), 432-441.

27. Wilsey, S.; Dowd, P.; Houk, K. N., Effect of Alkyl Substituents and Ring Size on Alkoxy Radical Cleavage Reactions. *J. Org. Chem.* **1999,** *64*, 8801-8811.

28. Mereau, R.; Rayez, M.-T.; Rayez, J. C.; Hiberty, P. C., Alkoxyl Radical Decomposition Explained by a Valence-Bond Model. *Phys. Chem. Chem. Phys.* **2001,** *3*, 3656-3661.

29. Wu, F.; Law, C. K., An Experimental and Mechanistic Study on the Laminar Flame Speed, Markstein Length and Flame Chemistry of the Butanol Isomers. *Comb. Flame* **2013,** *160* (12), 2744-2756.

30. Xu, X. S.; Hu, Z.; Jin, M. X.; Liu, H.; Ding, D., Studies on the Isomerization of Acetone CH_3COCH_3. *J. Mol. Struct. Theo.* **2003,** *638* (1-3), 215-228.

31. Zhou, C.-W.; Li, Z.-R.; Liu, C.-X.; Li, X., An ab initio RRKM Prediction of Rate Constant and Product Branching Ratios for Unimolecular Decomposition of Propen-2-ol and Related $H+CH_2COHCH_2$ Reaction. *J. Chem. Phys.* **2008,** *129*, 234301.

32. Continetti, R. E., Photoelectron-Photofragment Coincidence Studies of Dissociation Dynamics. *Int. Rev. Phys. Chem.* **1998,** *17* (2), 227-260.

33. Johnson, C. J.; Continetti, R. E., Dissociative Photodetachment Studies of Cooled $HOCO^-$ Anions Revealing Dissociation Below the Barrier to $H + CO_2$. *J. Phys. Chem. Lett.* **2010,** *1* (12), 1895-1899.

34. Alconcel, L. S.; Deyerl, H.-J.; DeClue, M.; Continetti, R. E., Dissociation Dynamics and Stability of Cyclic Alkoxy Radicals and Alkoxide Anions. *J. Am. Chem. Soc.* **2001,** *123*, 3125-3132.

35. Alconcel, L. S.; Continetti, R. E., Dissociation Dynamics and Stability of Cyclopentoxy and Cyclopentoxide. *Chem. Phys. Lett.* **2002,** *366*, 642-649.

36. Poad, B. L. J.; Ray, A. W.; Continetti, R. E., Dissociative Photodetachment of the Ethoxide Anion and Stability of the Ethoxy Radical CH_3CH_2O. *J. Phys. Chem. A* **2013,** *117* (46), 12035-41.

37. Johnson, C. J.; Shen, B. B.; Poad, B. L. J.; Continetti, R. E., Photoelectron-Photofragment Coincidence Spectroscopy in a Cryogenically Cooled Linear Electrostatic Ion Beam Trap. *Rev. Sci. Instrum.* **2011,** *82* (10), 105105.

38. Bowen, M. S.; Continetti, R. E., Photodetachment Imaging Study of the Vinoxide Anion. *J. Phys. Chem. A* **2004,** *108* (39), 7827-7831.

39. Hanold, K. A.; Luong, A. K.; Clements, T. G.; Continetti, R. E., Photoelectron-Multiple-Photofragment Coincidence Spectrometer. *Rev. Sci. Instrum.* **1999,** *70* (5), 2268-2276.

40. Sherwood, C. R.; Continetti, R. E., Dissociative Photodetachment Dynamics of O_2^-(H2O). *Chem. Phys. Lett.* **1996,** *258* (1-2), 171-179.

41. Sherwood, C. R.; Garner, M. C.; Hanold, K. A.; Strong, K. M.; Continetti, R. E., Energy and Angular-Distributions in Dissociative Photodetachment of O_4^-. *J. Chem. Phys.* **1995,** *102* (17), 6949-6952.

42. Montgomery, J. A.; Frisch, M. J.; Ochterski, J. W.; Petersson, G. A., A Complete Basis Set Model Chemistry. VI. Use of Density Functional Geometries and Frequencies. *J. Chem. Phys.* **1999,** *110* (6), 2822-2827.

43. Montgomery, J. A.; Frisch, M. J.; Ochterski, J. W.; Petersson, G. A., A Complete Basis Set Model Chemistry. VII. Use of the Minimum Population Localization Method. *J. Chem. Phys.* **2000,** *112* (15), 6532-6542.

44. Frisch, M. J.; Trucks, G. W.; Schlegel, H. B.; Scuseria, G. E.; Robb, M. A.; Cheeseman, J. R.; Montgomery, J., J. A.; Vreven, T.; Kudin, K. N.; Burant, J. C.; al., e. *Gaussian 03, Revision B.04*, Gaussian, Inc.: Wallingford, CT, 2004.

45. Fukui, K., The Path of Chemical Reactions - The IRC Approach. *Acc. Chem. Res.* **1981,** *14* (12), 363 - 368.

46. Dykstra, C. E., *Theory and Applications of Computational Chemistry : the First Forty Years*. 1st ed.; Elsevier: Amsterdam ; Boston, 2005.

47. Young, D. C., *Computational Chemistry: A Practical Guide for Applying Techniques to Real World Problems*. Wiley-Interscience: New York, 2001.

48. Ervin, K. M.; Ramond, T. M.; Davico, G. E.; Schwartz, R. L.; Casey, S. M.; Lineberger, W. C., Naphthyl Radical: Negative Ion Photoelectron Spectroscopy, Franck-Condon Simulation, and Thermochemistry. *J. Phys. Chem. A* **2001,** *105* (48), 10822-10831.

49. Ellison, G. B.; Engelking, P. C.; Lineberger, W. C., Photoelectron Spectroscopy of Alkoxide and Enolate Negative Ions. *J. Phys. Chem.* **1982,** *86* (25), 4839-5026.

50. Osborn, D. L.; Leahy, D. J.; Cyr, D. R.; Neumark, D. M., Photodissociation Spectroscopy and Dynamics of the $N_2O_2^-$ Anion. *Journal of Chemical Physics* **1996,** *104*, 5026-5039.

51. Duncan, M. A., Infrared Laser Spectroscopy of Mass-Selected Carbocations. *J. Phys. Chem. A* **2012,** *116*, 11477-11491.

52. Lu, Z.; Hu, Q. C.; Oakman, J. E.; Continetti, R. E., Dynamics on the HOCO Potential Energy Surface Studied by Dissociative Photodetachment of $HOCO^-$ and $DOCO^-$. *J. Chem. Phys.* **2007,** *126* (19), 194305.

53. Janousek, B. K.; Zimmerman, A. H.; Reed, K. J.; Brauman, J. I., Electron Photodetachment From Aliphatic Molecular Anions - Gas-Phase Electron-Affinities of Methoxyl, tert-Butoxyl, and Neopentoxyl Radicals. *J. Am. Chem. Soc.* **1978,** *100* (19), 5985-6298.

54. Gao, A.; Jiao, Z.; Li, A., The Alkoxy Radicals and their Anions: Structures and Electron Affinities. *J. Mol. Struct. Theo.* **2008,** *848*, 40-46.

55. Sanz, M. E.; McCarthy, M. C.; Thaddeus, P., Vibrational Excitation and Relaxation of Five Polyatomic Molecules in an Electrical Discharge. *J. Chem. Phys.* **2005,** *122*, 194319.

56. Welz, O.; Savee, J. D.; Eskola, A. J.; Sheps, L.; Osborn, D. L.; Taatjes, C. A., Low-Temperature Combustion Chemistry of Biofuels: Pathways in the Low-Temperature (550-700 K) Oxidation Chemistry of Isobutanol and tert-Butanol. *Proc. Combust. Inst.* **2013,** *34*, 493-500.

57. Buback, M.; Kling, M.; Schmatz, S., Decomposition of Tertiary Alkoxy Radicals. *Zeit. Physik. Chem.* **2005,** *219* (9), 1205-1222.

58. Choo, K. Y.; Benson, S. W., Arrhenius Parameters for the Alkoxy Radical Decomposition Reactions. *Int. J. Chem. Kin.* **1981,** *13* (9), 833-844.

59. Marque, S. R. A.; Siri, D., Beta-Fragmentation of Tertiary Alkoxyl Radicals: G3(MP2)-RAD and Natural Bond Orbital Investigations. *ChemPhysChem* **2012,** *13*, 703-707.

60. Coote, M. L., Reliable Theoretical Procedures for the Calculation of Electronic-Structure Information in Hydrogen Abstraction Reactions. *J. Phys. Chem. A* **2004,** *108*, 3865-3872.

61. Borrelli, R.; Peluso, A., The Vibrational Progressions of the N V Electronic Transition of Ethylene: A Test Case for the Computation of Franck-Condon Factors of Highly Flexible Photoexcited Molecules. *J. Chem. Phys.* **2006,** *125*, 194308.

62. Faulhaber, A. E.; Szpunar, D. E.; Kautzman, K. E.; Neumark, D. M., Photodissociation Dynamics of the Ethoxy Radical Investigated by Photofragment Coincidence Imaging. *J. Phys. Chem. A* **2005,** *109* (45), 10177-10473.

63. Frassoldati, A.; Grana, R.; Faravelli, T.; Ranzi, E.; Osswald, P.; Kohse-Hoeinghaus, K., Detailed Kinetic Modeling of the Combustion of the Four Butanol Isomers in Premixed Low-Pressure Flames. *Comb. Flame* **2012,** *159* (7), 2295-2311.

64. Wang, X.-B.; Woo, H.-K.; Wang, L.-S., Vibrational Cooling in a Cold Ion Trap: Vibrationally Resolved Photoelectron Spectroscopy of Cold C_{60}^- Anions. *J. Chem. Phys.* **2005,** *123*, 051106.

65. Hock, C.; Kim, J. B.; Weichman, M. L.; Yacovitch, T. I.; Neumark, D. M., Slow Photoelectron Velocity-Map Imaging Spectroscopy of Cold Negative Ions. *J. Chem. Phys.* **2012,** *137*, 244201.

Chapter 4: Photoelectron-Photofragment Coincidence Spectroscopy With Ions Prepared in a Cryogenic Octopole Accumulation Trap

4.1 Introduction

Measurement of energy partitioning for neutral dissociation processes provides significant insight into reaction dynamics of transient species, providing benchmarks for understanding reaction dynamics.[1, 2] Experimentally, such measurements are challenging due to the complexity of potential energy surfaces requiring spectroscopic probes for all resulting products of a photo-induced process. We make use of anion photodetachment coupled with photoelectron-photofragment coincidence (PPC) spectroscopy to provide a broad overview of the reaction dynamics at a fixed photon energy. The photoelectron kinetic energy (eKE) spectrum encodes the distribution of potential energies on the nascent neutral surface, and the corresponding eKE-resolved kinetic energy release (KER) spectra for the neutral products provides a measure of the subsequent reaction dynamics. Internal excitation in the precursor anions unfortunately generates congestion in PPC spectra [1, 3-5] leaving ambiguity in the energy available to the neutral fragments in the dissociative photodetachment (DPD) process. The capability to prepare precursor anions with known internal energies greatly enhances the ability to deduce the energy partitioning for the dissociative pathways. In an effort to better control the internal excitation of precursor anions, a cryogenic octopole accumulation trap (COAT) has been coupled to an existing photoelectron-photofragment coincidence (PPC) spectrometer enabling the preparation of both hot and cold precursor anions as demonstrated through PPC spectroscopy of O_3^-.

Spectroscopy of ions with high internal excitation yields complex and congested spectra often obscuring features that yield information about reaction dynamics. Supersonic expansions have been heavily utilized in gas-phase experiments for producing molecules with vibrational temperatures below 100 K and rotational temperatures below 20 K.[6] Unfortunately, the ionization process can induce significant amounts of internal energy resulting in system-dependent cooling efficacy.[1, 7, 8] Previous efforts in this laboratory to prepare colder ions by utilizing an electrostatic ion beam trap (EIBT) have successfully resulted in significantly colder ions primarily through permitting much stronger supersonic expansions owing to the reduced duty cycle and pumping speed requirements for the ion source when used in concert with the EIBT. This allowed more effective cooling of small molecules such as $HOCO^-$, allowing a detailed characterization of deep tunneling involved in the dissociation of *cis*-HOCO to H + CO_2.[9] Unfortunately, larger ions such as *tert*-butoxide ($(CH_3)_3CO^-$) are not efficiently cooled in a supersonic expansion resulting in observed dissociation dynamics only accessible through non-Boltzmann population of highly vibrationally excited anions.[8]

Various methods of preparing cold anions have been considered for the PPC spectrometer including buffer-gas-cooled radiofrequency (RF) ion traps. Due to the low-duty cycle, an RF ion trap alone is not an ideal approach to performing PPC measurements. PPC measurements provide kinematically complete information on events that lead to a free electron and momentum-matched neutral products detected in coincidence, so a high duty cycle and low event rate are required to minimize contamination of the data due to false coincidences. [10, 11] The addition of the EIBT to the PPC spectrometer decoupled the source duty cycle from the photodetachment laser interaction duty cycle through the

recycling of ions within the EIBT, allowing for the source repetition rate to be reduced to 10 Hz while maintaining the high photodetachment laser and reaction dynamics data acquisition duty cycle (1 kHz) required to carry out successful multiparticle coincidence experiments. The ability to decouple the source and the EIBT duty cycles has enabled the reconsideration of the low-repetition-rate cryogenic radiofrequency (RF) trap as a method for cooling ions.

RF ion traps have been proven to be a robust method of storing and cooling ions via collisions with cold buffer gas and have been extensively used in cooling clusters and larger biomolecules.[5, 12-14] The cooling ability of the RF trap is limited by not only the temperature of the ion trap but also by ion heating effects from RF electric fields.[12] Within an RF trap, ion oscillation at the frequency of the RF field causes heating through collisions with the buffer gas. The oscillation is highly dependent on the effective potential (V_{eff}) within the trap. Quadrupole traps have a parabolic effective potential, and the large field-induced gradient is expected to lead to a propensity for significan RF heating. Increasing the order (number of electrodes) for a linear RF trap creates an effective potential with a smaller radial field gradient through the flattening of the minima creating a steep rise in potential near the RF rods, an example being the well-known 22-pole trap of Gerlich and co-workers.[12] This allows for a larger area in the center of the trap relatively free of RF heating within which the ions are confined.

In the present application, RF ion traps provide flexibility in the preparation of ions for PPC spectroscopy by allowing for heating as well as cooling of ions. The ability to thermalize the anions to low temperatures provides a universal approach to cooling ions,

allowing for more clearly defined ion energetics for the subsequent study of photo-induced processes. The ability to collisionally heat the ions allows investigation of the effects of internal excitation on dissociation dynamics and thermally activated processes.

To demonstrate the effectiveness of COAT, PPC spectroscopy was performed on O_3^- at 388 nm ($E_{h\nu}$ = 3.20 eV), just below the threshold for autodetachment of $O_2^-(v\geq4)$ products from the photodissociation of O_3^-. The photoelectron spectrum of O_3^- at a photon energy $E_{h\nu}$ = 3.20 eV show three concurrent photophysical processes: (1) photodetachment $O_3^- + h\nu \rightarrow O_3 + e^-$; (2) photodissociation/autodetachment $O_3^- + h\nu \rightarrow O_2^-(^2\Pi) + O(^3P)$ and (3) photodissociation $O_3^- + h\nu \rightarrow O^-(^2P) + O_2(^1\Delta_g)$ followed by the photodetachment $O^-(^2P) + h\nu \rightarrow O(^3P)$ by a second photon. While all three processes are influenced by the internal excitation of the precursor anion, the most striking effect is observed in process (2). It is well known that vibrational excitation of $O_2^- > 4$ quanta results in autodetachment of the electron yielding $O_2(^3\Sigma_g^-)$.[15-17] Jarrold and coworkers recently observed the autodetachment of O_2^- as a result of photofragmentation of O_3^- to O_2^- (v>4) + O at 355 nm ($E_{h\nu}$ = 3.49 eV) photon energy,[18] and this process was further characterized at $E_{h\nu}$ = 3.20 eV in an initial report from our laboratory.[19] The onset for the autodetachment channel lies 3.24 eV above $O_3^-(\tilde{X}^2B_1)$ as shown in Figure 4.1. Access to the autodetachment channel is therefore energetically accessible only when the precursor anion (O_3^-) is vibrationally excited, making this an ideal candidate for testing the capabilities of COAT. In the following sections, the design and application of COAT in PPC spectroscopy is discussed in detail, including demonstration, using O_3^-, of the ability to prepare both hot and cold ions to exert control over product channel pathways.

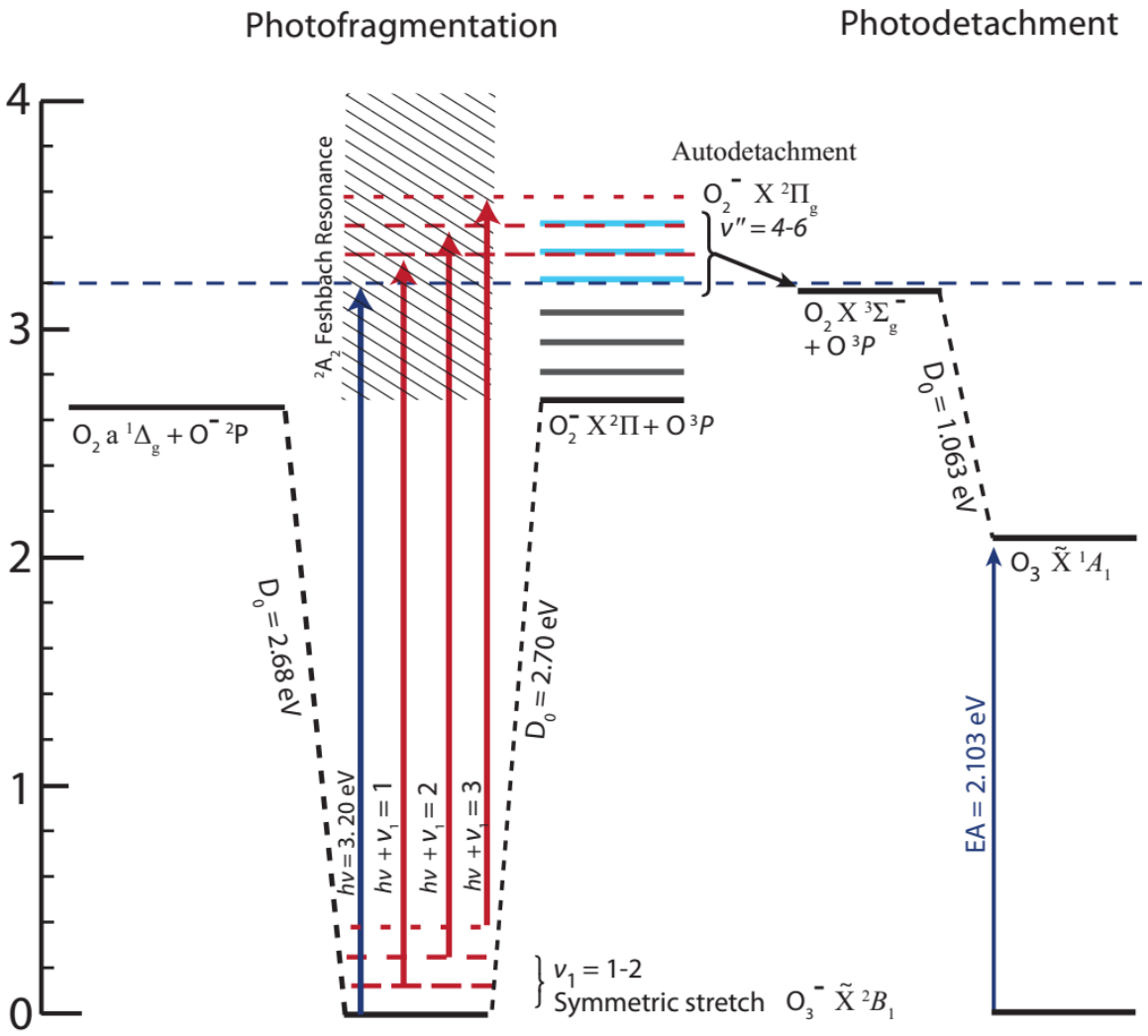

Figure 4.1. The energetics of available pathways relative to ground state O_3^- following photoabsorption at E_{hv} = 3.20 eV,[20, 21] including the Feshbach resonance identified in DEA studies,[15, 22] O_2 energetics,[23] and relevant excited states of O_3^-.[24] Dashed horizontal red lines indicate internal excitation in the anion resulting in opening the otherwise energetically inaccessible autodetachment channel.

4.2 Experimental Setup

The cryo-PPC spectrometer[9] has been modified to include a new source chamber and a cryogenic octopole accumulation trap (COAT) as shown in Figure 4.2. The new modifications can be divided into three sections discussed in detail below: source, COAT design and COAT operation. As a general overview, ions are generated in a supersonic expansion and perpendicularly extracted via a Wiley-McLaren-style mass spectrometer (region 1). Ions are focused and directed by a set of lenses and deflectors before being slowed for injection into COAT (region 2). If hot ions are desired, the ions are slowed to a lesser degree to increase the initial collision energy with the buffer gas. The entrance endcap is held at an attractive potential until the ions are within the trap, and is then switched to a repulsive potential for ion storage. If accumulation of ions is desired, the entrance endcap is held at a slightly repulsive potential, preventing ions from traversing and exiting the trap. While the ions are trapped within COAT, they undergo collisional cooling following initial collisional heating. After the designated trapping period, ions are extracted from COAT and directed into a differentially pumped chamber where they are accelerated to a kinetic energy of 7 keV, re-referenced to ground (region 3), and mass selected by time of flight (region 4) for trapping within a cryogenically cooled electrostatic ion beam trap (EIBT) for 100 ms (region 6). This aspect of the experiment has been described in detail previously.[9] Within the EIBT, the ion packet is bunched and phase-locked to a 387.8 nm ($E_{h\nu}$ = 3.20 eV) laser pulse from a Ti:Sapphire regenerative amplifier (Clark MXR CPA-2000; 1.2 ps pulse width) at a repetition rate of 1037 Hz using a field-programmable-gate-array-synced RF function generator (HP 3325). The oscillating ion packet interacts with the laser repeatedly over a 100 ms trapping period per experimental

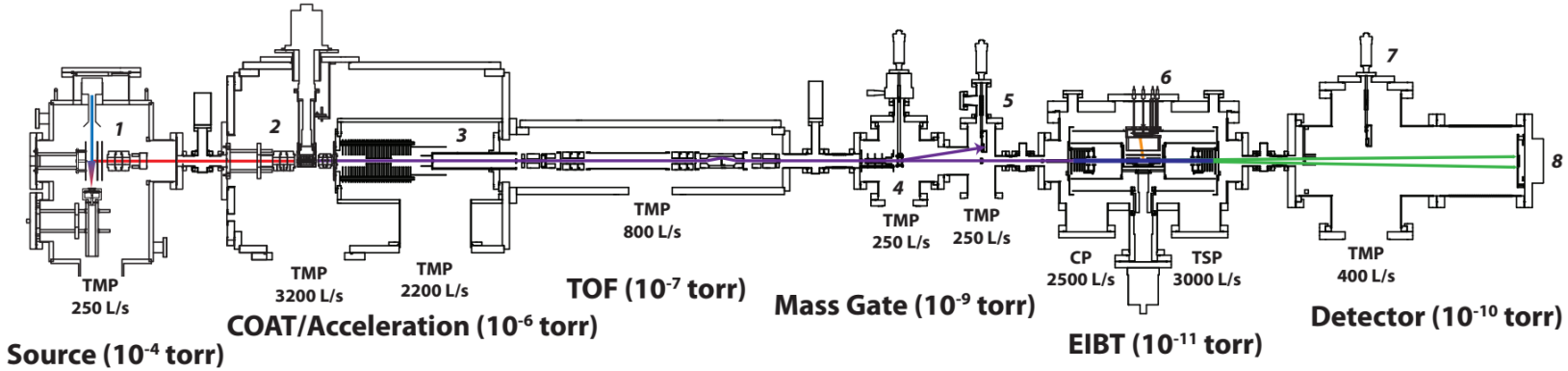

Figure 4.2. Overview of the modified PPC spectrometer incorporating a new source and COAT. Labeled sections are as follows: (1) Source with pulsed valve/discharge assembly with Wiley-McLaren-style extraction. (2) COAT (3) Acceleration stack with potential switch. (4) Electrostatic chopper. (5) Pre-EIBT ion detector (6) Electron Detector / EIBT (7) Neutral particle detector.

cycle, and the electron and neutral products are measured. The laser fluence was modulated by using a single 0.5 m focal length lens for high power density measurements versus collimation with a 2.5:1 telescope on the 3.5 mm-diameter doubled output beam of the Ti:Sapphire laser. The power density for the collimated laser was estimated to be $2x10^9$ W/cm^2 with the focused laser approximately 100x greater. Detached electrons were orthogonally extracted and mapped via a velocity map imaging setup to a time and position sensitive detector. The center-of-mass eKE is determined from the three-dimensional electron velocity vector as determined from the time and position of electron impact. Optimal resolution is achieved through selection of electrons with minimal z-velocities perpendicular to the detection plane as determined by the TOF of the center-of-mass for photoelectron detection by equatorially slicing the photoelectron spectra. This effect of slicing on the intensities in the photoelectron spectra was corrected for by dividing the sliced photoelectron spectrum by the energy-dependent acceptance function of the z-velocity slice.[25] Calibration of O_2^- photoelectron spectra as well as the O^- 2-photon events observed in the present experiments indicate $\Delta eKE/eKE$ ~4% full-width-at-half-maximum (FWHM) at 1.74 eV. After photodetachment, the resulting neutrals, no longer bound within the EIBT, exit and impinge on a multiparticle time-and position-sensitive detector 1.3 m away from the laser interaction region (region 8), allowing determination of the product mass and kinetic energy release (KER).

A. **Source Design**

A new source chamber was added to the existing PPC spectrometer to house a piezoelectric pulsed valve (PPV) with coaxial discharge plates and a Wiley-McLaren style

mass spectrometer. This source chamber is pumped by an Edwards NEXT240 turbomolecular pump maintaining 10^{-4} mbar pressure during operation. Ions are generated in a supersonic expansion from the PPV with a 1 keV electron beam counter-propagating down the expansion, oriented perpendicular to the ion beam axis of the PPC spectrometer. The ions are extracted from the expansion using three pulsed electrodes in a Wiley-McLaren configuration.[26] A gear system was constructed to allow the distance between the PPV and the Wiley-McLaren plates to be adjusted, enabling extraction of different portions of the supersonic expansion. The first two plates (14 cm outside diameter with 2 cm inner diameter apertures) are spaced 6 cm apart between which the supersonic expansion propagates. The plates are pulsed with negative potentials giving ions an average of ~225 eV translational kinetic energy while the third plate is typically held at -30 V. The ions are then guided through six focusing lens elements and one set of deflectors into COAT in the next chamber.

4.2.1 COAT Trap Design

COAT is a linear octopole trap, as shown in Figure 4.3, based on a similar design used by Wester and coworkers.[27] These devices have been known to be effective at cooling both external and internal degrees of freedom via buffer gas collisions.[14, 27-29] For linear RF traps, the effective radial field is $V_{eff}(r) \propto r^{n-2}$, where r is the radius and n is the number of poles. [12, 28] The V_{eff} plays a critical role in determining the trapping volume as mentioned previously. An octopole configuration provides an optimal compromise in trapping volume by confining the ions along a smaller radius from the center of the trap compared to traps with a larger number of poles, while still allowing for facile

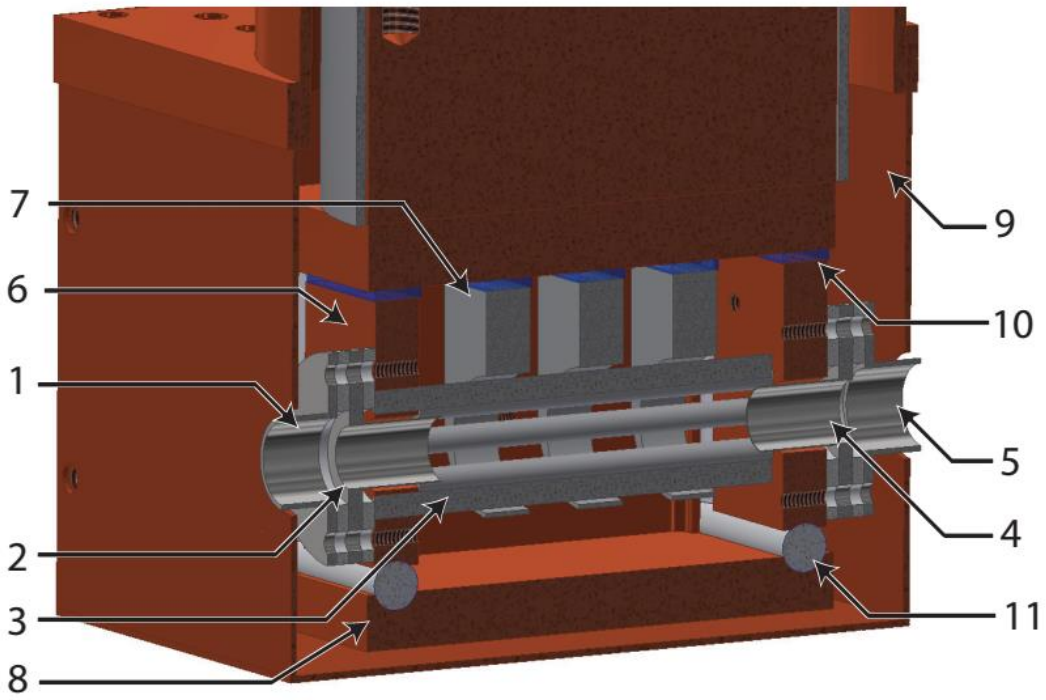

Figure 4.3. Cross sectional view of the COAT assembly. Labeled components are as follows: (1) Entrance lens. (2) Entrance Endcap. (3) RF rods. (4) Exit Endcap. (5) Exit Lens. (6) RF rod mount. (7) Shaping electrodes. (8) Buffer Gas Shield. (9) Thermal radiation shield. (10) Sapphire insulation. (11) Macor spacers

extraction of the ions. This also allows for maximal laser overlap with the trapped ions for future IR excitation experiments.

The design consists of RF rods which have a 2.5 mm diameter arranged in a cylindrical array, with an inscribed inner diameter of 7.5 mm. The construction (Figure 4.3) consists of four cylindrical rods mounted to each RF mount and assembled such that adjacent rods are mounted on opposing rod mounts. The trapping of ions in the radial direction is achieved by applying opposite RF phase to each RF rod mount giving adjacent cylindrical rods an alternating RF phase, generating an octopole field with a 4 MHz, 320 volt peak-to-peak RF waveform produced by a home-built RF generator, described by Anderson and coworkers.[30, 31] Longitudinal confinement is achieved by endcaps on both sides of COAT with a 6 mm diameter opening which can be switched, using home built high voltage MOSFET switches, for loading ions, trapping ions, and extracting ions. Three shaping electrodes are equally spaced apart and surround the RF rods whose limited field penetration generates a potential field ramp to bias longitudinal storage of ions towards the exit endcap of the trap. The RF mounts as well as the shaping electrodes are all electrically isolated from the copper base of the trap by sapphire plates, taking advantage of sapphire's high thermal conductivity at cryogenic temperatures. The RF mounts along with a buffer gas shield surrounds the rods and shaping electrodes to provide a cold closed environment for collisional cooling. A thin layer of Apiezon N is used between all areas of mechanical contact to improve thermal conductivity at cryogenic temperatures.

The entire trap is mounted to a heating block which allows for variable temperatures between ~10 K and 300 K via heaters clamped around the heating block. The heating block,

in turn, is mounted to the 2nd stage of a Sumitomo RDK-205D 4K Cryocooler cold head. COAT can be cooled to ~17 K as measured by a silicon diode (LakeShore DT-471-CO) though it is an upper limit as H_2 freezes onto the electrodes of COAT indicating an inner surface temperature of ~10 K. The 1st stage of the cold head is mounted to a thermal radiation shield (37 K) which encloses COAT. The buffer gas is pre-cooled to ~40 K through a 3 mm diameter copper tube in thermal contact with the 1st stage of the cold head prior to injection into COAT through a hole in the base of the trap. The entire assembly is mounted on a movable flange on top of the COAT chamber allowing for the COAT to be aligned or moved out of the ion beam-line axis.

4.2.2 COAT Operation:

COAT is generally operated in one of three modes: cooling mode, heating mode and accumulation mode. The ability to heat and cool ions comes from controlling the initial translational energy of the precursor ions as they enter into COAT as well as adjusting the duration of trapping. To reduce the initial translational energy of the ions entering the trap, the whole trap assembly is floated at an appropriate DC potential, and the incoming ions are focused into the trap using an entrance lens element. To further facilitate trapping and cooling of the ions, a pulse of pre-cooled buffer gas generated with a Gerlich-type valve[32] is used to raise the pressure in the trap to ~10^{-2} mbar prior to ion injection. Upon entering, the ions collide with the buffer gas, further reducing translational kinetic energy and trapping them within COAT.

All source timing signals are controlled by a Stanford Research DG645 digital delay generator triggered by and prescaled to $1/100^{th}$ of the laser repetition rate (1037 Hz) while all COAT timings are controlled by a Quantum Composer 9518 digital delay generator triggered off the prescaled signal. These timings control what mode COAT is run in: accumulation, cooling, or heating. In accumulation mode, the entrance endcap can be held at constant trapping voltage to facilitate accumulation of ions over multiple ion generation cycles. This can be synchronized with a faster rate of ion generation (20 Hz) and/or coupled with a longer EIBT trap time. In accumulation mode, only cold ions are available since the ions are trapped for a long duration. In cooling and heating mode, the entrance endcap is switched from an attractive potential to load ions to a repulsive potential to trap ions, maximizing the quantity of ions entering the trap for a single cycle. A typical map of voltages on the essential elements is shown in Figure 4.4 for this process.

Within COAT, the ions undergo collisional cooling with the buffer gas for a pre-set period of time determined by whether or not vibrationally excited ions are desired. Shorter trapping time limits the thermalization and cooling of the ions, allowing the preparation of hotter ions. Increasing the trapping time allows thermalization of the trapped ions to the temperature of COAT. Similar traps have shown thermalization of the anions under similar pressures ($\sim 10^{-2}$ mbar) within 30 ms.[4] Due to coupling with our EIBT, a trapping time of 80 ms is typical for maximizing the cooling time while still maintaining a 10 Hz duty cycle. After the set trapping time, the exit endcap is switched to attractive potential to extract the ions from within COAT.

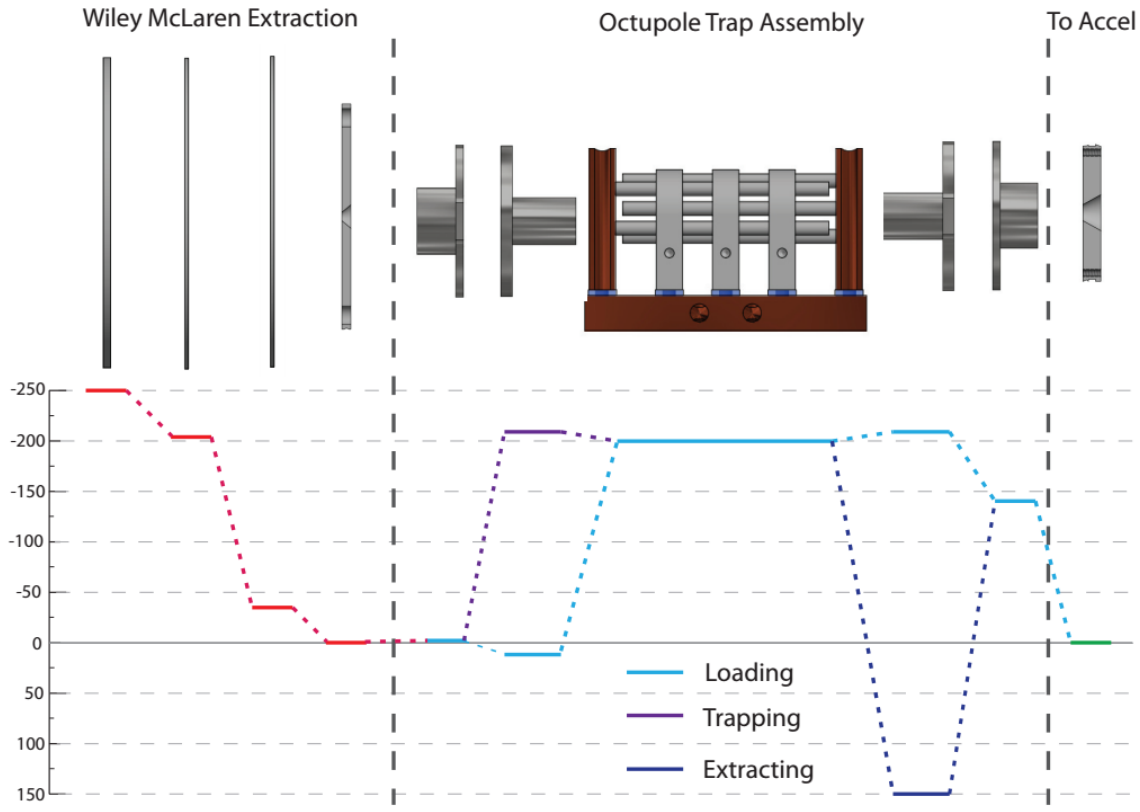

Figure 4.4. A voltage map for the new source is shown indicating typical voltages ions experience (not to scale). The red lines indicate the voltages for the Wiley McLaren extraction. The light blue line indicates the voltages for COAT while loading ions. The purple indicates the voltage of the entrance endcap for COAT while trapping ions. The dark blue line indicates the typical voltage for the exit endcap when extracting ions.

4.3 Results

The capabilities of COAT are demonstrated by comparing the signatures of the three concurrent photophysical channels occurring at $E_{h\nu}$ = 3.20 eV in the photoelectron spectra of O_3^-: (1) photodetachment $O_3^- + h\nu \rightarrow O_3 + e^-$, (2) photodissociation/autodetachment $O_3^- + h\nu \rightarrow O_2^-(^2\Pi_g) + O(^3P)$, and (3) photodissociation $O_3^- + h\nu \rightarrow O^-(^2P) + O_2(^1\Delta_g)$ followed by the photodetachment $O^-(^2P) + h\nu \rightarrow O(^3P)$ by a second photon. The performance of COAT under various cooling conditions and heating conditions will be compared as well as temperatures estimated through Franck-Condon simulations.

4.3.1 Cooling Performance

Over the course of an ion trapping cycle, ions within COAT collide with the pre-cooled buffer gas to remove both translational kinetic energy and internal energy, making the cooling performance dependent on COAT temperature, the trapping time, and the buffer gas density and identity. The effects of varying buffer gas conditions can be seen in the total photoelectron spectra (electrons in coincidence with both dissociative products and stable O_3) in Figure 4.5 with high and low laser fluence in the top and bottom panels, respectively. A structured signal is seen at low eKE (0.0 to 0.4 eV) originating from sequential autodetachment of $O_2^-(v''>4)$ produced by channel (2) while the primary feature in the spectra is a result of the photodetachment (1) $O_3^- + h\nu \rightarrow O_3 + e^-$ yielding a structured photoelectron spectrum in the 0.30 eV - 1.50 eV eKE range.[20, 21, 33, 34] The peak at eKE = 1.74 eV is a result of channel (3) as a 2-photon process in high laser fluence experiments

from significant sequential photodetachment of O^- photoproducts while 2-photon $O_2^-(v''<4)$ photoproducts, are observed as a broad baseline, produced by channel (2). Under no buffer gas conditions, as seen in the upper panel of Figure 4.5 (Purple line), no collisional heating or cooling takes place and this can be used as a reference for the initial internal excitation of the trapped anions.

The peaks at low eKE (0.07, 0.19 and 0.32 eV) originate from the photodissociation/autodetachment $O_3^- + h\nu \rightarrow O_2^-(^2\Pi) + O(^3P)$ pathway (2) via photoexcitation to the $^2A_2$ excited state as previously reported.[19, 34] At $E_{h\nu} = 3.20$ eV, access to $O_2^-(v'' = 4,5,6)$ is energetically forbidden without vibrational excitation of O_3^-, as shown in the energetics diagram in Figure 4.1, so observation of vibrationally autodetaching O_2^- provides a sensitive test of parent anion internal energy. The peaks at eKE = 0.07 eV and 0.19 eV correspond to the vibrational autodetachment of $O_2(v'=0) + e^- \leftarrow O_2^-(v'' = 4,5)$ and are most prominent under no buffer gas conditions, indicating significant initial vibrational excitation in O_3^-. Trapping the ions for 80 ms in COAT at a temperature <17 K significantly reduces the autodetachment channel when neat He (black lines) buffer gas was used and the channel is effectively eliminated when a 20:80 H_2/He (blue lines) buffer gas mix was used. The temperatures noted are the measured temperatures of COAT but their relation to the ion temperature is dependent on the duration of trapping to allow for the thermalization of the ions in buffer gas collisions. Even with longer trapping times there may be non-Boltzmann distributions of excitation in high-frequency vibrations. The 20:80 H_2/He buffer gas mix cools the precursor ions more effectively than neat He due to collisional cooling being more effective with lighter buffer gases.[35, 36] The empirical efficacy of He/H_2 gas

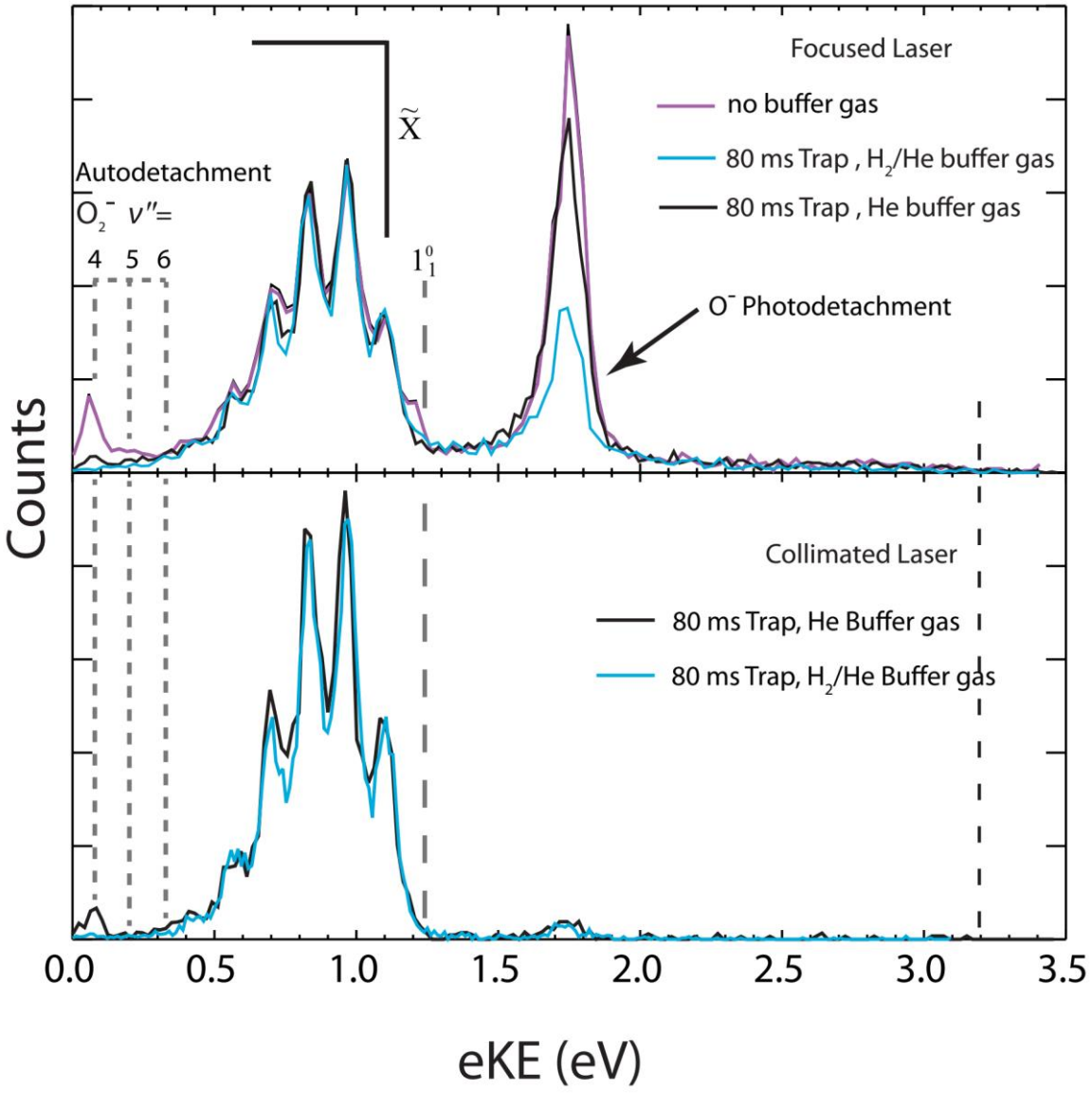

Figure 4.5. The total photoelectron spectrum for O_3^- produced with the COAT ion source under different buffer gas and laser configurations is shown. The top panel shows COAT with the laser focused using a single lens with neat He buffer gas cooling (black), with H_2/He buffer gas cooling (blue) and without buffer gas cooling (purple). The bottom panel shows the photoelectron spectrum with the collimated laser beam at 17 K with 80 ms trapping time with neat helium buffer gas (black) and H_2/He buffer gas (blue).

mixtures for collisional cooling, first reported by Wang and co-workers in photoelectron spectroscopy studies,[37] has also been found to be effective in other systems,[4, 38] and is seen to be very effective for O_3^-.

The dominant channel observed in the total photoelectron spectra (electrons in coincidence with either dissociative products or stable O_3) is the photodetachment (1) $O_3^- + h\nu \rightarrow O_3 + e^-$ yielding a structured photoelectron spectrum in the eKE range between 0.30 eV - 1.50 eV as shown in Figure 4.5. The photoelectron spectra are consistent with the electron affinity (EA) of O_3 previously determined to be 2.10 eV and a Franck-Condon vibrational progression in the totally symmetric ν_1 and ν_2 modes of the $O_3(\tilde{X}^1A_1)$ ground state.[21] The vibrational energies for O_3^- have been previously reported[21] and are summarized in Table 4.1 with the 1_1^0 hotband location annotated in Figure 4.5. Under the coldest conditions, the 1_1^0 hotband is within the noise of the spectra indicating little if any population in the ν_1 mode of O_3^-. Franck-Condon simulations (Figure 4.6) for the stable (1) $O_3^- + h\nu \rightarrow O_3 + e^-$ channel have been carried out with PESCAL[39] utilizing single point calculations in Gaussian 03[40] with previously reported geometries[21, 41] and frequencies (Table 1). [21] The Franck-Condon factors were calculated using the independent Morse oscillator approximation due to the strong effects of anharmonicity for transitions to high vibrational levels of O_3. The simulated spectra were generated by convolving the stick spectra with a Gaussian convolution consistent with the 4% ΔeKE/eKE resolution. The stick spectra were calculated at 0K in all modes for cold conditions (top panel, ν_1, ν_2, ν_3 = 0 K) and a Boltzmann distribution for hot conditions (bottom panel, ν_1 = 2000 K ν_2 = 1500 K ν_3 = 0 K). The dominant progression is the ν_1 symmetric stretch populating O_3 vibrational

Table 4.1. Vibrational energies used in Franck-Condon simulation.[21]

	ν_1 (100) (eV)	ν_2 (010) (eV)	ν_3 (001) (eV)
O_3^- $\tilde{X}$ $^2B_1$	0.121	0.068	0.109
O_3 $\tilde{X}$ $^1A_1$	0.137	0.087	0.129

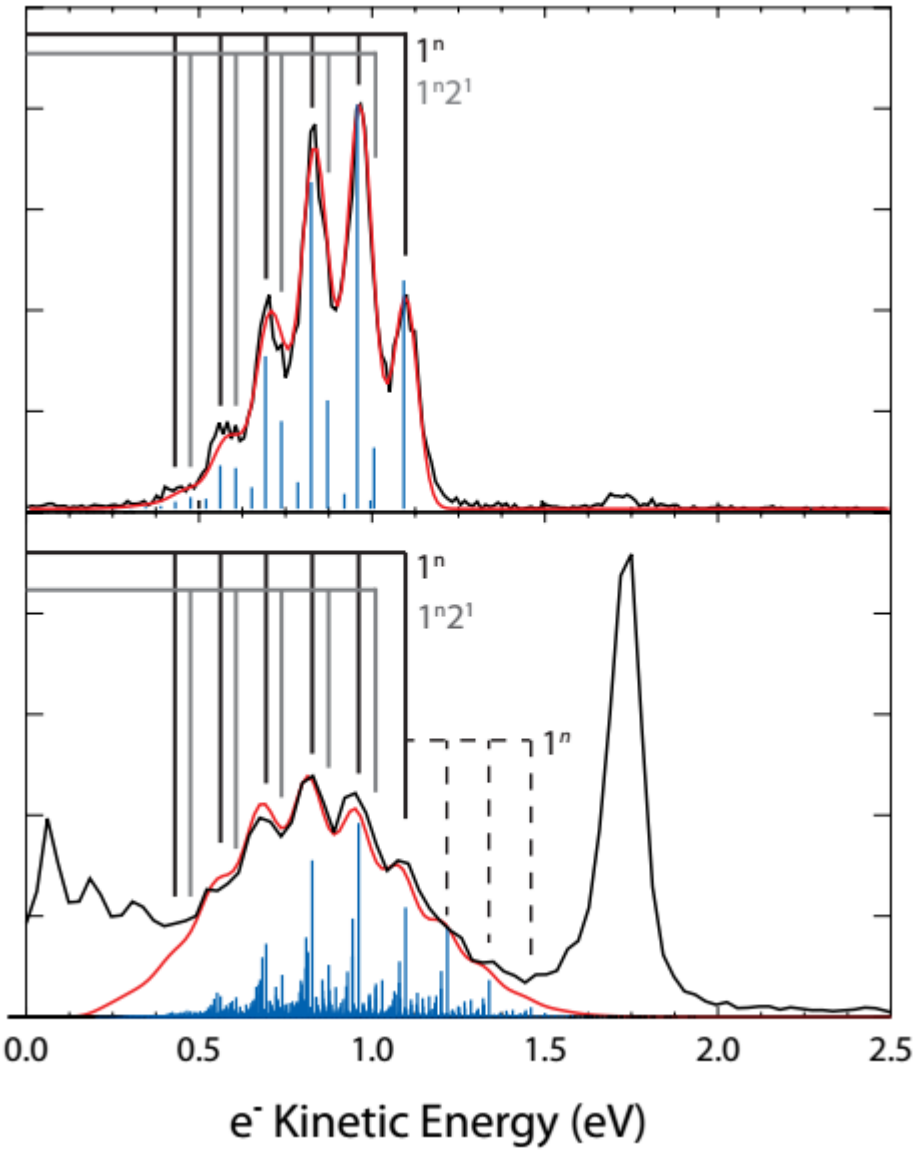

Figure 4.6. Franck-Condon simulations with stick spectra (blue sticks) gaussian convoluted to generate a simulated spectra (red solid line) overlaid on the coldest (top panel, black solid line, 80 ms Trap H_2/He buffer gas) and hottest (bottom panel, black solid line, 500μs, He buffer gas, high accel) O_3^- photoelectron spectra. The cold spectrum simulation assumes 0 K ion temperature while the hottest simulation assumes v_1 = 2000 K and v_2 = 1500 K. The vibrational combs indicate the dominant transitions with the dashed comb indicating hot bands.

states from ν_1=0 to ν_1=5 with the minor progression being combination bands of ν_2=1 with ν_1=0 to ν_1=5. The temperature of ν_3 was found to have no significant contribution to the spectra, consistent with previous assignments,[21] and was therefore left at 0 K. The 0 K simulation provides an acceptable match to the photoelectron spectrum under optimal cold conditions.

The feature at 1.74 eV eKE is a result of (3) photodissociation $O_3^- + h\nu \rightarrow O^-(^2P) + O_2(^1\Delta_g)$ followed by sequential photodetachment $O^-(^2P) + h\nu \rightarrow O(^3P)$.[19] As shown in the upper panel (Figure 4.5), using a focused laser the O^- photodetachment signal is much stronger, while use of a collimated laser caused a significant decrease in this two photon signal, increasing the sensitivity to the hot bands in the stable channel. Upon cooling (black line), the fraction of events resulting in channel (3) is reduced compared to the no buffer gas conditions (purple line) under similar laser fluence. The reduction in the signal under the H_2/He condition is due to lower laser fluence rather than an effect of cooling. The difference between collimated and focused laser are clearly observed in the VMI images where high fluence emphasizes the outermost ring (Figure 4.7 panel A) while under focusing conditions, the outermost ring is greatly diminished (Figure 4.7, panel B).

Overall COAT demonstrates the ability to thermalize the ions to a temperature cooler than through the use of supersonic expansion alone. The degree of cooling is heavily dependent on the duration in which the ions are trapped within COAT. The impact of cooling with COAT were observed as pathway (2) being effectively closed off while pathway (3) is reduced.

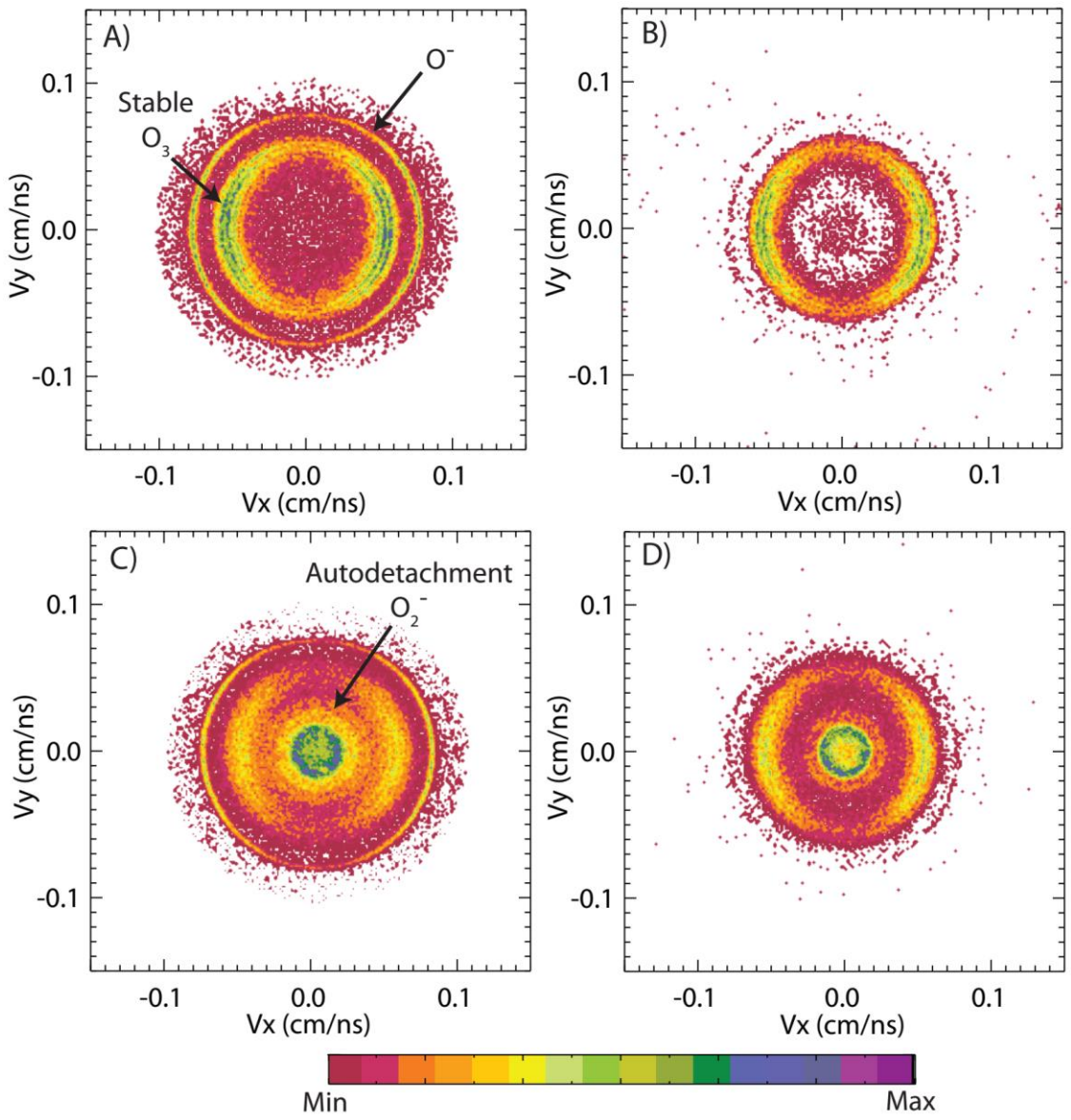

Figure 4.7. Photoelectron images recorded from O_3^- photodetachment at E_{hv} = 3.20 eV: (A) 17 K with H_2/He buffer gas and 80 ms COAT trapping with focused laser, (B) 17 K with H_2/He buffer gas and 80 ms COAT trapping with focused laser, and (C) 17 K with H_2/He buffer gas and 80 ms COAT trapping with collimated laser.

4.3.2 Heating Conditions

Upon loading into COAT, precursor anions collide with the buffer gas transforming translational kinetic energy into rovibrational heating of the ions. Thus, the primary parameters affecting the heating of the ions are settings that affect the kinetic energy of the precursor anion as well as the trapping time over which ions are allowed to cool through collisions with the buffer gas. Settings such as Wiley-Mclaren ion extraction voltage, the COAT float voltage, as well as the COAT entrance lens voltage can increase the temperatures of the ions by accelerating them to larger translational energies just prior to initial collisions within COAT. Similarly, the number density of the buffer gas in the trap affects the collisional heating and cooling. It should also be noted that ions which do not collide with buffer gas pass through COAT and are not trapped in either COAT or the EIBT. Total photoelectron spectra under various heating conditions are shown in Figure 4.8 in contrast to the cooling conditions shown in Figure 4.5.

Under heating conditions, the autodetachment from (2) $O_3^- + h\nu \rightarrow O_2^-(^2\Pi, v>4) + O(^3P)$, only accessible with vibrational excitation of the precursor anion, significantly increases in amplitude compared to the cold spectra (blue lines). The sensitivity of the autodetachment channel to O_3^- vibrational excitation infers a strong coupling of vibrational excitation within the $^2A_2$ excited state to highly vibrationally excited products.[19] The expansion of the parent anion wavefunction upon vibrational excitation of O_3^- may lead to an increase in Franck-Condon overlap with the $^2A_2$ excited state. This is also observed in the photoelectron image in Figure 4.7 (panels C and D) where the autodetachment features at low eKE appears in the center of the image with greatly enhanced intensity with the

$O_2^-(v''= 6)$ band clearly coming into view in the hottest settings. Autodetachment peaks corresponding to electrons arising from $O_2^-(v''= 4, 5$ and $6)$, with peaks located at 0.07, 0.19, and 0.32 eV respectively, are clearly defined under all hot conditions. Under collimated laser conditions, the shortened trapping time in COAT generates more highly vibrationally excited O_3^- than the ions thermalized under 300 K 30 ms conditions as shown in Figure 8 (bottom panel).

The hottest conditions (Figure 4.8, Red line) were achieved with a combination of short trapping time (500 μs), He buffer gas, and accelerating ions with the entrance lens just before trapping resulting in a significantly larger contribution from the autodetachment channel (2) as well as the O^- photodissociation channel (3) with the 2-photon O^- signal amplitude dominating over the stable channel. These spectra are scaled to the 0-0 peak in the photodetachment channel (1) to more clearly distinguish the differences in dissociation dynamics. Reducing the entrance lens acceleration voltage (by ~50 V) under the same source conditions (upper panel, purple line) still shows significant heating but to a lesser degree as indicated by the amplitude of the autodetachment signal. The increased spectral congestion with the autodetachment channel is due to autodetachment to $O_2(v'>0)$ as previously reported by Allan and coworkers in electron scattering experiments at high incident electron kinetic energy.[42] The relative amplitude of the $O_2^-(v''= 4)$ peak compared to $O_2^-(v''= 5$ and $6)$ significantly changes as the $O_2^-(v''= 5$ and $6)$ signals increase. This is consistent with DEA experiments carried out by Allan and coworkers where increased incident electron kinetic energy correlated with increased relative amplitude of $O_2^-(v''= 5$ and $6)$ providing further evidence the same excited state is being accessed. [42] The increase

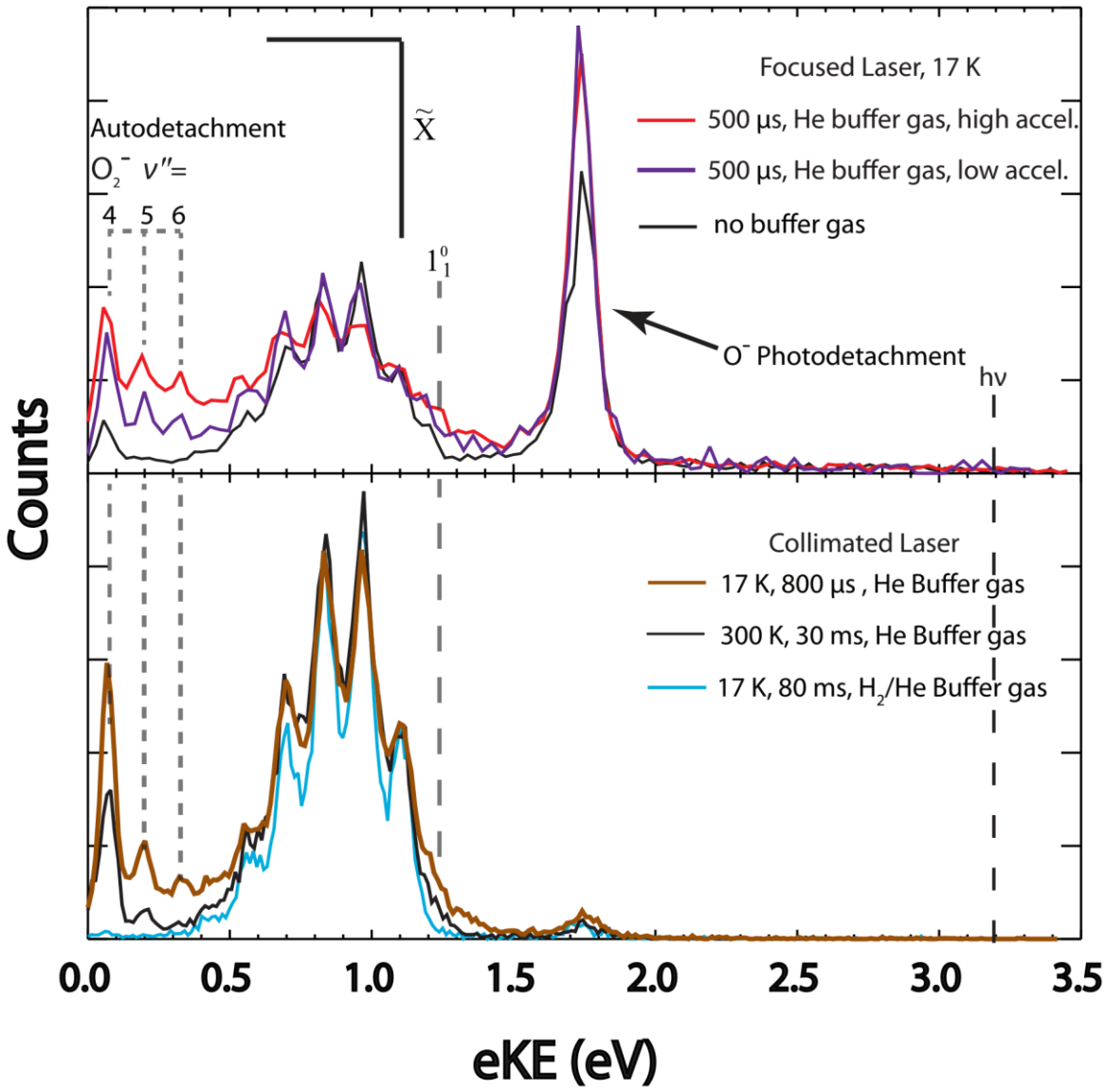

Figure 4.8. The total photoelectron spectrum for O_3^- produced with the COAT ion source under different temperatures, trap times, and laser configurations is shown. The top panel shows COAT with the laser focused using a single lens with no buffer gas (black line) compared to heating conditions (500 μs trapping time) with higher (red line) and lower (purple line) entrance lens acceleration. The bottom panel shows the photoelectron spectrum with the collimated laser beam at 17 K with 800 µs trapping time (brown) compared to 300 K with 30 ms trapping time with neat helium buffer gas (black) in contrast with H_2/He buffer gas (blue).

in precursor ion temperatures does not appear to significantly increase the 2-photon signal from $O_2^-(v'' < 4)$.

The stable channel upon heating shows a significant increase in hotbands, particularly for the 1_1^0 and 1_2^0 transitions. The amplitude for the hotbands in the bottom panel of Figure 4.8 is consistent with the expected trend from the amplitude of the autodetachment channel, with the shorter 800 μs trapping time exhibiting prominent peaks for 1_1^0 and 1_2^0 hotbands. The hottest spectra is in the top panel of Figure 4.8 (red line). It can be seen that the 1_1^0 hotband is nearly half the amplitude of the 0-0 transition in that spectrum. Additionally, a significant increase in spectral congestion due to sequence bands is observed, most notably in the hottest spectrum where even the peak amplitude distribution changes such that the 1_0^2 peak becomes the largest amplitude in the stable spectra.

A Franck-Condon simulation with the temperature of the vibrational modes set to ν_1 = 2000 K ν_2 = 1500 K is shown in Figure 4.6 providing an estimate for the temperature of the ions under very hot conditions. These temperatures should be considered a lower limit to the ion temperature given that a significant fraction of the ions undergo photodissociation, which is not taken into consideration in the simulation. The temperature difference in vibrational modes is explained by two factors: one is the expected non-Boltzmann distribution of vibrational excitation due to collisional heating and the second is the vibrational excitation enabling the autodetachment channel introducing competition between the stable and dissociative channels. Additionally, it has been found that the bending mode (ν_2) significantly contributes to channel (2).[19] The sequence bands shown in

the Franck-Condon simulation show that significant spectral congestion is caused by transitions from excitation of the ν_1 and ν_2 modes with up to 3 quanta of excitation in the precursor anion.

The ability to influence the dissociative pathways through heating the precursor ions is further demonstrated with channel (3). The 2-photon process is greatly enhanced upon heating while under similar laser power density. Under no buffer gas conditions (Figure 8, upper panel, black line) the amplitude for the O- photodetachment is lower than under heating conditions (red and purple lines). This is consistent with increased FC overlap with the $^2A_2$ state upon photoexcitation increasing the fraction of events from channels (2) and (3).

The heating of ions utilizing COAT is dependent on the trapping duration within COAT with a shorter trapping time resulting in hotter ions. Additionally, voltage settings to increase the kinetic energy of the ions just prior to their entry into COAT can significantly increase the temperature of the ions. In the case of ozonide, pathways (2) and (3) are significantly increased along with an increase in spectral congestion for pathway (1). This demonstrates an easy way to exert control over the ion temperature to examine the effects of internal excitation on dissociation dynamics and thermally activated processes.

4.4 Summary

The addition of COAT to the PPC spectrometer enables the preparation of colder anions than achievable with a supersonic expansion alone as well as the preparation of collisionally heated ions in a controlled manner. The cooling is demonstrated through the

elimination of the photodissociation/autodetachment channel (2) $O_3^- + h\nu \rightarrow O_2^-(^2\Pi_g, v>4) + O(^3P)$ channel and heating is demonstrated through enhancement of both channels (2) and (3) $O_3^- + h\nu \rightarrow O^-(^2P) + O_2(^1\Delta_g)$ as well as the appearance of hot bands in the photoelectron spectrum for channel (1), photodetachment forming stable O_3. Most importantly, COAT has demonstrated the ability to influence the dissociation dynamics of O_3^-. The ability to cool precursor ions to their vibrational ground states will be invaluable in future laser excitation experiments where the effects of direct infrared excitation of specific modes will be examined. Additionally, the ability to heat ions through collisional excitation can provide an approach for examination of thermally activated processes, providing increased flexibility in PPC spectroscopy.

Acknowledgements

We acknowledge helpful discussions with R. Otto and R.D. Thomas. KGL acknowledges partial support by a grant from the United States-Israel Binational Science Foundation (BSF), Jerusalem, Israel. This material is based on work supported by the U.S. Department of Energy, Office of Science, and Office of Basic Energy Sciences under award number DE-FG03-98ER14879.

Chapter 4 is a manuscript in preparation with authors Shen, B.; Lunny, K.; Benitez, Y; Continetti, R with the working title Photoelectron-photofragment coincidence spectroscopy with ions prepared in a cryogenic octopole accumulation trap. The dissertation author is the primary author and the dissertation advisor is the corresponding author.

4.5 References:

1. Johnson, C.; Otto, R.; Continetti, R., Spectroscopy and dynamics of the HOCO radical: insights into the OH + CO -> H + CO_2 reaction. *Physical Chemistry Chemical Physics* **2014,** *16* (36), 19091-19105.

2. Otto, R.; Ma, J.; Ray, A.; Daluz, J.; Li, J.; Guo, H.; Continetti, R., Imaging Dynamics on the F + H_2O -> HF + OH Potential Energy Surfaces from Wells to Barriers. *Science* **2014,** *343* (6169), 396-399.

3. Corderman, R.; Lineberger, W., Negative-ion spectroscopy. *Annual Review of Physical Chemistry* **1979,** *30*, 347-378.

4. Hock, C.; Kim, J.; Weichman, M.; Yacovitch, T.; Neumark, D., Slow photoelectron velocity-map imaging spectroscopy of cold negative ions. *Journal of Chemical Physics* **2012,** *137* (24).

5. Boyarkin, O.; Kopysov, V., Cryogenically Cooled Octupole Ion Trap for Spectroscopy of Biomolecular Ions. *Review of Scientific Instruments* **2014,** *85* (3).

6. Smalley, R.; Wharton, L.; Levy, D., Molecular Optical Spectroscopy With Supersonic Beams and Jets. *Accounts of Chemical Research* **1977,** *10* (4), 139-145.

7. Sanz, M.; McCarthy, M.; Thaddeus, P., Vibrational Excitation and Relaxation of Five Polyatomic Molecules in an Electrical Discharge. *Journal of Chemical Physics* **2005,** *122* (19).

8. Shen, B.; Poad, B.; Continetti, R., Photoelectron-Photofragment Coincidence Studies of the tert-Butoxide Anion $(CH3)_3CO^-$, the Carbanion Isomer $(CH_3)_2CH_2COH^-$, and Corresponding Radicals. *Journal of Physical Chemistry a* **2014,** *118* (44), 10223-10232.

9. Johnson, C. J.; Shen, B. B.; Poad, B. L. J.; Continetti, R. E., Photoelectron-Photofragment Coincidence Spectroscopy in a Cryogenically Cooled Linear Electrostatic Ion Beam Trap. *Review of Scientific Instruments* **2011,** *82* (10), 105105.

10. Stert, V.; Radloff, W.; Schulz, C.; Hertel, I., Ultrafast Photoelectron Spectroscopy: Femtosecond Pump-Probe Coincidence Detection of Ammonia Cluster Ions and Electrons. *European Physical Journal D* **1999,** *5* (1), 97-106.

11. Continetti, R., Coincidence spectroscopy. *Annual Review of Physical Chemistry* **2001,** *52*, 165-+.

12. Gerlich, D., Ion-Neutral Collisions in a 22-Pole Trap at Very-Low Energies. *Physica Scripta* **1995,** *T59*, 256-263.

13. Jasik, J.; Zabka, J.; Roithova, J.; Gerlich, D., Infrared Spectroscopy of Trapped Molecular Dications Below 4 K. *International Journal of Mass Spectrometry* **2013,** *354*, 204-210.

14. Redwine, J.; Davis, Z.; Burke, N.; Oglesbee, R.; McLuckey, S.; Zwier, T., A novel Ion Trap Based Tandem Mass Spectrometer for the Spectroscopic Study of Cold Gas Phase Polyatomic Ions. *International Journal of Mass Spectrometry* **2013,** *348*, 9-14.

15. Allan, M.; Asmis, K.; Popovic, D.; Stepanovic, M.; Mason, N.; Davies, J., Resonances in Collisions of Low-Energy Electrons With Ozone: Experimental Elastic and Vibrationally Inelastic Differential Cross Sections and Dissociative Attachment Spectra. *Journal of Physics B-Atomic Molecular and Optical Physics* **1996,** *29* (20), 4727-4747.

16. Matejcik, S.; Kiendler, A.; Stampfli, P.; Stamatovic, A.; Mark, T., Vibrationally Resolved Electron Attachment to Oxygen clusters. *Physical Review Letters* **1996,** *77* (18), 3771-3774.

17. Goebbert, D.; Sanov, A., Photodetachment, Photofragmentation, and Fragment Autodetachment of $[O_{2n}(H_2O)_m]^-$ clusters: Core-anion Structures and Fragment Energy Partitioning. *Journal of Chemical Physics* **2009,** *131* (10).

18. Nestmann, B.; Kumar, S.; Peyerimhoff, S., Contribution of Feshbach Resonance to the 1.3-eV Dissociative-Electron-Attachment Cross Section of Ozone. *Physical Review a* **2005,** *71* (1).

19. Shen, B.; Benitez, Y.; Lunny, K.; Continetti, R., Internal Energy Dependence of the Photodissociation Dynamics of O_3^- Using Cryogenic Photoelectron-Photofragment Coincidence Spectroscopy. *Journal of Chemical Physics* **2017,** *147* (9).

20. Novick, S.; Engelking, P.; Jones, P.; Futrell, J.; WC, L., Laser Photoelectron, Photodetachment, and Photodestruction Spectra of O_3^-. *Journal of Chemical Physics* **1979,** *70* (6), 2652-2662.

21. Arnold, D.; Xu, C.; Kim, E.; neumark, D., Study of Low-Lying Electronic States of Ozone by Anion Photoelectron-Spectroscopy of O_3^-. *Journal of Chemical Physics* **1994,** *101* (2), 912-922.

22. Rangwala, S.; Kumar, S.; Krishnakumar, E.; Mason, N., Cross Sections for the Dissociative Electron Attachment to Ozone. *Journal of Physics B-Atomic Molecular and Optical Physics* **1999,** *32* (15), 3795-3804.

23. Ervin, K.; Anusiewicz, W.; Skurski, P.; Simons, J.; Lineberger, W., The only Stable State of O_2^- is the X (2)Pi(g) Ground State and it (still!) has an Adiabatic Electron Detachment Energy of 0.45 eV. *Journal of Physical Chemistry a* **2003,** *107* (41), 8521-8529.

24. Cui, Q.; Morokuma, K., Ab Initio Studies on the Electronic Excited States and Photodissociation of O_3^- Anion. *Journal of Chemical Physics* **1998,** *108* (18), 7684-7694.

25. Bowen, M. S.; Continetti, R. E., Photodetachment Imaging Study of the Vinoxide Anion. *Journal of Physical Chemistry a* **2004,** *108* (39), 7827-7831.

26. Wiley, W.; McLaren, I., Time-of-flight Mass Spectrometer With Improved Resolution. *Review of Scientific Instruments* **1955,** *26* (12), 1150-1157.

27. Otto, R.; Xie, J.; Brox, J.; Trippel, S.; Stei, M.; Best, T.; Siebert, M.; Hase, W.; Wester, R., Reaction Dynamics of Temperature-Variable Anion Water Clusters Studied With Crossed Beams and by Direct Dynamics. *Faraday Discussions* **2012,** *157*, 41-57.

28. Gerlich, D., Inhomogeneous RF-fields - a Versatile Tool for the Study of Processes with Slow Ions. *Advances in Chemical Physics* **1992,** *82*, 1-176.

29. Wester, R., Radiofrequency Multipole Traps: Tools for Spectroscopy and Dynamics of Cold Molecular Ions. *Journal of Physics B-Atomic Molecular and Optical Physics* **2009,** *42* (15).

30. Jones, R.; Anderson, S., Simplified Radio-Frequency Generator for Driving Ion Guides, Traps, and Other Capacitive Loads. *Review of Scientific Instruments* **2000,** *71* (11), 4335-4337.

31. Jones, R.; Gerlich, D.; Anderson, S., Simple Radio-Frequency Power Source for Ion Guides and Ion Traps. *Review of Scientific Instruments* **1997,** *68* (9), 3357-3362.

32. D. Gerlich, G. J., U. Mueck; Person, U. Schnelles Ventil zur Erzeugung Sehr Kurzer Gasimpulse. http://www.tu-chemnitz.de/physik/ION/Technology.

33. Garner, M. C.; Hanold, K. A.; Resat, M. S.; Continetti, R. E., Stability and Dissociation Dynamics of the Low-Lying Excited States of Ozone. *Journal of Physical Chemistry a* **1997,** *101* (36), 6577-6582.

34. Mann, J.; Troyer, M.; Jarrold, C., Photoelectron Imaging and Photodissociation of Ozonide in O-3(-)center dot(O-2)(n) (n=1-4) clusters. *Journal of Chemical Physics* **2015,** *142* (12).

35. Moriwaki, Y.; Tachikawa, M.; Maeno, Y.; Shimizu, T., Collision Cooling of Ions Stored in Quadrupole Radiofrequncy Trap. *Japanese Journal of Applied Physics Part 2-Letters & Express Letters* **1992,** *31* (11B), L1640-L1643.

36. Moriwaki, Y.; Tachikawa, M.; Shimizu, T., Dependence of Temperature of Collision-Cooled Ions Stored in an RF Trap on Trapping Parameters. *Japanese Journal of Applied Physics Part 1-Regular Papers Short Notes & Review Papers* **1996,** *35* (2A), 757-760.

37. Wang, X.; Wang, L., Development of a Low-Temperature Photoelectron Spectroscopy Instrument Using an Electrospray Ion Source and a Cryogenically Controlled Ion Trap. *Review of Scientific Instruments* **2008,** *79* (7).

38. Kamrath, M.; Garand, E.; Jordan, P.; Leavitt, C.; Wolk, A.; Van Stipdonk, M.; Miller, S.; Johnson, M., Vibrational Characterization of Simple Peptides Using Cryogenic Infrared Photodissociation of H-2-Tagged, Mass-Selected Ions. *Journal of the American Chemical Society* **2011,** *133* (16), 6440-6448.

39. Ervin, K.; Ho, J.; lineberger, W., Ultraviolet photoelectron-spectrum of NO_2^-. *Journal of Physical Chemistry* **1988,** *92* (19), 5405-5412.

40. Frisch, M. J.; Trucks, G. W.; Schlegel, H. B.; Scuseria, G. E.; Robb, M. A.; Cheeseman, J. R.; Montgomery, J., J. A.; Vreven, T.; Kudin, K. N.; Burant, J. C.; al., e. *Gaussian 03, Revision B.04*, Gaussian, Inc.: Wallingford, CT, 2004.

41. Liang, J.; Zheng, H.; Zhang, X.; Li, R.; Cui, Z., Franck-Condon Simulation of Photoelectron Spectroscopy of O-3: Including Duschinsky effects. *Journal of Molecular Structure-Theochem* **2007,** *814* (1-3), 99-103.

42. Allan, M.; Asmis, K.; Popovic, D.; Stepanovic, M.; Mason, N.; Davies, J., Production of Vibrationally Autodetaching O_2^- in Low-Energy Electron Impact on Ozone. *Journal of Physics B-Atomic Molecular and Optical Physics* **1996,** *29* (15), 3487-3495.

Chapter 5: Internal Energy Dependence of the Photodissociation Dynamics of O_3^- using Cryogenic Photoelectron-Photofragment Coincidence Spectroscopy

5.1 Introduction

Due to its role in both the stratosphere and D region of the ionosphere,[1-3] there continues to be significant interest in the photochemistry of the ozonide anion, O_3^-. Over the last 40 years a number of studies have examined the photodetachment and photodissociation of O_3^-, with the most recent work by Jarrold and co-workers reporting photoelectron spectra of O_3^- at a photon energy E_{hv} = 3.49 eV revealing three competing processes: direct photodetachment to $O_3 + e^-$, photodissociation to $O^- + O_2$ and photodissociation to $O + O_2^-$. A striking result of that work was the observation of a strong autodetachment signal originating from fragment $O_2^-(v'' \geq 4) \rightarrow O_2 + e^-$, not previously observed in photodetachment studies at other wavelengths.[4] In the present work, we examine the photodestruction of O_3^- at E_{hv} = 3.20 eV using photoelectron-photofragment coincidence (PPC) spectroscopy with a new cryogenic ion trap to thermalize the parent anions at low temperatures. The coincidence experiments reported here provide a kinematically complete picture of the dynamics of the photodissociation and photodetachment processes at a photon energy where all three are competitive, and at the threshold for photodissociation followed by vibrational autodetachment of vibrationally excited O_2^-. This is achieved through photoexcitation of both cold and vibrationally excited O_3^-, providing new insights into the role played by vibrational excitation carried over from the parent anion in coupling of the excited states to the

dissociation reaction coordinate. It is found that the vibrational autodetachment pathway is promoted by unrelaxed vibrational excitation in the parent O_3^- anion and can be eliminated using cryogenic buffer gas cooling. These results and other insights into the energy partitioning and product channels in photodissociation will be discussed in the context of previous studies of the photophysics of O_3^- and studies of low-energy electron scattering by O_3.

There have been a number of previous studies of photoelectron, photodestruction, and photodissociation spectra for O_3^- and $O_3^-(H_2O)$ clusters over a range of photon energies. [5-13] The relevant pathways and energetics for photodestruction of O_3^- in the near UV are shown in Figure 1. A number of wavelength-dependent processes occur, including photodetachment yielding stable $O_3 + e^-$, dissociative photodetachment yielding $O(^3P) + O_2(^3\Sigma_g^-) + e^-$ products, as well as ionic photodissociation pathways. The photodissociation cross section measurements of Hiller and Vestal directly probed the energy range where concurrent photodissociation pathways producing $O^-(^2P)$ and $O_2^-(^2\Pi_g)$ occur.[8] They observed energy-dependent changes in the photodissociation branching ratios over a range of wavelengths from 380 nm ($E_{h\nu} = 3.26$ eV) to 650 nm ($E_{h\nu} = 1.91$ eV). At lower photon energies, from 1.9 eV to 2.4 eV, photodissociation yields the energetically allowed $O^-(^2P)$ products similar to a recent photodissociation study of $O_3^-(H_2O)$ clusters over the range of 2.0 - 2.9 eV.[13] This is also consistent with the measurements by Garner *et al.* of the kinetic energy release (KER) upon photodissociation of O_3^- at 523 nm ($E_{h\nu} = 2.37$ eV).[10] In that study, photoexcitation of ground state O_3^- synthesized by electron impact on O_2 was found to yield ground state

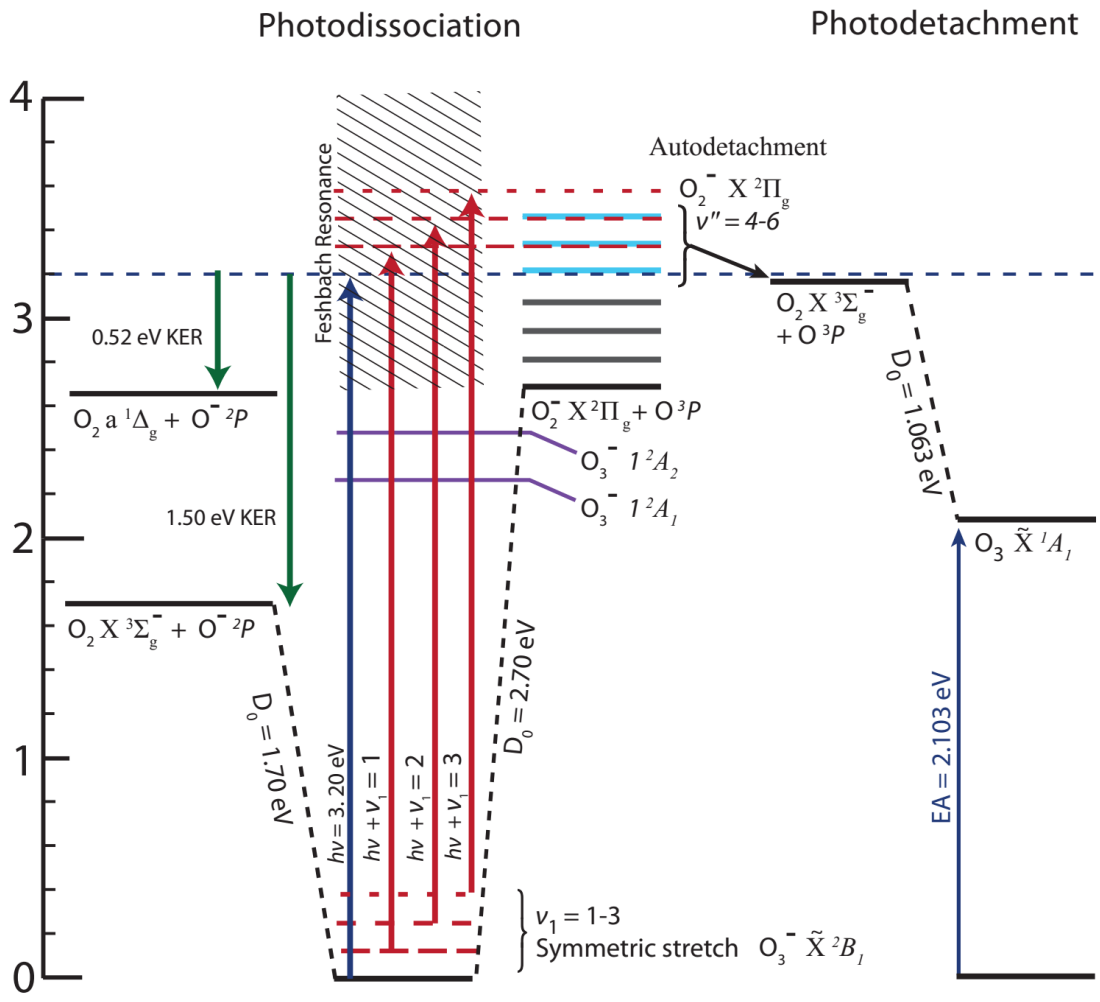

Figure 5.1 The energetics of available pathways relative to ground state O_3^- following photoabsorption at E_{hv} = 3.20 eV,[7, 9] including the Feshbach resonance identified in DEA studies,[22, 37] O_2 energetics,[38] and relevant excited states of O_3^-.[16] Dashed horizontal red lines indicate internal excitation in the anion resulting in opening the otherwise energetically inaccessible autodetachment channel.

$O^-(^2P) + O_2(^3\Sigma_g^-)$ products, but an alternate anion source (electron attachment to O_3) was found to produce a metastable excited state of the parent anion, $O_3^-(^2B_2)$, with photoexcitation yielding $O^-(^2P) + O_2(^1\Delta_g)$ photodissociation products.[10] Evidence for the metastable $O_3^-(^2B_2)$ excited state was also observed in ultrafast condensed phase studies of the photodissociation of O_3^-.[14] Prior to Jarrold's recent study,[4] Hiller and Vestal noted the opening of the $O_2^-(^2\Pi_g)$ photodissociation pathway above E_{hv} = 2.41 eV, with significant effects on the branching ratio at higher photon energies.[8] They also inferred from their data that photodissociation of ground state O_3 at photon energies above 2.75 eV results in excited state $O_2(^1\Delta_g) + O^-(^2P)$ products.

There have been relatively few theoretical studies focusing on the photodissociation of O_3^- over the years. Koch and coworkers carried out studies of the low-lying electronic states of O_3^- and calculated that the electronic transition moment for photoexcitation from $O_3^-(\tilde{X}^2B_1)$ to $O_3^-(^2A_2)$ is much larger than that for $O_3^-(^2A_1)$.[15] The most extensive study of the low-lying excited states and their potential dissociation pathways has been the work by Cui and Morokuma that characterized the four lowest electronic states of O_3^-. They also found a large transition moment for photoexcitation from $O_3^-(\tilde{X}^2B_1)$ to $O_3^-(^2A_2)$, and noted that the $^2B_1 \rightarrow {}^2A_1$ transition was 'vanishingly small'. As noted above, they also found that the first excited state, $O_3^-(^2B_2)$, is bound with a large $^2B_2 \rightarrow {}^2A_1$ transition moment, and showed that the $^2A_1$ excited state adiabatically correlates to both the $O_2(^1\Delta_g) + O^-(^2P)$ and $O(^3P) + O_2^-(^2\Pi)$ asymptotes.[16] This explained the experimental results of Garner *et al.* that inferred the long-lived $O_3^-(^2B_2)$ excited state underwent photodissociation to $O_2(^1\Delta_g) + O^-(^2P)$.[10] Cui and

Morokuma also found that the $^2A_2$ excited state diabatically correlates with the $O_2(^1\Delta_g)$ + $O^-(^2P)$ and predicted that dissociation by O^- elimination could yield both $O_2(^1\Delta_g)$ and $O_2(^3\Sigma_g^-)$ products. Since their study focused on the O^- elimination pathways, they did not examine in detail the correlation between the $^2A_2$ excited state and the $O(^3P)$ + $O_2^-(^2\Pi)$ asymptote and additionally noted that more theoretical work is needed to study the interaction of the electronic states leading to both $O_2(^1\Delta_g)$ and $O_2(^3\Sigma_g^-)$ channels.

The autodetachment of O_2^- from dissociation of an excited metastable anionic state has also been observed in electron scattering through the formation of temporary anions via capture of a low kinetic energy (KE_e) electron. Anionic resonances were first observed through dissociative electron attachment (DEA) experiments on O_3 with incident electrons of kinetic energy KE_e ~1.3 eV and were assigned to a Feshbach resonance in the $^2A_2$ state of O_3^-.[17, 18] DEA was found to occur by two competing dissociation pathways; O^- + O_2 and O + O_2^- in a process likely mediated by this Feshbach resonance.[19] Electron-molecule collision studies have reported a $^2A_2$ Feshbach resonance peaking at 1.3 eV above ground state O_3 using measurements of the cross sections for production of both O^- and O_2^- via DEA.[20-22] Rangwala and coworkers found that the peak production of O_2^- occurs at an incident KE_e ~ 1.15 eV, compared to the peak cross section for production of O^- at KE_e ~ 1.4 eV.[22] The total cross section for DEA (sum of both O^- and O_2^- dissociative channels) was reasonably reproduced by theoretical calculations for the $^2A_2$ Feshbach resonance of O_3^- with a theoretical maximum at KE_e=1.36 eV compared to the experimental maximum KE_e=1.33 eV.[18, 19] While the match between theoretical and experimental cross sections was good, the experimental

cross section was a lower limit since the measurements for O_2^- did not capture all of that pathway as a result of autodetachment: $O_2^-(v''>3) \rightarrow O_2 + e^-$. The autodetaching excited vibrational states of O_2^- have also been directly observed in studies of DEA of O_3 for incident electron kinetic energies KE_e = 1.2 – 2.0 eV and assigned to the decay of the $^2A_2$ Feshbach resonance.[23] At the lower incident electron energies, autodetachment from vibrationally excited $O_2^-(v''=4)$ only accesses the slightly exothermic ground state $O_2(v'=0) + e^-$ channel, with the difference in energy between the states carried away by the departing electron. Increasing the incident electron energy was found to result in opening of additional autodetachment channels with $O_2^-(v''=5,6)$ yielding neutral O_2 up to $v'=2$ as observed in vibrationally resolved KE_e spectra.

The current work reports a photoelectron-photofragment coincidence (PPC) spectroscopy study of both photodissociation and photodetachment of O_3^- at 388 nm ($E_{h\nu}$ = 3.20 eV). The effect of anion internal energy was examined by using a cryogenic radiofrequency (RF) ion trap[24, 25] to cool the parent anions to vibrational temperatures of <17 K. Ions stored in the RF ion trap can be thermalized via buffer gas cooling prior to injection into the PPC spectrometer. Experimentally changing the trapping conditions to promote collisional excitation and incomplete thermalization allows for exploring the effects of vibrational excitation of the precursor anion. PPC spectroscopy provides a direct measure of the energy partitioning in the photodissociation pathways operative at this photon energy by either autodetachment of $O_2^-(v''>4)$ or photodetachment of product O^- by a second photon. Figure 1 shows that photoexcitation at $E_{h\nu}$ = 3.20 eV is essentially the threshold for the onset of the photodissociation/autodetachment pathway involving

$O_2^-(v''>4)$. This makes for a sensitive experimental test of the effects of parent anion internal energy. A striking internal energy dependence of the branching ratio between the three competing photoinduced processes is observed, with the coldest parent O_3^- anions producing essentially none of the $O_2^-(v''>4)$ photodissociation/autodetachment pathway. These results will be discussed in the context of previous work on both photoexcitation and electron-impact preparation of the low-lying excited states of O_3^-.

5.2 Experimental

These experiments were carried out in a PPC spectrometer[26, 27] modified to incorporate a radio frequency (RF) cryogenic octopole accumulation trap (COAT) in the ion source based on a similar design used by Wester and coworkers.[24] A schematic of the new source configuration is shown in Figure 2. The precursor anion, O_3^-, was synthesized in a 10 Hz supersonic expansion of neat O_2 at 60 psig, acted upon by a coaxial pulsed discharge with a 1 keV electron beam counter-propagating down the expansion in region 1. O_3^- anions were then perpendicularly extracted using a Wiley-McLaren-style mass spectrometer.[28] The ions were focused and directed by a set of lenses and deflectors for injection into COAT, in regions 1 and 2, decelerating them to an energy of approximately 30 eV by floating COAT to improve trapping. To further facilitate trapping and cooling of the ions, a pulse of buffer gas generated with a Gerlich-type valve[29] was used to raise the pressure in the trap to ~10^{-2} mbar prior to ion injection. The buffer gases used were neat He as well as an 80:20 He/H_2 mixture, with the latter found to produce the best cooling. The entrance endcap electrode was switched open to allow ions to enter COAT for ~20 μs before closing to longitudinally trap the ions. Within COAT, the ions were

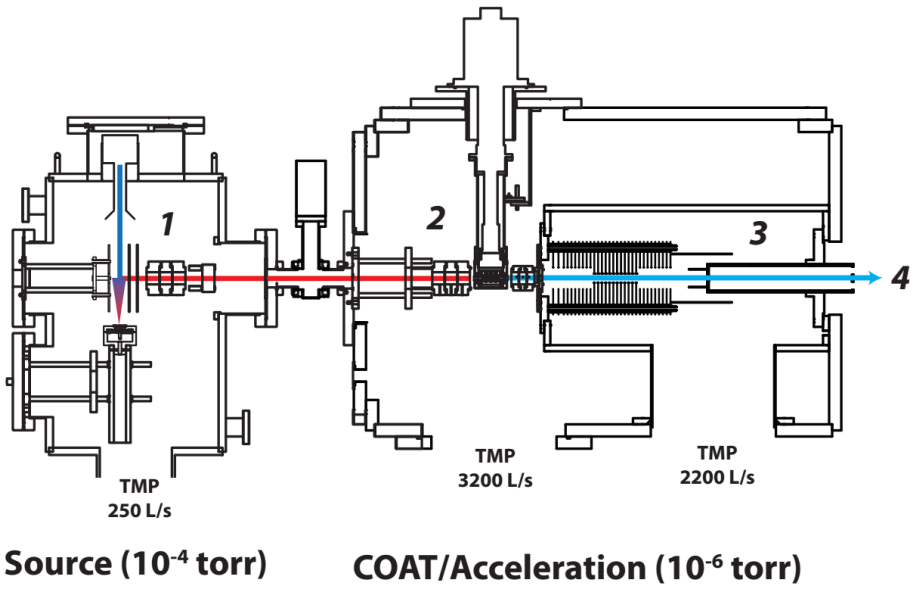

Figure 5.2 Overview of new ion source and RF COAT for thermalization of molecular anions on the front-end of the PPC spectrometer. Labeled sections are as follows: (1) Pulsed valve/discharge assembly with Wiley-McLaren-style extraction. (2) COAT. (3) Acceleration stack with potential switch. (4) TOF region and rest of the PPC spectrometer.

axially trapped in an octopole field with a 4 MHz, 320 volt peak-to-peak RF waveform produced by a home-built RF generator, described by Anderson and coworkers.[30, 31] The ions trapped in COAT were cooled by buffer gas collisions for times varying between 500 μs and 80 ms at temperatures ranging from 300 K to 17 K, as monitored with a silicon diode (LakeShore DT-471-CO) attached to the buffer gas shield of COAT. Cooling was achieved using a Sumitomo RDK-205D 4K Cryocooler cold head and is an upper limit, as H_2 freezes onto the electrodes of COAT indicating an inner COAT surface temperature of ~10 K. The experiments described here were carried out by loading and extracting ions on a 10 Hz time base.

After the designated trapping period, ions were extracted from COAT by switching the exit endcap to a small positive potential to extract the ions, and they were then directed into a differentially pumped chamber and accelerated to an energy of 7 keV, re-referenced to ground (region 3), and mass selected by time of flight for trapping within a cryogenically cooled electrostatic ion beam trap (EIBT) for 100 ms. This aspect of the experiment has been described in detail previously.[27] Within the EIBT, the ion packet is bunched and phase-locked to a 387.8 nm (E_{hv} = 3.20 eV) laser pulse from a Ti:Sapphire regenerative amplifier (Clark MXR CPA-2000; 1.1 ps pulse width) at a repetition rate of 1037 Hz using a field-programmable-gate-array-synced RF function generator (HP 3325). The oscillating ion packet interacted with the laser repeatedly over a 100 ms trapping period per experimental cycle, and the electron and neutral products were collected. The laser fluence was modulated by using a single 0.5 m focal length lens for high power density measurements versus collimation with a 2.5:1 telescope on the 3.5

mm-diameter doubled output beam of the Ti:Sapphire laser. The power density for the collimated laser was estimated to be $2x10^9$ W/cm^2 with the focused laser approximately 100x greater. Detached electrons were orthogonally extracted and mapped with electrostatic lenses to a time and position sensitive detector. The center-of-mass and electron kinetic energy (eKE) are determined by the time and position of electron impact. Optimal resolution is achieved through selection of electrons with minimal z-velocities perpendicular to the detection plane as determined by TOF by equatorially slicing the photoelectron spectra. This effect of slicing on the intensities in the photoelectron spectra was corrected for by dividing the sliced photoelectron spectrum by the energy-dependent acceptance function of the z-velocity slice.[32] Calibration of O_2^- photoelectron spectra as well as the O^- 2-photon events observed in the present experiments indicate ΔeKE/eKE ~4% full-width-at-half-maximum (FWHM) at 1.74 eV. After photodetachment, the resulting neutrals, no longer bound within the EIBT, exit and impinge on a multiparticle time-and position-sensitive detector 1.3 m away from the laser interaction region, allowing determination of the product mass and kinetic energy release (KER). Calibration of this detector using the dissociative photodetachment of O_4^- indicates a resolution ΔKER/KER ~10% at 0.5 eV.[33]

5.3 Results

In this section, the photoelectron spectra and images will be presented that show signatures and internal energy dependencies of the three concurrent photophysical channels: (1) photodetachment $O_3^- + h\nu \rightarrow O_3 + e^-$, (2) photodissociation/autodetachment $O_3^- + h\nu \rightarrow O_2^-(^2\Pi_g) + O(^3P)$, and (3) photodissociation $O_3^- + h\nu \rightarrow O^-(^2P) + O_2(^1\Delta_g)$

followed by the photodetachment $O^-(^2P) + h\nu \rightarrow O(^3P)$ by a second photon. Then the dynamics of the photodissociation channels occurring in (2) and (3) will be examined using the PPC spectrum to examine the eKE-selected KER distributions, allowing assignment of the $O^-(^2P) + O_2(^1\Delta_g)$ photodissociation pathway as well as evidence for state-resolved predissociation of $O_3^-(^2A_2) \rightarrow O_2^-(^2\Pi_g, v''=4) + O(^3P) \rightarrow O_2(^3\Sigma_g^-, v'=0) + O(^3P) + e^-$.

5.3.1 O_3^- Photodetachment channel

The dominant channel observed in the total photoelectron spectra (electrons in coincidence with both dissociative products *and* stable O_3) is the photodetachment (1) $O_3^- + h\nu \rightarrow O_3 + e^-$ yielding a structured photoelectron spectrum in the eKE range between 0.30 eV - 1.50 eV as shown in Figure 3. The upper panel shows the photoelectron spectrum at high laser fluence, with signal from both photodetachment channel (1) as well as significant sequential photodetachment of O^- photoproducts (channel (3), observed as the peak at eKE = 1.74 eV) and a structured signal at low eKE (0.0 to 0.4 eV) originating from sequential autodetachment of $O_2^-(v''<4)$ produced by channel (2). The middle and lower panel were recorded with the collimated laser beam, at much lower fluence, showing the expected significant decrease in the two photon events required to observe channel (3) and decreasing spectral congestion to more clearly observe hot bands in the photodetachment to $O_3 + e^-$. The decrease in spectral congestion is most clearly observed by comparing the cold spectrum at similar conditions with the focused laser (top panel, black line) and collimated laser (bottom panel, black line) as the spectra should be nearly identical with exception of the 2-photon events. The structured

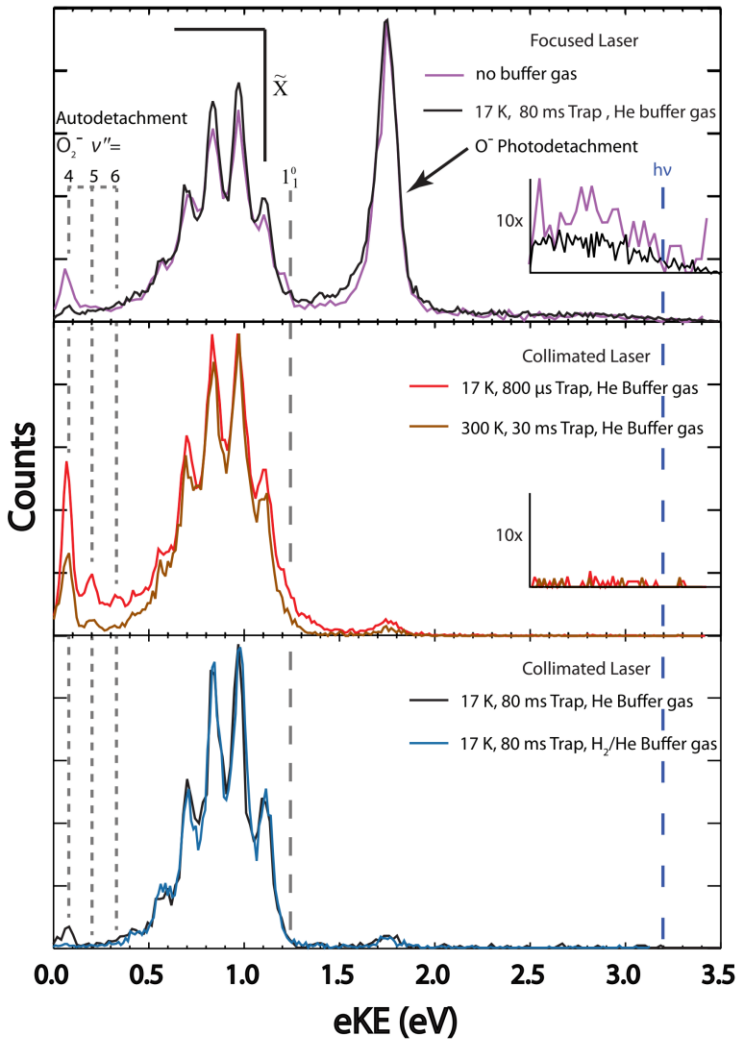

Figure 5.3 The total photoelectron spectrum for O_3^- produced with the COAT ion source under different temperatures, trap times, and laser configurations is shown. The top panel shows COAT with the laser focused using a single lens with neat He buffer gas cooling (black), and without buffer gas cooling (purple). The middle panel shows the photoelectron spectrum with the collimated laser beam with neat He buffer gas at 300 K, 30 ms trapping time (brown) and 17 K, with 800 µs trap time (red). The bottom panel shows the photoelectron spectrum with the collimated laser beam at 17 K with 80 ms trapping time with neat helium buffer gas (black) and He/H_2 buffer gas (blue). See text for discussion of levels of anion internal excitation under these varied trapping conditions.

photoelectron signal in the eKE = 0.40 – 1.50 eV range is consistent with the electron affinity (EA) of O_3 previously determined to be 2.10 eV and a Franck-Condon vibrational progression in the totally symmetric ν_1 and ν_2 modes of the $O_3(\tilde{X}^1A_1)$ ground state.[4, 7, 9, 11] The dominant progression is the ν_1 symmetric stretch populating O_3 vibrational states from ν_1=0 to ν_1=5. Adjustment of the COAT temperature and trapping time allows control of the internal excitation in precursor anions as demonstrated by the 1_1^0 hot bands appearing on the high-energy side of the stable O_3 signal at eKE = 1.22 eV. The temperatures noted are the measured temperatures of COAT with their relation to the ion temperature is dependent on the duration of trapping to allow for the thermalization of the ions in collisions with the buffer gas. Even with longer trapping times there may be non-Boltzmann distributions of excitation in high-frequency vibrations. The hot bands are notably present in both the no buffer gas conditions (top panel, purple line), and the 300 K, 30 ms COAT trap time He buffer gas conditions (middle panel, brown line), as well as the 17 K, 800 μs COAT trap time He buffer gas conditions (middle panel, red line). The 1_1^0 hot band is observed to be significantly reduced at 17 K with He and He/H_2 buffer gas and 80 ms trapping (bottom panel, black and blue lines, respectively) compared to the no buffer gas experiment (top panel, purple line). Incomplete thermalization in combination with collisional heating upon entry into COAT is observed for the short 800 μs COAT trap time (middle panel, red line) resulting in higher internal excitation of O_3^- compared to the 300 K spectrum despite the 17 K COAT temperature. It is also worth noting the increase in spectral congestion when thermalizing to 300 K, likely due to sequence bands from populating ν_2''=1 and ν_3''=1 as well as rotational excitation in the parent anion. As

discussed below, the coldest anions are produced with 80 ms trapping with a He/H_2 buffer gas mix, as shown in the bottom panel of Figure 3 (blue line).

5.3.2 $O_2^-(^2\Pi_g)$ + $O(^3P)$ Channel

The presence of the photodissociation channel (2) $O_3^- + h\nu \rightarrow O_2^-(^2\Pi_g, v''>4) + O(^3P)$ is revealed by the peaks from the autodetachment of vibrationally excited O_2^- in the photoelectron spectra. Specifically, the peaks at low eKE in Figure 3, with positions summarized in Table 5.2, are a signature of the vibrational autodetachment of $O_2(v'=0) + e^- \leftarrow O_2^-(v'' = 4,5 \text{ and } 6)$.[4] At $E_{h\nu} = 3.20$ eV, access to $O_2^-(v'' = 4,5,6)$ is energetically forbidden without vibrational excitation of O_3^-, as shown in the energetics diagram in Figure 1. The spectrally resolved autodetachment peaks are a more sensitive probe of parent anion excitation than the unresolved hot bands observed in the photodetachment channel (1). The striking effect of parent anion cooling on the autodetachment pathway is most dramatically seen in the coldest spectrum shown in blue the bottom panel of Figure 3, recorded with an 80:20 mixture of He/H_2 gas and 80 ms thermalization. The empirical efficacy of He/H_2 gas mixtures for anion collisional cooling, first reported by Wang and co-workers in photoelectron spectroscopy studies,[34] has been found to be effective in other systems,[25, 35] and is seen to be very effective for O_3^- as well. Thermalizing the precursor anions to lower temperatures is observed to have a dramatic effect, leading to elimination of the autodetachment channel.

This difference between hot and cold precursor anions is also clear in the photoelectron images presented in Figure 4, comparing images for cold conditions (17 K, 80 ms trap time with He buffer gas cooling) and with a focused laser (A) as well as hot

Table 5.1. Peak positions for autodetachment from O_2^- ($v'' \geq 4$)

Description	eKE (eV)
$O_2^-(v''=4) \rightarrow O_2(v'=0) + e^-$	0.07
$O_2^-(v''=5) \rightarrow O_2(v'=0) + e^-$	0.19
$O_2^-(v''=6) \rightarrow O_2(v'=0) + e^-$	0.32
$O_2^-(v''=7) \rightarrow O_2(v'=0) + e^-$	0.41[a]

[a] Expected position from Ref. [42]

conditions (300 K, 30 ms trap time with He buffer gas cooling) with a collimated laser (B) and the coldest anion conditions (17 K, 80 ms trap time with He/H_2 buffer gas cooling) with the collimated laser (C). In image (B), the autodetachment features are prominent in the center of the image. The electron angular distribution for the autodetachment features is characteristically isotropic. Upon cooling, the autodetachment channel is significantly reduced resulting in the stable O_3 channel dominating the image, as seen in (A) and (C). These results show that the autodetachment channel is effectively eliminated with cryogenic buffer-gas cooling at T < 17 K.

Based on the results of DEA studies,[21-23] it is expected that even at lower excitation energies the $^2A_2$ Feshbach resonance will continue to mediate dissociation to channel (2) $O(^3P) + O_2^-(v''<4)$. The broad baseline congestion extending out to near the photon energy in the high fluence data in the upper panel of Figure 3 is consistent with photodetachment of stable $O_2^-(v''<4)$ from this channel by a second photon. The fact that the eKE from the 2-photon photodetachment of O_2^- extends up to the photon energy indicates that even with cold O_3^-, significant energy is still partitioned into the internal excitation of the O_2^- fragment (the O_2^- (v=3) + hν → O_2(v=0) + e- photodetachment hot band would appear only 0.06 eV below the photon energy). Reduction of the laser fluence leads to a disappearance of this feature as shown in the bottom frame of Figure 3. These effects are also observed in the images in Figure 4 showing that high eKE events at large radial distance from the center are suppressed in the low-fluence images (B) and (C) compared to image (A).

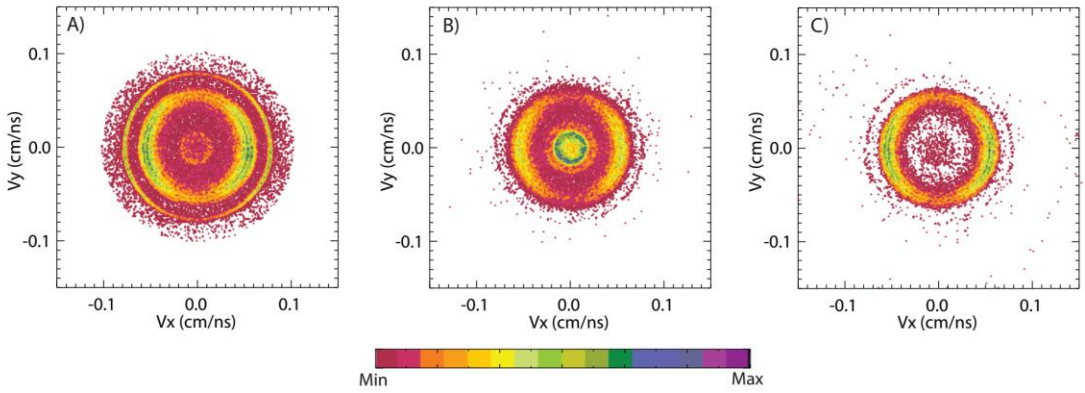

Figure 5.4 Photoelectron images for the photodetachment of O_3^- at (A) 17 K with He buffer gas and 80 ms COAT trapping with focused laser, (B) 17 K with He buffer gas and 800 μs COAT trapping with collimated laser, and (C) 17 K with He/H_2 buffer gas and 80 ms COAT trapping with collimated laser.

PPC measurements provide kinematically complete information on events that lead to a photoelectron and momentum-matched neutral products, so it is possible to gain further insights into this photodissociation process. In particular, by selecting photoelectrons corresponding to the autodetachment features for $O_2^-(v''= 4, 5$ and $6)$ observed in the PPC spectrum, the corresponding KER distribution among the neutral products can be examined. The autodetachment region of the PPC spectrum shown in Figure 5 shows the correlation between eKE along the y-axis and KER along the x-axis under hot source conditions characterized by short trapping times (17 K, 800 μs COAT trap time with He buffer gas). The white diagonal lines represent the expected maximum kinetic energy limits assuming 1 (solid line), 2 (dashed line), 3 (dot-dashed line), and 4 (dotted line) quanta of excitation in the symmetric stretch vibration of O_3^-, in order of increasing energy from the origin using the vibrational energies shown in Table 5.2 in the harmonic approximation. The autodetachment features appear as horizontal bands in the spectrum, since the eKE is determined by the energy difference between the initial vibrational state of $O_2^-(v'')$ and the final vibrational state $O_2(v'=0)$. Given the significant centrifugal barrier for autodetachment of O_2^-, maximum Δv processes are favored as they produce the highest eKE autodetached electrons.[36] The extent of the KER for the autodetachment $O_2(v'=0) + e^- \leftarrow O_2^-(v''=4)$ shows that the parent O_3^- has the equivalent of 1 - 2 quanta of symmetric stretch excitation, with the excess energy partitioned to KER in dissociation producing the specific $O(^2P) + O_2^-(v''=4)$ final state. Similarly, the $O_2(v'=0) + e^- \leftarrow O_2^-(v''=5)$ channel requires 2 - 3 quanta of excitation in O_3^-. The weak $O_2(v'=0) + e^- \leftarrow O_2^-(v''=6)$ autodetachment peak at eKE=0.32 eV in the PPC spectrum in Figure 5 requires internal energy on the order of 3 quanta of symmetric stretch excitation.

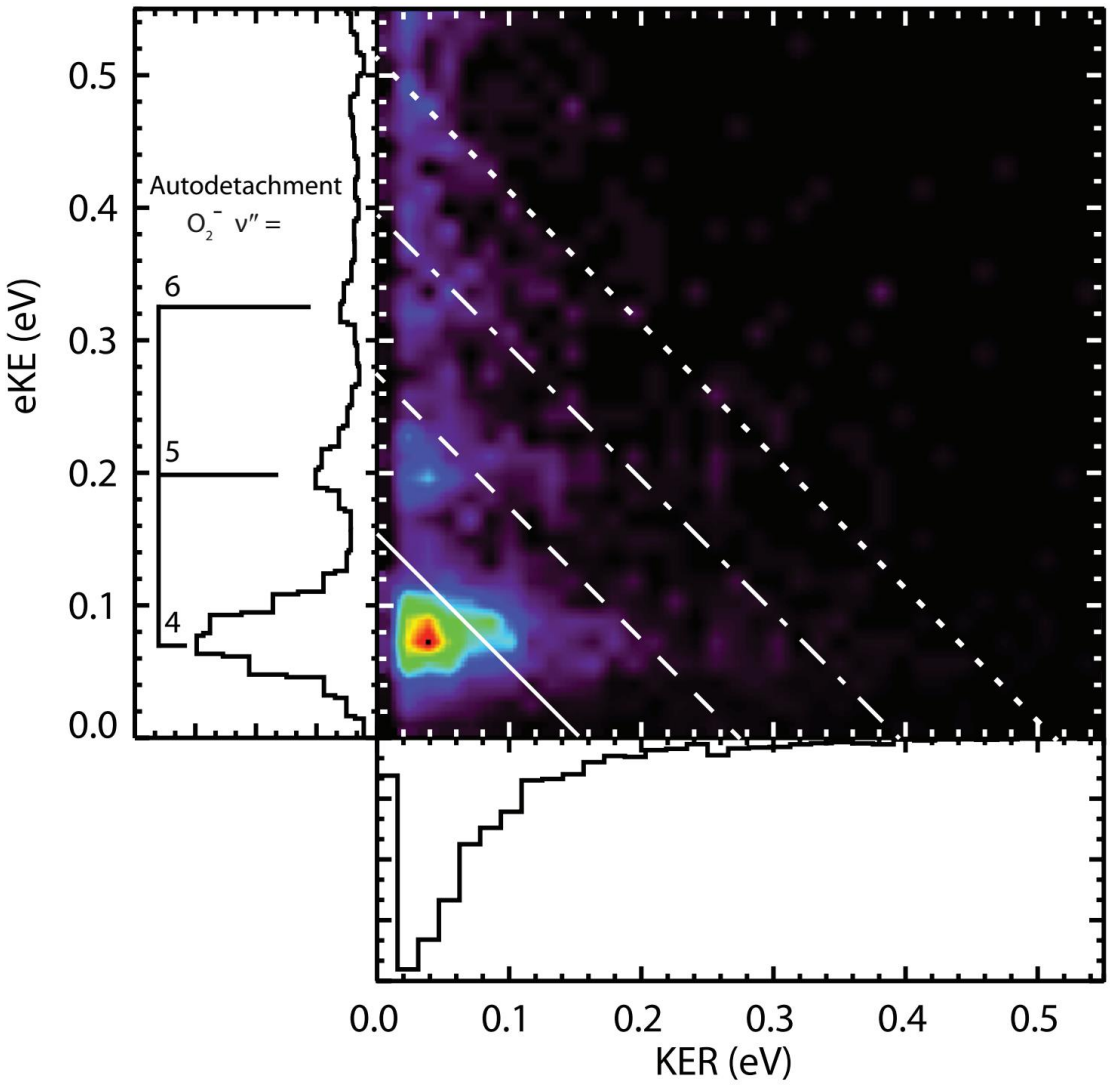

Figure 5.5 PPC spectrum in the energy range where $O_2^-(v\geq4)$ autodetachment features are observed for the photodissociation of O_3^- with a collimated laser beam and 800 μs COAT trapping. The diagonal lines indicate the maximum total energy available assuming 1 (solid line), 2 (dashed line), 3 (dot-dashed line) and 4 (dotted line) quanta of excitation in the symmetric stretch of the precursor anion.

Table 5.2. Vibrational modes of $O_3^- \tilde{X}\ ^2B_1$

Mode	Description	Energy (eV)[9]
ν_1 (100)	Symmetric Stretch	0.121 ± .006
ν_2 (010)	Bend	0.068 ± .006
ν_3 (001)	Asymmetric Stretch	0.109 ± .006

The events in the eKE = 0.4-0.5 eV range indicate the presence of some $O_2^-(v''=7)$ autodetachment and the equivalent of a fourth quantum of stretch excitation in O_3^-. There is no evidence observed for vibrational autodetachment sequence bands from the higher-lying O_2^- states yielding $O_2(v'=1)$ but some contribution cannot be ruled out as these were seen as weak shoulders degraded to lower eKE in the DEA experiments by Allan and coworkers.[23]

Further insights into the internal energy distribution in the parent O_3^- can be gained by examining the KER corresponding to autodetachment from $O_2^-(v''=4)$, integrated from $0 < eKE < 0.14$ eV in the PPC spectrum, shown in the top panel of Figure 6. The dominant feature is split at low KER, and the annotations on the spectrum show that the splitting is consistent with the expected KERs for dissociation of $O_3^-(010)$ and $O_3^-(001)$ intermediate states to the specific $O(^2P) + O_2^-(v''=4)$ channel that produces the autodetachment signal. The annotations indicate the expected KER_{MAX} assuming specified initial vibrational excitation in the precursor O_3^-, based on the expanded view of the energetics shown in Figure 7. These KER_{MAX} values are calculated using $KER_{MAX} = E_{hv} + E_{int}(O_3^-) - eKE - EA(O_3) - D_0(O_2+O)$, where E_{int} is the vibrational excitation of the precursor O_3^-. The third annotated weak feature is the KER_{MAX} assuming a combination band with one quantum in both the asymmetric and symmetric stretch ($O_3^-(101)$). The intensities suggest that bending and asymmetric stretch excitation in the anion strongly promote decay of the intermediate state into $O_2^-(v=4)$.

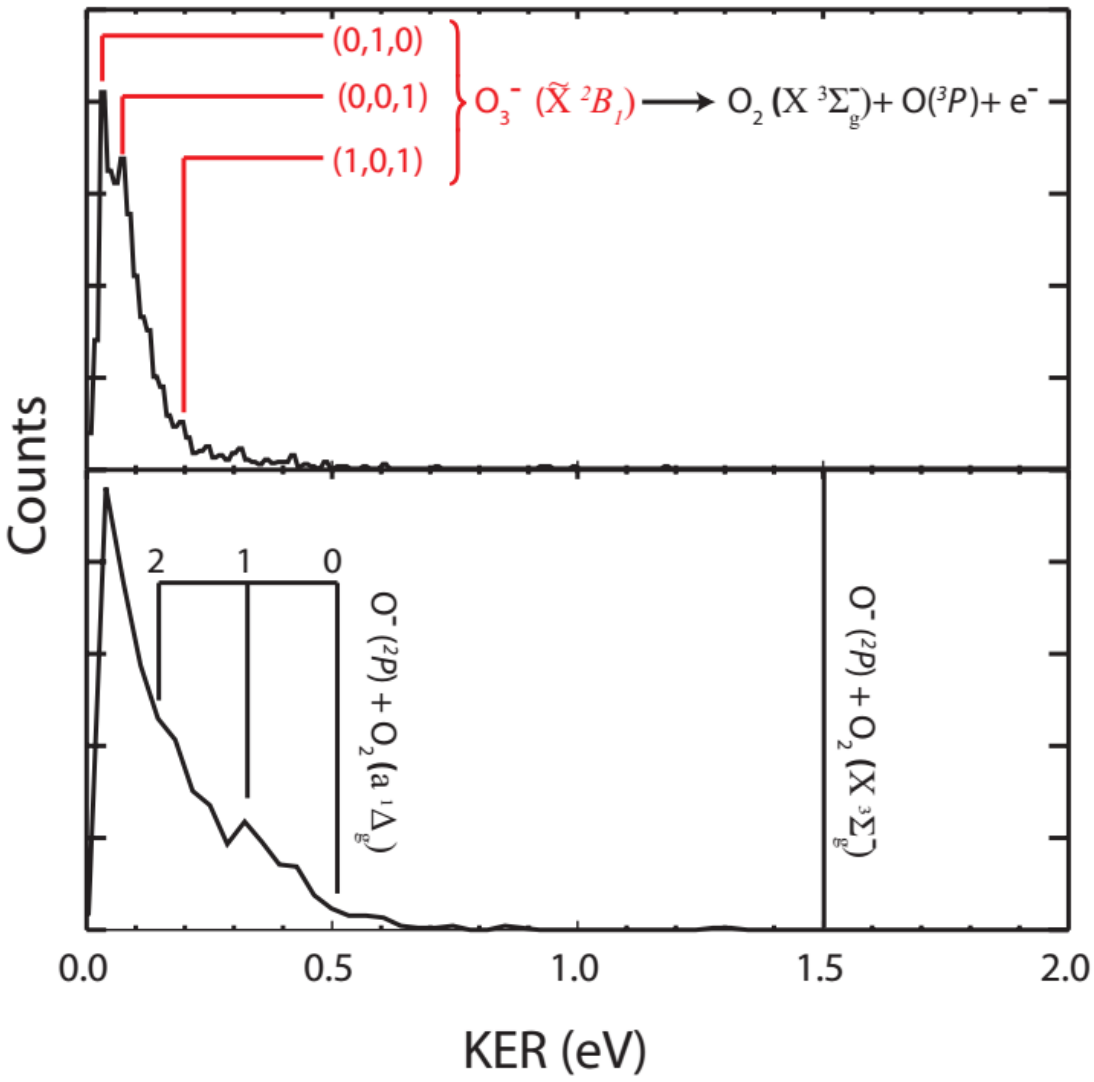

Figure 5.6. KER spectra generated from the PPC spectrum for the O + O_2^-(v=4) channel (top) and O_2 + O^- channel (bottom) are shown. These are generated by integrating the PPC spectrum over the ranges 0 < eKE < 0.14 (shown in Figure 5) and 1.5 < eKE < 2.0 eV (not shown), respectively. In the top panel, the vertical lines indicate the calculated KER_{MAX} value with excitation in the precursor anion in the indicated vibrational modes. The bottom panel shows the theoretical KER_{MAX} for photodissociation to the $O_2(^1\Delta_g)$ + $O^-(^2P)$ state with a vibrational comb indicating internal excitation in the O_2 product. The vertical line at 1.50 eV indicates the theoretical KER_{MAX} assuming photodissociation to $O_2(X^3\Sigma_g^-)$ + $O^-(^2P)$.

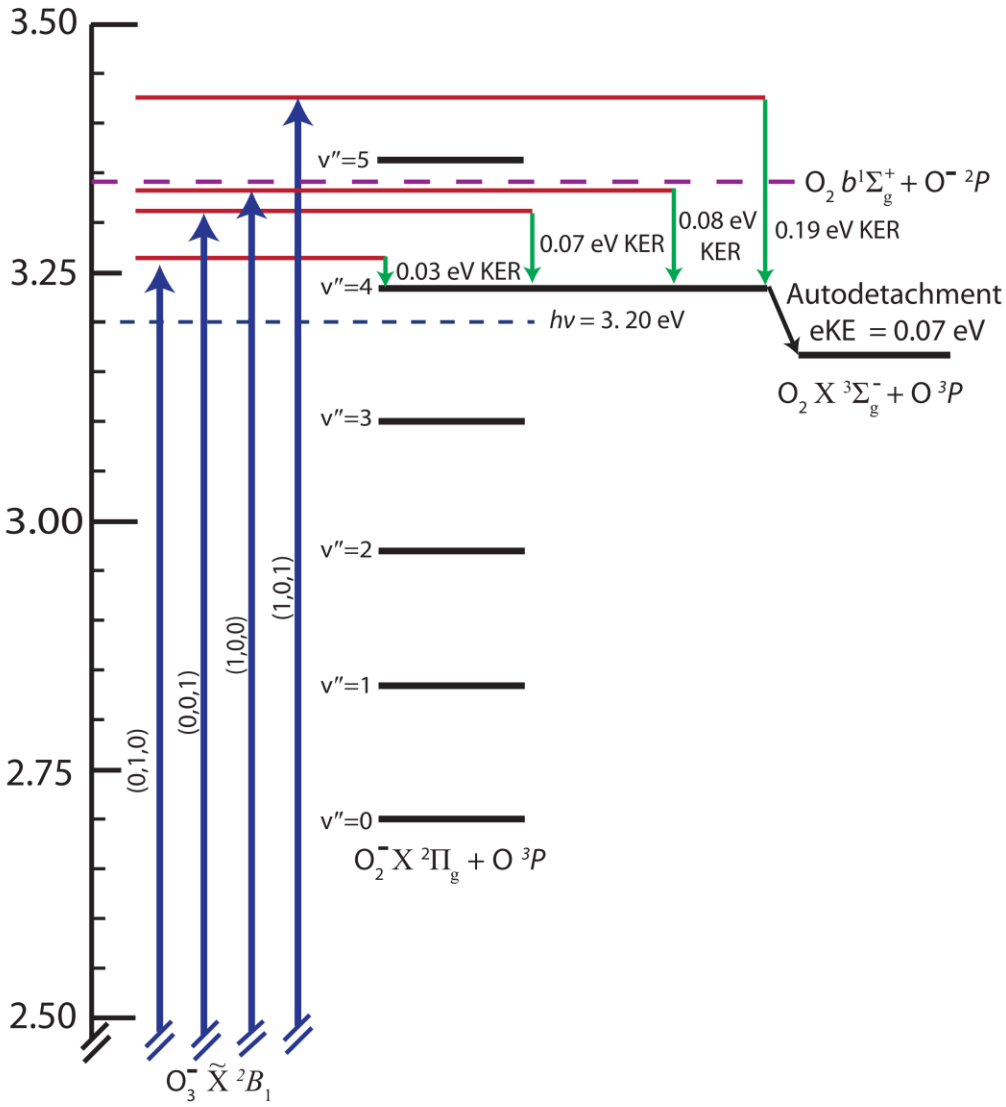

Figure 5.7. Energetics diagram relative to ground state O_3^- showing the energy partitioning to KER from dissociation of photoexcited O_3^- with the annotated vibrational excitation, concurrent with the state-specific autodetachment $O_2(v'=0) + e^- \leftarrow O_2^-(v''=4)$.

5.3.3 $O_2(^1\Delta_g) + O^-(^2P)$ Channel

The O^- photodissociation product is detected through a 2-photon process (3) yielding the peak at eKE=1.74 eV in the total photoelectron spectrum and the ring at large radius in the photoelectron images. The assignment of the peak is confirmed by laser fluence dependence as shown in Figures 3 and 4, with a significant reduction in the 2-photon O^- signal with the use of the collimated laser. The KER spectrum for this channel, determined by gating on the O^- pathway peaking at eKE=1.74 eV in the photelectron spectrum, is shown in the bottom panel of Figure 6. While dissociation to the $O_2(^3\Sigma_g^-) + O^-(^2P)$ and $O_2(^1\Delta_g) + O^-(^2P)$ channels are both accessible at $E_{h\nu}$ = 3.20 eV, the observed KER_{MAX}=0.60 eV is more consistent with the theoretical KER_{MAX}=0.52 eV for $O_2(^1\Delta_g) + O^-(^2P)$ products compared to the KER_{MAX}=1.5 eV calculated for $O_2(^3\Sigma_g^-) + O^-(^2P)$ products, confirming the inference by Hiller and Vestal that excited $O_2(^1\Delta_g)$ products would be observed at this photon energy. Additionally, photodissociation of ground state $O_3^-(\tilde{X}^2B_1)$ to $O_2(^3\Sigma_g^-) + O^-(^2P)$ at lower photon energies is known to yield a vibrationally structured KER.[10] The absence of any significant signal above KER=0.6 eV indicates that the excited state accessed does not dissociate to $O_2(^3\Sigma_g^-) + O^-(^2P)$. The vibrational comb indicates excitation in the O_2 product, with v=0 marking KER_{MAX} for this dissociative pathway. Evidence for a feature corresponding to O_2(v=1) is observed, with the KER distribution peaking towards ~0 eV indicating a preference for vibrational/rotational excitation in the product O_2. This is consistent with the O^- kinetic energy measured in DEA experiments by Allan and coworkers.[37]

5.4 Discussion

These measurements have shown that photodissociation of ground state O_3^- results in O_2^- ($^2\Pi_g$) + O(^{3}P) with a vibrationally mediated autodetachment channel as well as the $O_2(^1\Delta_g)$ + O^- (^{2}P) channel. DEA studies have attributed both the O_2^- and O^- pathways as a result of the $^2A_2$ excited state of O_3^-,[18, 19] however, previous photodissociation measurements on O_3^- have attributed the O^- pathway to the $^2A_1$ excited state of O_3^-.[8] Theoretical considerations for the photodissociation from ground state $O_3^-(\tilde{X}^2B_1)$ indicate that while both $^2A_2$ and $^2A_1$ are electric dipole-allowed by symmetry, only the $^2A_2$ excited state of O_3^- has a significant transition dipole moment according to the work of both Koch *et al.* and Cui and Morokuma.[15, 16] In addition, the observation of the O^- 2-photon peak in the eKE spectra (Figure 3) indicates that the electronic state mediating this dissociation process is short lived as the excited state must dissociate followed by photodetachment within a single laser pulse (~1.1 ps).[16] Theoretical lifetimes for the $^2A_1$ and $^2A_2$ Feshbach resonances when accessed via DEA were found to be 2.1 ps and 25 fs respectively.[18] If the lifetimes are similar when these states are accessed via photoexcitation, then this experiment should be less sensitive to dissociation of the $^2A_1$ state due to the short (1.1 ps) laser pulse width. While the $^2A_1$ state was accessed in previous experiments from the metastable $O_3^-(^2B_2)$ excited state,[10] the photoelectron spectra (Figure 3) and KER distribution (Figure 6) indicate that $O_3^-(^2B_2)$ was not produced in the present experiments. These considerations support assignment of the $^2A_2$ excited state as the source for both photodissociation channels.

The role of parent O_3^- vibrational excitation in the dissociation yielding the highly vibrationally excited O_2^- products in the autodetachment channel is of interest. This

dissociation has been discussed before,[5, 7, 10, 16, 21] and in general there are symmetric and asymmetric mechanisms. Symmetric dissociation proceeds by ejection of the central atom with the two terminal atoms eliminated as O_2 or O_2^-. The internuclear distance between the terminal O atoms is ~2.2 Å,[9] vastly different from O_2^-(1.35 ± 0.01 Å).[38] Assuming an impulsive model, direct photodissociation with the symmetric mechanism would be expected to yield highly vibrationally excited O_2^- with little rotational excitation as suggested by Walker and coworkers.[21] Isotopic labeling experiments on O_3, however, have found no evidence for a central atom elimination channel[39] and photodissociation experiments on NO_2^- have also not observed a corresponding N-atom channel consistent with central atom elimination[40] despite the similarities in the DEA dynamics of O_3 and NO_2.[41] This casts doubt on symmetric elimination being the source of the O_2^-. A second plausible mechanism is an asymmetric dissociation where a terminal O atom is ejected, either impulsively or in the predissociation of a metastable state. Since the O-O internuclear distance in O_3^- (1.36 ± 0.02 Å)[9] is similar to the O_2^- bond length, direct photodissociation to low vibrational levels in O_2^- with high rotational excitation would be expected in the impulsive dissociation. To explain the highly vibrationally excited O_2^- product, a charge-transfer mechanism has been proposed as a possible source of the observed O_2^- autodetachment,[4] similar to autodetachment of O_2^- observed in photofragmentation studies of O_4^-[33,42, 43] and $[O_{2n}(H_2O)_m]^-$ (n=2–4, m=0–3).[44] At E_{hv} = 3.20 eV, however, photodissociation to $O_2(b^1\Sigma_g^+)$ + $O^-(^2P)$ with subsequent charge transfer to form $O_2^-(^2\Pi)$ + $O(^3P)$ is energetically inaccessible (3.33 eV relative to $O_3^-(\tilde{X}\,^2B_1)$). The KER spectrum (top frame of Figure 6) shows autodetachment of $O_2^-(v''=4)$ originating from O_3^- in the (0,1,0) and (0,0,1) vibrational states, below the

energetic limit for the $O_2(b^1\Sigma_g^+)$ + $O^-(^2P)$ channel as shown in Figure 7. An alternative explanation comes from the theoretical study by Nestmann and coworkers which attribute the production of O_2^- in DEA measurements to the Feshbach resonance formed by the $^2A_2$ excited state.[18, 19] This state is calculated to have an average bond length of ~1.5 Å,[16] a large geometry change from $O_3^-(\tilde{X}^2B_1)$. Photoexcitation to this state would presumably be enhanced by parent vibrational excitation. The lifetime of the $^2A_2$ Feshbach resonances was calculated to be ~25 fs,[18, 19] on the order of the period of the vibrational modes of the excited state, with the subsequent fragmentation potentially leading to highly vibrationally excited O_2^- through asymmetric photodissociation.

The sensitivity of the autodetachment channel to O_3^- vibrational excitation infers a strong coupling of vibrational excitation within the $^2A_2$ excited state to highly vibrationally excited products. The expansion of the parent anion wavefunction upon vibrational excitation of O_3^- may lead to an increase in Franck-Condon overlap with the $^2A_2$ excited state. Similar dynamics have also been observed in the photodissociation of O_3 to $O(^1D)$ + $O_2(^1\Delta_g)$, where excitation of the antisymmetric mode of ozone resulted in an increased $O(^1D)$ production by two orders of magnitude due to Franck-Condon effects.[45, 46] Evidence for the role of vibrational excitation in the $^2A_2$ state on the dissociation is seen in the KER spectrum for the autodetachment channel shown in the top frame of Figure 6. Structure in the spectrum is consistent with bend and asymmetric stretching vibrations of O_3^- promoting the formation of the autodetaching $O_2^-(v''=4)$ product, with the symmetric stretch only observed in a weak combination band with the asymmetric stretch. Given the KER resolution in the experiment, we cannot rule out

unresolved contributions from symmetric stretch excitation. Asymmetric dissociation proceeds along the asymmetric stretch as the reaction coordinate, so strong coupling would be expected. The bending mode also plays an important role. Since the bond angle for the $^2A_2$ state is significantly different than that of the $^2B_1$ ground state,[9, 18,16] excitation of the bending mode in the electronic transition is expected. Additionally, any parent bending mode excitation would be expected to lead to a strong Franck-Condon enhancement. Theoretical calculations by Morokuma and coworkers indicate that the O-O-O bond angle plays a significant role governing the crossing between excited states.

The dynamics of the vertical transition to the $^2A_2$ state from ground state O_3^- resulting in $O^- + O_2(^1\Delta_g)$ requires further investigation. The theoretical calculations by Morokuma and coworkers indicate that dissociation of the $^2A_2$ state into $O^-(^2P)$ products could produce both $O_2(^1\Delta_g)$ and $O_2(^3\Sigma_g^-)$, however, only $O_2(^1\Delta_g)$ products are observed.[16] The study of Garner *et al.* at E_{hv} = 2.37 eV found evidence for photodissociation of the long-lived $O_3^-(^2B_2)$ metastable state to $O^-(^2P) + O_2(^1\Delta_g)$. In the present ion source there is no evidence for formation of this excited state. The fact that only $O_2(^1\Delta_g)$ products are observed from 3.20 eV photoexcitation to the $^2A_2$ state from ground state O_3^- while $O_2(^3\Sigma_g^-)$ products are observed from photodissociation of ground state O_3^- at lower photon energies[10] indicates a crossover to $O_2(^1\Delta_g)$ products rather than a simultaneous production of both $O_2(^1\Delta_g)$ and $O_2(^3\Sigma_g^-)$. The cross section measurements by Hiller and Vestal provide evidence that electronically excited $O_2(^1\Delta_g) + O^-(^2P)$ is produced as soon as it becomes energetically accessible,[8] which is essentially in resonance with the opening of the $O(^3P) + O_2^-(^2\Pi_g)$ channel 0.58 eV above ground state O_3. The observed

KER peaks near 0 eV for the $O^- + O_2(^1\Delta_g)$ pathway, indicating high internal excitation of $O_2(^1\Delta_g)$ in that photodissociation channel. The sharp rise towards 0 eV KER in channel (3), with limited evidence for vibrational state resolution, indicates a trend towards high rotational excitation in the $O_2(^1\Delta_g)$ products. This is evidence for an impulsive dissociation from a bent excited state, likely coupled with vibrational excitation since the bond length of $O_2(^1\Delta_g)$, 1.215 Å,[47] is shorter than for $O_2^-(^2\Pi_g)$.

5.5 **Conclusion**

The dissociation dynamics for O_3^- was studied at E_{hv} = 3.20 eV by optically probing low-lying excited states. These studies complement prior work at other photon energies as well as the observation of Feshbach resonances in electron scattering on O_3. PPC spectroscopy allowed the identification of two ionic dissociation pathways, $O_2(^1\Delta_g) + O^-(^2P)$ and $O_2^-(^2\Pi_g) + O(^3P)$, and determined the energy partitioning among the fragments. The $O_2(^1\Delta_g) + O^-(^2P)$ product channel was observed as 2-photon photodetachment of $O^-(^2P)$ in the photoelectron spectra with coincidence measurements of the energy partitioning supporting the assignment of excited $O_2(^1\Delta_g)$ as a product. The $O_2^-(^2\Pi_g, v''>3) + O(^3P)$ product channel was observed by autodetachment of vibrationally excited O_2^- in the photoelectron spectra. Both ionic dissociation pathways are consistent with DEA experiments assigned to the $^2A_2$ Feshbach resonance. Anions thermalized at 300 K exhibit a strong autodetachment pathway while cooling to < 17 K in COAT effectively turns off the autodetachment pathway. The influence of vibrational excitation of parent O_3^- on the production of vibrationally excited $O_2^-(^2\Pi)$ yielding autodetachment indicates a strong coupling of the vibration in the $^2A_2$ excited state with dissociation to

highly vibrationally excited $O_2^-(^2\Pi_g)$. The addition of COAT to the PPC spectrometer allows controlled heating and cooling of the precursor anions, with the onset of autodetachment from vibrationally excited $O_2^-(^2\Pi_g)$ providing a sensitive probe of the internal excitation as well as unique insights into the photodissociation dynamics. The sensitivity of the autodetachment channel to vibrational excitation in the parent anion makes it an ideal candidate for a state-resolved measurement to provide further insight into the coupling between vibrational excitation of O_3^- and the photodissociation/autodetachment pathway.

Acknowledgements

We acknowledge helpful discussions with R. Otto and preliminary experiments without COAT by C.J. Johnson and R.D. Thomas. KGL acknowledges partial support by a grant from the United States-Israel Binational Science Foundation (BSF), Jerusalem, Israel. This material is based on work supported by the U.S. Department of Energy, Office of Science, and Office of Basic Energy Sciences under award number DE-FG03-98ER14879.

Chapter 5, in full, is a reprint of the material as it appeared in Shen, B.; Benitez, Y.; Lunny, K.; Continetti, R., Internal energy dependence of the photodissociation dynamics of O_3^- using cryogenic photoelectron-photofragment coincidence spectroscopy. *Journal of Chemical Physics* **2017,** *147* (9). The dissertation author is the primary author and the disertation advisor is the corresponding author.

5.6 References

1. Pavlov, A. V., Influence of Atmospheric Solar Radiation Absorption on Photodestruction of Ions at D-region Altitudes of the Ionosphere. *Surv. Geophys.* **2016,** *37* (4), 811-844.

2. Anglada, J. M.; Martins-Costa, M.; Francisco, J. S.; Ruiz-Lopez, M. F., Interconnection of Reactive Oxygen Species Chemistry Across the Interfaces of Atmospheric, Environmental, and Biological Processes. *Acc.Chem. Res.* **2015,** *48*, 575-583.

3. Senn, G.; Skalny, J. D.; Stamatovic, A.; Mason, N. J.; Scheier, P.; Mark, T. D., Low Energy Dissociative Electron Attachment to Ozone. *Phys. Rev. Lett.* **1999,** *82* (25), 5028-5031.

4. Mann, J. E.; Troyer, M. E.; Jarrold, C. C., Photoelectron Imaging and Photodissociation of Ozonide in $O_3^-(O_2)_n$ (n=1-4) Clusters. *J. Chem. Phys.* **2015,** *142* (12), 124305.

5. Cosby, P. C.; Moseley, J. T.; Peterson, J. R.; Ling, J. H., Photodissociation Spectroscopy of O_3^-. *J. Chem. Phys.* **1978,** *69* (6), 2771-2778.

6. Smith, G. P.; Lee, L. C., Photodissociation Spectroscopy of O_3^- and $O_3^-(H_2O)$ From 4170 - 4700 A. *J. Chem. Phys.* **1979,** *71* (5), 2323-2324.

7. Novick, S. E.; Engelking, P. C.; Jones, P. L.; Futrell, J. H.; Lineberger, W. C., Laser Photoelectron, Photodetachment, and Photodestruction Spectra of O_3^-. *J. Chem. Phys.* **1979,** *70* (6), 2652-2662.

8. Hiller, J. F.; Vestal, M. L., Laser Photodissociation of O_3^- by Triple Quadrupole Mass Spectrometry. *J. Chem. Phys.* **1981,** *74* (11), 6096-6105.

9. Arnold, D. W.; Xu, C. S.; Kim, E. H.; Neumark, D. M., Study of Low-Lying Electronic States of Ozone by Anion Photoelectron Spectroscopy of O_3^-. *J. Chem. Phys.* **1994,** *101* (2), 912-922.

10. Garner, M.; Sherwood, C.; Hanold, K.; Continetti, R., Photodissociation Dynamics of O_3^- at 523 nm. *Chem. Phys. Lett.* **1996,** *248* (1-2), 20-26.

11. Garner, M. C.; Hanold, K. A.; Resat, M. S.; Continetti, R. E., Stability and Dissociation Dynamics of the Low-Lying Excited States of Ozone. *J. Phys. Chem. A* **1997,** *101* (36), 6577-6582.

12. Luong, A. K.; Clements, T. G.; Continetti, R. E., Three-body Dissociation Dynamics of Excited States of $O_3(D_2O)$. *J. Phys. Chem. A* **1999,** *103* (49), 10237-10243.

13. Lehman, J. H.; Lineberger, W. C., Visible Spectrum Photofragmentation of $O_3^-(H2O)_n$, n <= 16. *J. Chem. Phys.* **2014,** *141* (15), 154312.

14. Walhout, P.; Silva, C.; Barbara, P., Ultrafast Study of the Photodissociation and Recombination of Aqueous O_3^-. *J. Phys. Chem. A* **1996,** *100*, 5188-5199.

15. Koch, W.; Frenking, G.; Steffen, G.; Reinen, D.; Jansen, M.; Assenmacher, W., The Low Lying Electronic States of O_3^-. *J. Chem. Phys.* **1993,** *99*, 1271-1277.

16. Cui, Q.; Morokuma, K., Ab Initio Studies on the Electronic Excited States and Photodissociation of O_3^- Anion. *J. Chem. Phys.* **1998,** *108* (18), 7684-7694.

17. Curran, R. K., Negative Ion Formation in Ozone. *J. Chem. Phys.* **1961,** *35* (5), 1849-1851.

18. Nestmann, B. M.; Brems, V.; Dora, A.; Kumar, S., Total Cross Sections for Dissociative Electron Attachment to Ozone Caused by the $^2A_2$ Feshbach Resonance. *J. Phys. B.-At. Mol. Opt. Phys.* **2005,** *38* (1), 75-81.

19. Nestmann, B.; Kumar, S.; Peyerimhoff, S., Contribution of Feshbach Resonance to the 1.3-eV Dissociative-Electron-Attachment Cross Section of Ozone. *Phys. Rev. A* **2005,** *71*, 012705.

20. Skalny, J. D.; Matejcik, S.; Kiendler, A.; Stamatovic, A.; Mark, T. D., Dissociative Electron Attachment to Ozone Using a High-Resolution Crossed Beams Technique. *Chem. Phys. Lett.* **1996,** *255* (1-3), 112-118.

21. Walker, I. C.; Gingell, J. M.; Mason, N. J.; Marston, G., Dissociative Electron Attachment (DEA) in Ozone 0-10 eV. *J. Phys. B.-At. Mol. Opt. Phys.* **1996,** *29* (20), 4749-4759.

22. Rangwala, S.; Kumar, S.; Krishnakumar, E.; Mason, N., Cross Sections for the Dissociative Electron Attachment to Ozone. *J. Phys. B.-At. Mol. Opt. Phys.* **1999,** *32* (15), 3795-3804.

23. Allan, M.; Asmis, K. R.; Popovic, D. B.; Stepanovic, M.; Mason, N. J.; Davies, J. A., Production of Vibrationally Autodetaching O_2^- in Low-Energy Electron Impact on Ozone. *J. Phys. B.-At. Mol. Opt. Phys.* **1996,** *29* (15), 3487-3495.

24. Otto, R.; Xie, J.; Brox, J.; Trippel, S.; Stei, M.; Best, T.; Siebert, M. R.; Hase, W. L.; Wester, R., Reaction Dynamics of Temperature-Variable Anion Water Clusters Studied With Crossed Beams and by Direct Dynamics. *Farad. Disc.* **2012,** *157*, 41-57.

25. Hock, C.; Kim, J. B.; Weichman, M. L.; Yacovitch, T. I.; Neumark, D. M., Slow Photoelectron Velocity-Map Imaging Spectroscopy of Cold Negative Ions. *J. Chem. Phys.* **2012,** *137*, 244201.

26. Hanold, K. A.; Luong, A. K.; Clements, T. G.; Continetti, R. E., Photoelectron-Multiple-Photofragment Coincidence Spectrometer. *Rev. Sci. Instrum.* **1999,** *70* (5), 2268-2276.

27. Johnson, C. J.; Shen, B. B.; Poad, B. L. J.; Continetti, R. E., Photoelectron-Photofragment Coincidence Spectroscopy in a Cryogenically Cooled Linear Electrostatic Ion Beam Trap. *Rev. Sci. Instrum.* **2011,** *82* (10), 105105.

28. Wiley, W. C.; McLaren, I. H., Time-of-flight Mass Spectrometer With Improved Resolution. *Rev. Sci. Instrum.* **1955,** *26* (12), 1150-1157.

29. D. Gerlich, G. J., U. Mueck and U. Person Schnelles Ventil Zur Erzeugung Sehr Kurzer Gasimpulse. http://www.tu-chemnitz.de/physik/ION/Technology.

30. Jones, R. M.; Gerlich, D.; Anderson, S. L., Simple Radio-Frequency Power Source for Ion Guides and Ion Traps. *Rev. Sci. Instrum.* **1997,** *68* (9), 3357-3362.

31. Jones, R. M.; Anderson, S. L., Simplified Radio-Frequency Generator for Driving Ion Guides, Traps, and Other Capacitive Loads. *Rev. Sci. Instrum.* **2000,** *71* (11), 4335-4337.

32. Bowen, M. S.; Continetti, R. E., Photodetachment Imaging Study of the Vinoxide Anion. *J. Phys. Chem. A* **2004,** *108* (39), 7827-7831.

33. Hanold, K. A.; Continetti, R. E., Photoelectron-Photofragment Coincidence Studies of the Dissociative Photodetachment of O_4^-. *Chem. Phys.* **1998,** *239*, 493-509.

34. Wang, X. B.; Wang, L. S., Development of a Low-Temperature Photoelectron Spectroscopy Instrument Using an Electrospray Ion Source and a Cryogenically Controlled Ion Trap. *Rev. Sci. Instrum.* **2008,** *79*, 073108.

35. Kamrath, M. Z.; Garand, E.; Jordan, P. A.; Leavitt, C. M.; Wolk, A. B.; Van Stipdonk, M. J.; Miller, S. J.; Johnson, M. A., Vibrational Characterization of Simple Peptides Using Cryogenic Infrared Photodissociation of H_2 Tagged, Mass-Selected Ions. *J. Am. Chem. Soc.* **2011,** *133* (16), 6440-6448.

36. Schulz, G. J., Resonances in Electron Impact on Diatomic Molecules. *Rev. Mod. Phys.* **1973,** *45*, 423 - 486.

37. Allan, M.; Asmis, K.; Popovic, D.; Stepanovic, M.; Mason, N.; Davies, J., Resonances in Collisions of Low-Energy Electrons With Ozone: Experimental Elastic and Vibrationally Inelastic Differential Cross Sections and Dissociative Attachment Spectra. *J. Phys. B.-At. Mol. Opt. Phys.* **1996,** *29* (20), 4727-4747.

38. Ervin, K. M.; Anusiewicz, W.; Skurski, P.; Simons, J.; Lineberger, W. C., The Only Stable State of O_2^- is the X ^2Pi_g Ground State and it (still!) has an Adiabatic Electron Detachment Energy of 0.45 eV. *J. Phys. Chem. A* **2003,** *107* (41), 8521-8529.

39. Ndengue, S.; Madronich, S.; Gatti, F.; Meyer, H. D.; Motapon, O.; Jost, R., Ozone photolysis: Strong Isotopologue/Isotopomer Selectivity in the Stratosphere. *J. Geophys. Res.-Atmos.* **2014,** *119* (7), 4286-4302.

40. Dinu, L.; van der Zande, W. J., Photodestruction of NO_2^- Using Time Resolved Multicoincidence Detection Photofragment Spectroscopy. *Chem. Phys.* **2004,** *300*, 133-141.

41. Rangwala, S. A.; Krishnakumar, E.; Kumar, S. V. K., Dissociative-Electron-Attachment Cross Sections: A Comparative Study of NO_2 and O_3. *Phys. Rev. A* **2003,** *68*, 052710.

42. Li, R.; Hanold, K. A.; Garner, M. C.; Luong, A. K.; Continetti, R. E., Excited State Dynamics in Clusters of Oxygen. *Farad. Disc.* **1997,** *108*, 115-130.

43. Khuseynov, D.; Goebbert, D. J.; Sanov, A., Oxygen Cluster Anions Revisted: Solvent-Mediated Dissociation of the Core O_4^- anion. *J. Chem. Phys.* **2012,** *136*, 094312.

44. Goebbert, D. J.; Sanov, A., Photodetachment, Photofragmentation, and Fragment Autodetachment of [O2n(H2O)m]- clusters: Core-Anion Structures and Fragment Energy Partitioning. *J. Chem. Phys.* **2009,** *131*, 104308.

45. Zittel, P. F.; Little, D. D., Photodissociation of Vibrationally Excited Ozone. *J. Chem. Phys.* **1980,** *72* (11), 5900-5905.

46. Baloitcha, E.; Balint-Kurti, G. G., Theory of the Photodissociation of Ozone in the Hartley Continuum; Effect of Vibrational Excitation and O(D-1) Atom Velocity Distribution. *Phys. Chem. Chem. Phys.* **2005,** *7* (22), 3829-3833.

47. Huber, K.-P., *Molecular spectra and molecular structure: IV. Constants of diatomic molecules*. Springer Science & Business Media: 2013.

Appendix A: Interlock for Machine C

A.1. Instrument Interlock Logic

The interlock for circuit for the machine provides a safety system to protect vital components of the instrument in case of vacuum failures, power distribution problems, and other unforeseen issues. With the installation of COAT, the logic has been modified to include protection circuits for the new source chamber and for COAT. The logic is shown in Figure A1.2 and will be briefly outlined. The instrument can be split into two sections: the HV chambers and the UHV chambers. The interlock system controls the pneumatic valves for the foreline and gate valves as well as the power to essential systems such as power supplies, cryo-heads, and vacuum pumps. The overall goal of the system is to leave the machine in a safe state after a problem has been detected. While it could be designed to simply shut everything down in the case of a problem, a more elegant solution was implemented to only shut down sections where an error has occurred. This means if an error is detected in the source, only the source sections are affected while the UHV detector sections are unaffected. The implementation of the logic is shown in Figure A1.1. The logic is carried out by relays with LEDs indicating the status for each system.

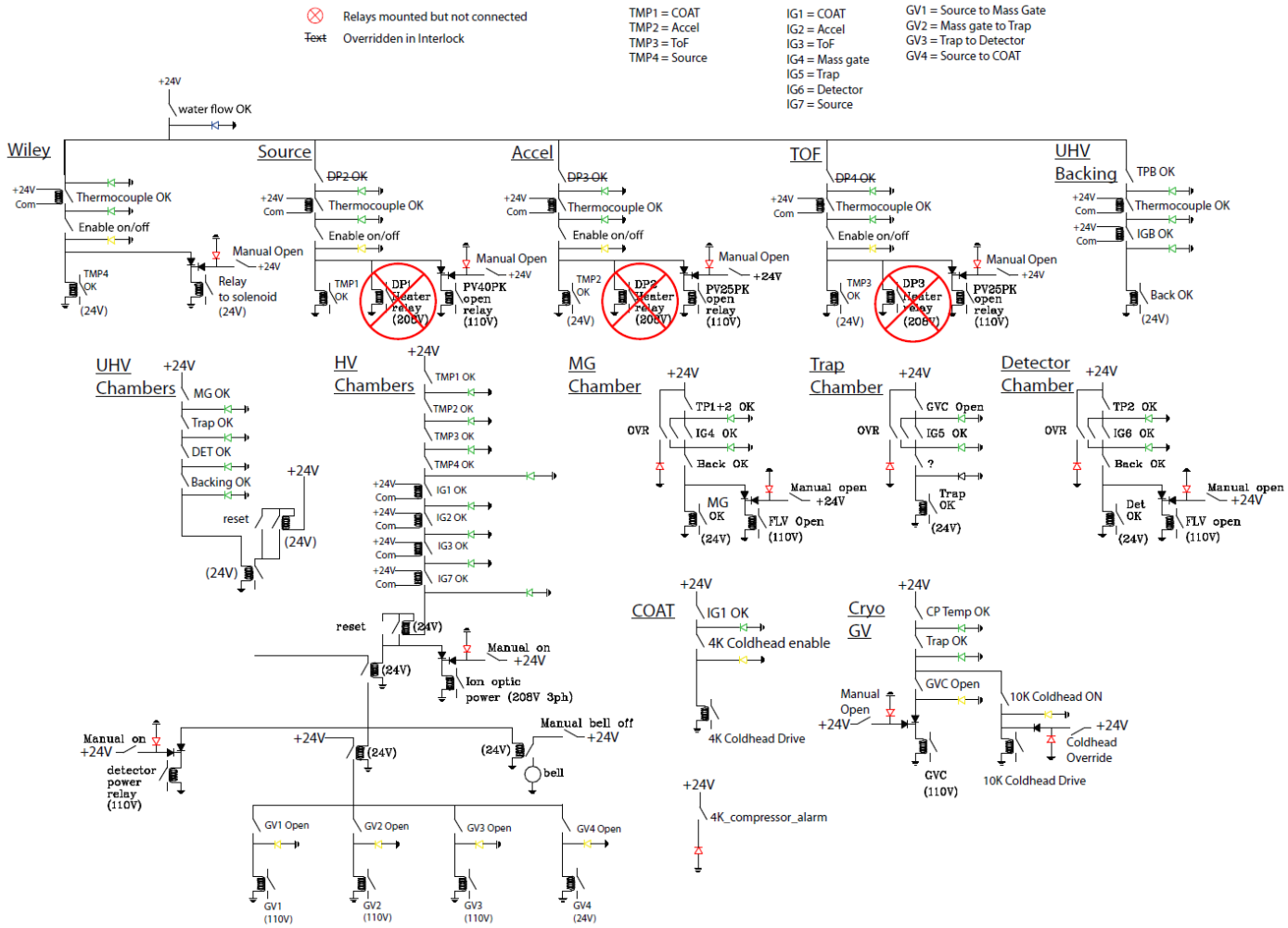

Figure A1.1 Relay and LED map for the operation of the PPC Spectrometer interlock system

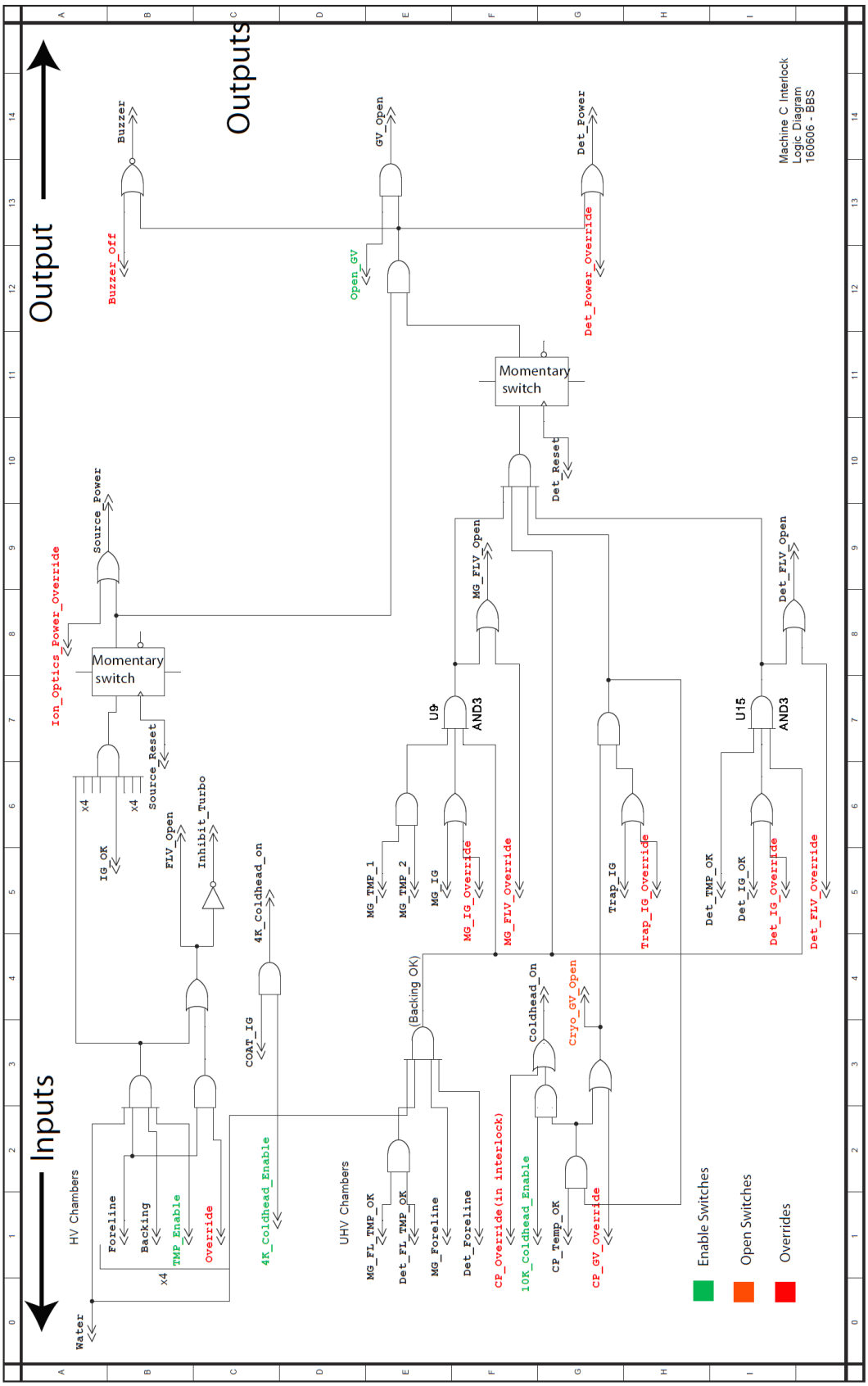

Figure A1.2 Logic diagram for the operation of the PPC Spectrometer interlock system